TLT

TECHNISCHE UNIVERSITÄT MÜNCHEN
Fakultät für Chemie

Lehrstuhl für Technische Chemie II

Unsupported transition metal sulfides for hydrotreating of conventional and renewable feedstock

Manuel Florian Wagenhofer

Vollständiger Abdruck der von der Fakultat für Chemie der Technischen Universität München zur Erlangung des akademischen Grades eines

Doktors der Naturwissenschaften (Dr. rer. nat)

genehmigten Dissertation.

Vorsitzender	Prof. Dr.-Ing. Kai-Olaf M. Hinrichsen
Prüfer der Dissertation	1. Prof. Dr. Johannes A. Lercher
	2. Prof. Dr. Klaus Köhler
	3. Prof. Dr. Roel Prins

Die Dissertation wurde am 24.06.2020 bei der Technischen Universität München eingereicht und durch die Fakultät für Chemie am 11.08.2020 angenommen.

Für meine Eltern und meine Frau Anila,
für Eure Liebe, Geduld und Unterstützung.

One of the symptoms of approaching nervous breakdown

is the belief that one's work is terribly important.

Bertrand Russel, *The Conquest of Happiness* (1930).

Declaration by the author

I declare that I have authored this thesis independently, that I have not used other than the declared resources, and that I have explicitly marked all material which has been quoted either literally or by content from the used resources.

Published content is marked at the beginning of the relevant chapters and reused according to the terms of the publisher. The content and structure of these sections has not been altered except for the numbering and placement of graphic elements (figures, schemes, and tables). Collaborators and their specific contributions are addressed in the acknowledgments section at the end of the relevant chapters.

<div align="right">

Manuel Wagenhofer

June 2020

</div>

Acknowledgements

When I first thought about getting a PhD, I imagined it to be a sure thing that would just require a certain amount of time and dedication. Now, as I am concluding this long journey, I cannot but smile about my earlier self's misjudgement. The truth is, writing this thesis has been an exercise in prolonged suffering which I wouldn't have sustained without vast quantities of coffee and, most importantly, the support of the following people:

I first want to express my gratitude to my doctoral advisor Prof. Dr. Johannes Lercher. Thank you for putting your trust in me and letting me freely follow my scientific curiosity. Even though it was sometimes hard to convince you about a new idea, I always appreciated your genuine interest and straightforward feedback – lousy writing, misleading hypotheses, or sloppy experiments were certainly things you would call by their name.

I am also deeply grateful to my supervisors Dr. Eszter Baráth, Dr. Oliver Gutiérrez, and Dr. Hui Shi, who accompanied me during different stages of my PhD. Eszter, even though you had just joined the group, you took me by the hand and helped me overcome the first obstacles. Thank you for sharing your knowledge about organic chemistry and for always being encouraging and supportive. Oliver, I truly appreciated our discussions about the most minute aspects of hydrotreating catalysis – just as much as our conversations about other important aspects of life, such as food, Game of Thrones, or Mexican wrestling. Thanks for pushing me forward, for patiently listening to my worries, and for convincing me that my work was not as bad as I thought. Hui, you joined me at quite a late stage but nevertheless made a huge impact. Thanks for getting into the matter so quickly and enduring with me the tedious finalization of the "leaching paper". Your clear thinking and concise writing were an essential asset during this last stage of my PhD.

A big thanks goes also to Apl. Prof. Dr. Andreas Jentys. Andy, thank you for your valuable input on EXAFS, for random discussions on the hallway, and for repeatedly prolonging my user agreement. I truly enjoyed listening to your entertaining stories during our late lunch breaks "beim Griechen".

Abstract

Mixed sulfides based on Mo and Ni consist typically of MoS_2, NiMoS, and NiS_x phases. The latter are detrimental to catalytic activity because of intrinsically low activity of NiS_x, leading to quasi-inert catalyst mass, blocking active sites. For reductive desulfurization, the post-synthetic removal of NiS_x enhances hydrogenation rates of the mixed sulfide phase and highlights correlations between active site concentration and activity. For fatty acid deoxygenation, all phases show comparable intrinsic rates but vastly different selectivity. Here, Ni opens an additional pathway involving the breaking of C-C bonds.

Kurzfassung

Mischsulfide auf Basis von Mo und Ni bestehen typischerweise aus MoS_2-, NiMoS- und NiS_x-Phasen. Letztere sind aufgrund der an sich geringen Aktivität von NiS_x für die katalytische Aktivität schädlich, da sie ein quasi-inerter Festkörper sind, der aktive Zentren blockiert. Für die reduktive Entschwefelung erhöht die post-synthetische Entfernung von NiS_x die Hydrierraten an NiMoS und zeigt Zusammenhänge zwischen Struktur und Aktivität auf. Die Deoxygenierung von Fettsäuren verläuft an allen Katalysatoren mit ähnlichen intrinsischen Raten, aber sehr unterschiedlicher Selektivität. Hier eröffnet Ni einen zusätzlichen Weg, der das Spalten von C-C-Bindungen beinhaltet.

Symbols and abbreviations

4,6-DMDBT	4,6-Dimethyl dibenzothiophene
4HDBT	1,2,3,4-tetrahydro-DBT
4-MDBT	4-Methyl dibenzothiophene
6HDBT	1,2,3,4,4a,9b-hexahydro-DBT
AAc	2-Adamantanylacetic acid
at%	Atomic percent
BCH	Bicyclohexyl benzene
BEM	Bond energy model
BET	Brunauer-Emmet-Teller theory of physisorption
BP	Biphenyl
BT	Benzothiophene
c	Concentration
CHB	Cyclohexylbenzene
CLR	Carbon loss reactions (carbon loss route)
CoS_x	Unspecified Co sulfide
CO_x	Unspecified carbon oxide
CUS	Coordinatively unsaturated site
D	Diffusion coefficient
d	Diameter
DBT	Dibenzothiophene
DCO	Decarbonylation
DFT	Density functional theory
DMDS	Dimethyldisulfide
DO	Deoxygenation
e.g.	For example
E_0	Energy of element-specific absorption edge
E_A	Energy of activation

EC	European Comission
ED	Edge decoration
EDX	Energy dispersive X-ray spectroscopy
EU	European Union
EXAFS	Extended X-ray absorption fine structure
f	Fraction
FAEE	Fatty acid ethyl ester
FAME	Fatty acid methyl ester
FCC	Fluid (fluidized-bed) catalytic cracking
FFA	Free fatty acid
FID	Flame ionization detector
FWHM	Full width at half maximum
GC	Gas chromatograph(y)
H ($\bar{H}$)	(Mean) stacking height
HAA	Hexadecanoic acid anhydride
HAADF	High-angle annular dark-field (electron microscopy)
HDM	Hydrodemetalation
HDN	Hydrodenitrogenation
HDO	Hydrodeoxygenation
HDS	Hydrodesulfurization
HEFA	Hydrotreated esters and fatty acids
HOMO	Highest occupied molecular orbital
HRJ	Hydrotreated renewable jet fuel
HVO	Hydrotreated vegetable oil
i.e.	That is
ICSD cc.	Inorganic Crystal Structure Database collection code
IER	Isotopic exchange rate
IR	Infrared
K	Equilibrium constant

K	Shape factor
k	Reaction rate constant
L (suffix)	Leached sulfide
L	Length
LHSV	Liquid hourly space velocity
M	Metal (as in "M edge")
M	Molecular weight
m	Mass
m/z	Mass-to-charge ratio
MES	Mössbauer emission spectroscopy
mol%	Mole percent
N	Coordination number
n	Amount of substance
N ($\bar{N}$)	(Mean) stacking degree
N_S	Number of sites
ND	Number density (of sites)
NiS_x	Unspecified Ni sulfide
NMR	Nuclear magnetic resonance
OCS	Oxygen chemisorption
p (suffix)	Parent sulfide
p	Pressure
ppm	Parts per million
R	Interatomic distance
r	Reaction rate
RE	Rate enhancement factor
Ref.	Reference
rpm	Revolutions per minute
S	Selectivity
SATP	Standard ambient temperature and pressure

SEM	Scanning electron microscopy
SHE	Standard hydrogen electrode
SI	International system of units
(S)SA	(Specific) surface area
STEM	Scanning transmission electron microscopy
STM	Scanning tunneling microscopy
T	Temperature
t	Time
TAG	Triacylglycerol
TEM	Transmission electron microscopy
TG	Triglyceride
TMS	Transition metal sulfide(s)
TOF	Turn-over frequency
TP	Thiophene
V	Volume
vol%	Volume percent
W/F	Catalyst weight-to-volume flow ratio
WHSV	Weight hourly space velocity
wt%	Weight percent
X	Conversion
XANES	X-ray absorption near edge structure
XPS	X-ray photoelectron spectroscopy
XRD	(Powder) X-ray diffraction
ΔG^0	Standard (Gibbs) free energy of reaction
ΔH^0	Standard enthalpy of reaction
ΔNi	Fractional loss of Ni
ΔS	Fractional loss of S
η	Effectiveness factor
θ	Diffraction angle

λ	Wavelength of electromagnetic radiation
μ_i	Stoichiometric coefficient
μ_S	Chemical potential of S
σ^2	Mean square variation in path length
ϕ	Thiele modulus
χ	Molar fraction
ψ	Weisz modulus

Table of contents

1　Introduction

*A*s global petroleum consumption increases and resources are depleted, it is expected that conventional oil production will decline, and production of oil from residua, heavy oils, and tar sand bitumen will increase significantly. Over the next decade, refineries will need to adapt to receiving heavier oils as well as a range of bio-feedstocks. It is likely that current refineries could not handle such a diverse slate of feedstocks without experiencing shut-downs and related problems. As feedstocks to refineries change, there must be an accompanying change in refinery technology.

J. G. Speight, *The Refinery of the Future* (2011).

1.1 The significance of hydrotreating

Hydrotreating is a refinery technology in which petroleum fractions are reacted with hydrogen at high temperature and pressure over transition metal sulfide catalysts. The main purpose is the removal of heteroatoms (sulfur, nitrogen, oxygen, and metals) present in the organic constituents of petroleum. According to the element to be primarily removed, hydrotreating processes are typically referred to as hydrodesulfurization (HDS), hydrodenitrogenation (HDN), hydrodeoxygenation (HDO), or hydrodemetalation (HDM). However, these reactions are not strictly separated and may take place simultaneously in one and the same catalytic unit.

Even though the removal of heteroatoms is the main objective, there are other favorable reactions that occur during hydrotreating. Depending on the reaction conditions and the catalyst, heteroatom removal is typically accompanied by the (partial) hydrogenation of dialkenes, olefins, and polynuclear aromatics – substances which may otherwise act as coke precursors in downstream upgrading processes. To a limited extent, also more severe molecular transformations such as isomerization or cracking may take place. However, this is not the main purpose, and there are dedicated technologies which are more suitable for such "destructive" reactions. It should be emphasized that the term hydrotreating, as used in the broader sense and in this thesis, is limited to "nondestructive" transformations (heteroatom removal and hydrogenation) which leave the molecular size and boiling point of the feedstock essentially unchanged.

Due to its critical role in fuel production, hydrotreating is nowadays employed in virtually every refinery in the world.[1] As fuels are produced and used in inconceivably large quantities, it is no suprise that hydrotreating is the largest industrial application of catalysis by volume of feedstock processed.[2] To put this into perspective, it is worth noting that Germany alone produced 46 million metric tons of diesel/gas oil in 2016, which, however, constituted only about 3 % of the world production of that year.[3]

The great success of hydrotreating has been notably driven by growing environmental concerns. Fuel specifications have become increasingly tight over the past few decades, as governments and policy makers impose ever stricter regulations to cut down on SO_2 and NO_x emissions from fuel combustion. This is not only true for Europe and North America but also for other highly populated areas such as China and Russia.[4] As of today,

all these countries have adopted fuel standards specifying a maximum sulfur content equal to or below 50 mg/kg for on-road diesel and gasoline (Figure 1.1). For example, the latest EU directive on the quality of automotive fuels (2009/30/EC) specifies a maximum sulfur content of 10 mg/kg (or ppm).
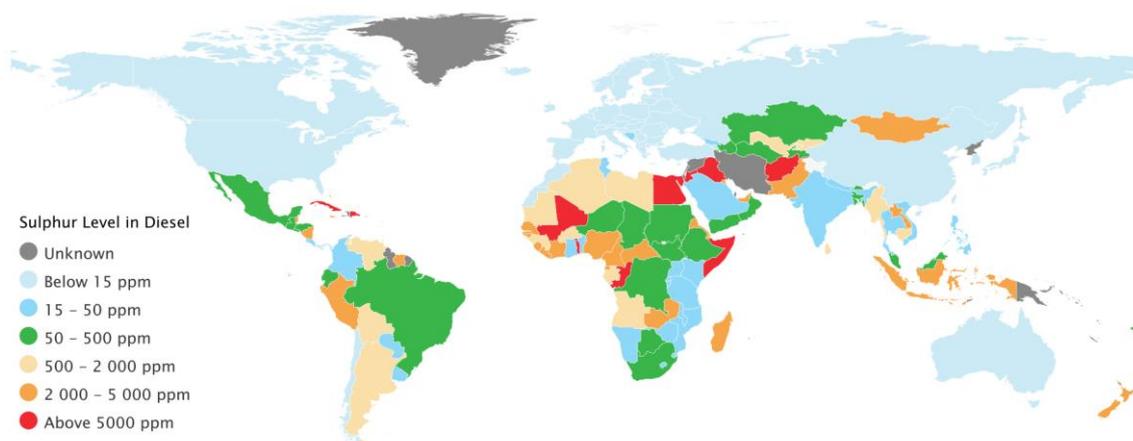
Figure 1.1. Global status of diesel fuel sulfur levels as of July 2019 (reproduced from ref. [4]).

In contrast to these environmental concerns, the second important reason for hydrotreating lies within the refinery. As other processes often use catalysts that are easily and irreversibly deactivated (poisoned) by heteroatom-containing compounds, they may thus operate only on essentially heteroatom-free feedstock. The prime example is catalytic reforming, a process which employs a noble metal catalyst (Pt, Re) for improving gasoline octane ratings by isomerization, cyclization, and aromatization. However, direct poisoning by heteroatoms is not the only issue, as deactivation occurs also by coking. This is especially relevant for the upgrading of highly unsaturated feedstock with low H/C ratio, for example cracked naphtha. In any of these cases, hydrotreating ensures that feedstock quality is sufficient for subsequent refinery operations.

Historically, it were these refining-specific reasons (and not environmental concerns) that stimulated the introduction of hydrogen treatment for improving product quality.[5] First of all, there were no significant indigenous sources of hydrogen in the refinery that could have been used for hydrogenation processes before the introduction of catalytic reforming in the 1940s; and it was only after switching to noble metal reforming catalysts in the late 1940s that a real necessity for heteroatom removal led to the development of a variety of hydrotreating processes.

It is unclear whether the success story of hydrotreating will continue into the future. As large parts of the world have already adopted very stringent fuel standards – at the edge of what is technologically and economically feasible – there are now only few regions left with significant room for improvement: among them Africa, South America, and the Middle East.[4] With an increasing living standard and a growing population owning cars, also these countries may finally adopt more stringent fuel standards, but the growth potential for conventional hydrotreating is small nevertheless. This projected stagnation may finally turn into a decline once essentially sulfur-free fuels from renewable sources[6] become widely available.

As of today, the vast majority of liquid fuels is still produced from crude oil and according to some estimates this situation will not change significantly over the next few decades.[7] While renewable sources such as vegetable oils will substantially gain importance, conventional refinery-produced fuels will stagnate at the current high level and continue to provide the bulk of liquid fuels long into the 2040s. Until then, hydrotreating will face a number of technological and scientific challenges. The declining demand for heavy oils and residues – the so-called "bottom of the barrel" – and the necessity to convert these into lower-boiling products will greatly incentivize further research.[1,8-9] Note also that advancements in the exploration and production of fossil raw materials now allow for the utilization of resources that might have been considered unsuitable in the past: for example, "heavy" and "extra-heavy" crudes, tar sand bitumen, and kerogen.[10] This shift towards lower quality petroleum and the emergence of renewable refinery feedstock will substantially affect hydrotreating catalysis and technology in the years to come.

1.2   Scope and delimitations

The introductory section in chapter 1 is followed by an extensive review of the literature on hydrotreating catalysis and technology in chapter 2. A variety of aspects is discussed from an applied and a fundamental point of view, while a clear focus is put on hydro-desulfurization reactions of conventional petroleum-based feedstock. The major part of chapter 2 is dedicated to the catalytic materials used for such processes, in particular their preparation, structure, and catalytic properties. Special attention is paid to unsupported promoted transition metal sulfides, especially Ni-MoS$_2$, as these are the basis for the original research presented in the later chapters 4 and 5. In this context, a detailed account of the phenomenon of promotion and the role of segregated promoter metal sulfides is given as well.

In contrast to that, the following chapter 3 covers a more recent and unconventional application of hydrotreating: the conversion of renewable raw materials to hydrocarbon-based transportation fuels. After a general introduction to biofuels, special attention is paid to fuels produced by hydrotreating of biogenic lipids such as vegetable or animal oils and fats. The challenges and potential of this emerging technology are put in perspective with the current state-of-the-art. This is followed by a discussion of the chemistry of lipid hydrodeoxygenation, in particular, molecular-level reaction mechanisms, as well as thermodynamic and kinetic aspects. The catalysts used for such transformations, most importantly transition metal sulfides, are covered in the final section of chapter 3. Just as in conventional hydrodesulfurization, an emphasis is put on the ambiguous role of segregated promoter metal sulfides.

The first piece of original research, presented in chapter 4, is concerned with bulk Ni-MoS$_2$ catalysts for conventional hydrotreating application: More specifically, it deals with the hydrodesulfurization of dibenzothiophene, which is a sulfur containing, binuclear, aromatic compound. In view of the current shift to more refractory feedstock, bulk catalysts are becoming increasingly interesting for refiners, as they promise unprecedented volumetric activities. Unfortunately, these materials are notoriously difficult to characterize because of their complex three-dimensional structure and multi-phasic composition. Consequently, there is still no standard experimental protocol able to link the catalytic activity to the physical, structural and chemical properties of the catalysts.

Such structure-function relations are, however, at the core of any rational approach for preparing and selecting optimal catalysts. The present work is aimed at closing this gap.

For this purpose, a post-synthetic acid treatment is applied to a series of bulk Ni-MoS$_2$ catalysts with varying Ni concentration. This procedure modifies the catalysts such that meaningful structure-function relations can be obtained. First, the procedure itself as well as its effects on the composition and structure of the catalysts is systematically evaluated. Special attention is paid to the local environment of the Ni-containing active sites and the global distribution of Ni among the different phases. Next, the catalysts are analyzed with respect to their selectivity and activity in the conversion of dibenzothiophene under typical hydrotreating conditions. Finally, the results of the kinetic measurements are correlated and discussed in connection with the catalysts' structural properties. Having successfully established a concept for determining site-specific activity in bulk sulfides, the intrinsic reaction rates are then compared to those of a typical supported catalyst. Even though acid treatment has substantial effects on activity, it should be noted that the catalysts in this study are not specifically designed for superior performance. The preparation is rather targeted at maximal performance differences within the series, in hope of facilitating the isolation of the common activity parameters. Due to the focus on hydrodesulfurization, the present work cannot account for phenomena related to the simultaneous presence of other heteroatom-bearing compounds (e.g., inhibition by N-organic bases), even though this is a highly relevant complication occurring in real hydrotreating operations. Further, it is unclear whether the effects observed in this study are applicable to related hydrotreating reactions, in particular denitrogenation, deoxygenation, and demetalation.

The second piece of original research, presented in chapter 5, is dedicated to the hydroconversion of renewable lipid feedstock over conventional hydrotreating catalysts. The main motive of this work is to determine how the reaction can be controlled in such a way that the output of the desired product is maximized, while the consumption of energy, raw and auxiliary materials is kept at a minimum. Numerous reports show that lipid hydroprocessing is feasible using the reaction conditions and catalyst systems devised for conventional hydrotreating. However, much of the literature is only superficial when it comes to molecular-level aspects, even though it would be vital to

understand how exactly the given catalyst systems work in combination with unconventional feedstock. This is particularly important in view of the emerging co-hydroprocessing of renewable lipids. Hence, the present study is not focused on developing an optimal catalyst from a selection of available or novel materials. It is rather dedicated to identifying the catalytically active features in conventional HDS catalysts and understanding their interaction with lipid molecules. In the longer term, this should enable the hydrotreating community to modify or re-design existing catalyst systems and choose the most suitable reaction conditions for the conversion of oxygen-rich lipid feedstock.

These objectives are achieved by means of physico-chemical characterization, focused on the properties of the catalysts, and test reactions with different model reactants. First, a reaction network is established using the common intermediate of lipid deoxygenation (a free fatty acid), while intentionally ignoring the more trivial steps of triglyceride decomposition. The conversion of subsequent products and intermediates is then studied separately under identical conditions. Key evidence is provided by reactants with "restricted" reactivity, used for falsifying certain mechanistic hypotheses. In an additional series of experiments, temperature and H_2 partial pressure are varied separately to determine activation barriers and reaction orders, giving further clues about the elementary surface reactions. These results are then combined with an analysis of the chemical and physical properties of the catalyst. Note that the catalysts chosen for this study are designed to exhibit maximal differences in selectivity, whereas high activity is not a criterion. Potential artifacts associated with functional groups on the support are excluded by the use of unsupported catalysts. It is worth noting that this study is focused solely on the elimination of oxygen from renewable model reactants: That is, additional chemical transformations necessary for producing renewable fuels are not within the scope of this work (e.g., dewaxing or the adjustment of molecular size via hydrocracking). Neither does the present work intend to answer scientific and technological questions arising due to the feedstock's chemical properties (e.g., corrosiveness, increased heat release, release of water and of oxygenated gases).

The pressures and temperatures used in the experimental part of chapters 4 and 5 are within the approximate range of industrial hydrotreating, but other parameters may not be representative of an industrial setting. First, the model reactants and solvents used in

the present work are highly pure substances, which is necessary to facilitate product analysis. Of course, this approach must ignore the potential influence of impurities found in commercially available, mass-produced feedstock. Second, the high dilution of the reactant has to be considered when generalized conclusions are to be drawn. Compared to industrial applications, substantial differences are expected to arise because of the design and size of the laboratory-style reactor setups. While the batch reactor used for lipid deoxygenation offers practical advantages, such as the possibility to quickly record full conversion curves, it is far from representing the situation in an industrial fixed-bed hydrotreater. Potential limitations of the setup are addressed in the supporting information of chapter 5, for example, the fact that H_2 concentration cannot be held constant, or that gaseous products (H_2O, CO, CO_2) may accumulate and interfere with the model reactants. In contrast to that, the fixed-bed reactor used for hydrodesulfurization in chapter 4 is much more similar to its industrial counterpart. Even in this case, however, substantial differences are likely to be present due to the reactor's small internal volume and the dilution of both the catalyst and the reactant. The resulting homogeneous temperature distribution cannot be compared to the complex profiles found in industrial-sized reactors. Another important aspect is catalyst deactivation. While care was taken to stabilize the model catalysts by prolonged exposure to the reaction conditions before kinetic measurements, the time scale used is still negligible compared to real-life applications, which are in the range of months or years of continuous operation. Accordingly, it remains to be elucidated whether the present findings are also applicable to aged or multiply regenerated hydro-treating catalysts. In the specific case of acid-treated catalysts (chapter 4), it is unknown whether the observed structural changes are stable over time and how much of a benefit can be expected after longer operation. This is especially concerning in view of the continuous addition of metal impurities contained in extra heavy feedstock (e.g., during asphaltene demetalation).

1.3   References

(1)   Chianelli, R. R.; Berhault, G.; Torres, B. *Catal. Today* **2009,** 147, 275-286.

(2)   Prins, R. *Hydrotreating*. In *Handbook of Heterogeneous Catalysis*, Ertl, G., Knözinger, H., Schüth, F., Weitkamp, J. Eds. Wiley-VCH: Weinheim, Germany **2008**, pp 2695-2718.

(3)   *Energy Statistics Yearbook*. United Nations **2016**, unstats.un.org/unsd/energystats/pubs/yearbook (19.04.2019).

(4)   *Global Sulfur Levels*. United Nations Enviroment Programme **2019**, unenvironment.org/global-sulphur-levels (19.04.2019).

(5)   Alfke, G.; Irion, W. W.; Neuwirth, O. S. *Oil Refining*. In *Ullmann's Encyclopedia of Industrial Chemistry*, Wiley VCH: Weinheim **2007**, pp 207-261.

(6)   Gosselink, R. W.; Hollak, S. A.; Chang, S. W.; van Haveren, J.; de Jong, K. P.; Bitter, J. H.; van Es, D. S. *ChemSusChem* **2013,** 6, 1576-1594.

(7)   *BP Energy Outlook 2019 edition*. BP **2019**, bp.com/energyoutlook (14.04.2019).

(8)   Furimsky, E. *Appl. Catal., A* **1998,** 171, 177-206.

(9)   Ancheyta, J.; Speight, J. G. *Hydroprocessing of heavy oils and residua*. CRC Press: Boca Raton, Florida **2007**, 376 pages.

(10)   Speight, J. G. *Hydrotreating Processes*. In *Handbook of petroleum refining*, CRC Press: Boca Raton, Florida **2017**, pp 409-455.

2   Fundamentals of hydrotreating catalysis

Es war damals ein allgemein anerkanntes Dogma, daß Kontaktsubstanzen, welche die Anlagerung von Wasserstoff an Elemente oder Verbindungen zu katalysieren vermögen, grundsätzlich durch die Gegenwart selbst kleinster Mengen freien oder gebundenen Schwefels vergiftet, d.h. ihrer Wirksamkeit beraubt werden. [...] Da nun die für die in Aussicht genommene Druckhydrierung in Frage kommenden Rohstoffe (Kohle, Teere, Mineralöle) durchweg schwefelhaltig sind, erschien nach dem damaligen Stande von Wissenschaft und Technik die Anwendung von Katalysatoren bei der Druckhydrierung der genannten Materialien aussichtslos. [...] In systematischer Arbeit wurde das periodische System der Elemente durchprobiert, und im Molybdän und Wolfram wurden Elemente gefunden, die an sich eine sehr gute Hydrieraktivität aufweisen und diese auch in Gegenwart von Schwefel beibehalten.

W. Krönig, *Die katalytische Druckhydrierung von Kohlen, Teeren und Mineralölen* (1950).

Free translation: *"It was then a generally acknowledged dogma that contact substances, which catalyze hydrogen addition to the elements or to compounds, are categorically poisoned by the presence of even minuscule amounts of free or bound sulfur. That is, they are deprived of their efficacy. [...] According to the technological and scientific state-of-the-art of those times, it seemed illusory to use catalysts for pressure hydrogenation, because the raw materials considered for this process (coals, tars, mineral oils) all contain sulfur. [...] The periodic table of elements was then tested systematically, and the elements molybdenum and tungsten were found to have a very good intrinsic hydrogenation activity, which they also maintain in presence of sulfur."*

2.1 Industrial application

Hydrotreating plants represent the highest capacities of all secondary refining processes worldwide.[1] A typical refinery has not one but multiple hydrotreating units installed in strategic locations (Figure 2.1). In these units, petroleum fractions of varying origin and composition (Table 2.1) are reacted with hydrogen at elevated temperature, most typically in the range of 300–400 °C, and moderate to high pressure in the range of 7–160 bar over a fixed bed of sulfided $Co\text{-}Mo/Al_2O_3$ or $Ni\text{-}Mo/Al_2O_3$ catalyst (see also section 2.3).[2-3] Other important process parameters include the H_2/oil ratio and the space velocity. These individual process parameters are often summarized under the term "process severity", where a high severity is associated with high temperature, high pressure, high H_2/oil ratio, and low space velocity.

Figure 2.1. Example of a refinery process flow scheme illustrating the key role of hydrotreating in the modern petroleum refinery (adapted from ref. [4]).

A conventional hydrotreating unit typically operates in co-current down flow mode, i.e., (vaporized) oil and hydrogen both flow in vertical direction towards the bottom of the reactor.[5] Hydrogen is introduced at several points along the reactor in a quantity corresponding to multiples of the chemical consumption rate. This is done in order to maintain high reaction rates and to suppress the build-up of carbonaceous deposits.[2] The heteroatoms are removed in the form of H_2S, NH_3, and water, and subsequently scrubbed from the reactor effluent at the reactor outlet, whereas hydrogen is recycled by means of a (high-pressure) separator.[6-7] While S-, N-, and O-containing contaminants form products that are easily separated from the liquid oil stream, metal salts and metallo-porphyrins (Ni, V) are much more problematic, because the non-volatile metal-containing entities cannot leave the reactor and will hence form metal sulfide deposits on the active phase. This can severely limit the lifetime of the catalyst from typically 2 to 3 years to only a few months,[2] especially in the processing of heavy feedstock. It should be emphasized that the concentration of contaminants, particularly refractory S- and N-compounds and metals in distillation residues, can significantly exceed that of the distilled crude oil fractions.[2]

Table 2.1. Elemental composition of crude oils (wt%). Heavy crudes will generally have lower H/C ratio and higher heteroatom content than light crudes.[2]

Carbon	83–87	Oxygen	0.05–1.5
Hydrogen	10–14	Sulfur	0.05–6.0
Nitrogen	0.1–2.0	Metals (Ni, V)	< 0.1

Of the multiple hydrotreating units in a typical refinery, at least one is generally dedicated to treating reformer feedstock, which needs to be essentially sulfur free because of the heteroatom-sensitive catalysts employed there. Other hydrotreating units are dedicated to treating the various middle distillates serving as ingredients and precursors of diesel, fuel oils, and jet-fuel.[2] The process parameters can vary within the ranges given in Table 2.2 and are strongly dependent on the properties of the catalyst, the desired product slate, and the properties of the feedstock (i.e., density, viscosity, boiling point, H/C ratio, content and structure of the heteroatom-bearing compounds). As it is not within the scope of this work to provide a comprehensive treatise on the large variety of hydrotreating processes, the following paragraphs will only briefly outline the fundamental requirements for processing different feedstocks, using naphtha and atmospheric residue as an

example.[2] A more extensive review of the process conditions used in hydrotreating can be found elsewhere.[1-3,5-11]

Table 2.2. Process parameters for the hydrodesulfurization of different petroleum fractions.[2]

Feedstock	Boiling range (°C)	Process conditions			
		Temperature (°C)	H_2 pressure (bar)	H_2/oil (Nm³/m³)	LHSV [a] (h⁻¹)
Naphtha	70–170	300–370	7–32	50–270	5–8
Kerosene	160–240	330–370	11–35	90–270	4–6
Gas oil	240–350	340–400	11–49	180–360	2–6
Vacuum gas oil	350–650	360–400	32–56	180–710	1–3
Residua	> 650	370–450	53–158	270–1800	0.5–2

[a] LHSV: Liquid Hourly Space Velocity (m³ of liquid feed per m³ of reactor volume per hour).

Naphtha is the lowest-boiling liquid fraction in the refinery and originates either directly from the distillation column ("virgin" or "straight-run" naphtha) or from carbon rejection routes, such as coking or catalytic cracking. Fluid catalytic cracking, or FCC, is often the major source of naphtha in the refinery.[3] Straight-run naphthas are poor in olefins and aromatics, and thus need to be further processed in the reformer which optimizes octane ratings for later gasoline blending. Because of its low-boiling point, naphtha can be easily brought to evaporation before introducing it into the reactor. With the reactants completely in the gas phase, naphtha HDS is thus rarely affected by pore diffusion limitation. This has beneficial consequences for catalyst choice, which is not restricted by pore diameter, and allows for a lower reaction temperature because of the high diffusion rate. Depending on the origin of the naphtha, sulfur contents may range from as little as 0.01 wt% in straight-run fractions up to 1 wt% in coker or FCC naphtha. However, the S compounds in this fraction are relatively reactive and their C–S bonds are broken easily at moderate temperature without requiring prior hydrogenation (see sections 2.2.1 and 2.2.2).[12] Because of this, catalysts used in naphtha HDS need only a low to moderate hydrogenation activity, which is found, for example, in Co-Mo/Al_2O_3. The right choice of catalyst helps reducing the consumption of hydrogen by selectively promoting HDS and disfavoring saturation of valuable olefins. Olefin concentration may be considerable in cracked naphtha, in which case the hydrogen partial pressure needs to be fine-tuned between optimized coke suppression and retaining of olefins (favored by high and low H_2 pressures, respectively). Due to the mild process conditions and the absence of metallic

impurities in the feedstock, naphtha HDS catalysts are among those with the longest life time in the refinery.

In contrast to naphtha, the higher-boiling fractions of the same crude generally need more severe process conditions and more specific catalyst design. For example, in the HDS of atmospheric residue (a liquid-phase process), catalyst pore diameters need to be larger to improve diffusion of the high-boiling, bulky compounds found in that fraction, e.g., asphaltenes, metallo-porphyrins, and substituted dibenzothiophenes. Larger pore diameter and volume also help in delaying catalyst deactivation, which occurs extensively due to coking of unsaturated molecules and the build-up of metal deposits from demetalation. Because of the refractory nature of the heavier heteroatom-bearing compounds, residue HDS is best performed in presence of catalysts with a stronger intrinsic hydrogenation activity, e.g., $Ni-Mo/Al_2O_3$ and (rarely) $Ni-W/Al_2O_3$ (see section 2.3). In combination with a high hydrogen pressure, this helps to suppress extensive coking but comes at the cost of increased hydrogen consumption. Despite high catalyst activity, residue HDS needs high temperatures in order to improve diffusion in the liquid phase and to increase the reaction rate of refractory impurities via pre-hydrogenation (see section 2.2.2). In practice, even higher temperatures would be desirable, but that would sacrifice some of the catalyst's life time and increase the yield of low value, small molecules due to the onset of hydrocracking reactions. As the maximum temperature is limited (technically and thermodynamically), space velocity needs to be decreased accordingly to ensure sufficient conversion.

2.2   The chemistry of hydrotreating processes

The following section describes well-established facts about the reactions of molecules occurring in typical hydrotreating processes. This extensive body of knowledge has been reviewed periodically in a number of books,[1-7,9-10,13] encyclopedic entries,[8,14] and review articles.[15-20] Unless stated otherwise, the information presented in the following is based on these references.

In general terms, petroleum or any other refinery feedstock is a mixture of hydrocarbons and hetero compounds. The heteroatom content alone is, however, insufficient for determining the processing requirements of one particular kind of feedstock, and the reactivity depends critically also on the molecular structure of the individual constituents. These are divided into the following categories:

- Saturates: linear and branched alkanes, and cycloalkanes
- Aromatics: benzene, toluene, xylene, naphthalene, phenanthrene, etc.
- Sulfur compounds: thiols (mercaptans), thioethers, and thiophene derivatives
- Nitrogen compounds: pyridines, pyrroles, amides
- Oxygen compounds: phenols, carboxylic acids
- Metallic constituents: dissolved organometallics (e.g., porphyrins) and suspended metal salts

While all these compounds may be simultaneously present in hydrotreating feedstock, not all are equally relevant. Chemical transformations of saturates and aromatics, for example, occur regularly during hydrotreating, but it is not the main objective of the process and there are more efficient, dedicated processes to achieve these goals: e.g., reforming, catalytic cracking, and hydrocracking. This is equally valid for metallic constituents. These are extremely difficult to remove but often not volatile enough to be found in distilled fractions. Their removal from the distillation residue is best addressed separately in specialized reactors. Hence, the main task to be accomplished by the hydrotreater is the removal of S, N, and O from organic compounds. Of these three, mainly S and N are targeted, as oxygen compounds are usually not that highly concentrated and typically less problematic during processing and later fuel use. Nitrogen is generally more difficult to remove than sulfur, and nitrogen-rich feedstock will often

require a special catalyst. In addition, N-containing molecules can severely inhibit the reactivity of other molecules due to strong adsorption to the catalyst surface.[19] As far as this work is concerned, the focus is on the removal of sulfur from petroleum constituents, and hence there will be no detailed descriptions in regard of other reactant molecules. Note that oxygen compounds in the form of lipids are addressed separately in chapter 3 in connection with hydrotreating of renewable feedstock. Lipids are typically not found in conventional hydrotreating feedstock.

2.2.1 Organosulfur compounds

Several classes of organosulfur compounds are found in petroleum fractions (Figure 2.2). Small molecules such as propanethiol and simple thiophenes (TP) are more likely to be present in the light petroleum fractions, while larger molecules like benzothiophenes (BT) and dibenzothiophenes (DBT) are typically found in the diesel and jet range hydrocarbon fractions (so-called "middle distillates"). Even larger heterocycles, containing more than three aromatic rings, are characteristic for heavy fractions and distillation residues. It is worth noting that that the S content generally increases in proportion with the boiling range of the distillate; that is, there is more S bound in heavy molecules than in lighter ones. Middle distillates may nevertheless contain disproportionately more S due to the thermal decomposition of heavy S compounds during distillation.
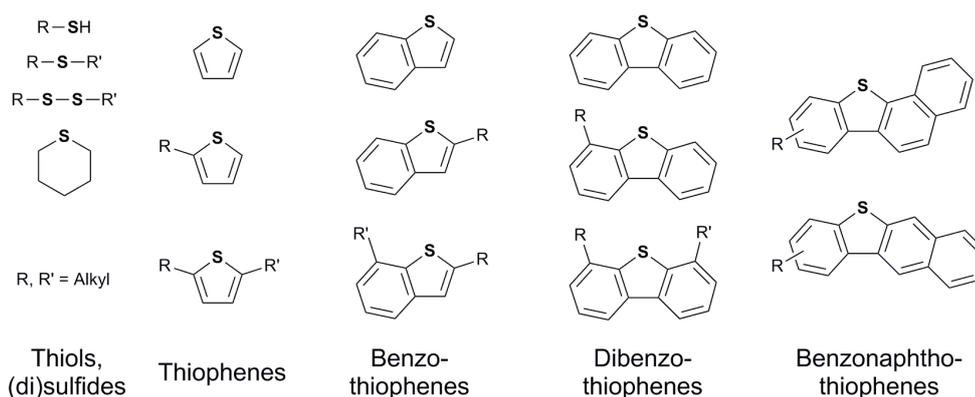
Figure 2.2. Selected classes of S compounds found in typical HDS feedstock.

For HDS, the overall S content of the feedstock is much less relevant than the structure of the S bearing molecules. This is because the local configuration around the S atom has

a dramatic impact on the molecule's reactivity. While lighter hetero compounds are in general much easier to desulfurize than heavier ones (Figure 2.3 A), this trend is not directly related to the molecular weight but rather to the steric and electronic effects that follow the complexity (size) of the molecule. It was found that the higher analogues of thiophene are substantially more refractory in HDS than thiophene: DBT, for example, is approximately two orders of magnitude less reactive than TP under identical reaction conditions. This has been attributed to the decreased accessibility of the S atom in BT and DBT and to the stabilization by the more extended π-electron system. The steric effect is nicely demonstrated by comparing the HDS rate constants of dialkylated DBTs (Figure 2.3 B). Methyl substituents in the 4 and 6 positions, adjacent to the S atom, have a more substantial impact than substituents in the 2/8 or 3/7 positions. This causes 4,6-DMDBT to be roughly 10 times less reactive than unsubstituted DBT and, in fact, it is often found that 4,6-alkylated DBTs remain intact until the final stages of HDS. Note that already a single methyl group vicinal to sulfur has a tremendous impact on the rate (4-MDBT).
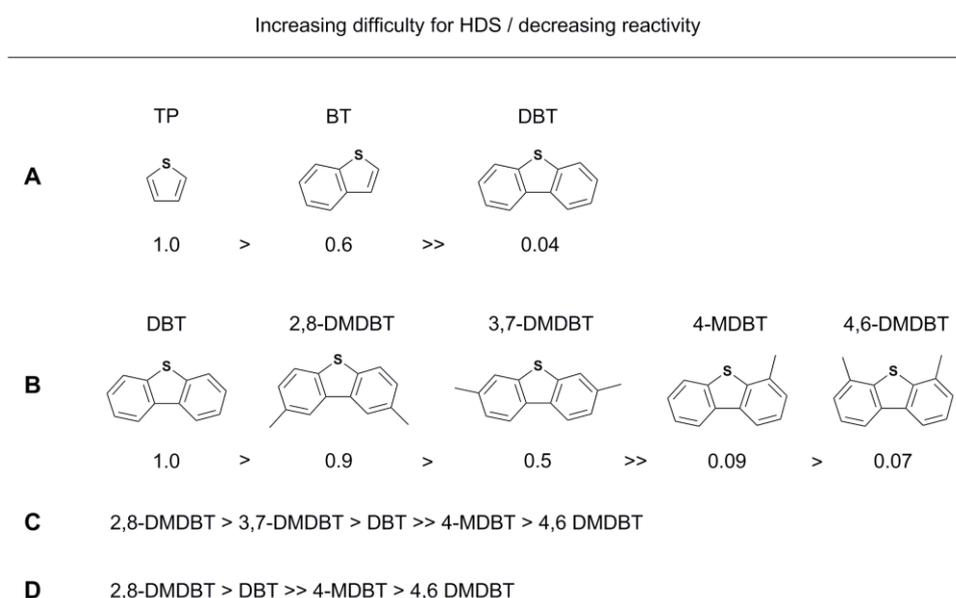
Figure 2.3. Reactivity of organosulfur compounds in HDS. (**A**) Rate constant of thiophene (TP), benzothiophene (BT), and dibenzothiophene (DBT) relative to TP.[21] (**B**) Effect of methyl substituents in methyl- and dimethyl-dibenzothiophene (MDBT and DMDBT, respectively) relative to DBT.[22] Reactivity sequence of alkyl-DBTs according to refs. [23-24] (**C**) and ref. [25] (**D**).

Substituents may induce electronic effects, even though these are typically less significant than the effects of steric repulsion. It was found that distant methyl groups in the 2/8 or 3/7 positions, which barely affect the steric situation of sulfur, may even

enhance HDS rates compared to unsubstituted DBT (Figure 2.3 C and D). The fact that these substituted analogues react more readily than DBT was attributed to the inductive effect of the methyl groups, which increases electron density at the S atom, and therefore enhances the interaction with Lewis-acidic surface sites (exposed metal cations). Note, however, that this effect is rather subtle and might be absent or even reversed under different reaction conditions.

2.2.2   Desulfurization mechanisms

All HDS reactions share a fundamental pattern, which is independent of the reactant and best described by a Langmuir-Hinshelwood-type mechanism: (1) adsorption and coordination of the reactant at the coordinatively unsaturated metal cations of the metal sulfide, (2) surface reaction with dissociated ("active") hydrogen aided by so-called SH groups, and (3) desorption of desulfurized hydrocarbon and H_2S. The third step regenerates the coordinatively unsaturated site and the cycle is repeated with a new reactant molecule (see section 2.3.3 for detailed accounts of hydrogen activation and the nature of the active sites). Depending on the structure of the molecule, there are differences in the mode of adsorption and in the complexity of the surface reaction which typically involves multiple steps.

The desulfurization of aliphatic and aromatic thiols is among the simplest reactions in HDS. It takes place via β-hydrogen elimination of H_2S and subsequent hydrogenation of the resulting alkene or via direct C-S hydrogenolysis:

$$\beta\text{-H elim. / hydrogenation:}\quad R-CH_2-CH_2-SH \xrightarrow{-H_2S} R-CH=CH_2 \xrightarrow{+H_2} R-CH_2-CH_3$$

$$\text{Hydrogenolysis:}\quad R-CH_2-CH_2-SH \xrightarrow[-H_2S]{+H_2} R-CH_2-CH_3$$
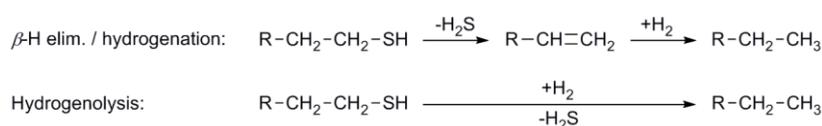
The elimination step occurs via well-known acid-base reactions at the catalyst surface, involving sites on the metal sulfide phase and, if present, on the support. Hydrogenation and hydrogenolysis, on the other hand, need dissociated hydrogen which is supplied only by the metal sulfide phase. In general, the elimination route is more rapid than the hydrogenolysis route for aliphatic thiols, except for thiols that lack β-H atoms (like CH_3SH). In this case, hydrogenolysis is the only possible reaction route. Also arylthiols, like thiophenol, react predominantly via hydrogenolysis yielding benzene and H_2S.

The simplest aromatic S-heterocycle, thiophene, has also a relatively well-understood reaction mechanism, which occurs mainly via hydrogenation to tetrahydrothiophene under typical HDS conditions (the low-pressure mechanism is still under debate, even after decades of research). The saturated intermediate may then undergo two successive β-H eliminations (as shown above for thiols) to give butadiene and finally n-butane. Given their high reactivity, the thiol intermediates and butadiene are difficult to observe experimentally and it is possible that the mechanism may actually consist of an alternating sequence of elimination and hydrogenation:
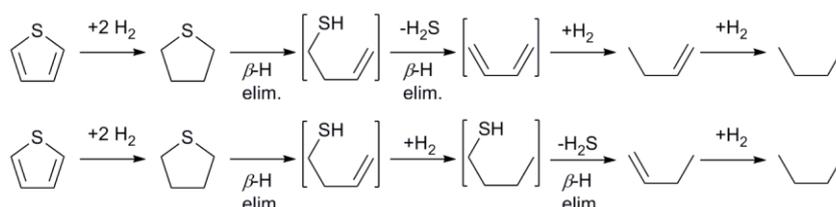
Desulfurization of the larger heterocycles, BT, DBT, and alkyl-DBTs, is more complex than for TP and thiols. It can in principle occur via two distinct routes, referred to as hydrogenation (HYD) and direct desulfurization (DDS) (Figure 2.4). In DDS no intermediates are observed, hence its "direct" character, even though it is unlikely that both C-S hydrogenolysis steps occur in a concerted fashion. That is, there should be an intermediary biphenyl-2-thiol (surface species) which reacts rapidly without desorbing from the catalyst. At incomplete DBT conversion, biphenyl (BP) is usually not further hydrogenated to cyclohexyl benzene (CHB) and bicyclohexyl (BCH) because it adsorbs much more weakly than DBT (apart from potential thermodynamic limitations). Under laboratory conditions, i.e., at low or differential conversion, it is thus very easy to distinguish between DDS and HYD products, as there is no interconversion between the two routes. For unsubstituted DBT, it is generally found that DDS is the major route over Co-MoS$_2$ and Ni-MoS$_2$ catalysts (DDS selectivity of roughly 90 % and 70 %, respectively). Note, however, that different product distributions have been observed in a few cases, especially in connection with bulk Ni-MoS$_2$ (see chapter 5).

While direct sulfur extrusion is the major route for unsubstituted DBT, it may be preceded by partial hydrogenation (HYD route, Figure 2.4). The tetrahydro-DBT intermediate formed in this process is further hydrogenated to its hexahydro form, which

now allows C-S bond scission via elimination/hydrogenation or hydrogenolysis as described earlier for thiophene. The resulting arylthiol is finally hydrogenolyzed to CHB. Further hydrogenation of this S free intermediate does generally not occur until DBT has been fully consumed (analogous to the situation of BP in DDS). The partially hydrogenated intermediates and the arylthiol are typically not observed, as the first hydrogenation step to tetrahydro-DBT is rate limiting and the subsequent steps, accordingly, much faster.
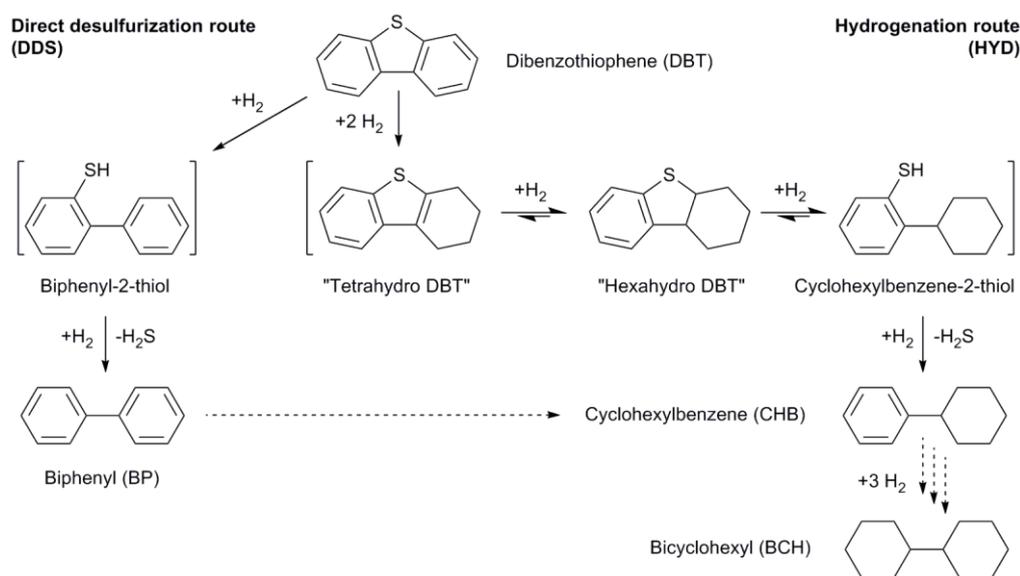
Figure 2.4. Reaction network of dibenzothiophene HDS. Dashed arrows indicate reactions that are typically only observed after full conversion of DBT.

It is believed that the different reactivity of DBT in the DDS and HYD route arises because of different modes of adsorption (Figure 2.5). Adsorption of DBT perpendicular to the catalyst surface allows for the formation of a strong σ-bond between the coordinatively unsaturated metal site and the S atom. This weakens the C-S bond and enables direct sulfur extrusion. Hydrogenation, on the other hand, is initiated from a parallel ("flat") adsorption state, where the main interaction with the catalyst surface occurs via the aromatic π-electrons. While this does not sufficiently weaken the C-S bond and C-S cleavage is still unfavorable in this state, it enables hydrogenation of one of the benzene rings. This not only mitigates steric hindrance by allowing the methyl group to rotate out of the formerly rigid plane; it also reduces C-S bond strength and creates the

possibility for β-hydrogen elimination.[26] The successive steps may then proceed with relative ease according to the mechanisms outlined for TP and thiophenol.
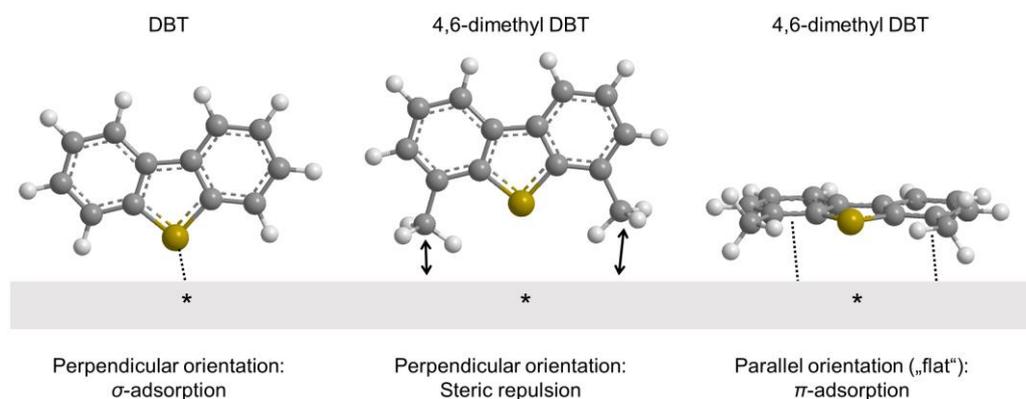
Figure 2.5. Possible adsorption modes of unsubstituted and 4,6-dimethylated dibenzothiophene. Perpendicular adsorption is associated with direct desulfurization (hydrogenolysis) and parallel adsorption with the hydrogenation route. The asterisk indicates a coordinatively unsaturated metal site on the metal sulfide surface.

In alkylated DBT and BT, the perpendicular adsorption mode is hindered by steric repulsion, and thus DDS is strongly suppressed. This is especially true for DBT with alkyl groups in the 4- and/or 6-position (adjacent to the sulfur atom). For these molecules only the parallel adsorption mode is feasible, and thus HYD becomes the only route. This restriction towards the slower HYD route is the main reason why 4,6-alkylated DBTs are among the most refractory molecules in HDS feedstock.

Quite often, HDS studies and catalyst design specifically target the least reactive constituents of HDS feedstock, especially DBT and its 4,6-methylated analogues. DBT is readily commercially available and thus a good model compound when both DDS and HYD pathways are to be explored, such as in the present study. 4,6-DMDBT, on the other hand, is often chosen when novel catalysts are to be screened for HYD activity or when there is an isolated interest in HYD reaction mechanisms or HYD active sites.

2.2.3 Thermodynamics of hydrodesulfurization

The majority of HDS reactions are significantly exothermic (Table 2.3), with a heat release approximately proportional to the amount of hydrogen needed to desulfurize and/or saturate the reactant (i.e., similar reaction enthalpy per mole H_2). In the β-H

elimination of thiols, by contrast, no hydrogen is added and the reaction is endothermic (entry 3). It is driven entropically and will proceed to completion only above approximately 250 °C or when the resulting alkene is removed from the balance by hydrogenation. Thermodynamics may also affect the hydrogenation of alkenes and aromatics, including the intermediates BP and CHB (entries 10 and 11). While strongly exothermic, these reactions are entropically unfavorable and may thus be already severely equilibrium limited ($K < 1$) at moderate temperatures (300 °C) if hydrogen pressure is low.

Table 2.3. Equilibrium constants (K) and standard enthalpies of reaction ($\Delta H°_{rxn}$) for selected reactions occurring during hydrotreating (compiled from refs. [27-29]).

Reactant class	$\log_{10}(K)$ (−)			$\Delta H°_{rxn}$ (kJ)	
Entry | Reaction	at 200 °C	at 300 °C	at 400 °C	per mol reactant	per mol H_2
Thiols					
1 $\quad$ $CH_3SH + H_2 \rightleftharpoons CH_4 + H_2S$	8.38	7.06	6.15	−72	−72
2 $\quad$ $C_2H_5SH + H_2 \rightleftharpoons C_2H_6 + H_2S$	6.99	5.91	5.16	−59	−72
3 $\quad$ $C_2H_5SH \rightleftharpoons C_2H_4 + H_2S$	−0.25	1.26	2.31	+78	n.a.
Thiophenes					
4 $\quad$ $TP + 4 H_2 \rightleftharpoons$ *n*-butane + H_2S	14.13	9.33	6.04	−262	−66
5 $\quad$ $TP + 2 H_2 \rightleftharpoons$ tetrahydro-TP	3.17	1.12	−0.21	−116	−58
Benzothiophenes					
6 $\quad$ $BT + 3 H_2 \rightleftharpoons$ ethylbenzene + H_2S	16.65	12.85	10.20	−203	−68
7 $\quad$ $DBT + 2 H_2 \rightleftharpoons BP + H_2S$	15.23	12.50	10.61	−148	−74
8 $\quad$ $BT + H_2 \rightleftharpoons$ dihydro-BT	1.55	0.49	−0.23	−58	−58
9 $\quad$ $DBT + 3 H_2 \rightleftharpoons$ hexahydro-DBT	5.47	1.54	−0.98	−230	−77
Sulfur free hydrocarbons					
10 $\quad$ $BP + 3 H_2 \rightleftharpoons CHB$	3.13	−1.20	−4.25	−225	−75
11 $\quad$ $CHB + 3 H_2 \rightleftharpoons BCH$	2.47	−1.86	−4.91	−225	−75

Negative values of $\log_{10}(K)$, highlighted in grey, indicate that the equilibrium constant is less than unity. Abbreviations: thiophene (TP), benzothiophene (BT), dibenzothiophene (DBT), biphenyl (BP), cyclohexylbenzene (CHB), bicyclohexyl (BCH).

As expected for exothermic reactions, an increase in temperature decreases the equilibrium constant and therefore negatively affects the product yield. In the case of pure hydrogenolysis this is irrelevant because K is sufficiently large over a wide range of temperatures (entries 1, 2, and 7). Hydrogenolysis will generally proceed to completion

in presence of a stoichiometric amount of hydrogen and may thus be considered irreversible under practical HDS conditions. However, this is not necessarily true for combined reactions comprising both hydrogenation and hydrogenolysis, as some of the steps can be thermodynamically unfavorable. The full HDS of TP (entry 4), for example, requires initial saturation of the double bonds (entry 5), which becomes severely equilibrium limited at temperatures just short of 400 °C. The same applies to the HDS of BT which is also typically initiated by hydrogenation (entry 8). In general, all sulfur removal pathways that involve pre-hydrogenated intermediates may be notably affected by thermodynamics. This has to be considered, especially when targeting 4,6-alkylated DBT and similar molecules, as these can only react via hydrogenated intermediates with potentially low equilibrium concentrations (analogous to entries 8 and 9). The operating window of conventional HDS catalysts is therefore subject to an upper temperature limit given by thermodynamics, and a lower temperature limit given by the activity of the catalyst. In practice, this situation can be mitigated by applying higher H_2 pressures, which may reach up to 200 bar for heavy feedstock. This is costly, however, and it would be much more desirable if catalysts could operate efficiently at a temperature of 200–250 °C at which almost all hydrotreating reactions are thermodynamically favorable.

2.3 Transition metal sulfides as hydrotreating catalysts

Since the very beginning of technical heterogeneous catalysis, workers in the field have struggled with the problems of catalyst deactivation, poisoning, regeneration, and reactivation. In this regard, sulfur compounds are probably the most obnoxious poisons. This is because of their ubiquity in technical raw materials like petroleum or coal and their deteriorating effects on many types of catalysts.[13] For smaller applications, one could of course separately remove sulfur (compounds) prior to the reaction of interest, e.g., via selective adsorption or oxidation, but this is not economically feasible for the vast volumes of basic raw materials processed in the fuel industry. The solution in this case, revolutionary at the time, was to make the poison an integral constituent of the catalyst. It was in 1924, when systematic research conducted by Krauch and Pier[30] at the former Badische Anilin und Sodafabrik led to the discovery of transition metal sulfides (TMS), in particular MoS_2 and WS_2, as efficient hydrogenation catalysts in the presence of sulfur. To the present day, these materials continue to be the very basis of hydrotreating catalysts, representing one of the largest catalyst businesses worldwide.[5]

Modern hydrodesulfurization catalysts typically consist of Mo or W as the base metal and a so-called "promoter" metal from the iron group, typically Co or Ni. The metals are impregnated onto a porous alumina support and subsequently sulfided (see also section 2.3.1).[2,5,9,11] Quite often the promoter is present in high concentrations (sometimes in a 1:1 atomic ratio with the base metal). The most popular choice for HDS, especially for straight-run petroleum fractions, are $Co-MoS_2$ catalysts.[1] They minimize hydrogen consumption for easy-to-process feedstock by combining a maximum activity for sulfur removal with a low activity for aromatics hydrogenation. $Ni-MoS_2$ catalysts, on the other hand, generally offer a higher activity for aromatics saturation, as well as for HDN and HDS of refractory sulfur compounds.[1] Their application is, however, limited to specific situations because their superior performance comes at the price of increased hydrogen consumption and higher catalyst costs. Similarly, Ni-W catalysts are also only employed for refractory feedstock, when very high activity for aromatics saturation is required along with maximum HDS and HDN performance.[31] In addition to the traditional Co(Ni)-Mo(W) combinations, virtually all monometallic and binary transition metal sulfides of the first, second, and third row have been studied in connection with hydrotreating.[32-33]

More recently, there has also been some interest in transition metal carbides, phosphides, and nitrides as hydrotreating catalysts, even though these have not yet seen broader application.

While alumina-supported TMS always were and still are the work-horse of the refinery, also highly-active unsupported ("bulk") TMS have started to see broader application in recent years.[31,34] This development is driven significantly by the ever increasing demand for cleaner fuels and the shift to more refractory feedstock as outlined earlier (section 1.1). Consisting essentially of active metal sulfide only, the volumetric activity of unsupported TMS can exceed that of contemporary supported catalysts by 50 to 100 % or more.[3] As this high activity comes with massively increased hydrogen consumption and heat release, unsupported catalysts are rarely used alone but rather in addition to the less active supported materials, for example, in multiple-bed reactors. On the other hand, bulk catalysts with improved activity and selectivity have the advantage that heavier feedstock can be processed without capital-intensive changes to the existing process and equipment, hence providing higher flexibility for refiners. From a scientific perspective, unsupported catalysts are interesting because they lack potentially confounding metal-support interactions that could be detrimental for mechanistic studies and the analysis of active sites (see, for example, "Type-I sites" in section 2.3.3.6).[34]

2.3.1   Preparation

A large variety of procedures for the preparation of transition metal sulfides is described in the literature (reviewed in refs. [4-5,31,34-38]) as well as in numerous patents held by catalyst manufacturers (e.g., Exxon Mobil[39] and Chevron[40]). Industrial supported catalysts are typically prepared in the form of oxidic precursors and transformed into sulfides at the site of operation. The oxide precursor is prepared by impregnation of an alumina or silica-alumina support using aqueous salt solutions of the base metal, e.g., ammonium heptamolybdate, and the promoter metal, e.g., Ni nitrate. Most typically, pore volume impregnation is used for this purpose (also referred to as "dry" or "incipient wetness" impregnation), whereas soaking of the support in excess salt solution is less common because the amount of metal deposited is harder to control. The metal salt solutions may be applied at the same time or sequentially and sometimes one metal is added not at once

but in several impregnation steps, each followed by drying and/or calcination. As the metals may be added in deliberate quantities, there are virtually no limitations in regard to the attainable metal loading and the promoter/base metal ratio. In practice, the dried or calcined MoO_3/Al_2O_3 precursors typically contain less than about 30 wt% of MoO_3 (20 wt% Mo) and exhibit maximum catalytic activity at a Co(Ni)/Mo atomic ratio of approximately 0.3–0.4.[41-42] The precursors are then sulfided by slowly heating to about 300–400 °C under hydrogen flow in presence of a sulfiding agent.

In industry, sulfidation is typically performed at the site of operation by passing pressurized hydrogen and a S-containing petroleum fraction over the catalyst bed (e.g., straight run gas oil spiked with a "labile" S compound like dimethyl disulfide).[43] The liquid agent has the advantage to be more efficient in heat distribution, thus greatly minimizing hot spot formation due to exothermic O-S exchange.[44-45] The reaction extent during the various stages of sulfidation is also much easier to control as H_2S is released only gradually by decomposition of the sulfiding agent. Exothermicity is less of a problem in small-scale academic setups, where the use of gaseous H_2S/H_2 mixtures is often more convenient and still widely used.[43]

It should be noted that the chemical transformations occurring during sulfidation are generally not topotactic, i.e., the microscopic structure of the precursor is not preserved, even though the catalytic performance of the final sulfide is greatly influenced by the properties of the precursor.[46] Accordingly, there is a large body of research dedicated exclusively to the understanding of precursor formation[37] and sulfidation[43] which, however, is not in the scope of the present work.

While the preparation of supported sulfides follows a common scheme, bulk sulfides can be synthesized using much more diverse approaches (Figure 2.6).[34] Some routes lead to the formation of oxide precursors, just as in the preparation of supported catalysts, whereas others are essentially oxygen free and directly yield metal sulfides or thio compounds. Common preparation routes of bulk sulfides include the co-precipitation of oxidic precursors,[40] homogeneous sulfide precipitation,[47-49] thiosalt decomposition,[48,50-57] hydro- and solvothermal reaction,[39,58-61] as well as co-maceration.[62] The reaction can be carried out in a variety of solvents (aqueous, organic, oils) in a wide range of reaction conditions, in presence or absence of hydrogen. Organic ligands, such as citric acid or

amines, are sometimes added to chelate metal ions and modify the structure of the catalyst (precursor).[40,63]

In those cases where a bulk oxidic precursor is obtained, sulfidation has to be performed in much the same way as with supported catalysts, i.e., in H_2 atmosphere using liquid or gaseous sulfiding compounds. This is not strictly required for some thio compounds, as those already contain sufficient amounts of sulfur. Nevertheless, also in these cases a heat treatment is performed in reducing (H_2) or inert atmosphere to decompose the thiosalts (e.g., $(NH_4)_2MoS_4$) to metal sulfides. A large body of research[51,53-54,64] specifically deals with thiosalt precursors containing NR_4^+ ions (R = alkyl) as their decomposition yields sulfides of extremely high surface area (> 300 m²/g). They also tend to incorporate significant amounts of carbon during decomposition, which some believe to have beneficial effects on catalyst activity due to the formation of surface carbides or improved dispersion of the active phase.[65-67]
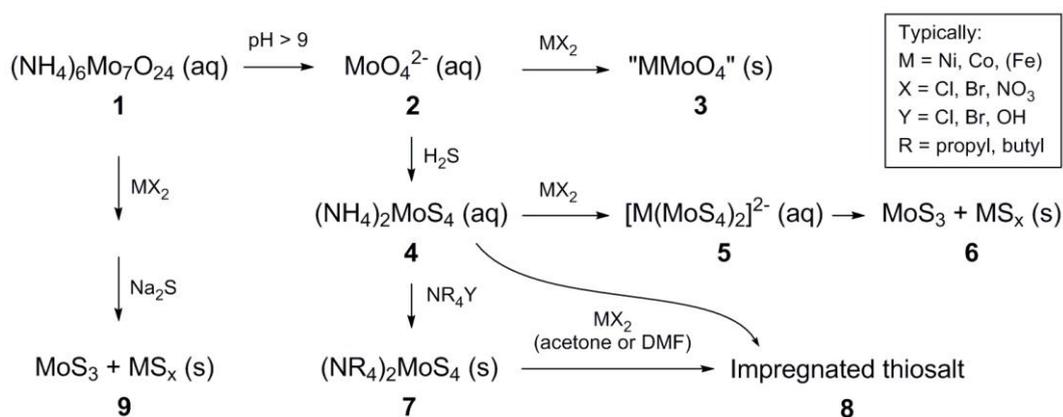
Figure 2.6. Exemplary reaction routes (schematic) for the preparation of bulk TMS precursors. The numbers are used in the main text to refer to the depicted compounds.

Some exemplary reaction routes towards bulk TMS (or their precursors) are shown in Figure 2.6. Ammonium heptamolybdate tetrahydrate (**1**), a relatively inexpensive and widely available compound, is often used as a starting material for precursors of bulk TMS. It readily dissociates into molybdate ions (**2**) in alkaline solution, most typically aqueous NH_4OH. Molybdate and an added M(II) salt, e.g., containing Ni^{2+}, Co^{2+}, or Fe^{2+}, can then be co-precipitated to yield (partly) crystalline solids, such as Ni(II) molybdate or Ni-Mo mixed hydroxides (**3**). Alternatively, addition of H_2S or water-soluble sulfides transforms the molybdate ion to the isoelectronic thiomolybdate (**4**), which may be

precipitated as ammonium salt and subsequently decomposed to MoS_2. Promoted MoS_2 may be prepared by addition of M(II) salt to thiomolybdate solutions, leading to complex formation (**5**). Note, however, that isolation of the complex is rarely possible due to its propensity for oxidation. Typically, an ill-defined mixture (**6**) of monometallic sulfides is obtained, possibly containing some bimetallic thio compounds. Other uses of ammonium thiomolybdate include ligand exchange with "bulky" tetralkylammonium ligands (NR_4Y). Depending on the size and structure of the alkyl chain, the resulting compound (**7**) can be decomposed to MoS_2 with extremely high surface area. Dry thiosalts (**4** and **7**) may be impregnated with Ni^{2+} using polar aprotic solvents (**8**) instead of direct reaction in aqueous solution (**4** $\rightarrow$ **5**). Some of the above methods may also be combined to a procedure typically referred to as "homogeneous sulfide precipitation". In this case, molybdate, M^{2+} and S^{2-} ions are present at the same time in a hot aqueous solution, which is then evaporated to dryness. Just like in (**6**), the resulting solid (**9**) may contain some bimetallic thio-compounds in addition to various monometallic sulfide phases.

One common aspect of many bulk sulfide synthesis routes is the formation of stoichio-metric compounds, which sets boundaries to the attainable promoter/base metal ratio. Because of this, the promoter/base metal ratios of bulk sulfides are typically much greater than the optimum found in supported catalysts (0.3–0.4). In the thiosalt route, for example, two MoS_4^{2-} (WS_4^{2-}) anions form a square planar complex with one Ni(II) cation, resulting in a fixed Ni/Mo(W) ratio of 0.5.[68] Similarly, co-precipitation of oxide precursors in aqueous solution also typically produces stoichiometric solids, e.g., layered hydroxides of the form $(NH_4)HNi_2(OH)_2(MoO_4)_2$ or Ni metalates of the form $NiMo(W)O_4$ both exhibiting a Ni/Mo(W) ratio of 1.[69-70] Other procedures appear to be more versatile in this aspect (e.g., oxide-based hydrothermal routes[39] or homogeneous sulfide precipitation), but promoter and base metal phases may precipitate separately, thus essentially creating a physical mixture instead of a bimetallic compound. It is generally more difficult to obtain defined phases in bulk sulfides than in conventional supported TMS.

The limited stoichiometry of bulk sulfides can be hindering in systematic studies where different promoter contents are to be explored over a wide range of concentrations. Additionally, the multi-phasic composition significantly complicates characterization.

Bulk sulfides also generally exhibit much lower specific surface areas than their supported pendants, i.e., typically much less than $100\,m^2/g$ (with the exception of sulfides prepared from "bulky" tetraalkylammonium thiometalates). This means that only a tiny fraction of the material is at the accessible surface and thus available for catalytic surface reactions. The informative value of bulk characterization techniques (e.g., XRD, EXAFS, or TEM) is greatly diminished because of this circumstance. In terms of catalytic performance, however, the lower dispersion is typically outweighed by the fact that the whole surface of bulk TMS consists of potentially active phases only, whereas supported sulfides also expose inactive alumina surfaces.

2.3.2 Structure and morphology

All forms of MoS_2 (and the isostructural WS_2) exhibit an anisotropic layered structure, in which each layer is composed of an atomic plane of Mo sandwiched between two atomic planes of S (Figure 2.7 A, B).[71] Several of these S-Mo-S layers ("slabs") may be stacked upon each other, especially in unsupported MoS_2. The top and bottom of the stacked crystallite is terminated by low-energy surfaces called the "basal planes", while the lateral terminations ("edges") are energetically less favorable. Accordingly, growth parallel to the basal plane is typically more extended than in stacking direction.[5] The energetic situation can be modified in presence of a support by interacting with Mo atoms at the edges of the crystallite (e.g., Mo-O-Al linkages on Al_2O_3), thus disrupting crystal growth and stabilizing small, single layer patches of MoS_2 (see also "Type-I sites" in section 2.3.4.3).[4,71-73] As a result, supported sulfides are typically much better dispersed than bulk sulfides.

Depending on the arrangement of S with respect to Mo within the S-Mo-S layers and the orientation of the S-Mo-S layers with respect to each other, several polymorphs of MoS_2 can be distinguished.[74] The basic building blocks of the naturally occurring 3R (rhombohedral) and 2H (hexagonal) phases are edge-connected trigonal prisms, i.e., formal "MoS_6" units with six S atoms at the corners and one Mo atom at the center (Figure 2.7 A).[71] Within the layers, Mo and S are bonded via covalent interactions (Figure 2.7 D), whereas adjacent layers are held together by relatively weak van-der-Waals forces only (Figure 2.7 C). Applying shear stress parallel to the basal planes will easily dislocate the

layers with respect to each other, lending bulk MoS$_2$ its very effective lubricating properties.[31] The most frequent MoS$_2$ phase in hydrotreating catalysts is the 2H poly-morph, which is the form usually adopted by synthetic MoS$_2$ due to the more favorable energetics. 2H-MoS$_2$ crystallizes in hexagonal symmetry and exhibits an AB-type alternating sequence of S-Mo-S layers, i.e., adjacent layers are rotated by 60° with respect to each other, which is the main difference to the 3R polymorph. Both forms have semiconducting properties with a band gap of about 1.2 eV (multilayer) and 1.8 eV (monolayer), making them useful for applications in nano- and optoelectronics.[75] A meta-stable 1T modification with octahedral Mo-S coordination and metallic conductivity has also been described.[74]
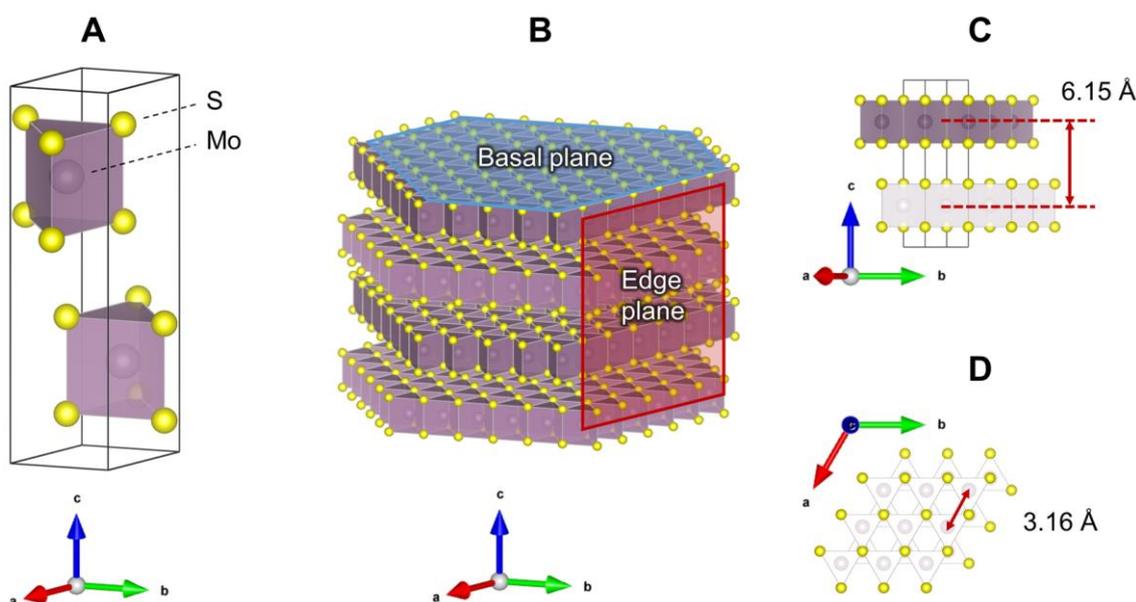
Figure 2.7. Structure of bulk MoS$_2$ (2H-MoS$_2$, ICSD cc. 644245). (**A**) Hexagonal unit cell showing the trigonal prismatic coordination of Mo by six S atoms. (**B**) Stack of four truncated MoS$_2$ layers terminated by two basal and six edge planes. (**C**) View onto edge of two layers of MoS$_2$ held together by van-der-Waals interactions (arrow indicates interlayer Mo-Mo separation). (**D**) View onto basal plane (arrow indicates intralayer Mo-Mo separation). Structural representations were created with VESTA.[76]

The typical dimension of supported MoS$_2$ crystallites as determined from transmission electron micrographs (TEM) is on average about 50 Å along the basal plane and less than the interlayer distance (6.15 Å) in stacking direction, corresponding to a stacking degree of less than 2 slabs (i.e., predominantly monolayers).[77-80] Lacking a structure-directing substrate, unsupported sulfides tend to form considerably larger crystallites in both the

basal plane and the stacking direction (Figure 2.8 A, B).[69,81-82] Bulk MoS_2 for catalytic applications often also exhibits stacking faults, folding or bending of layers and overall poor crystallinity (Figure 2.8 B).[83] These irregularities, paired with the natural anisotropy, are the reason why structural characterization of MoS_2 is a challenging task. The following techniques are routinely applied for this purpose: (i) calculating the mean particle size from Mo-Mo coordination number as determined by extended X-ray absorption fine structure (EXAFS); (ii) directly measuring and counting of layers/crystallites in TEM micrographs (Figure 2.8 A, B); (iii) analyzing line widths in powder X-ray diffractograms via the Scherrer equation[84] (Figure 2.8 C). While these techniques should give consistent results, this often only works for well-defined systems, e.g., supported metal nanoparticles. For MoS_2 this is typically not the case. For example, EXAFS-based particle size estimates are often smaller than those obtained from TEM or XRD because the latter tend to misrepresent small crystallites and monolayers of MoS_2. As far as TEM is concerned, only a small fraction of particles is visualized (those aligned with the electron beam), and thus several hundred particles have to be evaluated to obtain a representative measurement. That said, TEM is the only technique that also yields information on the particle size distribution and the overall homogeneity of the sample.[85-86]
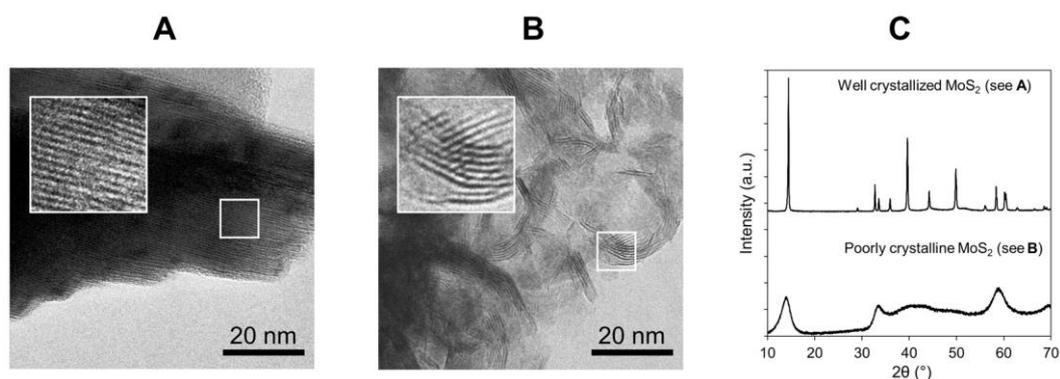
Figure 2.8. Structure of bulk MoS_2 analyzed by transmission electron microscopy (TEM) and powder X-ray diffraction (XRD) (unpublished work by the author). (**A**) TEM of crystalline MoS_2 (high-temperature annealed). (**B**) TEM of poorly crystalline MoS_2 (from low-temperature synthesis method as typically used for catalytic applications). Note the lower stacking degree and overall higher disorder as compared to sample A (**C**). XRD patterns. The mean stacking degrees are about 200 and 5 for sample A and B, respectively, and were determined by line width analysis[84] of the (002) reflection.

The equilibrium morphology of pure MoS_2 layers is preferentially triangular under sulfiding conditions, i.e., when excessive S is present (Figure 2.9 A). In this case, the edges

of the triangle are structurally uniform and preferentially expose the more stable "Mo edge" around the whole perimeter.[87] An additional type of termination, the "S edge", is formed when the triangle becomes truncated due to hydrogen adsorption (at low H_2S/H_2 ratio), presence of other atoms (promoters), or support interactions.[88] It is important to note that the edges are the key features of TMS catalysts, as the basal planes were shown to be essentially inactive for hydrotreating reactions.[31,89-91]
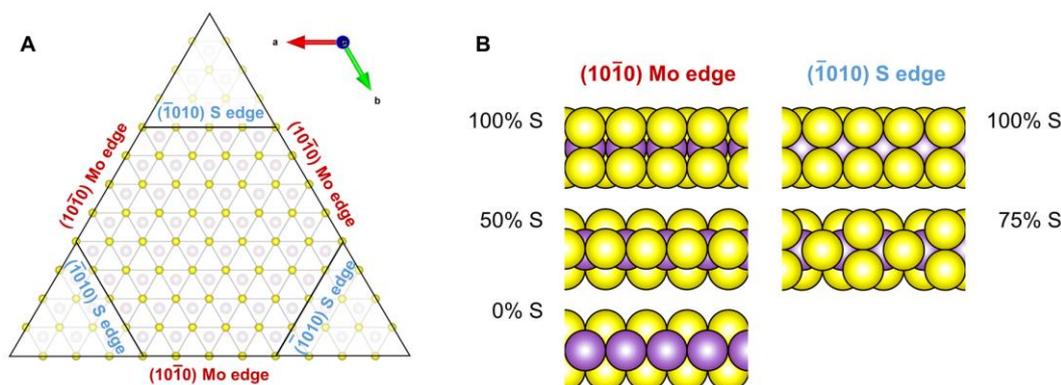
Figure 2.9. Structure of MoS₂ layers. (**A**) Truncated MoS₂ layer terminated by Mo and S edges in fully sulfided state (100 % S). The purely triangular shape of unperturbed MoS₂ (opaque) preferentially exposes the Mo edge under typical sulfiding conditions. (**B**) Edge structures with various S contents induced by different chemical potential of S during sulfiding (H_2S/H_2 ratio) (adapted from ref. [87]). Only the first row of Mo atoms with the closest S atoms is shown.

Extended X-ray absorption fine structure (EXAFS) studies of the Mo K-edge have revealed that the environment of the average Mo atom in hydrotreating catalysts is similar to that of well crystallized MoS₂.[72,92] However, it was also shown that the structure at the edge is distorted compared to the structure within the crystal (or monolayer).[93] In general, the edges of MoS₂ crystallites are highly dynamic structures and strongly influenced by the reaction conditions, most importantly by temperature and the chemical potential of S compared to that of H₂ (i.e., gas phase composition). Depending on the reaction conditions, each edge type will exhibit a certain fraction of coordinatively unsaturated Mo sites (CUS) and bridging S atoms that together enable hydrogenation reactions and heteroatom removal. Because of this critical role in hydrotreating catalysis, the equilibrium structures of the edges have been the subject of a great many studies.[87-88,94-97]

It is generally agreed that the S-coverage of the edges can be increased by adsorption of H₂S, whereas dissociative H₂ adsorption and successive H₂S desorption can lead to a

desaturation of the edge (Figure 2.9 B). There is still some dispute concerning the stable (equilibrium) edge configurations, but it is accepted that the Mo edge exhibits a higher variety of S-coverages (0–100 %), while the coverage of the S edge is typically more restricted (50–100 %). A combined experimental-theoretical study by Lauritsen et al.[87], for example, has found that the Mo edge has two almost equally stable configurations under sulfo-reductive conditions ($H_2S:H_2 = 0.02$–0.1). The first is fully saturated (100 % S-coverage) and Mo is coordinated approximately as within the lattice. That is, there are two exposed S atoms located close to the crystallographic S positions of MoS_2 (Figure 2.9, B). The second configuration is only half-decorated, with one bridging S between two Mo ions (50 % S-coverage, Figure 2.9, B). The partially unsaturated edge states are crucial for direct heteroatom removal because the exposed Mo cations act as adsorption sites for S-, N-, and O-organic compounds.

2.3.3 Reactivity and active sites

2.3.3.1 The role of edge planes

In MoS_2 based catalysts, only a relatively small fraction of the accessible surface is responsible for the total catalytic activity, just like in most other heterogeneous catalyst systems. A more distinctive feature of MoS_2 is that its active sites exhibit a highly anisotropic distribution which is directly linked to the structural peculiarities of this material. As the basal planes do not expose any appreciable amount of potentially reactive metal sites because of the closely packed S layers, the genesis and stabilization of active sites is limited to locations at or near the edges.
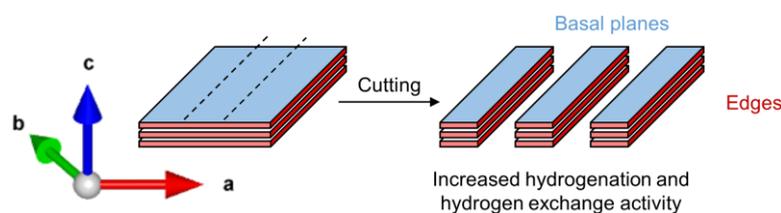
Figure 2.10. Schematic drawing of the Tanaka experiment: Cutting a single crystal of MoS_2 along its c-axis selectively increases its edge area and hydrogenation activity (adapted from ref. [89].)

First evidence for the crucial role of the edge planes was obtained in the 1980s by Tanaka et al.,[89-90] who used MoS_2 single crystals cut along the c-axis, i.e., perpendicular to the basal planes (Figure 2.10). While having no effect on the basal plane area, cutting along the c-axis substantially increased the edge area and at the same time the activity for hydrogenation and hydrogen exchange reactions of olefins. Similarly, driven by the poor correlation of activity with total surface area, Tauster et al.[91] showed that HDS activity was associated with the edges only. This was achieved by exploiting the higher oxidation sensitivity of the edge planes (as compared to the basal planes) to quantify their area via O_2 chemisorption.

2.3.3.2   Coordinatively unsaturated sites

Coordinatively unsaturated sites (CUS), often also referred to as "sulfur anion vacancies" or simply "vacancies", are considered to be the primary sites for the adsorption of heteroatom bearing compounds. As such, they are especially important for the direct extrusion pathways in HDS, HDN, and HDO (as compared to reaction routes that require hydrogenation prior to C-X bond scission). The defining feature of CUS is an exposed (accessible) metal cation with at least one S anion missing in its coordination sphere, so that the reacting molecule can chemically bind to the Mo cation. The Mo cation acts as a Lewis acid by accepting the heteroatom's free electron pair, thus weakening the C-heteroatom bond.[5] The Lewis-acidic nature of the metal centers is nicely demonstrated by their sensibility towards NH_3 poisoning, which strongly suppresses direct S-extrusion of DBT or similar compounds. This is considered as key evidence for the role of CUS as active sites.[79]

Direct extrusion of heteroatoms on CUS is likely to proceed according to a reverse Mars-van-Krevelen mechanism,[79,98-99] in which the vacancy is "filled" by the heteroatom of the reactant in the first step (Figure 2.11). C-S hydrogenolysis then occurs with the help of adjacent sulfhydryl (SH) groups that act as donors of dissociated hydrogen. The desulfurized molecule then desorbs, leaving behind a sulfur-saturated site. In the last step the vacancy is regenerated by dissociatively adsorbing H_2 and desorbing H_2S, thus closing the catalytic cycle. For HDN and HDO the steps are essentially identical, except for the desorption products (NH_3 and H_2O, respectively).
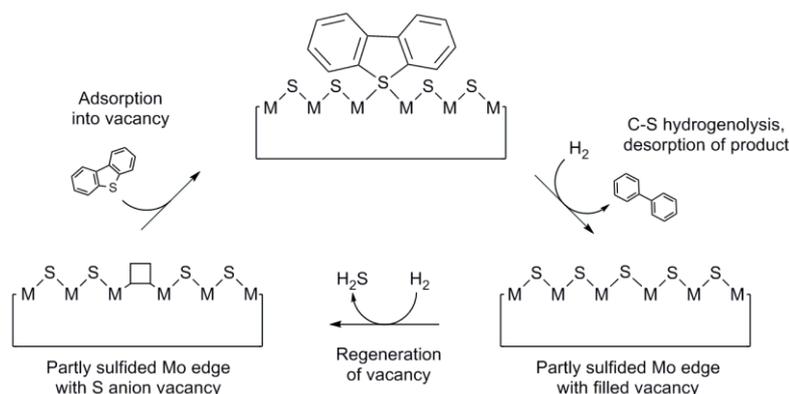
Figure 2.11. Illustration of catalytic HDS cycle following a reverse Mars-van-Krevelen mechanism.[98] Note: Dissociative H_2 adsorption and C-S hydrogenolysis by sulfhydryl (SH) groups not shown. M: Mo or W.

Vacancies do not generally occur in an isolated fashion but may regularly expose more than one metal ion at the edges (Figure 2.12). Multiple vacancies are favorable from a steric point of view, as they facilitate access of bulkier molecules to the metal ion and enable a wider range of adsorption geometries. For example, the parallel π-complexation of binuclear aromatics (e.g., DBT) is expected to occupy more than one vacancy, whereas perpendicular σ-bonding could also occur on single vacancies (see section 2.2.2). As the adsorption complex determines the preferred reaction pathway, an increased surface density of CUS may thus not only increase activity but also influence selectivity. Among others, exposed Mo pairs, "V-sites" and "corner sites" have been proposed in the literature to account for reactions that are too sterically demanding for "regular" edge vacancies (Figure 2.12).[4] It is important to note that the static situation depicted in Figure 2.12 may be significantly altered under typical sulfo-reductive conditions. Extensive edge reconstructions occur depending on pressure, temperature, the concentration of vacancies (or, inversely, S coverage), the coverage with H adsorbates (SH groups), and even the size of the nanocrystal.[87,100] These rearrangements are aided by the significant mobility[101] of S atoms, which typically adopt bridging positions between Mo ions as the S coverage decreases (as shown previously in Figure 2.9 B).
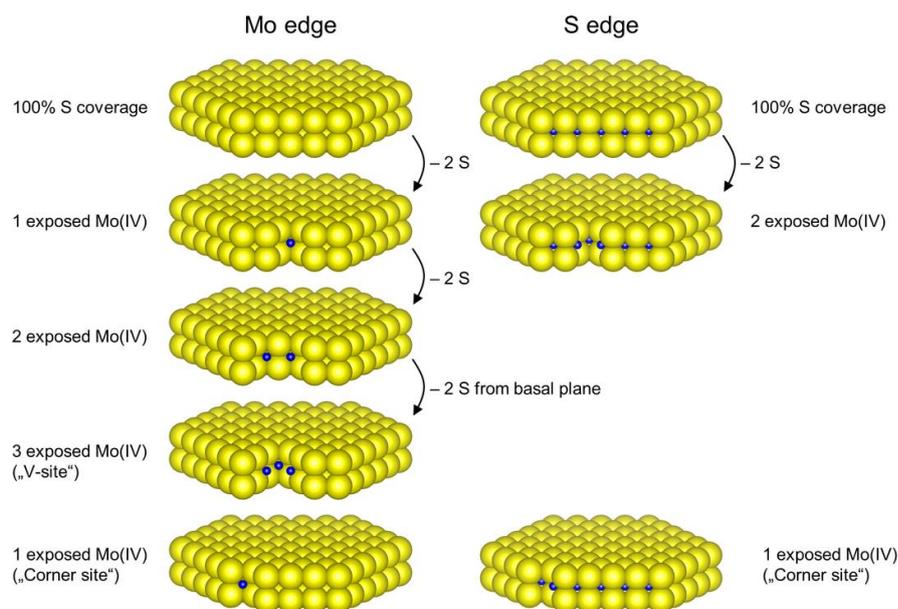
Figure 2.12. Illustration of different CUS arrangements possible at the Mo and S edge (adapted from ref. [4]). Note that the illustrations do not account for the dynamic edge reconstruction occurring under typical sulfo-reductive conditions and that the oxidation state of the exposed Mo ions (formal Mo(IV)) may change accordingly. The "regular" edge vacancy referred to in the main text is best represented by the structures in the second row.

2.3.3.3   Chemical probes for active sites

Several experimental techniques have been developed over the years to quantify coordinatively unsaturated edge sites and many of these are based on the adsorption of probe molecules, such as H_2S, NH_3, O_2, NO, and CO. Very often the adsorbed molecules are analyzed via spectroscopic techniques like infrared (IR) to differentiate between the typically multiple adsorbed species (physisorbed or chemisorbed). For such analyses, however, the material has to be transparent to the incident radiation, which is generally not the case for bulk sulfides.[102] One reason is that the sulfide phase itself is a good absorber of light in the IR region. The low specific surface area of bulk sulfides is also detrimental for spectroscopic analysis, as the surface concentration of the probe molecule will be accordingly low. Finally, it is extremely difficult to form mechanically stable and sufficiently thin wafers from bulk sulfides. The information obtained from active site titration on bulk sulfides is thus often limited to the total uptake of the probe molecule, which may be determined gravimetrically[103], volumetrically[104], or by monitoring the gas phase concentration of the titrant during adsorption[78-79] or desorption[105]. In some situations also surface spectroscopic techniques like X-ray photoelectron spectroscopy (XPS) may be applicable to quantify the adsorbed species.[106]
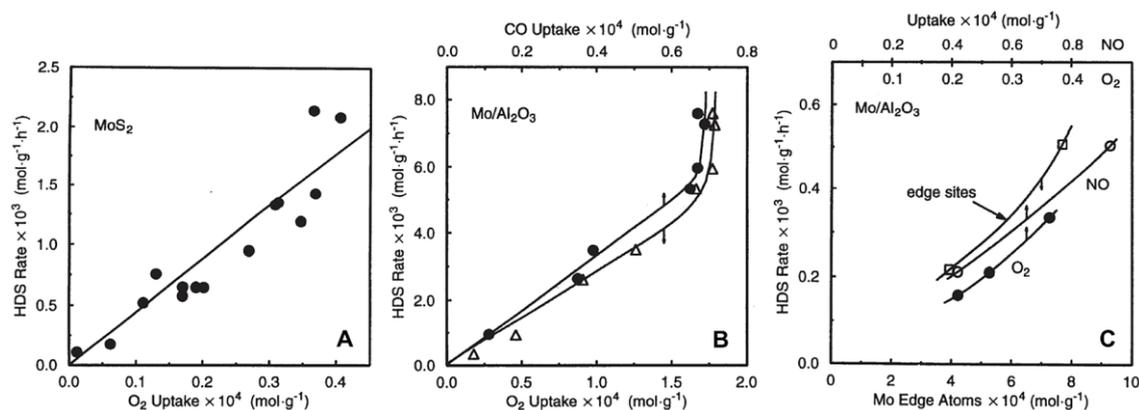
Figure 2.13. Correlations of HDS activity and chemisorption capacity of unpromoted MoS$_2$ (reproduced from ref. [4]). (**A**) Rate of dibenzothiophene HDS as a function of O$_2$ uptake on unpromoted MoS$_2$. (**B**) Rate of thiophene HDS as a function of O$_2$ (circles) and CO uptake (triangles). (**C**) Rate of thiophene HDS as a function of O$_2$ and NO uptake. The quantity "edge sites" was calculated from Mo K-edge EXAFS data and represents the total concentration of Mo edge atoms, i.e., CUS as well as saturated Mo ions.

Oxygen chemisorption (OCS) has been used extensively to characterize HDS catalysts and good correlations were found between O$_2$ uptakes and the catalytic activity of unpromoted MoS$_2$ (Figure 2.13).[91,103-104,107] It is questionable, however, whether OCS actually probes specific sites like CUS because the oxidation processes do not only affect exposed Mo ions but also subsurface and deeper lying Mo ions.[5] Due to its selective interaction with the edges,[91] OCS may therefore be rather an indicator for the general dispersion of the MoS$_2$ phase. As the active sites are confined to the edges, a linear relationship between activity and O$_2$ uptake may still be obtained in a series of closely related catalyts.[4]

Just like OCS, nitric oxide chemisorption is another titration technique which has seen wide application in the quantification of CUS, and some of these studies report a linear relationship between NO uptake and activity (Figure 2.13 B, C).[79,99,108-109] It is suggested that NO adsorbs as a dimeric (dinitrosyl) species on exposed Mo cations,[110-112] but there may be differences depending on the location of CUS. A combined theoretical-experimental study by Topsøe et al.[109] confirmed that the Mo edge is indeed dominated by dinitrosyl species (Figure 2.14 D), whereas mononitrosyl species are dominant on the S edge. The variable stoichiometry between probe molecule and adsorption site is of course a limitation to the validity of NO uptake as a quantitative measure for CUS concentration. Furthermore, it was shown that NO may not only adsorb onto existing

vacancies but could also create vacancies itself via a "push-pull" mechanism.[109] In this situation, NO actively displaces S anions at the edge (Figure 2.14 A-C) and calculations suggest a fully NO-substituted edge to be energetically favorable. This could mean that NO uptake, just like O_2, may rather reflect the general dispersion of the MoS_2 phase instead of specific sites. However, it is important to note that this limitation of NO chemisorption was observed under very specific conditions far from those used in hydrotreating. Specifically, the push-pull mechanism was evidenced only after all S anions at the edge had been converted to SH groups by exposure to atomic hydrogen. This is probably not the case under typical HDS conditions, where the catalyst is exposed to molecular hydrogen and SH groups are not formed independently from CUS.[108]
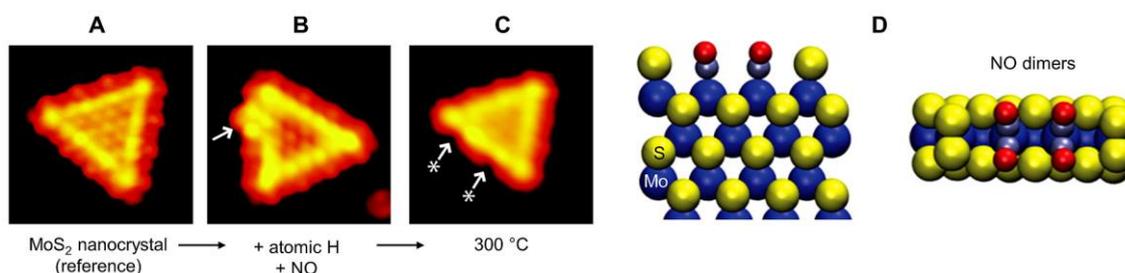
Figure 2.14. Proposed adsorption structure and reactivity of NO with unpromoted MoS_2 edges (adapted from ref. [109]). (**A**) Au-supported MoS_2 reference nanocrystal, fully sulfided, as visualized by scanning tunneling microscopy (35 x 35 Å^2). (**B**) Similar nanocrystal after exposure to atomic H and, subsequently, to NO. The arrow indicates two adjacent dinitrosyl species as shown in panel D. (**C**) Nanocrystal after heating to 300 °C. Arrows indicate newly created edge vacancies. (**D**) Ball model, showing two adjacent dinitrosyl groups from different perspectives.

In view of the extensive surface rearrangements that may occur upon the adsorption of NO and O_2, carbon monoxide has seen some application as a potentially less reactive alternative.[113-115] Compared to NO and O_2, it binds only weakly to MoS_2 and its adsorption is fully reversible. However, the weak interaction requires CO adsorption to be performed at very low temperature, whereas NO and O_2 readily adsorb at ambient temperature. CO has also not seen such a wide use as NO in the study of supported MoS_2, partly because its IR spectrum is more difficult to interpret. With respect to total uptakes, similar activity correlations were found for the application of CO, NO, and O_2 (Figure 2.13), suggesting that the potential reactivity of NO and O_2 might not be too important after all.

It is not immediately clear why good chemisorption-activity correlations are found using different probe molecules with very different adsorption properties. The nature of

the information provided by each technique is most likely unique and the sites probed by each molecule may not represent the same set, even though they probably overlap to a significant extent.[79] The fraction of sites probed by NO and CO, for example, is typically somewhat smaller than for O_2 (Figure 2.13 B, C). It is also important to point out that the sites probed by titration may not be exactly identical to those responsible for catalysis. In both cases, the concentration and nature of sites is highly dependent on the pretreatment and reaction conditions, which are typically vastly different for chemisorption and catalytic test reaction (low and high temperature/pressure for chemisorption and catalytic tests, respectively). It is thus not surprising that different correlations have been obtained in the same experimental setting at low and high pressure[116] or after longer time-on-stream[117]. While the larger picture suggests that CUS represent a significant fraction of the sites probed by NO, CO, and O_2, good activity correlations may result only within series of closely related catalysts under condition that reaction and chemisorption para-meters are kept fixed. This is normally the case for the experiments within one specific study. Care should be taken, however, when generalized conclusions are to be inferred from such results.

2.3.3.4 Sulfhydryl groups

In contrast to coordinatively unsaturated adsorption sites, the primary role of SH groups is to provide dissociated ("active") H_2 for hydrogenation and hydrogenolysis reactions. SH groups are formed at the edges in close proximity to CUS, thus creating a favorable situation for the supply of H to the adsorbed reactant. The formation of SH groups occurs readily and H_2 activation on MoS_2 may be observed even at low temperature (e.g., in the form of H_2-D_2 exchange).[90,118] Early direct experimental evidence for SH groups was provided by Maternova[119], who used silver salts to titrate SH groups on unpromoted Mo and CoMo sulfides, as well as by Wright et al.[118] and Sundberg et al.[120], who evidenced SH groups via inelastic neutron scattering.

It has been debated whether the dissociation of H_2 occurs homolytically or hetero-lytically on MoS_2 and, accordingly, SH group formation has been rationalized in different ways.[121] A recent proposal is shown in Figure 2.15. The fact that Mo hydride (H⁻) species have never been directly observed seems to be in favor of homolytic dissociation. However, it is still possible that hydride species are transiently involved in H_2 activation.

It was proposed that a transiently formed hydride may quickly react with an adjacent S anion to form an additional SH group, while the excess electrons could either partially reduce the exposed Mo^{3+} cations or be delocalized due to the semiconducting properties of MoS_2 (Figure 2.15 B).[80] The structure resulting after H_2 dissociation would thus be a vacancy exposing two Mo^{2+} cations and two identical neighboring SH groups with only weakly Brønsted-acidic properties. Note that SH groups can also be formed by dissociative H_2S adsorption (Figure 2.15 A). In that case, due to electrostatic reasons, the resulting SH groups are expected to be moderately Brønsted-acidic (i.e., proton donors). This is supported by the observation that hydrocracking of *n*-dodecane on MoS_2/Al_2O_3 can be significantly enhanced by increasing H_2S partial pressure during the sulfiding stage.[122] Similarly, other workers[123-124] have demonstrated via IR spectroscopy of adsorbed N-organic bases that H_2S adsorption leads to a notable increase in the Brønsted acidity of the sulfide phase. The dual nature of SH groups as hydrogen donors and Brønsted acids is nowadays well established, even though it should be noted that their Brønsted acidity does not play a major role in most typical HDS, HDN, and HYD reactions.[4]
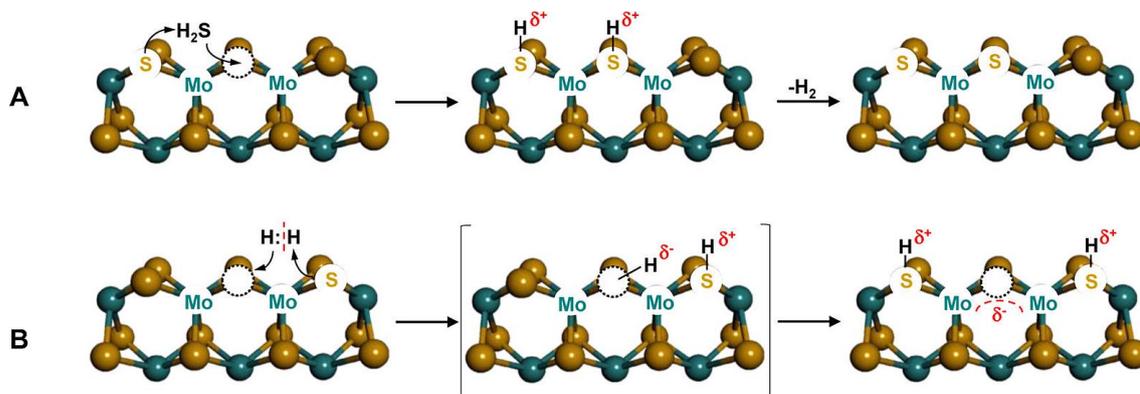
Figure 2.15. Proposals for H_2 activation and SH group formation on unpromoted MoS_2 (reproduced from ref. [80]). (**A**) Formation of SH groups by dissociative H_2S adsorption on S vacancy, followed by recombinative desorption of H_2. (**B**) Heterolytic H_2 dissociation forming transient Mo hydride species. The negative charge of the hydride may partially reduce the Mo cations or could be delocalized due to the semiconducting properties of MoS_2.

Like anion vacancies, SH groups are located at the edges, and thus a certain proportionality of SH group concentration and the total number of MoS_2 edge sites can be

expected. Indeed, such correlations have been reported (e.g., refs. [80,125-126], and more recently in ref. [108]) and some even suggest the existence of well-defined bifunctional sites, i.e., CUS and SH groups occurring in a fixed stoichiometry. Because of this co-existence it is, however, difficult to assess the kinetic importance of SH groups separately from that of the anion vacancies. In fact, some of the reported correlations found for SH groups in HDS reaction settings may rather reflect the importance of CUS. This is supported by the inhibiting effect of H_2S on HDS, which reduces the concentration of CUS but at the same time increases the concentration of SH groups. It is therefore unlikely that the concentration of SH groups is a kinetically limiting factor under most reaction conditions. Note that the inverse (i.e., promoting) effect of H_2S for other types of reactions (cracking) is related to the increased Brønsted acidity created by dissociative H_2S adsorption as discussed above. Finally, it should be pointed out that a causal correlation of SH group concentration and activity may be valid for reactions that do not primarily rely on CUS as adsorption sites as recently shown by Luo et al.[108] for the hydrogenation of phenanthrene.
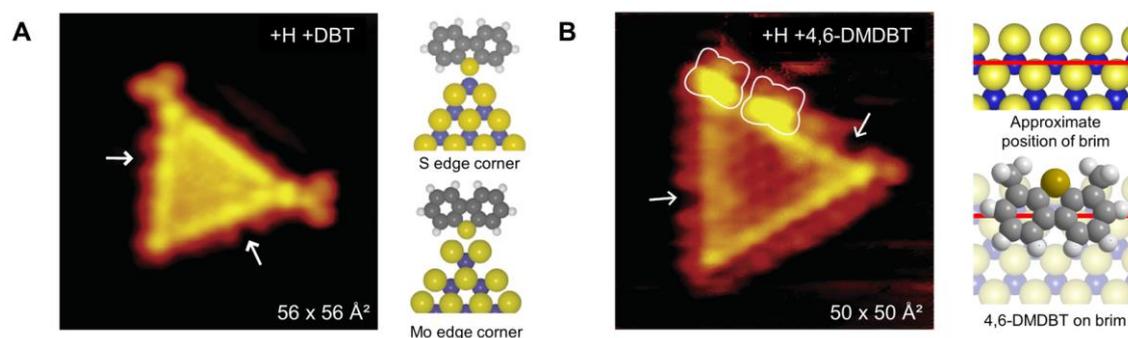
Figure 2.16. Scanning tunneling micrographs of DBT and 4,6-DMDBT adsorbed on triangular model clusters of MoS₂ (adapted from refs. [127-128]) (**A**) DBT adsorption onto MoS₂ corners. Top ball model: S atom of DBT replacing lattice S atom of MoS₂ at the S edge corner, leading to short Mo-S bond (~2.0 Å) representative of chemical bonding. Bottom: Physisorbed DBT on corner S atom of Mo edge corner (Mo-S_{DBT} bond length ~3.2 Å). Arrows indicate regular edge vacancies without adsorbates. (**B**) 4,6-DMDBT adsorbed onto "brim" (bright edge region). The white outlines indicate the approximate position of 4,6-DMDBT, whereas the white arrows indicate edge vacancies without adsorbates. Top ball model: Approximate position of the brim at the Mo edge. Bottom: Suggested position of 4,6- DMDBT above the Mo edge brim.

2.3.3.5   Rims, brims, and corner sites

While the synergistic action of CUS and SH groups in direct S extrusion (DDS) is generally acknowledged, there is still controversy about the nature of sites giving rise to

the HYD pathway.[128-129] This is particularly relevant for molecules that are sterically too demanding for σ-type ("plug-in") interaction with Mo ions (see also section 2.2.2). In the conventional two-site model, it is proposed that S extrusion of bulky molecules is preceded by one or more hydrogenation steps occurring on a different type of site, where adsorption is less sterically hindered than on regular edge vacancies (see Figure 2.12).[130] It was proposed that such sites may consist of ensembles of adjacent CUS as discussed earlier, or could involve CUS in more exposed positions, such as those at the corners of the slab.[71,127-128,131] In addition to the less severe steric constraints, corners seem to be suitable adsorption sites as they are expected to have a higher probability for the formation of adjacent vacancies.[107] Using scanning tunneling microscopy (STM) of MoS_2 model clusters, it was shown that corner vacancies may indeed chemisorb DBT and that corner adsorption was even more preferable than on regular edge vacancies (Figure 2.16 A).[127-128] However, the bulkier 4,6-DMDBT could not be observed in any of these locations. It was thus concluded that there must be sites other than corners or edges for the adsorption and activation of the larger and more refractory S compounds.

Further investigations revealed that those molecules could be adsorbed in a flat-lying configuration at the so-called "brim".[127-128] This region just within the edges of the basal planes can be observed in scanning tunneling micrographs in form of a bright stripe or, more exactly, as a protrusion of about 0.5 Å on top of the slab (Figure 2.16 B). Compared to the semi-conducting interior, the brim exhibits a metallic character, i.e., it has a high local density of electronic states at the Fermi level, allowing electrons within this region to participate in metal-type interactions (e.g., π-bonding). Within this line of argument, it is proposed that the brim regions (rather than CUS) are the primary adsorption sites for bulky aromatics (with or without sulfur), while hydrogen addition is still performed by conventional SH groups in close proximity. It is not clear whether these one-dimensional metallic states are also present in bulk (i.e., multilayer) systems because all of the experimental evidence is based on single layer model catalysts. If applicable, however, it would mean that only the top and bottom layers of multilayer MoS_2 may participate in the hydrogenation of large molecules. This is somewhat in contrast to the often observed superior hydrogenation performance of bulk sulfides.[34,132-133]
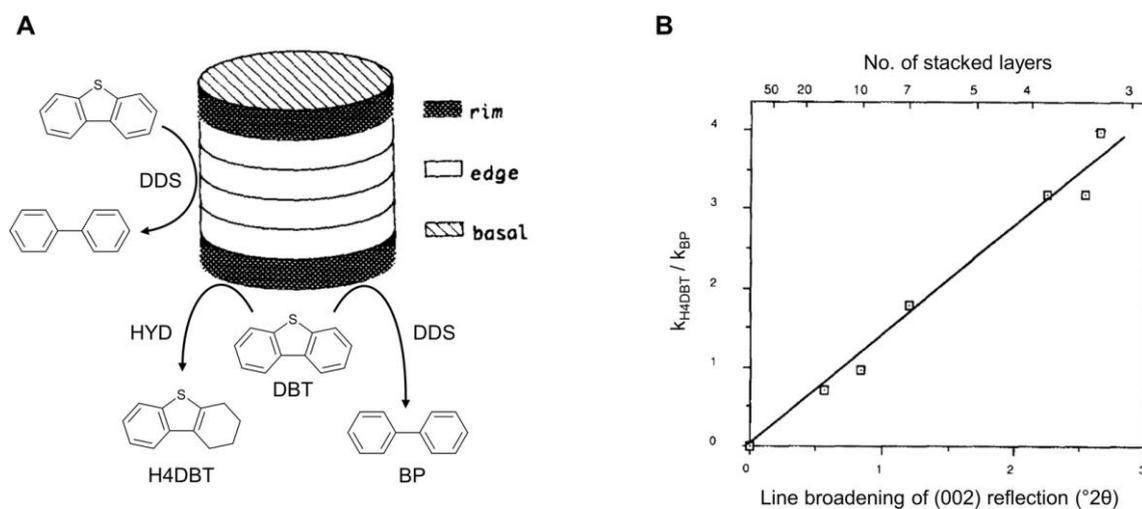
Figure 2.17. The rim-edge model (adapted from ref. [134]). (**A**) Stack of MoS_2 slabs (represented as discs) exposing "rims" and "edges" at the top/bottom layers and intermediate layers, respectively. Flat adsorption, leading to hydrogenation (HYD), is only possible at the rims due to steric constraints at the regular edges. Perpendicular bonding, leading to direct S extrusion (DDS) occurs at both rim and edge sites. (**B**) HYD/DDS ratio as a function of stacking height (determined by XRD line broadening of (002) reflection).

The distinct role of the top and bottom layers in stacked MoS_2 is a well-established concept that significantly predates the idea of brim sites. It is typically referred to as the "rim-edge" model (Figure 2.17 A).[134-135] While the brim site model claims electronic and geometric effects to be responsible for the improved hydrogenation capability of the top and bottom layers, the rim-edge model is a purely geometric (steric) approach. It is also perhaps the most widely applied concept for rationalizing the structure-dependent selectivity of MoS_2 based catalysts. Based on selectivity measurements on differently stacked MoS_2, it was observed that the edges of the top and bottom layers ("rims") contribute much more to the hydrogenation of DBT than the edges of intermediate layers. A mathematical model was developed, in which the DDS/HYD ratio was successfully correlated with the stacking height, while the extension parallel to the basal planes did not have any effect (Figure 2.17 B). It was proposed that the reduced HYD activity of the sandwiched edges was the result of steric hindrance induced by adjacent layers and neighboring S anions within the same layer. In this respect, rim sites are believed to allow both perpendicular (σ-type Mo-S_{DBT} bond) and flat adsorption modes (aromatic π-complex), leading to direct S-extrusion and hydrogenation, respectively. Regular edges, on the other hand, are sterically too crowded to accommodate aromatic reactants in a flat configuration and may thus only exhibit DDS-type reactivity.

Despite its exact mathematical formulation, the rim-edge model is generally only used to qualitatively correlate selectivity with catalyst structure. This is mainly due to the difficulties in precisely determining the dimensions of MoS_2 crystals in real (i.e., non-model) catalysts, which are often poorly crystalline, highly disordered materials ("rag structure").[31,83,85] Quite often it is also applied indifferently to promoted and supported systems, even though its use might not always be justified.[51,107,136-140] Finally, it should be stressed that this purely geometric approach does not make any claims about the electronic nature or structural configuration of the active sites themselves (except for their location). At the time it was developed, it was already clear that defects leading to coordinative unsaturation played a key role in hydrotreating catalysis, and thus it was simply concluded that the reactivity of rims and edges relied on CUS with different steric limitations (due to their different locations). The additional electronic effects discovered later on, most importantly brim sites, are now considered a compatible extension of this early geometric model.[128]

2.3.3.6   Type-I and Type-II sites

Additional differentiation mechanisms of active sites were observed in connection with alumina supported sulfides, i.e., the so-called Type-I and Type-II sites.[141-144] Type-I reactivity is exhibited by edge sites of single-layer sulfides, as well as the bottom layer of stacked sulfides (i.e., those anchoring the sulfide to the support). These sites interact strongly with the support, possibly via Mo-O(S)-Al linkages, which are considered to be responsible for stabilizing highly dispersed sulfides under HDS conditions. However, this kind of interaction will also result in less covalent and stronger metal-sulfur bonds, which in turn leads to lower activity by hindering vacancy formation. This is particularly detrimental for S-extrusion reactions (see also section 2.3.3.2).[143] By contrast, the more active Type-II sites are formed when Mo-O(S)-Al linkages are broken upon high-temperature sulfiding, which is also typically accompanied by sintering and increasing stacking degree (i.e., decreasing dispersion). Because of this negative side effect, there have been efforts to create Type-II sites without high-temperature treatment, for example, by using additives, such as phosphorous.[145] Type-II sites are also typically formed in sulfides supported on weakly interacting materials (e.g., carbon) or in unsupported sulfides, which, by definition, only exhibit Type-II sites.

2.3.4 Promoted catalysts

2.3.4.1 The promoter effect

In the context of hydrotreating, the term "promoter effect" is used to refer to the synergistic enhancement of activity in multi-metallic TMS. Promotion occurs when one ore more promoter metals (iron-group metals, typically Co or Ni) interact with the base metal (Mo and/or W) to give a new TMS phase of much higher activity than the physical mixture of the same monometallic sulfide phases. The promoting effect may be quantified by comparing the activity of the unpromoted catalysts (MoS_2, WS_2) with that of the promoted system. In thiophene HDS, for example, the promoting effect of Ni (Co) typically leads to a rate enhancement by a factor 10–30 (Figure 2.18 A), but it should be noted that the observed promotional behavior depends on a multitude of parameters, most importantly, the studied catalyst system, the reaction conditions, and the test reaction itself (Figure 2.18 B). The basis for rate normalization (mass-, atom- or surface area) can also have a great impact on such comparisons. Despite these complications, there seems to be a universal maximum of activity found at a promoter content of approximately 0.3 to 0.5 (total metals base).[146]

The phenomenon of promotion is well-known throughout technical heterogeneous catalysis. A prominent example is the Haber-Bosch process for ammonia synthesis, where tiny amounts (few percent) of K_2O, CaO, and Al_2O_3 act as electronic and structural promoters of the α-FeO phase.[147] In hydrotreating catalysts, the role of the promoter is somewhat different: In this case, in addition to being an electronic and/or structural modifier, the promoter is often also a major constituent of the catalyst, with a content typically in excess of 30 at% (total metals basis).

The first descriptions of a synergistic interaction between Mo and iron-group metals were published in the 1920s shortly after the introduction of MoS_2-based hydrotreating catalysts.[148-149] However, it was not until much later that the first systematic investigations appeared in the literature and the term "promoter effect" became used in connection with hydrotreating catalysts in 1959.[150] In the following years, there was hardly any need for significantly optimizing the available catalyst technology and, accordingly, fundamental understanding of the promoter effect never really caught up with the important role it already played in industrial hydrotreating. Beginning approximately in the 1970s,

however, a series of developments drastically changed this "comfortable" situation, when the first oil crisis, as well as the increasing withdrawal of light fractions for petro-chemicals and fuels, led to an increasing shortage of raw material. To make up for these deficits, it became necessary to also convert the heavier fractions, i.e., the "bottom of the barrel", which contained the most refractory compounds in the highest concentrations.[20,31] At about the same time, also the first environmental regulations concerning fuel quality were put in place. The resulting need for more active, selective, and stable catalysts sparked new research interest in the field of hydrotreating catalysis in general and the promoter effect in particular. This development was further assisted by the introduction and increasing availability of a number of powerful analytical techniques, such as EXAFS and high resolution TEM.
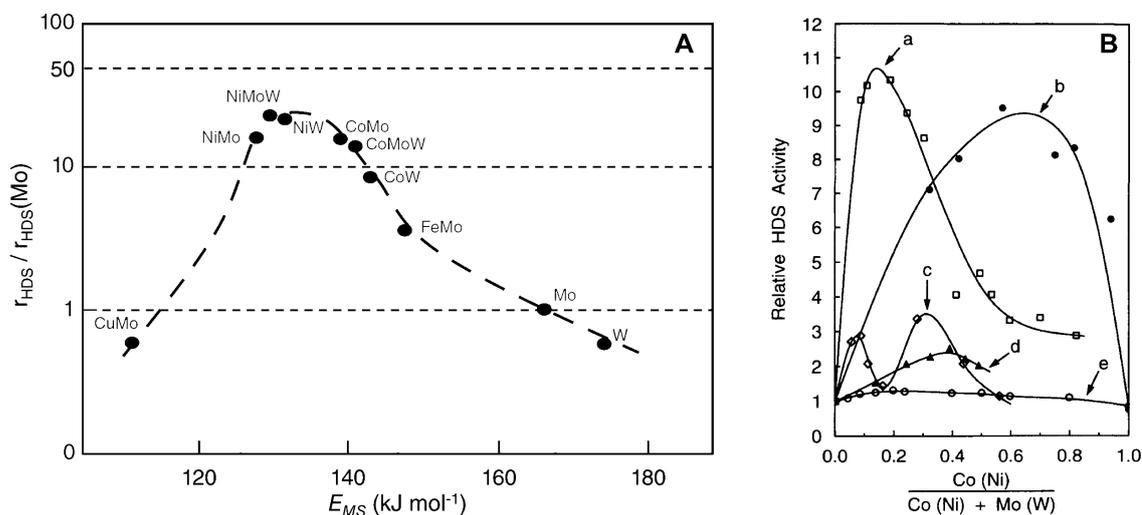
Figure 2.18. Illustration of the promoter effect. (**A**) Thiophene HDS activity of selected binary and ternary TMS relative to unpromoted MoS_2 as a function of M-S bond energy (adapted from ref. [151]). The promoter metal sulfides (e.g., Ni_3S_2, Co_9S_8, not shown here) have a relative activity of typically < 1 and are found at the left end of the bond energy scale (i.e., E_{MS} of less than approx. 120 kJ/mol). (**B**) Promoter effect for thiophene HDS under various reaction conditions as a function of promoter metal content (reproduced from ref. [4]): (**a**) unsupported Ni-WS_2, (**b**) unsupported Ni-MoS_2, (**c**) Co-MoS_2/SiO_2, (**d**) Co-MoS_2/Al_2O_3, (**e**) unsupported Co-MoS_2.

2.3.4.2   Models of promotion

A remarkable variety of models have been suggested in order to explain the promoter effect of group VI metals (Co, Ni, Fe) on group VIII metal sulfides (MoS_2, WS_2). From about 1970 to the mid 1990s, the hydrotreating community had produced roughly 30

different proposals[4], most of which fell into one or more of the following general categories:

- Structural enhancement of the base metal sulfide by the promoter, leading to a greater number and/or stability of the original active sites (e.g., "Monolayer model")

- Promoter metals as active sites with much higher intrinsic activity than the original sites in MoS_2 (e.g., "Co-only model")

- Synergy between sulfide phases, i.e., promoter metal sulfides "assisting" but not modifying the original active sites (e.g., "Contact synergy model")

- Formation of a bimetallic sulfide phase, leading to the formation of new active sites different from those in the monometallic sulfides (e.g., "Co-Mo-S model")

This multitude of views, differing in such crucial aspects as the location, local configuration and mode of action of the promoter, was a direct result of the difficulties in characterizing TMS and the inability to establish firm structure-activity correlations.

Before proceeding with the discussion of individual promotion models, it is worth noting that much of the fundamental work on promoted sulfides was performed using Co-promoted MoS_2. While the primary reason was most certainly the predominance of Co-MoS_2 among industrial HDS catalysts of the era, it was also extremely helpful for researchers that Co, in contrast to Ni, could be analyzed with Mössbauer emission spectroscopy (MES) by doping the catalyst with ^{57}Co isotope.[152] Even though rarely used today, MES is one of the few characterization techniques that can be applied in-situ to obtain direct information about the chemical state of promoter atoms. That said, it is generally acknowledged that promotion by Co and Ni involves the same basic principles, even though substantial differences may exist on a quantitative level.
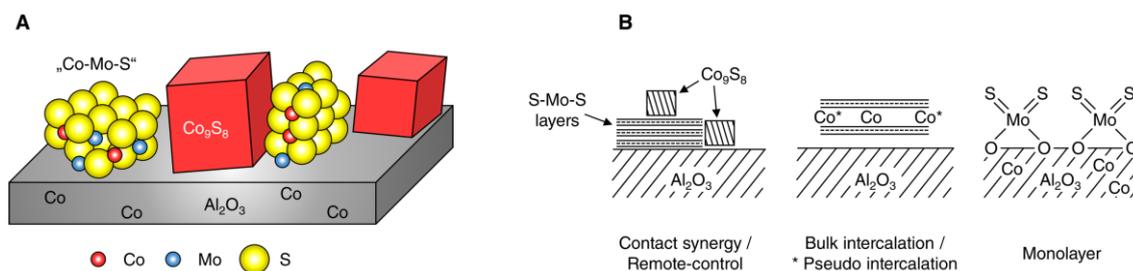
Figure 2.19. Structure of promoted MoS₂ and models for promotion. (**A**) Schematic representation of supported Co-MoS₂, with Co atoms in the support ("Co"), segregated Co sulfides ("Co₉S₈", other compositions possible), and bimetallic "Co-Mo-S" phase.[16] A similar situation is encountered in Ni-MoS₂. (**B**) Illustration of various proposals for promotion (exemplary for Co but also valid for Ni). Contact synergy model: H₂ activation on segregated promoter sulfides and H migration to MoS₂ phase. Bulk intercalation: promoter metal atoms between MoS₂ layers. Pseudo intercalation: as in bulk intercalation, but promoter metal atoms intercalated close to the edges of the layer. Monolayer model: promoter atoms in the support modify the behavior of MoS₂ monolayer on top of the support.

One of the earlier structural proposals for promoted Co-Mo sulfide was the so-called "Monolayer" model (Figure 2.19 B).[20] Here, promotion is attributed to the presence of Co ions in the support, which are thought to primarily increase the number of active sites (Mo³⁺ ions) and, secondarily, to stabilize the supported MoS₂ monolayer. A direct participation of the promoter in the HDS reaction is not implied and neither is the formation of new types of sites more active than those already present in unpromoted MoS₂. The monolayer model was soon discarded after realizing that the observed stoichiometry pointed to a mixture of MoS₂ and Co₉S₈ rather than the MoS$_{1-x}$ stoichiometry required for the monolayer model.[153] The monolayer model also fails to account for promotion in bulk Co(Ni)-MoS₂, where multiple layers are stacked upon each other without a support.

The observation of segregated Co₉S₈ crystallites was the basis for another interpretation of the promoter effect referred to as the "Contact synergy" or "Spill-over" model (Figure 2.19 B).[41,154-155] In this model, Co₉S₈ crystallites are in close contact with the MoS₂ phase and the two separate phases act together synergistically. Evidence in support of this theory comes from experiments on physical mixtures of unsupported Co₉S₈ and MoS₂ (both stable under HDS conditions[156]), where the mixtures show higher activities than the pure compounds. The HDS reaction is suggested to take place at the interface of the two phases, with MoS₂ providing the adsorption site for the reactant and nearby Co₉S₈ generating dissociated H₂. The active hydrogen species then spill over from the Co sulfide to the MoS₂ phase via surface diffusion and create reduced Mo centers, which are assumed

to be the true active sites for desulfurization. This kind of interaction has also become known as the "Remote control" mechanism, relating to the ability of Co_9S_8 to remotely determine the activity of MoS_2 without directly participating in the reaction itself. While initially popular, the contact synergy model has now been largely discarded as the single most important mechanism for promotion. In addition to the lacking experimental evidence for H migration from Co_9S_8 to MoS_2, it could be shown that promotion occurs also in catalysts that are essentially devoid of Co_9S_8 as indicated by the absence of characteristic MES signals.[157] That said, contact synergy between monometallic sulfides may still contribute to the promoter effect as a minor component. Some have argued that the concept of contact synergy should be viewed within the frame of a bigger picture, i.e., as the middle regime in a "synergy continuum", where one extreme is given by a Co(Ni)-promoted MoS_2 phase and the other by a Mo-promoted Co(Ni) sulfide phase.[67,158]

Alternative theories have argued that the primary role of Co(Ni) is simply to act as a structural promoter by increasing the dispersion of the MoS_2 phase.[159-161] According to this view, the presence of promoter atoms inhibits growth parallel to the basal plane and thus favors the formation of edge planes, thereby leading to an increased number of the original active sites (without increasing the intrinsic activity). In this context, it was also suggested that Co(Ni)-induced defects may change the morphology of MoS_2 (e.g., ratio of rim and edge sites), thus selectively promoting hydrogenation pathways. While such purely structural effects may be involved in promotion, it is almost impossible to isolate them from non-structural effects. That is, it is difficult to exclude any further influence of the exposed promoter atoms in addition to terminating the edge.

The majority of the models presented so far share the common idea that promoter and base metal (sulfides) form separate entities without direct chemical interaction. In contrast to that, it was also proposed that Co(Ni) atoms can be absorbed into the $Mo(W)S_2$ phase, where the former occupy octahedral positions in the van-der-Waal gap between two S-Mo(W)-S layers. This theory became known as the "intercalation" model.[162] It was shown later, however, that intercalation of Co or Ni in ideal MoS_2 or WS_2 crystals is energetically impossible and the model was subsequently modified such that intercalation was restricted to the more favorable edge region of the slabs ("pseudo-intercalation" model; Figure 2.19 B).[163] In this case, the promoter effect was attributed to a Co(Ni)-induced surface reconstruction at the edge resulting in an increased concentration of Mo^{3+} edge

ions. Again, the original active sites are only modified in number while keeping the same intrinsic activity as in the unpromoted catalyst.

A completely different understanding of the promoter effect was based on the observation that Co alone, when supported on carbon, can achieve similar intrinsic HDS activities as Co-promoted MoS_2.[164] In this "Co only" model, the promoter atoms are thought to be the real active sites, whereas MoS_2 is regarded as an inert support serving to disperse the much more active Co atoms and, if supported on alumina, to separate Co from this (secondary) support. This line of argument was deduced from similarities in the MES signals of Co/C and Co-MoS_2,[165] and from experiments with highly dispersed Co, Ni, and Mo sulfides in zeolites,[166] which showed extremely high activities in absence of a real synergetic effect. Others have argued that these results, while interesting, may not be used to explain the properties of Co-MoS_2 catalysts, as the similar spectral features in MES were not obtained in-situ, or under conditions different from those used in HDS.[144]

Considering the great number of experimental observations it is hardly surprising that no one has been able to reconcile the different views on promotion in a universal model. While it is certainly possible that more than one of the described scenarios contributes to promotion in typical HDS settings, it is also fair to assume that some of the discrepancies result from differences in catalyst formulation, reaction and characterization conditions, as well as synthesis and pretreatment protocols. The wealth of different test reactions used to assess the activity of TMS is another major factor for the inability to draw universal conclusions. On the characterization level, it is particularly the co-existence of promoter atoms in different phases in the same catalyst that often leads to disagreement between studies. Also, many analytical techniques are simply unable to provide true in-situ information about the highly dispersed irregular structures thought to be responsible for much of the activity of TMS.

2.3.4.3   The edge decoration model

It is nowadays widely accepted that the single most important promotion mechanism involves the formation of a so-called "Co-Mo-S" phase, in which Co atoms decorate the edges of the MoS_2 slabs as shown in Figure 2.19 A.[142] While first evidenced in connection with Co-MoS_2 catalysts, such structures appear to be quite general and analogous phases

were found also in Ni- and Fe-promoted Mo(W)S$_2$ (e.g., Ni-W-S[167]). The Co-Mo-S or "edge decoration" model is structurally not all that dissimilar from the earlier pseudo-intercalation model, with the difference that the promoter atoms reside directly on the slab edges (instead of in-between) and are chemically bonded to the base metal sulfide. The latter is a fundamental difference, which has important implications on the reactivity of the Co-Mo-S phase. Key evidence for the in-plane location of promoter atoms was provided by IR spectroscopy of adsorbed NO on sulfided Co-MoS$_2$/Al$_2$O$_3$ and Ni-MoS$_2$/Al$_2$O$_3$ (Figure 2.20).[110,168-170] Specifically, it was found that the intensity of NO-Mo and NO-Co(Ni) bands changes inversely when the concentration of the promoter is varied. This was interpreted as Mo edge sites becoming increasingly covered (or substituted) by Co(Ni) as the promoter concentration increases. As pointed out earlier, there seems to be a universal optimum for the promoter concentration, which is found at a Co(Ni)/metals ratio of roughly 0.3 to 0.5 (see section 2.3.4.1).[146] Note, however, that this bulk concentration is not necessarily related to the degree of edge decoration. As the edges make up only a small portion of all metal atoms, full edge decoration may be already reached at a much lower promoter concentration (see also section 2.3.5).
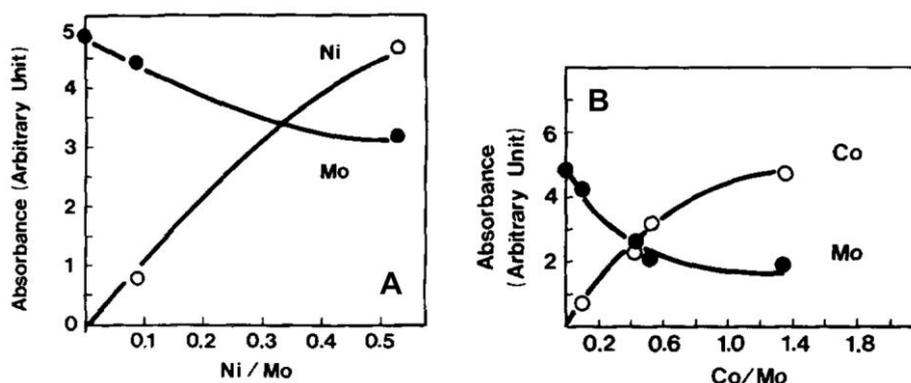
Figure 2.20. Coverage of Mo edge sites by (**A**) Ni or (**B**) Co atoms at increasing loading as evidenced by infrared spectroscopy of adsorbed NO (adapted from ref. [110]).

Co-Mo-S structures have been observed in supported and bulk sulfides, as well as in single and multilayer structures. The existence of a Co-Mo-S phase was established by combining activity measurements with various analytical techniques; in particular, in-situ MES, EXAFS, and IR spectroscopy of adsorbed NO.[16,110,144,146,157] More recent investigations into the nature of the Co-Mo-S phase include also advanced microscopic techniques, as well as computational approaches.[97,109,171-173] It is important to note that

the Co-Mo-S structure is not a single chemical phase in the conventional sense but rather a family of structures with a wide range of Co(Ni) concentrations, ranging from pure MoS_2 up to virtually full coverage of the MoS_2 edges by promoter atoms. In addition to the Co-Mo-S phase (or an equivalent Ni-Mo-S phase), segregated sulfides of Co (Ni) are typically present (see also section 2.3.5).

Even though they share some common features, Co-Mo-S and Ni-Mo-S phases also exhibit important structural differences, which may be responsible for their different catalytic behavior. Both elements substitute Mo at very specific edge sites, leading to a truncation of the otherwise preferentially triangular MoS_2 shape (see also section 2.3.2). Combined microscopic evidence and simulations evidence a strong preference for Co to substitute Mo at the ($\bar{1}010$) S edge only.[172] The almost regular hexagonal morphology found for Co-Mo-S clusters was attributed to this selective incorporation pattern, in which unpromoted ($10\bar{1}0$) M edges and fully Co-promoted ($\bar{1}010$) S edges are exposed in roughly the same proportion. Ni, by contrast, seems to be able to adopt positions at the ($10\bar{1}0$) M edge as well, especially in smaller clusters. The more diverse incorporation pattern was associated with additional slab terminations (e.g., ($11\bar{2}0$) edges), leading to an overall more complex slab morphology (e.g., dodecahedral). It is not exactly clear to which extent the different edge arrangements in Ni- and Co-Mo-S contribute to differences in catalytic behavior.[97]
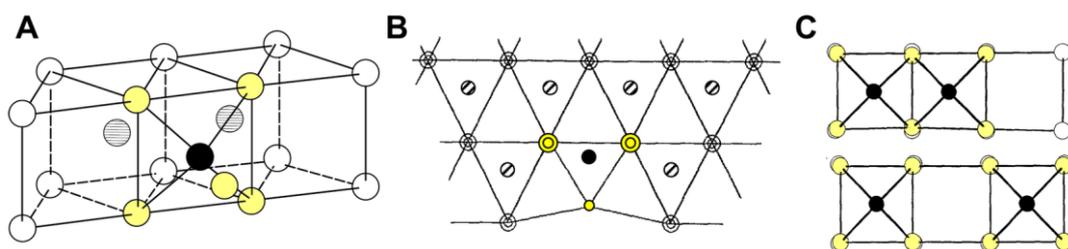
Figure 2.21. Schematic structure and local environment of Ni atoms at the MoS_2 edge. (**A**) Five-fold coordinated, tetragonal pyramidal NiS_5 entity as evidenced by EXAFS. The S atoms assigned to the NiS_5 unit are highlighted in yellow (white spheres: S; black spheres: Ni; hatched spheres: Mo; adapted from ref. [5]). (**B**) View from top of slab showing the "retracted" position of Ni compared to regular Mo lattice (legend: see (A); concentric circles indicate S atoms on top of each other; adapted from ref. [174]). (**C**) View onto slab edge showing distortions of the S atoms associated with Ni as compared to the regular lattice positions in pure MoS_2 (legend: see (A); adapted from ref. [174]).

Based primarily on EXAFS results, it was shown that the promoter atoms reside in five-fold coordinated sites of tetragonal pyramidal-like geometry with a Co-S (Ni-S) distance

of approximately 2.21 Å and a Co-Mo (Ni-Mo) distance of about 2.85 Å (Figure 2.21).[69,92,174-176] These results allow for some important conclusions: The Co-S (Ni-S) distance is significantly and consistently shorter than that of Co (Ni) sulfides, indicating that the promoter atoms must be contained in an other phase. This is in good agreement with the Co-Mo-S model, in which the promoter atoms and the base metal sulfide are chemically associated and form a new bimetallic sulfide (see also section 2.3.5). The Co(Ni)-S distance of 2.21Å is also significantly shorter than that of Mo-S in MoS_2 (2.41 Å). Accordingly, while the promoter atoms are located in the same plane as the Mo atoms, the edge structure with the promoter atoms must be somewhat distorted compared to the MoS_2 phase farther within the layer. That is, the promoter atoms are positioned close to but not exactly on Mo lattice positions. This is also supported by the Co(Ni)-Mo distance of approximately 2.85 Å, which is significantly shorter than the intralayer separation of Mo atoms (about 3.16 Å). More recent experimental investigations on bulk sulfides such as those presented in chapter 2 of this thesis have confirmed the earlier results that were primarily obtained with supported sulfides.

It is important to note that the above coordination geometry, just like the structure of MoS_2 edges in general, is not static but rather highly dependent on the reaction conditions. While the five-fold, tetragonal pyramidal-like coordination seems to be the normal case under sulfiding conditions, it was shown that reductive or sulfo-reductive conditions lead to the formation of four-fold coordinated, square-planar CoS_4 or NiS_4 units.[174] Theoretical calculations, on the other hand, suggest that the most stable structure of four-fold coordinated promoter species should be actually tetrahedral under typical HDS conditions, hence leading to much stronger distortions of the edge than anticipated from EXAFS results.[172]

Due to the "averaging" nature of EXAFS (and many other analytical techniques) it is often not possible to distinguish more than one type of configuration for the promoter atoms in one catalyst. However, it was found that such variations occur, for example, as the simple result of different promoter locations along the MoS_2 edge (in analogy to the "corner" and "regular" sites depicted in Figure 2.12 for unpromoted MoS_2).[177] Lateral Co-Co (Ni-Ni) interactions at high edge decorations,[146,157] as well as variations in sulfur coordination due to varying gas phase composition[178-179] may also lead to deviations from the idealized, static picture described above.

2.3.4.4 Periodic trends and electronic effects

Much of what has been said on the reactivity and the active sites of unpromoted MoS_2 (see section 2.3.3) also applies to promoted catalysts. Coordinatively unsaturated sites, in particular, are believed to be essential for S-extrusion reactions in both unpromoted and promoted TMS. Accordingly, one way to explain the enhanced activity of promoted sulfides is to assume that the promoter atoms in Co-Mo-S structures simply labilize the metal-sulfur bonds, thus enhancing the ability to create and stabilize CUS.[122,178,180-181] IR studies of adsorbed NO have indeed shown that the average M-S bond strength in Co-Mo-S is reduced compared to MoS_2.[110] The corresponding "reduced" (coordinatively unsaturated) and "oxidized" Co-Mo-S structures have been evidenced directly, for example, via MES.[182] In agreement with these early results, numerous recent studies similarly report that the incorporation of promoter atoms leads to an increased concentration of CUS. [78,80,183] In contrast to this emphasis on CUS "quantity", others have defended the notion that the promoter atoms mainly affect the "quality" of CUS.[32,184-186]
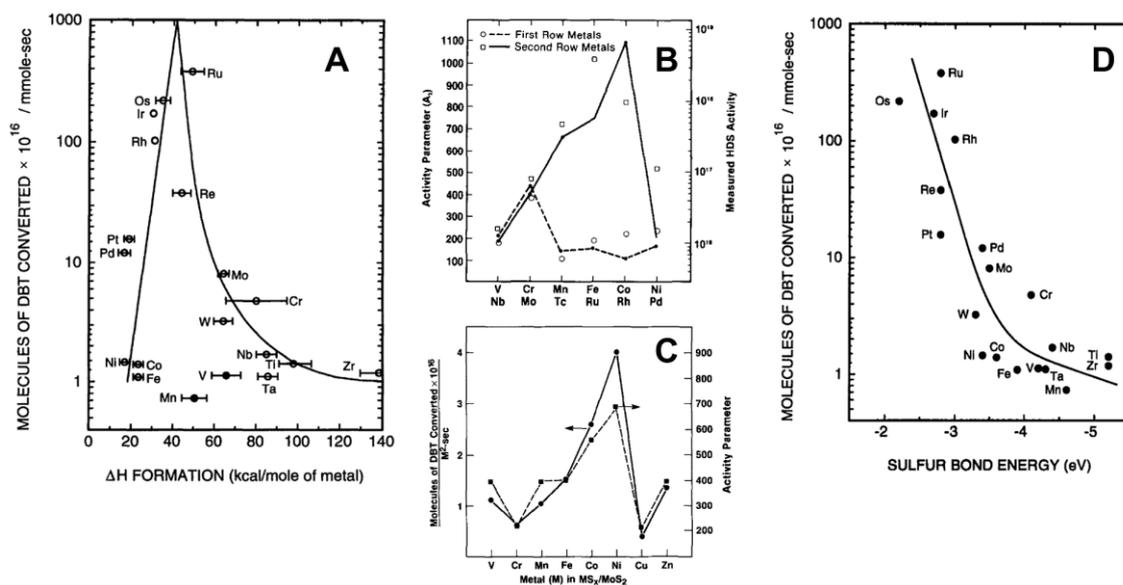
Figure 2.22. Periodic trends of monometallic and bimetallic TMS. (**A**) Model by Pecoraro and Chianelli[32] correlating HDS activity with metal-normalized M-S bond strength (reproduced from ref. [122]). Note how especially Mn does not follow the general activity trend. (**B**) Model by Harris and Chianelli (reproduced from ref. [184]). Experimental HDS activity (lines) of monometallic TMS in agreement with calculated activity descriptor (symbols). (**C**) Analogous model for bimetallic TMS (reproduced from ref. [185]). (**D**) Bond energy model, correlating S-normalized bond strength of monometallic TMS with their HDS activity (reproduced from ref. [122]).

There has been some success in addressing these issues by analyzing trends in activity of different metal sulfides (alone or in combination) in dependence of their position in the periodic table (extensively reviewed in refs. [151,186]). This systematic approach is clearly led by the hope that a meaningful pattern might emerge which is correlated to the properties of the metals' valence electrons. Not only do such findings help to identify the electronic parameters relevant for hydrotreating catalysis, but they can also provide rational guidelines for the design of new catalysts.

An early account of such periodic trends was brought forward by Pecoraro and Chianelli,[32] who systematically studied bulk monometallic TMS of the first, second and third row in the HDS of a model compound (DBT). Their main result was a "volcano-type" curve, obtained by plotting the metal-normalized activity against the metals' periodic position. They also noticed that the heat of S adsorption, approximated by the enthalpy of formation of the bulk sulfide, correlated well with activity data. This was interpreted in terms of the Sabatier principle,[187] in which a too strong heat of adsorption leads to "reactant poisoning" of the surface, whereas a too low heat of adsorption leads to insufficient interaction (activation) of the reactant with the metal (i.e., too strong M-S_{DBT} bond and too weak M-S_{DBT} bond, respectively). According to this reasoning, an optimal HDS catalyst should have a moderate heat of adsorption for the organic substrate. However, this intuitive understanding fails to account for the behavior of the first-row transition metals and particularly for Mn, which is by far the least active despite its calculated optimal heat of adsorption as shown in Figure 2.22 A. While initially promising, it was thus concluded that such a crude approach, based solely on the heat of adsorption, could not fully explain the observed trends.

In a later set of studies, Harris and Chianelli[184-185] employed a more refined approach. Instead of simply using the heat of adsorption as an "activity descriptor", they calculate an empirical parameter, which is based on the electronic properties of charged octahedral MS_6^{n-} and $MoMS_6^{n-}$ clusters. The new descriptor accounts for the number of d electrons in the highest occupied molecular orbital (HOMO), the degree of covalency (the degree of metal-sulfur d-p interaction) and the covalent bond strength. This results in a much better fit of the experimental activities of monometallic sulfides (Figure 2.22 B). In the bimetallic case, it was found experimentally that Co and Ni have a significant promoting effect on bulk MoS_2, whereas the effect of V, Cr, Mn, Fe and Zn is little (Cu even shows

a negative influence). This was interpreted as an electronic effect of the promoter atoms on the electron density of the Mo atoms, with Co and Ni being able to donate electrons, and Cu having a tendency to withdraw electrons from Mo. It was concluded that the number of $3d$ electrons of the promoter and their orbital energies have the largest influence on the activity of the bimetallic TMS. Specifically, it was argued that the increased number of d electrons, formally associated with Mo, leads to a stronger binding of the heterocyclic ring sulfur, further weakening the C-S bond via π-backdonation from the metal. The experimental and theoretical results are in good agreement (Figure 2.22 C), but the approach has been criticized because of the crude approximation of a working HDS catalyst by an octahedral non-neutral cluster. The other main criticism is the purely empirical (i.e., non-rational) construction of the activity descriptor: Even though it follows the activity trend, it cannot explain why this specific combination of parameters should be so important for HDS. From a thermodynamic point of view, the most appropriate descriptor would be a well-defined free energy of adsorption, but this would require solid surfaces that are accordingly well-defined – a situation which is rarely found in real catalysts.

In an attempt to circumvent these shortcomings, Nørskov et al.[122,181] developed what came to be known as the "bond-energy model" (BEM). Here, the important parameter is the average binding energy of one S atom, which differs from the earlier model of Pecoraro and Chianelli by normalizing the binding energy on the S atom instead of the M atom. Furthermore, in contrast to the earlier model by Harris and Chianelli, the activity descriptor is now a single parameter whose relevance for HDS can be directly rationalized (instead of using an "arbitrary" combination of parameters of little informative value). In brief, the BEM reduces the activity of TMS on their ability to form and stabilize S vacancies in inverse proportion to their average M-S bond strength (on a sulfur basis). Accordingly, there is no optimal bond-strength: the weaker the M-S bond, the higher the propensity to lose an S atom and the higher the concentration of CUS (Figure 2.22 D). Notice that this is in stark contradiction to the Sabatier principle as invoked in the earlier models, and that sulfur coordination, as well as crystal structure, are not taken into account.

Thanks to advances in computational chemistry, Toulhoat and Raybaud et al.[188-189] have been partially successful in reconciling these differing views on the electronic nature of

promotion, i.e., bringing together the Sabatier principle (effect on "site quality") and CUS concentration (effect on "site quantity"). By using the concept of cohesive energy, which is based on the energy of atomization instead of the heat of formation, a much more realistic estimate of M-S interaction is obtained. Most importantly, these activity descriptors are able to account for changes in both the quantity and the quality of CUS arising from incorporation of promoter metals into the MoS_2 edges. Indeed, both factors appear to be relevant for catalysis and neither of these alone may be able to account for differences in activity between promoted and unpromoted sulfides. It is typically found, for example, that bulk $Ni-MoS_2$ is more active than supported MoS_2/Al_2O_3, even though the latter may have a higher concentration of CUS due to the much higher dispersion of the active phase.[183] If it were just for the concentration of CUS, the inverse outcome would be expected. Similarly, the fact that Cu-induced weakening of M-S bonds leads to a higher propensity for CUS formation but not to higher activity, implies that the promoter's influence on the quality of the sites has also to be considered.[186]

Despite the significant progress made by analyzing periodic trends, it is questionable whether this knowledge will directly lead to the development of substantially improved catalysts. First, the most effective metal combinations for TMS are most likely already known. Accordingly, the approach of "chemical interpolation" of single sulfide properties to find multi-metallic TMS of superior activity may therefore be of limited success. Second, the optimal composition as predicted by such an approach might not be synthetically accessible or simply not stable under the relevant reaction conditions. Nevertheless, the periodic approach has contributed significantly to a better understanding of the electronic nature of active sites in TMS in general and, in particular, in promoted sulfides. The knowledge of the electronic situation at the level of a single site is one more step towards a reliable formal model of the kinetics of catalytic reactions on TMS.

2.3.5   Segregated promoter metal sulfides

2.3.5.1   Origin and structure

Promoter metals in multimetallic TMS can exist in different forms in one and the same catalyst (see examples in Figure 2.19). The most prominent and perhaps most debatable

representatives of this group are the monometallic promoter metal sulfides, such as Ni_3S_2 or Co_9S_8, which are often simply referred to as "segregated" sulfides. Their ubiquity in both bulk and supported TMS has led to divergent conclusions regarding their relevance for hydrotreating catalysis. While often merely considered an "eye-catching" inactive feature, some have argued that segregated sulfides may contribute to catalytic hydrotreating reactions; either directly as active phases in their own right, or indirectly in connection with the contact synergy model (see also section 2.3.4.2).[86,190]
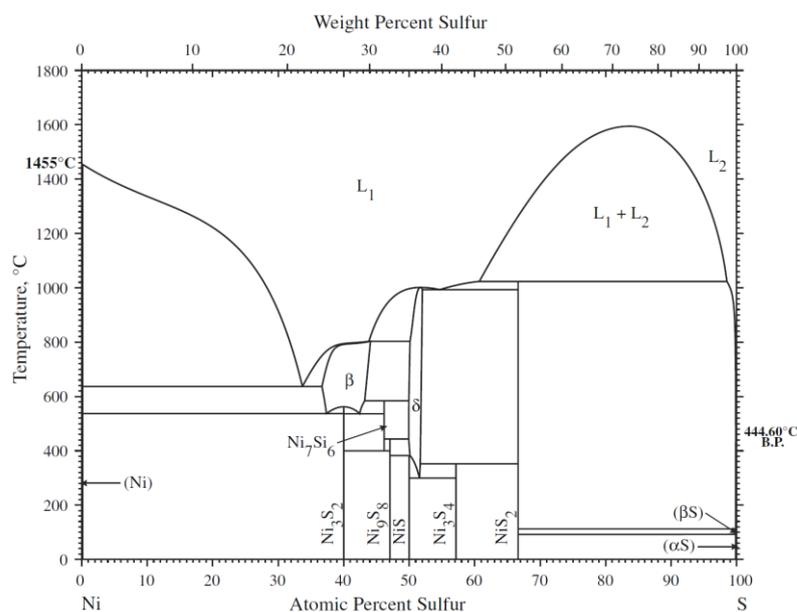
Figure 2.23. Ni-S phase diagram (reproduced from ref. [191]). Several different forms of Ni sulfide are thermodynamically stable under typical hydrotreating conditions (i.e., approx. 300–400 °C).

Segregated sulfides can represent a considerable fraction of the promoter metal atoms in TMS catalysts. For example, up to 85 % of Co was found to be present as Co_9S_8 in a series of model $Co\text{-}MoS_2$ catalysts.[157] NiS_x contents can be similarly high, typically 30–50 % of the total Ni present,[190] with some estimates even higher than that (see, for example, chapter 4 of this thesis). It is generally accepted that $Co\text{-}MoS_2$ catalysts typically exhibit only one form of segregated Co sulfide, Co_9S_8,[110,157] whereas Ni forms a whole palette of different sulfides that are thermodynamically stable under typical hydrotreating conditions (Figure 2.23).[191] Ni_3S_2, Ni_9S_8, and NiS are among those most frequently found in fresh or spent $Ni\text{-}MoS_2$ catalysts,[85,183,192] while Ni_3S_4, Ni_7S_6, NiS_2 are reported less frequently.[133,183,193] All of these compounds are well-known in their bulk form, as they

also exist in the form of naturally occurring minerals (e.g., NiS: millerite; Ni_3S_2: heazle-woodite; Co_9S_8: a rare form of pentlandite).

The formation of segregated Co(Ni) sulfides may occur via different mechanisms and at different stages during the lifetime of a hydrotreating catalyst, that is, precursor preparation, sulfidation, and finally operation in the reactor. Regarding the precursor stage, a simple "overloading" of the oxidic precursor with Co or Ni salt, as well as inhomogeneous mixing or impregnation may lead to promoter-rich domains that are retained throughout subsequent sulfidation. This carry-over of the precursor's elemental distribution is a well-known phenomenon. In one MES study, for example, it was shown that Co_3O_4 species in the calcined precursor are selectively converted to Co_9S_8.[157] Apart from inadequate preparation protocols, segregation is typically induced during the sulfiding and reaction stage, in which the extent of segregation and the nature of the segregate are affected also by other factors in addition to stoichiometry and material distribution. In particular, temperature, gas phase composition, and time on stream have to be considered.

2.3.5.2   Thermodynamic and kinetic aspects of segregation

Segregation of Co(Ni) from Mo(W)S_2 edges is a thermodynamically favorable process.[190,194-195] Owing to the trivial fact that the edge area of the base metal sulfide is limited, segregation tends to be generally more severe in catalysts with higher promoter to base metal-ratio. Excessive promoter atoms that cannot be accommodated at the edges are thus invariably bound to form a separate phase. Note, however, that segregation does not necessarily require prior edge saturation. In fact, segregation may take place much earlier, starting at edge decorations of about 50 % depending on the promoting metal (Co or Ni), the edge type (M or S edge; see section 2.3.2), as well as the chemical potential of S ($\Delta\mu_S$), which is determined by temperature and gas phase composition.[194] The latter is particularly important, as it indirectly influences segregation by affecting the S coverage of the edges.

According to theoretical calculations, Co and Ni promoted edges are better at stabilizing high S coverages than the unpromoted MoS$_2$ edge (and vice versa).[194,196-197] Following a generalized Le Chatelier principle, the catalyst will hence counteract the effect of high

$\Delta\mu_S$ by preferentially exposing promoted edges in order to stabilize high S coverages. At low $\Delta\mu_S$, by contrast, promoter atoms are segregated from the edge in order to better stabilize a low S coverage. This effect was found to be dependent on the edge type, i.e., it affects M and S edges to a different extent, and may thus lead to adaptations in the catalyst's morphology in addition to changes in promoter content. A particularly strong tendency towards segregation was found for Co at the M edge of MoS_2, which will cause segregation of Co already under moderate hydrotreating conditions. In general, segregation tends to follow the severity of the reaction regime, that is, it will be more extensive at high temperature and high H_2 pressure (low H_2S/H_2 ratio).

Another important factor that affects segregation during sulfiding and reactor operation is the sintering of the primary Co(Ni)-Mo-S crystallites, which leads to decreasing dispersion and, consequently, to a decreasing capacity for accommodating promoter atoms.[141,190,198] As the extent of sintering-induced segregation increases over time, it significantly contributes to the progressive deterioration of the catalyst during reactor operation (deactivation). Note that sintering is substantially accelerated by exposure to high temperatures. This is particularly relevant for catalyst particles at the reactor entry (due to the higher reaction exotherm) and those at the reactor bottom (due to the higher operation temperature). The same applies to catalysts used in high-severity operations (section 2.1) and high-temperature sulfiding protocols for Type-II site generation (section 2.3.3.6). During sulfidation, high temperatures may also occur inadvertently, e.g., when the concentration of the sulfiding agent is too high or the sulfidation exotherm is inadequately controlled (section 2.3.1). Highly dispersed supported catalysts are particularly affected by sintering, as high temperatures eliminate Mo-O(S)-Al linkages that would otherwise prevent excessive migration over the support surface.

Regarding the time-dependent aspects of segregation, there is a notable difference between Ni and Co sulfides, which is associated with their melting points or, more specifically, with their Tamman[199] and Hüttig[200] temperatures. These are the temperatures, at which bulk and surface atoms, respectively, become sufficiently mobile for re-crystallization (with $T_{Tam} > T_{Hüt}$). While the Ni atoms in any of the various Ni sulfides are already appreciably mobile at the temperatures used in hydrotreating (approx. 300 to 400 °C), this is not the case for Co_9S_8, which is much more stable against sintering in this regime (T_{Tam} for Ni_3S_2: 257 °C, Ni_7S_6: 259 °C, NiS: 352 °C, Co_9S_8: 413 °C).[193,200]

Accordingly, NiS_x crystallites are relatively prone to continuous sintering during reactor operation and may thus reach hundreds of nanometers in diameter in spent hydrotreating catalysts.[190]

2.3.5.3   Significance for hydrotreating catalysis

There has been a lot of debate about the actual role of segregated sulfides in hydrotreating catalysis, particularly in connection with the "contact synergy" model (discussed in detail in section 2.3.4.2). Even though contact synergy is now ruled out as origin of the promoter effect, the general idea is quite plausible given the intimate contact of the two phases. This coexistence is best seen in micrographs obtained by various techniques (Figure 2.24). High-resolution TEM micrographs often show that $Mo(W)S_2$ layers in bulk TMS follow the contour of segregated sulfide crystals (Figure 2.24 A). If this two-dimensional projection is analyzed in three dimensions, such as by advanced micro-tomographic techniques, one can easily see that the segregated particles are, in fact, fully wrapped by the $Mo(W)S_2$ matrix (Figure 2.24 C). This is somewhat different from the situation encountered in supported sulfides (Figure 2.24 B). Elemental mapping shows that the phase distribution is rather two-dimensional in this case, as it follows the contour of the support. For bulk TMS, it has been argued that the embedded crystallites could act as a kind of support for the active Co(Ni)-Mo-S phase, which might improve its dispersion and provide a greater stability against sintering.[133,190,192]
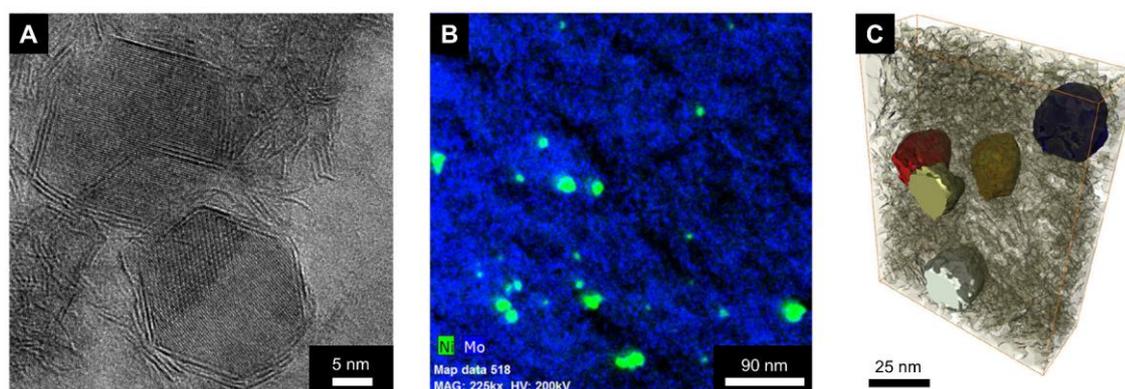
Figure 2.24. Segregated Ni sulfides (NiS_x) visualized by different techniques (adapted from ref. [190]). (**A**) Individual NiS_x crystals in bulk $Ni-MoS_2$, covered by Ni-Mo-S (MoS_2) layers. (**B**) STEM-EDX elemental map of $Ni-MoS_2/Al_2O_3$, showing Ni-rich particles (green) on a Mo-rich substrate (blue). (**C**) STEM-HAADF tomography of bulk $Ni-MoS_2$, showing NiS_x particles (false colors) embedded in a matrix of Ni-Mo-S (MoS_2) layers.

In contrast to the indirect mode of action of the contact synergy model, there have been other proposals in which the segregated sulfides function as active sites themselves. It is well-known, in fact, that pure CoS_x and NiS_x have a measurable activity in hydrotreating reactions (HDS, HDN, and hydrogenation).[33,117,201-203] However, their intrinsic activity is much smaller compared to Co(Ni)-Mo-S phases and typically even smaller than the activity of unpromoted MoS_2.[157] In addition, segregated sulfides tend to form rather large crystallites of accordingly low specific surface area,[190] especially after long time-on-stream. This further reduces their contribution to the overall reaction rate (except for rare cases with high segregate dispersion[16]). As a result, CoS_x and NiS_x are nowadays largely considered as quasi-inert solids within the catalyst matrix.[5,190]

Despite their quasi-inert nature in HDS and HDN, segregated sulfides still have important effects on the activity of the catalyst, most trivially, by "diluting" the active components and by covering ("blocking") active sites. The negative impact of Co_9S_8 in particular has been demonstrated numerous times.[16,165,204] In general, if the preparation conditions are chosen such as to maximize the formation of segregated sulfides, a decrease in activity is almost always seen. Among other means, such a situation can be reached by increasing the promoter concentration, the calcination or sulfidation temperature. Given an increasing promoter content, activity will first level off and finally decrease at even higher concentrations of Co (Figure 2.25 B). While this may be attributed to site blocking by progressive Co_9S_8 formation, a closer look at the Co distribution suggests a different conclusion (Figure 2.25 A). In fact, it appears that the activity primarily follows the concentration of Co present as Co-Mo-S, while the influence of an increasing Co_9S_8 concentration has little effect. In this specific study, it was therefore concluded that HDS activity depends only on the concentration of Co present as Co-Mo-S, which makes a site blocking effect of Co_9S_8 rather unlikely.[46,157] However, given the large uncertainty in the data, particularly at Co/Mo $\approx$ 1.2, it is questionable whether this interpretation is truly correct. Also, it remains to be elucidated why an increasing amount of Co would lead to a lower concentration of Co present as Co-Mo-S, as that would be incompatible with Le Chatelier's principle. A possible interpretation of this discrepancy is the "self-accelerated" growth of Co_9S_8 at high concentrations of Co (in analogy to Ostwald ripening[205]). As more Co is initially present, more nucleation sites will form during sulfidation and less Co will be available for Co-Mo-S formation. More

recently, a combined theoretical-experimental study demonstrated that similar effects also apply to NiS_x in supported $Ni-MoS_2$.[78] It was shown that NiS_x growth can be initiated at edge-incorporated Ni atoms, which then serve as nucleation sites for NiS_x, thus lowering the concentration of Ni promoted sites in their immediate vicinity by either withdrawing Ni from already formed Ni-Mo-S structures or by depleting the environment of Ni during Ni-Mo-S formation.
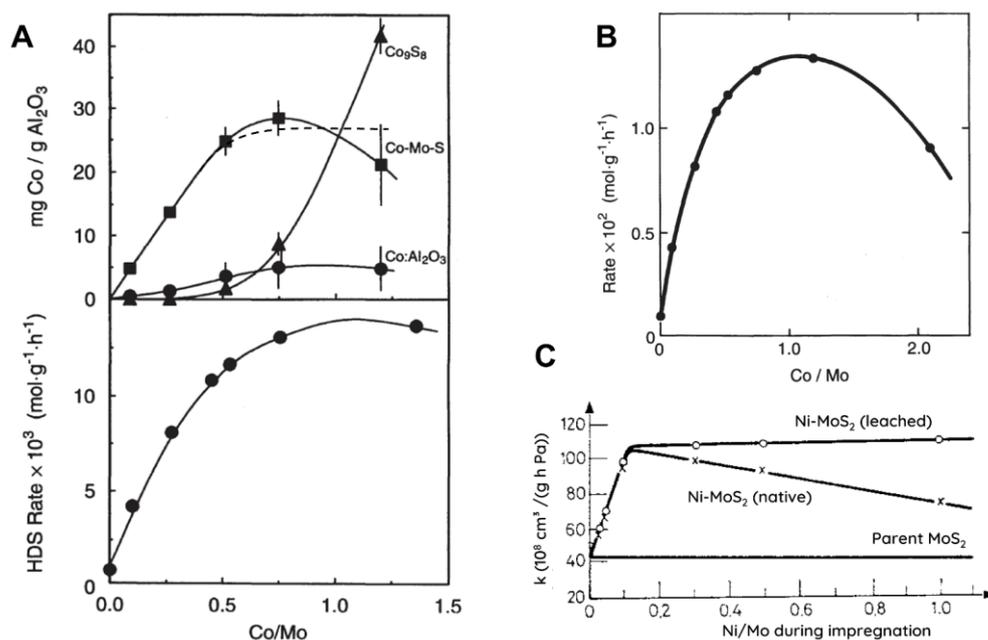
Figure 2.25. Effect of promoter metal content on activity. (**A**) Upper panel: evolution of Co species as evidenced by MES, including an alternative interpretation (dashed line). Lower panel: HDS rate as a function of Co/Mo ratio (diagram adapted from ref. [4]; data: ref. [157]) (**B**) Rate of thiophene HDS on $Co-MoS_2/Al_2O_3$ as a function Co/Mo ratio (diagram adapted from ref. [4]; data: ref. [206]). (**C**) Rate constant of *o*-xylene hydrogenation over bulk $Ni-MoS_2$ as a function of Ni/Mo ratio. The open symbols show the same catalyst after segregated sulfides have been removed via acidic treatment (adapted from ref. [207]).

The above observations seem to indicate that site-blocking by segregated sulfides may be of little practical importance. Indeed, some have argued that segregated sulfide forma-tion should be considered a by-product, rather than the cause of deactivation in operating catalysts.[190] Specifically, it was pointed out that deactivation is mainly driven by sintering of the MoS_2 phase, which directly decreases the concentration of promoted sites by decreasing the edge area (which in turn leads to the segregation of Co_9S_8 or NiS_x as a side effect). Site-blocking is nevertheless often considered as a negative consequence of segregation.[69,81,108] On one hand, this is backed up by experiences with real catalysts, in

particular those used for demetalation. These have a much shorter lifetime than other hydrotreating catalysts, which is partly caused by the build-up of metal sulfide deposits, among them NiS_x (see section 2.1). On the other hand, there is supporting evidence also from laboratory experiments,[207] in which the activity of bulk $Ni-MoS_2$ was substantially enhanced ("restored") after the post-synthetic removal of segregated NiS_x (Figure 2.25 C). Such acid treatments may increase the activity well beyond the level expected for a mere elimination of inert mass, thereby highlighting the site-blocking role of NiS_x (as shown in chapter 4 of this thesis).

2.3.5.4 Consequences for catalyst characterization

The presence of segregated sulfides has substantially contributed to the troublesome history of TMS characterization. This is true for commercial catalysts in particular, due to their high promoter metal content (Co(Ni)/Mo(W) > 0.4–0.5),[86] as well as for many laboratory catalysts that were synthesized to match the activity of their industrial counterparts. Only in the case of true model catalysts with very low promoter contents (e.g., Co/Mo = 0.09) is it possible to selectively generate the active Co-Mo-S phase without inducing segregation (at least on short time scales).[144] The ubiquity of segregated sulfides and the difficulties in separating their contribution from that of the active Co(Ni)-Mo-S phase have always been a major problem. Even today, with advanced characterization techniques, there is still no standard analytic approach that isolates the properties of the active phase, e.g., active site concentration, from the confounding $Co(Ni)S_x$ phases.

The concentration of active sites is one of the most important properties of a catalyst and an essential piece of information on the way to a structure-function relationship. The "site count" is thus a common objective of catalyst characterization, which often uses probe molecules like NO or CO for this purpose (see section 2.3.3.3). These probes, however, are rather unselective for the sites of interest, as they will also adsorb on the surface of segregated sulfides (i.e., both on the "active" CUS of Co(Ni)-Mo-S and the "inactive" CUS of $Co(Ni)S_x$).[81] Consequently, the informative value of the total adsorption capacity, or "uptake" of probe molecule, is only very limited. Some researchers have therefore employed a combination of additional analytic techniques to single out the contribution of $Co(Ni)S_x$ to the total site count. Theoretically, this is most

easily done by determining the dimensions of the segregated particles by XRD or electron microscopy and calculating the number of sites given by $Co(Ni)S_x$.[190] In practice, however, this can be a rough estimate at best. The stable surface structure of the segregate is typically not known, which means that the areal density of sites (accessible promoter ions) is equally ill-determined. More importantly, only particles of a certain minimum size can be visualized by electron microscopy, typically only those larger than about 5 to 10 nm. This applies similarly to XRD, which may not detect small NiS_x crystals due to excessive line broadening.[208] In addition, it has been shown by EXAFS measurements that NiS_x domains in bulk $Ni-MoS_2$ may also be present in an X-ray amorphous form.[183] Because the smallest particles are also those with the highest dispersion, it is expected that such approximations considerably underestimate the contribution of segregated metal sulfides to the total site count.

In contrast to that, IR spectroscopy of adsorbed probe molecules has been partially successful at separating contributions of different sulfide phases. Complications related to the presence of segregated sulfides are still quite common, for example, overlapping or ill-defined IR bands.[78,80,108,113] Such analytical difficulties, related to the co-adsorption of probe molecules on segregated sulfides, can be avoided altogether if the confounding phases are removed prior to the measurement. This approach has been applied successfully to a series of supported $Ni-MoS_2$ catalysts that were then analyzed with IR spectroscopy of adsorbed NO.[209] Note, however, that IR spectroscopy is only applicable to transparent materials like Al_2O_3-supported sulfides but not to bulk sulfides (see section 2.3.3.3).

Spectroscopic techniques with higher site specificity, like MES for ^{57}Co-doped catalysts, are not affected by such problems, as the active Co ions (those in the Co-Mo-S phase) are selectively quantified without being confounded by CoS_x.[157] This method is particularly useful for the analysis of the "two-dimensional" active phase of supported TMS, as the active sites detected by MES are then essentially all located at the accessible surface (in contrast to the three-dimensional bulk sulfides). Even in this case, however, a meaningful structure-function relationship may only be established when segregated sulfides at the surface are absent. This is due to the fact that CoS_x restricts the accessibility of active sites at the Co-Mo-S edges, thus leading to a discrepancy between site count and activity (even though the site count is unaffected).

Establishing structure-function relations for bulk sulfides is generally much more challenging than for supported materials, as only a small fraction of active sites (those at the surface) is actually accessible for reactants. Surface-sensitive techniques, such as titration with probe molecules, are therefore one of the few feasible alternatives for site quantification in these materials. However, as described earlier, the significance of titration measurements is severely diminished in presence of segregated sulfides, which is even more unfortunate in view of the pronounced segregation tendency of bulk TMS. The post-synthetic removal of $Co(Ni)S_x$ as demonstrated in chapter 4 of this thesis, may therefore be a promising auxiliary method for quantifying sites and establishing meaningful structure-function relationships in unsupported sulfides.
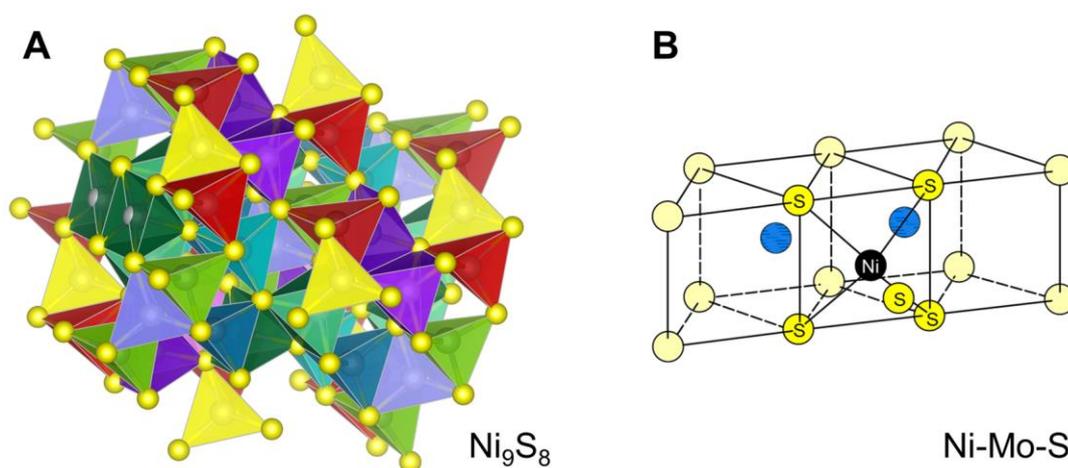
Figure 2.26. (**A**) Structure of Ni_9S_8 (ICSD cc. 63080, visualized with VESTA[76]) as an example for the various Ni sulfides found in Ni-promoted TMS. Different colors indicate different NiS_x coordination polyhedra, each with a unique configuration of Ni and S (i.e., Ni-S distance and coordination number). (**B**) Structure of Ni-Mo-S (adapted from ref. [5]). Ni present in NiS_x significantly contributes to the average structural parameters determined by EXAFS.

Regarding the structure of the active sites (in contrast to their quantity), the most valuable technique has perhaps been X-ray absorption, particularly EXAFS. Also in this case, segregated sulfides add complication to the analysis and diminish the significance of the measurement. Bulk sulfides are particularly affected because only a small fraction of the promoter is actually incorporated into the Co(Ni)-Mo-S phase, while the large remainder is present as $Co(Ni)S_x$. This distorts the most important EXAFS results, such as the average Co(Ni)-S coordination number and interatomic distance, which tend to overrepresent the segregated phase. A further problem is introduced by the sheer variety

and complexity of segregated sulfides, in particular those of Ni, as these cannot be fitted individually due to the limited information content of the spectra (Figure 2.26). The "unresolved" individual sulfides lead to a broadening of the spectral features and thus to wrong estimates of the coordination number.[69,78,82,183] As with site quantification, the post-synthetic removal of $Co(Ni)S_x$ can be helpful also in connection with EXAFS studies. It should be pointed out, however, that this does not completely resolve the issue, as fully embedded $Co(Ni)S_x$ crystals may be inaccessible to the acidic reagent (see chapter 4).

2.4   References

(1)   Bartholomew, C. H.; Farrauto, R. J. *Petroleum Refining and Processing*. In *Fundamentals of Industrial Catalytic Processes*, Bartholomew, C. H., Farrauto, R. J. Eds. John Wiley and Sons: Hoboken, New Jersey **2010**.

(2)   Speight, J. G. *Hydrotreating Processes*. In *Handbook of petroleum refining*, CRC Press: Boca Raton, Florida **2017**, pp 409-455.

(3)   Kokayeff, P.; Zink, S.; Roxas, P. *Hydrotreating in Petroleum Processing*. In *Handbook of Petroleum Processing*, Treese, S. A., Pujadó, P. R., Jones, D. S. J. Eds. Springer International Publishing: Cham **2015**, pp 361-434.

(4)   Topsøe, H.; Clausen, B. S.; Massoth, F. E. *Hydrotreating Catalysis*. In *Catalysis: Science and Technology*, Anderson, J. R., Boudart, M. Eds. Springer: Berlin, Heidelberg **1996**, pp 1-269.

(5)   Prins, R. *Hydrotreating*. In *Handbook of Heterogeneous Catalysis*, Ertl, G., Knözinger, H., Schüth, F., Weitkamp, J. Eds. Wiley-VCH: Weinheim, Germany **2008**, pp 2695-2718.

(6)   Gary, J. H.; Handwerk, G. E.; Kaiser, M. J. *Hydrotreating*. In *Petroleum Refining: Technology and Economics*, Gary, J. H., Handwerk, G. E., Kaiser, M. J. Eds. CRC Press: Boca Raton, FL **2007**, pp 195-205.

(7)   Speight, J. G.; Özüm, B. *Hydrotreating*. In *Petroleum Refining Processes*, Marcel Dekker: New York **2002**, pp 439-484.

(8)   Alfke, G.; Irion, W. W.; Neuwirth, O. S. *Oil Refining*. In *Ullmann's Encyclopedia of Industrial Chemistry*, Wiley VCH: Weinheim **2007**, pp 207-261.

(9)   Ancheyta, J.; Speight, J. G. *Hydroprocessing of heavy oils and residua*. CRC Press: Boca Raton, Florida **2007**, 376 pages.

(10)   Zhu, F.; Hoehn, R.; Thakkar, V.; Yuh, E. *Diesel Hydrotreating Process*. In *Hydroprocessing for Clean Energy*, Zhu, F., Hoehn, R., Thakkar, V., Yuh, E. Eds. American Institute of Chemical Engineers and John Wiley and Sons: Hoboken, New Jersey **2016**.

(11)   Furimsky, E. *Appl. Catal., A* **1998,** 171, 177-206.

(12)   Andari, M. K.; Bchbehani, H.; Stanislaus, A. *Fuel Sci. Technol. Int.* **1996,** 14, 939-961.

(13)   Weisser, O.; Landa, S. *Sulphide catalysts, their properties and applications*. Pergamon Press: Oxford, New York **1973**, 506 pages.

(14)   Dabelstein, W.; Reglitzky, A.; Schütze, A.; Reders, K.; Brunner, A. *Automotive Fuels*. In *Ullmann's Encyclopedia of Industrial Chemistry*, Wiley VCH: Weinheim **2016**, pp 2-41.

(15)   Startsev, A. N. *Catal. Rev.* **1995,** 37, 353-423.

(16)   Topsøe, H.; Clausen, B. S. *Catal. Rev.* **1984,** 26, 395-420.

(17)   Vasudevan, P. T.; Fierro, J. L. G. *Catal. Rev.* **1996,** 38, 161-188.

(18)   Vrinat, M. L. *Appl. Catal.* **1983,** 6, 137-158.

(19)   Girgis, M. J.; Gates, B. C. *Ind. Eng. Chem. Res.* **1991,** 30, 2021-2058.

(20)   Schuit, G. C. A.; Gates, B. C. *AlChE J.* **1973,** 19, 417-438.

(21)   Nag, N. K.; Sapre, A. V.; Broderick, D. H.; Gates, B. C. *J. Catal.* **1979,** 57, 509-512.

(22)   Houalla, M.; Broderick, D. H.; Sapre, A. V.; Nag, N. K.; de Beer, V. H. J.; Gates, B. C.; Kwart, H. *J. Catal.* **1980,** 61, 523-527.

(23)   Houalla, M.; Broderick, D. H.; de Beer, V. H. J.; Gates, B. C.; Kwart, H. *Am. Chem. Soc., Div. Petrol. Chem. Prepr.* **1977,** 22, 941.

(24)   Katti, S. S.; Westermann, D. W. B.; Gates, B. C.; Youngless, T.; Petrakis, L. *Ind. Eng. Chem. Process. Des. Dev.* **1984,** 23, 773.

(25)   Kilanowski, D. R.; Teeuwen, H.; de Beer, V. H. J.; Gates, B. C.; Schuit, G. C. A.; Kwart, H. *J. Catal.* **1978,** 55, 129-137.

(26)   Prins, R.; Egorova, M.; Röthlisberger, A.; Zhao, Y.; Sivasankar, N.; Kukula, P. *Catal. Today* **2006,** 111, 84-93.

(27)   Ali, S. A. *Thermodynamics of Hydroprocessing Reactions*. In *Hydroprocessing of Heavy Oils and Residua*, Ancheyta, J., Speight, J. G. Eds. CRC Press: Boca Raton, FL **2007**, pp 51-69.

(28)   Speight, J. G. *The Desulfurization of Heavy Oils and Residua*. Marcel Dekker: New York **1981**, 224 pages.

(29)   Gates, B. C.; Katzer, J. R.; Schuit, G. C. A. *Chemistry of Catalytic Processes*. McGraw Hill: New York **1979**, 464 pages.

(30)   Krauch, C.; Pier, M. *Z. Angew. Chem.* **1931,** 44, 953-958.

(31)   Chianelli, R. R.; Berhault, G.; Torres, B. *Catal. Today* **2009,** 147, 275-286.

(32)   Pecoraro, T. A.; Chianelli, R. R. *J. Catal.* **1981,** 67, 430-445.

(33)   Chianelli, R. R.; Pecoraro, T. A.; Halbert, T. R.; Pan, W. H.; Stiefel, E. I. *J. Catal.* **1984,** 86, 226-230.

(34)   Eijsbouts, S.; Mayo, S. W.; Fujita, K. *Appl. Catal., A* **2007,** 322, 58-66.

(35)   Bonduelle-Skrzypcak, A.; Guichard, B. *Where Coordination Chemistry Meets HDT Catalyst Synthesis: Organic Additives*. In *Catalysis by Transition Metal Sulphides: From Molecular Theory to Industrial Application*, Raybaud, P., Toulhoat, H. Eds. Editions Technip: Paris **2013**, pp 181-207.

(36)   Lamonier, C.; Payen, E. *Alumina-supported Oxide Precursors Prepared from Heteropolyanions*. In *Catalysis by Transition Metal Sulphides: From Molecular Theory*

to Industrial Application, Raybaud, P., Toulhoat, H. Eds. Editions Technip: Paris **2013**, pp 151-180.

(37)   Digne, M. *Principles Involved in the Preparation of Hydrotreatment Catalysts*. In *Catalysis by Transition Metal Sulphides: From Molecular Theory to Industrial Application*, Raybaud, P., Toulhoat, H. Eds. Editions Technip: Paris **2013**, pp 117-150.

(38)   Breysse, M.; Geantet, C.; Afanasiev, P.; Blanchard, J.; Vrinat, M. *Catal. Today* **2008,** 130, 3-13.

(39)   Eijsbouts, S.; Miseo, S.; Plantenga, F. L.; Soled, S. L. *Hydroprocessing using hydrothermally-prepared bulk multimetallic catalysts*. US 7,686,943 B2, 2010.

(40)   Maesen, T. L. M.; Kuperman, A. E. *Hydroconversion multi-metallic catalyst and method for making thereof*. US 8,702,970 B2, 2014.

(41)   Hagenbach, G.; Courty, P.; Delmon, B. *J. Catal.* **1973,** 31, 264-273.

(42)   Ahuja, S. P.; Derrien, M. L.; Le Page, J. F. *Product R&D* **1970,** 9, 272-281.

(43)   Geantet, C.; Payen, E. *Activation and Genesis of the Active Phase by Sulphidation*. In *Catalysis by Transition Metal Sulphides: From Molecular Theory to Industrial Application*, Raybaud, P., Toulhoat, H. Eds. Editions Technip: Paris **2013**, pp 275-300.

(44)   Arnoldy, P.; van den Heijkant, J. A. M.; de Bok, G. D.; Moulijn, J. A. *J. Catal.* **1985,** 92, 35-55.

(45)   Riddick, F. C.; Peralta, B. *Hydrodesulfurization of oil feedstock with presulfided catalyst*. US 4,213,850 A, 1980.

(46)   Wivel, C.; Clausen, B. S.; Candia, R.; Mørup, S.; Topsøe, H. *J. Catal.* **1984,** 87, 497-513.

(47)   Inamura, K.; Prins, R. *J. Catal.* **1994,** 147, 515-524.

(48)   Fuentes, S.; Diaz, G.; Pedraza, F.; Rojas, H.; Rosas, N. *J. Catal.* **1988,** 113, 535-539.

(49)   Candia, R.; Clausen, B. S.; Topsøe, H. *Bull. Soc. Chim. Belg.* **1981,** 90, 1225-1232.

(50)   Alonso, G.; Aguirre, G.; Rivero, I. A.; Fuentes, S. *Inorg. Chim. Acta* **1998,** 274, 108-110.

(51)   Alonso, G.; Siadati, M. H.; Berhault, G.; Aguilar, A.; Fuentes, S.; Chianelli, R. R. *Appl. Catal., A* **2004,** 263, 109-117.

(52)   Alonso, G.; Berhault, G.; Paraguay, F.; Rivera, E.; Fuentes, S.; Chianelli, R. R. *Mater. Res. Bull.* **2003,** 38, 1045-1055.

(53)   Espinoza-Armenta, Y.; Cruz-Reyes, J.; Paraguay-Delgado, F.; del Valle, M.; Alonso, G.; Fuentes, S.; Romero-Rivera, R. *Appl. Catal., A* **2014,** 486, 62-68.

(54)   Alonso, G.; Berhault, G.; Aguilar, A.; Collins, V.; Ornelas, C.; Fuentes, S.; Chianelli, R. R. *J. Catal.* **2002,** 208, 359-369.

(55)   Alonso, G.; del Valle, M.; Cruz, J.; Petranovskii, V.; Licea-Claverie, A.; Fuentes, S. *Catal. Today* **1998,** 43, 117-122.

(56)   McDonald, J. W.; Friesen, G. D.; Rosenhein, L. D.; Newton, W. E. *Inorg. Chim. Acta* **1983,** 72, 205-210.

(57)   Alonso, G.; Berhault, G.; Chianelli, R. R. *Inorg. Chim. Acta* **2001,** 316, 105-109.

(58)   Luo, H.; Xu, C.; Zou, D.; Wang, L.; Ying, T. *Mater. Lett.* **2008,** 62, 3558-3560.

(59)   Yoosuk, B.; Kim, J. H.; Song, C.; Ngamcharussrivichai, C.; Prasassarakich, P. *Catal. Today* **2008,** 130, 14-23.

(60)   Lai, W.; Chen, Z.; Zhu, J.; Yang, L.; Zheng, J.; Yi, X.; Fang, W. *Nanoscale* **2016,** 8, 3823-3833.

(61)   Song, W.; Lai, W.; Chen, Z.; Cao, J.; Wang, H.; Lian, Y.; Yang, W.; Jiang, X. *ACS Appl. Nano Mater.* **2018,** 1, 442-454.

(62)   Hagenbach, G.; Courty, P.; Delmon, B. *J. Catal.* **1971,** 23, 295-298.

(63)   Castillo-Villalón, P.; Ramirez, J.; Vargas-Luciano, J. A. *J. Catal.* **2014,** 320, 127-136.

(64)   Genuit, D.; Afanasiev, P.; Vrinat, M. *J. Catal.* **2005,** 235, 302-317.

(65)   Berhault, G.; Mehta, A.; Pavel, A. C.; Yang, J.; Rendon, L.; Yácaman, M. J.; Araiza, L. C.; Moller, A. D.; Chianelli, R. R. *J. Catal.* **2001,** 198, 9-19.

(66)   Kelty, S. P.; Berhault, G.; Chianelli, R. R. *Appl. Catal., A* **2007,** 322, 9-15.

(67)   Chianelli, R. R.; Berhault, G. *Catal. Today* **1999,** 53, 357-366.

(68)   Müller, A.; Diemann, E.; Jostes, R.; Bögge, H. *Angew. Chem. Int. Ed. Engl.* **1981,** 20, 934-955.

(69)   Hein, J.; Gutiérrez, O. Y.; Albersberger, S.; Han, J.; Jentys, A.; Lercher, J. A. *ChemCatChem* **2017,** 9, 629-641.

(70)   Amaya, S. L.; Alonso-Núñez, G.; Cruz-Reyes, J.; Fuentes, S.; Echavarría, A. *Fuel* **2015,** 139, 575-583.

(71)   Kasztelan, S.; Toulhoat, H.; Grimblot, J.; Bonnelle, J. P. *Appl. Catal.* **1984,** 13, 127-159.

(72)   Clausen, B. S.; Topsoe, H.; Candia, R.; Villadsen, J.; Lengeler, B.; Als-Nielsen, J.; Christensen, F. *J. Phys. Chem.* **1981,** 85, 3868-3872.

(73)   Hayden, T. F.; Dumesic, J. A. *J. Catal.* **1987,** 103, 366-384.

(74)   Zhao, X.; Ning, S.; Fu, W.; Pennycook, S. J.; Loh, K. P. *Adv. Mater.* **2018,** 30, 1802397.

(75)   Ganatra, R.; Zhang, Q. *ACS Nano* **2014,** 8, 4074-4099.

(76)   Momma, K.; Izumi, F. *J. Appl. Crystallogr.* **2011,** 44, 1272-1276.

(77)   Schachtl, E.; Yoo, J. S.; Gutiérrez, O. Y.; Studt, F.; Lercher, J. A. *J. Catal.* **2017,** 352, 171-181.

(78)   Schachtl, E.; Zhong, L.; Kondratieva, E.; Hein, J.; Gutiérrez, O. Y.; Jentys, A.; Lercher, J. A. *ChemCatChem* **2015,** 7, 4118-4130.

(79)   Gutiérrez, O. Y.; Singh, S.; Schachtl, E.; Kim, J.; Kondratieva, E.; Hein, J.; Lercher, J. A. *ACS Catal.* **2014,** 4, 1487-1499.

(80)   Schachtl, E.; Kondratieva, E.; Gutiérrez, O. Y.; Lercher, J. A. *J. Phys. Chem. Lett.* **2015,** 6, 2929-2932.

(81)   Albersberger, S.; Hein, J.; Schreiber, M. W.; Guerra, S.; Han, J.; Gutiérrez, O. Y.; Lercher, J. A. *Catal. Today* **2017,** 297, 344-355.

(82)   Hein, J.; Gutierrez, O. Y.; Schachtl, E.; Xu, P. H.; Browning, N. D.; Jentys, A.; Lercher, J. A. *ChemCatChem* **2015,** 7, 3692-3704.

(83)   Chianelli, R. R.; Prestridge, E. B.; Pecoraro, T. A.; Deneufville, J. P. *Science* **1979,** 203, 1105-1107.

(84)   Scherrer, P. *Göttinger Nachrichten Math. Phys.* **1918,** 2, 98-100.

(85)   Eijsbouts, S.; Heinerman, J. J. L.; Elzerman, H. J. W. *Appl. Catal., A* **1993,** 105, 53-68.

(86)   Eijsbouts, S. *Appl. Catal., A* **1997,** 158, 53-92.

(87)   Lauritsen, J. V.; Bollinger, M. V.; Lægsgaard, E.; Jacobsen, K. W.; Nørskov, J. K.; Clausen, B. S.; Topsøe, H.; Besenbacher, F. *J. Catal.* **2004,** 221, 510-522.

(88)   Walton, A. S.; Lauritsen, J. V.; Topsøe, H.; Besenbacher, F. *J. Catal.* **2013,** 308, 306-318.

(89)   Tanaka, K.-I. *Catalysis Controlled by the Constitution of Active Sites*. In *Advances in Catalysis*, Eley, D. D., Pines, H., Weisz, P. B. Eds. Academic Press: New York **1985,** pp 99-158.

(90)   Tanaka, K.-i.; Okuhara, T. *J. Catal.* **1982,** 78, 155-164.

(91)   Tauster, S. J.; Pecoraro, T. A.; Chianelli, R. R. *J. Catal.* **1980,** 63, 515-519.

(92)   Bouwens, S. M. A. M.; Koningsberger, D. C.; de Beer, V. H. J.; Louwers, S. P. A.; Prins, R. *Catal. Lett.* **1990,** 5, 273-283.

(93)   Shido, T.; Prins, R. *J. Phys. Chem. B* **1998,** 102, 8426-8435.

(94)   Raybaud, P. *Appl. Catal., A* **2007,** 322, 76-91.

(95)   Raybaud, P.; Hafner, J.; Kresse, G.; Kasztelan, S.; Toulhoat, H. *J. Catal.* **2000,** 189, 129-146.

(96)   Schweiger, H.; Raybaud, P.; Kresse, G.; Toulhoat, H. *J. Catal.* **2002,** 207, 76-87.

(97)   Besenbacher, F.; Brorson, M.; Clausen, B. S.; Helveg, S.; Hinnemann, B.; Kibsgaard, J.; Lauritsen, J. V.; Moses, P. G.; Nørskov, J. K.; Topsøe, H. *Catal. Today* **2008,** 130, 86-96.

(98)   Mars, P.; van Krevelen, D. W. *Chem. Eng. Sci.* **1954,** 3, 41-59.

(99)   Hrabar, A.; Hein, J.; Gutiérrez, O. Y.; Lercher, J. A. *J. Catal.* **2011,** 281, 325-338.

(100)   Lauritsen, J. V.; Kibsgaard, J.; Helveg, S.; Topsøe, H.; Clausen, B. S.; Laegsgaard, E.; Besenbacher, F. *Nat. Nanotechnol.* **2007,** 2, 53-58.

(101)   Massoth, F. E.; Zeuthen, P. *J. Catal.* **1994,** 145, 216-222.

(102)   Maugé, F.; Lamotte, J.; Nesterenko, N. S.; Manoilova, O.; Tsyganenko, A. A. *Catal. Today* **2001,** 70, 271-284.

(103)   Zmierczak, W.; MuraliDhar, G.; Massoth, F. E. *J. Catal.* **1982,** 77, 432-438.

(104)   Burch, R.; Collins, A. *Appl. Catal.* **1985,** 17, 273-308.

(105)   Okamoto, Y.; Maezawa, A.; Imanaka, T. *J. Catal.* **1989,** 120, 29-45.

(106)   Shuxian, Z.; Hall, W. K.; Ertl, G.; Knözinger, H. *J. Catal.* **1986,** 100, 167-175.

(107)   Hensen, E. J. M.; Kooyman, P. J.; van der Meer, Y.; van der Kraan, A. M.; de Beer, V. H. J.; van Veen, J. A. R.; van Santen, R. A. *J. Catal.* **2001,** 199, 224-235.

(108)   Luo, W.; Shi, H.; Schachtl, E.; Gutierrez, O. Y.; Lercher, J. A. *Angew. Chem. Int. Ed.* **2018,** 57, 14555-14559.

(109)   Topsøe, N.-Y.; Tuxen, A.; Hinnemann, B.; Lauritsen, J. V.; Knudsen, K. G.; Besenbacher, F.; Topsøe, H. *J. Catal.* **2011,** 279, 337-351.

(110)   Topsøe, N.-Y.; Topsøe, H. *J. Catal.* **1983,** 84, 386-401.

(111)   Topsøe, N.-Y.; Topsøe, H. *Bull. Soc. Chim. Belg.* **1981,** 90, 1311-1317.

(112)   Topsøe, H.; Clausen, B. S.; Topsøe, N.-Y.; Pedersen, E.; Niemann, W.; Müller, A.; Bögge, H.; Lengeler, B. *J. Chem. Soc., Faraday Trans. 1* **1987,** 83, 2157-2167.

(113)   Travert, A.; Dujardin, C.; Maugé, F.; Veilly, E.; Cristol, S.; Paul, J. F.; Payen, E. *J. Phys. Chem. B* **2006,** 110, 1261-1270.

(114)   Chen, J.; Maugé, F.; El Fallah, J.; Oliviero, L. *J. Catal.* **2014,** 320, 170-179.

(115)   Travert, A.; Dujardin, C.; Maugé, F.; Cristol, S.; Paul, J. F.; Payen, E.; Bougeard, D. *Catal. Today* **2001,** 70, 255-269.

(116)   Qusro, Q.; Massoth, F. E. *Appl. Catal.* **1987,** 29, 375-379.

(117)   Vissers, J. P. R.; Groot, C. K.; van Oers, E. M.; de Beer, V. H. J.; Prins, R. *Bull. Soc. Chim. Belg.* **1984,** 93, 813-822.

(118)   Wright, C. J.; Sampson, C.; Fraser, D.; Moyes, R. B.; Wells, P. B.; Riekel, C. *J. Chem. Soc., Faraday Trans. 1* **1980,** 76, 1585-1598.

(119)   Maternová, J. *Appl. Catal.* **1982,** 3, 3-11.

(120)   Sundberg, P.; Moyes, R. B.; Tomkinson, J. *Bull. Soc. Chim. Belg.* **1991,** 100, 967-976.

(121)   Breysse, M.; Furimsky, E.; Kasztelan, S.; Lacroix, M.; Perot, G. *Catal. Rev.* **2002,** 44, 651-735.

(122) Topsøe, H.; Clausen, B. S.; Topsøe, N.-Y.; Nørskov, J. K.; Ovesen, C. V.; Jacobsen, C. J. H. *Bull. Soc. Chim. Belg.* **1995,** 104, 283-291.

(123) Petit, C.; Maugé, F.; Lavalley, J.-C. *Stud. Surf. Sci. Catal.* **1997,** Volume 106, 157-166.

(124) Travert, A.; Maugé, F. *Stud. Surf. Sci. Catal.* **1999,** 127, 269-277.

(125) Stuchlý, V.; Beránek, L. *Appl. Catal.* **1987,** 35, 35-45.

(126) Miciukiewicz, J.; Zmierczak, W.; Massoth, F. E. *Bull. Soc. Chim. Belg.* **1987,** 96, 915-924.

(127) Tuxen, A. K.; Füchtbauer, H. G.; Temel, B.; Hinnemann, B.; Topsøe, H.; Knudsen, K. G.; Besenbacher, F.; Lauritsen, J. V. *J. Catal.* **2012,** 295, 146-154.

(128) Lauritsen, J. V.; Besenbacher, F. *J. Catal.* **2015,** 328, 49-58.

(129) Moses, P. G.; Hinnemann, B.; Topsøe, H.; Nørskov, J. K. *J. Catal.* **2007,** 248, 188-203.

(130) Egorova, M.; Prins, R. *J. Catal.* **2004,** 225, 417-427.

(131) Kasztelan, S. *Langmuir* **1990,** 6, 590-595.

(132) Eijsbouts, S.; Plantenga, F.; Leliveld, B.; Inoue, Y.; Fujita, K. *Prepr. Pap. - Am. Chem. Soc., Div. Fuel Chem.* **2003,** 48, 495.

(133) Garreau, F. B.; Toulhoat, H.; Kasztelan, S.; Paulus, R. *Polyhedron* **1986,** 5, 211-217.

(134) Daage, M.; Chianelli, R. R. *J. Catal.* **1994,** 149, 414-427.

(135) Chianelli, R. R.; Daage, M. *Stud. Surf. Sci. Catal.* **1989,** 50, 1-19.

(136) Berhault, G.; Perez de la Rosa, M.; Mehta, A.; Yácaman, M. J.; Chianelli, R. R. *Appl. Catal., A* **2008,** 345, 80-88.

(137) Romero-Rivera, R.; Camacho, A. G.; Valle, M.; Alonso, G.; Fuentes, S.; Cruz-Reyes, J. *Top. Catal.* **2011,** 54, 561-567.

(138) Liu, H.; Liu, C.; Yin, C.; Chai, Y.; Li, Y.; Liu, D.; Liu, B.; Li, X.; Wang, Y.; Li, X. *Appl. Catal., B* **2015,** 174-175, 264-276.

(139) Scott, C. E.; Perez-Zurita, M. J.; Carbognani, L. A.; Molero, H.; Vitale, G.; Guzmán, H. J.; Pereira-Almao, P. *Catal. Today* **2015,** 250, 21-27.

(140) Nava, H.; Pedraza, F.; Alonso, G. *Catal. Lett.* **2005,** 99, 65-71.

(141) Candia, R.; Sørensen, O.; Villadsen, J.; Topsøe, N.-Y.; Clausen, B. S.; Topsøe, H. *Bull. Soc. Chim. Belg.* **1984,** 93, 763-774.

(142) Topsøe, H. *Appl. Catal., A* **2007,** 322, 3-8.

(143) Hinnemann, B.; Nørskov, J. K.; Topsøe, H. *J. Phys. Chem. B* **2005,** 109, 2245-2253.

(144) Topsøe, H.; Candia, R.; Topsøe, N.-Y.; Clausen, B. S.; Topsøe, H. *Bull. Soc. Chim. Belg.* **1984,** 93, 783-806.

(145) Eijsbouts, S.; van Gestel, J. N. M.; van Veen, J. A. R.; de Beer, V. H. J.; Prins, R. *J. Catal.* **1991,** 131, 412-432.

(146) Topsøe, H.; Clausen, B. S.; Candia, R.; Wivel, C.; Mørup, S. *J. Catal.* **1981,** 68, 433-452.

(147) Appl, M. *Ammonia, 2. Production Processes*. In *Ullmann's Encyclopedia of Industrial Chemistry*, Wiley VCH: Weinheim **2011**, pp 139-225.

(148) Pease, R. N.; Keighton, W. B. *Ind. Eng. Chem.* **1933,** 25, 1012-1013.

(149) Byrns, A. C.; Bradley, W. E.; Lee, M. W. *Ind. Eng. Chem.* **1943,** 35, 1160-1167.

(150) Beuther, H.; Flinn, R. A.; McKinley, J. B. *Ind. Eng. Chem.* **1959,** 51, 1349-1350.

(151) Toulhoat, H.; Raybaud, P. *Periodic Trends in Catalysis by Sulphides*. In *Catalysis by Transition Metal Sulphides: From Molecular Theory to Industrial Application*, Raybaud, P., Toulhoat, H. Eds. Editions Technip: Paris **2013**, pp 3-26.

(152) Niemantsverdriet, J. W. *Mössbauer Spectroscopy*. In *Spectroscopy in Catalysis. An Introduction*, Wiley: Weinheim **2007**, pp 121-146.

(153) de Beer, V. H. J.; van Sint Fiet, T. H. M.; van der Steen, G. H. A. M.; Zwaga, A. C.; Schuit, G. C. A. *J. Catal.* **1974,** 35, 297-306.

(154) Delmon, B. *Bull. Soc. Chim. Belg.* **1979,** 88, 979-987.

(155) Karroua, M.; Grange, P.; Delmon, B. *Appl. Catal.* **1989,** 50, L5-L10.

(156) Furimsky, E. *Catal. Rev.* **1980,** 22, 371-400.

(157) Wivel, C.; Candia, R.; Clausen, B. S.; Mørup, S.; Topsøe, H. *J. Catal.* **1981,** 68, 453-463.

(158) Phillips, R. W.; Fote, A. A. *J. Catal.* **1976,** 41, 168-172.

(159) Fuentes, S.; Avalos-Borja, M.; Acosta, D.; Pedraza, F.; Cruz, J. *Stud. Surf. Sci. Catal.* **1993,** 75, 611-620.

(160) Cruz-Reyes, J.; Avalos-Borja, M.; Farías, M. H.; Fuentes, S. *J. Catal.* **1992,** 137, 232-242.

(161) Roxlo, C. B.; Daage, M.; Ruppert, A. F.; Chianelli, R. R. *J. Catal.* **1986,** 100, 176-184.

(162) Voorhoeve, R. J. H.; Stuiver, J. C. M. *J. Catal.* **1971,** 23, 228-235.

(163) Farragher, A. L.; Cossee, P. In *Proceedings of the 5th International Congress on Catalysis*, Hightower, J. W., Ed. North Holland, Amsterdam: 1973; p 1301.

(164) de Beer, V. H. J.; Duchet, J. C.; Prins, R. *J. Catal.* **1981,** 72, 369-372.

(165) van der Kraan, A. M.; Crajé, M. W. J.; Gerkema, E.; Ramselaar, W. L. T. M.; de Beer, V. H. J. *Hyperfine Interact.* **1989,** 46, 567-574.

(166) Brooks, C. S.; Pilney, D. G. *Surf. Technol.* **1979,** 9, 119-133.

(167) Breysse, M.; Bachelier, J.; Bonnelle, J. P.; Cattenot, M.; Cornet, D.; Décamp, T.; Duchet, J. C.; Durand, R.; Engelhard, P.; Frety, R.; Gachet, C.; Genested, P.; Grimblot, J.; Gueguen, C.; Kasztelan, S.; Lacroix, M.; Lavalley, J. C.; Leclercq, C.; Moreau, C.;

de Mourgues, L.; Olivé, J. L.; Payen, E.; Portefaix, J. L.; Toulhoat, H.; Vrinat, M. *Bull. Soc. Chim. Belg.* **1987,** 96, 829-844.

(168) Topsøe, N.-Y.; Topsøe, H.; Sørensen, O.; Clausen, B. S.; Candia, R. *Bull. Soc. Chim. Belg.* **1984,** 93, 727-734.

(169) Silvy, R. P.; Delannay, F.; Grange, P.; Delmon, B. *Polyhedron* **1986,** 5, 195-198.

(170) Agudo, A. L.; Gil Llambías, F. J.; Tascón, J. M. D.; Fierro, J. L. G. *Bull. Soc. Chim. Belg.* **1984,** 93, 719-726.

(171) Lauritsen, J. V.; Helveg, S.; Lægsgaard, E.; Stensgaard, I.; Clausen, B. S.; Topsøe, H.; Besenbacher, F. *J. Catal.* **2001,** 197, 1-5.

(172) Lauritsen, J. V.; Kibsgaard, J.; Olesen, G. H.; Moses, P. G.; Hinnemann, B.; Helveg, S.; Nørskov, J. K.; Clausen, B. S.; Topsøe, H.; Lægsgaard, E.; Besenbacher, F. *J. Catal.* **2007,** 249, 220-233.

(173) Zhu, Y.; Ramasse, Q. M.; Brorson, M.; Moses, P. G.; Hansen, L. P.; Kisielowski, C. F.; Helveg, S. *Angew. Chem. Int. Ed.* **2014,** 53, 10723-10727.

(174) Louwers, S. P. A.; Prins, R. *J. Catal.* **1992,** 133, 94-111.

(175) Niemann, W.; Clausen, B. S.; Topsøe, H. *Catal. Lett.* **1990,** 4, 355-363.

(176) Louwers, S. P. A.; Prins, R. *J. Catal.* **1993,** 139, 525-539.

(177) Bouwens, S. M. A. M.; van Zon, F. B. M.; van Dijk, M. P.; van der Kraan, A. M.; de Beer, V. H. J.; van Veen, J. A. R.; Koningsberger, D. C. *J. Catal.* **1994,** 146, 375-393.

(178) Byskov, L. S.; Hammer, B.; Nørskov, J. K.; Clausen, B. S.; Topsøe, H. *Catal. Lett.* **1997,** 47, 177-182.

(179) Byskov, L. S.; Bollinger, M.; Nørskov, J. K.; Clausen, B. S.; Topsøe, H. *J. Mol. Catal. A: Chem.* **2000,** 163, 117-122.

(180) Byskov, L. S.; Nørskov, J. K.; Clausen, B. S.; Topsøe, H. *J. Catal.* **1999,** 187, 109-122.

(181) Nørskov, J. K.; Clausen, B. S.; Topsøe, H. *Catal. Lett.* **1992,** 13, 1-8.

(182) Clausen, B., S.; Mørup, S.; Topsøe, H.; Candia, R. *J. Phys., Colloq.* **1976,** 37, 249-252.

(183) Hein, J.; Hrabar, A.; Jentys, A.; Gutiérrez, O. Y.; Lercher, J. A. *ChemCatChem* **2014,** 6, 485-499.

(184) Harris, S.; Chianelli, R. R. *J. Catal.* **1984,** 86, 400-412.

(185) Harris, S.; Chianelli, R. R. *J. Catal.* **1986,** 98, 17-31.

(186) Chianelli, R. R.; Berhault, G.; Raybaud, P.; Kasztelan, S.; Hafner, J.; Toulhoat, H. *Appl. Catal., A* **2002,** 227, 83-96.

(187) Sabatier, P. *Ber. Dtsch. Chem. Ges.* **1911,** 44, 1984-2001.

(188) Toulhoat, H.; Raybaud, P.; Kasztelan, S.; Kresse, G.; Hafner, J. *Catal. Today* **1999,** 50, 629-636.

(189)   Raybaud, P.; Hafner, J.; Kresse, G.; Toulhoat, H. *J. Phys.: Condens. Matter* **1997,** 9, 11107-11140.

(190)   Eijsbouts, S.; Li, X.; Bergwerff, J.; Louwen, J.; Woning, L.; Loos, J. *Catal. Today* **2017,** 292, 38-50.

(191)   Okamoto, H. *J. Phase Equilib. Diffus.* **2009,** 30, 123-123.

(192)   Houssenbay, S.; Kasztelan, S.; Toulhoat, H.; Bonnelle, J. P.; Grimblot, J. *J. Phys. Chem.* **1989,** 93, 7176-7180.

(193)   Zhao, X. J.; Wei, J. *J. Catal.* **1994,** 147, 429-440.

(194)   Krebs, E.; Silvi, B.; Raybaud, P. *Catal. Today* **2008,** 130, 160-169.

(195)   Guichard, B.; Roy-Auberger, M.; Devers, E.; Pichon, C.; Legens, C.; Lecour, P. *Catal. Today* **2010,** 149, 2-10.

(196)   Krebs, E.; Daudin, A.; Raybaud, P. *Oil Gas Sci. Technol.* **2009,** 64, 707-718.

(197)   Raybaud, P.; Hafner, J.; Kresse, G.; Kasztelan, S.; Toulhoat, H. *J. Catal.* **2000,** 190, 128-143.

(198)   Eijsbouts, S.; Heinerman, J. J. L.; Elzerman, H. J. W. *Appl. Catal., A* **1993,** 105, 69-82.

(199)   Tammann, G. *Z. Anorg. Allg. Chem.* **1926,** 157, 321-325.

(200)   Moulijn, J. A.; van Diepen, A. E.; Kapteijn, F. *Appl. Catal., A* **2001,** 212, 3-16.

(201)   Hoodless, R. C.; Moyes, R. B.; Wells, P. B. *Catal. Today* **2006,** 114, 377-382.

(202)   Ledoux, M. J.; Michaux, O.; Agostini, G.; Panissod, P. *J. Catal.* **1986,** 102, 275-288.

(203)   Eijsbouts, S.; H.J. de Beer, V.; Prins, R. *J. Catal.* **1988,** 109, 217-220.

(204)   Delmon, B. *Stud. Surf. Sci. Catal.* **1989,** 53, 1-40.

(205)   Philippe, T.; Voorhees, P. W. *Acta Mater.* **2013,** 61, 4237-4244.

(206)   Derouane, E. G.; Pedersen, E.; Clausen, B. S.; Gabelica, Z.; Candia, R.; Topsøe, H. *J. Catal.* **1986,** 99, 253-261.

(207)   Landau, M. V.; Nikulina, L. I.; Nefedov, B. K.; Slinkin, A. A. *React. Kinet. Catal. Lett.* **1984,** 25, 115-119.

(208)   Niemantsverdriet, J. W. *Diffraction and Extended X-Ray Absorption Fine Structure (EXAFS)*. In *Spectroscopy in Catalysis. An Introduction*, Wiley: Weinheim **2007**, pp 147-178.

(209)   Luo, W.; Shi, H.; Wagenhofer, M.; Gutiérrez, O.; Lercher, J. *J. Phys. Chem. Lett.* **2019,** 10, 5617-5622.

3   Hydrotreating of renewable feedstock

*G*lobalisation of the internal combustion engine has been key to the mobility revolution and may be considered one of the defining technological developments of the 20th century. [...] Attempts to substitute established fossil fuels with biofuels in the future must take into account the broad range of factors that have shaped combustion engines and fuel demand to date and generated the myriad of fuel qualities that currently exist around the world.

<div align="right">———————————</div>

<div align="right">L. Clarke, Biofuels in Operation. In Biofuels and Bioenergy, J. Love, J. A. Bryant, Eds. (2017).</div>

3.1   Biofuels

3.1.1   Conventional vs. drop-in biofuels

Renewable fuels or biofuels are fuels derived immediately from living matter[1], that is, without resorting to geological time spans such as those involved in the formation of petroleum or coal. This definition encompasses traditional biofuels (e.g., wood, charcoal, and animal fat) as well as their modern versions that are destined for replacing fossil fuels in the energy and transportation sector. It is the latter kind of biofuels that will be dealt with in the present work. The focus is on so-called "drop-in" biofuels: liquid bio-hydrocarbons that are functionally equivalent to petroleum fuels and fully compatible with existing fossil-fuel and petroleum infrastructure.[2]

The connection between environmentally sustainable biofuels and the petroleum-rooted hydrotreating process may not be immediately obvious. It is therefore rather surprising that commercially significant quantities of renewable diesel and jet fuel are currently produced only by conventional refinery technology, in particular by hydrotreating of lipid biomass (see section 3.1.3).[2-3] To be fair, there are other types of biofuels that are produced on much larger scales, most importantly biodiesel and bioethanol, and whose production has nothing in common with hydrotreating. However, these do not fulfill the requirements for drop-in application.

Biodiesel, for example, is chemically quite different from its petroleum counterpart (Figure 3.1). While conventional automotive diesel is a mixture of middle- to long-chain aliphatic hydrocarbons (typically C9 to C25), biodiesel is composed of fatty acid methyl esters (FAME). Even though the length of the aliphatic chain is similar, FAMEs have a distinct chemical nature leading to severe problems such as accumulation in engine oil and incompatibility with certain metal and plastic parts (cast iron, natural rubber, copper-based alloys). Cold-flow behavior is also generally much worse than that of petrodiesel. Perhaps the most important limitation, however, is related to the sophisticated exhaust gas treating systems that are now found on all modern diesel engines.[4] Because of these restrictions, biodiesel can only be used as an admixture (up to 7 vol% in the EU) but not as a replacement for conventional petroleum diesel.

Similarly, bioethanol has some serious disadvantages over conventional gasoline. Even though engines could be adapted to run on pure (bio)ethanol, typical gasoline engines suffer from issues related to material compatibility, spark timing, and fuel injection.[4] Just like biodiesel, bioethanol may not fully replace its petroleum based pendant, and accordingly, the allowable ethanol content in gasoline in the EU is currently limited to a mere 10 vol% ("E10" fuel). In addition, due to the distinct chemical nature of biodiesel and bioethanol, these biofuels have to be delivered through separate distribution channels, as they are not compatible with the existing petroleum infrastructure (pipelines, storage tanks, etc.). A true drop-in biofuel should be able to completely substitute one specific fossil fuel without requiring significant engine or infrastructure adjustments.

A

CH$_3$

H$_3$C–O

O

Methyl oleate (C$_{19}$H$_{36}$O$_2$)

Composition (wt.-%):
C, 76.97; H, 12.24; O, 10.79

B

H$_3$C

H$_3$C

n-Hexadecane (C$_{16}$H$_{34}$)

Composition (wt.-%):
C, 84.87; H, 15.13
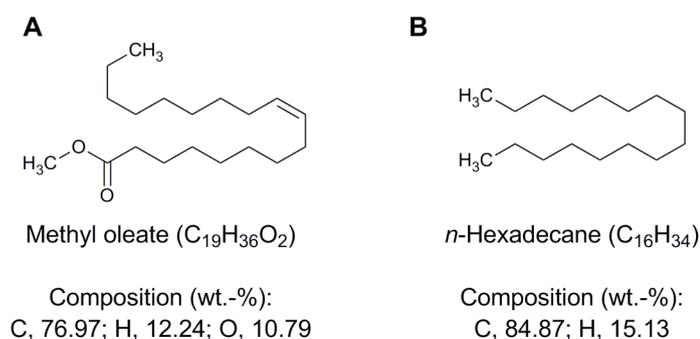
Figure 3.1. Typical constituents of biodiesel (**A**) and petroleum diesel (**B**).

As far as land transportation vehicles are concerned, biofuels are not the only alternative to conventional fossil fuels: Electrification, methanol, and hydrogen are all more or less viable options for increasing sustainability in this sector. Aviation, by contrast, is much less flexible in this regard, as it uniquely depends on energy-dense hydrocarbon fuels. Given the high power-to-weight requirements, jet engines cannot be easily electrified using current battery technology, and, for the same reason, alternative fuels with lower energy density like cryogenic hydrogen or methanol are not an option either. Conventional biofuels like FAMEs could be a suitable replacement from the perspective of energy density but do not meet the numerous other requirements for jet fuel (e.g., cold-flow properties). To further complicate things, the aviation industry uses highly unified, global standards that cannot easily adapt to new developments. In view of these limitations, it is no surprise that refiners, airlines, and plane manufacturers are concentrating their efforts on developing fully compatible drop-in alternatives to jet fuel.[5-6]

3.1.2 Biofuel feedstock

Fossil fuels are characterized by a high degree of saturation and the virtual absence of oxygen. This is true for all kinds of transportation fuels like diesel, gasoline, and jet fuel (which may also contain about 20 to 30 vol% of aromatics, but this is not a requirement). An ideal renewable raw material should therefore be poor in oxygen, have a high degree of saturation and a molecular structure close to that of the intended fuel product. From this perspective, many renewable sources like starch, sugars, lignin, and lignocellulose may be already ruled out simply because of their low effective H/C ratio[7] (Figure 3.2). In this comparison, oleochemical feedstock clearly stands out with an effective H/C ratio of about 1.8, which is very close to that of conventional fuels (H/C $\approx$ 2).
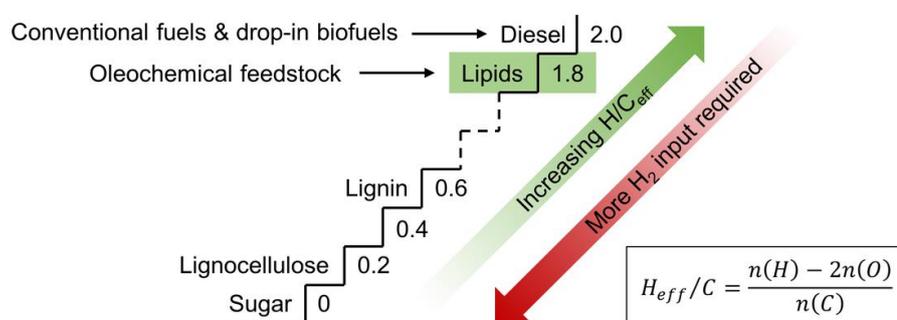
Figure 3.2. The effective H/C ratio "staircase" (adapted from refs.[2-3,8]). The effective H/C ratio is the ratio between hydrogen and carbon atoms in the molecule adjusted by heteroatoms (here: oxygen). It is a simple measure for the "hydrogen cost" associated with the conversion of biomass resources to fuels.

Oleochemical feedstock can be any oil or fat (lipid) originating from animals, plants, and other organisms such as microalgae. The primary constituents are triglycerides (or triacylglycerols, TAGs), as well as minor amounts of di- and monoglycerides, free fatty acids (FFAs), phospholipids, and other related compounds. While all TAGs have an identical glycerol backbone, the length and structure of the fatty acid side chains may vary substantially depending on the origin of the lipid. Most commercially used oil crops today have a side chain length of roughly 16 to 22 C atoms (Table 3.1), which falls nicely within the range of diesel hydrocarbons. In contrast to the latter, TAGs are usually at least mono-unsaturated, and even doubly or triply unsaturated bonds are no exception (Table 3.1). As each organism has its individual fatty acid profile (Table 3.1), not all lipid sources are suitable raw materials for renewable diesel, gasoline, or jet fuel. For example, while

almost all vegetable oils can be used for diesel production, there are only few lipids with chain lengths in the jet fuel range, such as those derived from oil palm kernel.[9]

Table 3.1 Fatty acid composition of commercially used oil crops and other organisms.[9-10]

Species	16:0	18:0	18:1	18:2	18:3	Others
Peanut	11	2	48	32		7
Soybean	11	4	24	54	7	
Oil-seed rape/Canola	4	2	60	22	10	2
Flax/Linseed	3	7	21	16	53	
Sunflower	7	5	19	68	1	
Oil palm kernel	8	3	15	2		72 [b]
Oil palm mesocarp	45	4	40	10		1
Jatropha	14	7	45	33		1
Microalgae [a]	23	22	7	7	17	24

[a] Microalga *Chlorella vulgaris* cultivated in photobioreactor. [b] Palm kernel oil is rich in short-chain saturated fatty acids: 4 % 10:0, 48 % 12:0, 16 % 14:0.

Fuel production from lipids has been intensely debated, most notably because of the "food-versus-fuel" dilemma, i.e., the risk of diverting arable land and food crops for biofuels to the disadvantage of the food supply.[11] This has sparked interest in cultivating oil-producing species that are non-edible and able to thrive on marginal agricultural land, e.g., *Jatropha* or *Camelina*. Similarly, also microalgae are being investigated as an option that not only avoids competition with food crops, but has the potential to dramatically exceed oil yields of traditional crops.[12-18] Some microalgae species can be cultivated to produce up to 70 wt% of lipids[13] (on a dry mass basis), while the possibility of "stacked" cultivation in photobioreactors[15,17] could significantly reduce land use. Hardly surprising, this option has been investigated with quite some interest in the past two decades or so, for example, in the German AUFWIND[19-20] and AlgenFlugKraft[21] research campaigns. After initial optimism, some major obstacles were identified in the pursuit of this approach, most importantly the energy intensive thermal dewatering of the algae slurry and lipid extraction from the cells. Accordingly, significant technological advancements are necessary before algal biofuels can become a commercial reality.[11,22]

Despite these limitations, lipids are currently the most promising candidates for substituting fossil raw materials in fuel production – at least in the near future. Lipids are readily available and supply chains are already in place. Their low oxygen content, as compared to other bio-based feedstock, and their chemical similarity with fuel-range

hydrocarbons makes them relatively easy to process.[2] These favorable properties are already being exploited on a global scale, most notably for the production of biodiesel. However, for the reasons explained earlier, that may not be making the best use of lipid feedstock.

Unlike the transesterification used in biodiesel production, processes for drop-in fuel production from lipids must be able to break off the aliphatic side chain, remove all oxygen atoms, and (partially) saturate the double bonds. Conventional refinery operations, notably cracking and hydrotreating, have been explored for this purpose. In cracking, triglycerides are thermally or catalytically decomposed to alkanes, alkenes and fatty acids over conventional cracking catalysts used in the petroleum industry, i.e., zeolites and other acidic alumino-silicates. The major problem of this approach is the low selectivity for fuel range hydrocarbons,[23-24] with triglyceride side chains being broken down to less valuable short-chain products that often still contain oxygen. Hydrotreating, on the other hand, acts more conservatively on the C-C bonds and removes oxygen much more effectively. It has been noted early on that the requirements for triglyceride deoxygenation and petroleum upgrading are indeed very similar, especially in the aspect of heteroatom removal and saturation. Hardly surprising, lipid hydrotreating has become an active area of research being pursued by numerous groups from industry and academia. The next section takes an in-depth look at the potential and challenges associated with this approach.

3.1.3   Hydrotreated esters and fatty acids

Drop-in biofuels derived from renewable lipids are widely referred to as "hydrotreated esters and fatty acids" (HEFA) or "hydrotreated vegetable oils" (HVO). The terms "renewable diesel" and "green diesel" are typically used to distinguish HEFA-based diesel from FAME-based biodiesel. Similarly, HEFA-based jet fuel is often referred to as "hydrotreated renewable jet fuel" (HRJ).

HEFA are currently the only drop-in biofuels that are produced in commercially significant quantities,[2-3] mostly in the form of renewable diesel and to a smaller extent as renewable jet fuel. One of the largest producers of HEFA is Neste, a Finnish company with operational facilities in Porvoo (Finland), Rotterdam (Netherlands), and Singapore,

having a combined production capacity of 2.7 million tons per year (Mt/a) of HEFA renewable diesel.[25] This is still small compared to the world biodiesel production of 31 Mt/a and even smaller compared to world diesel production, which was 1363 Mt/a including fuel oil uses of diesel (2016 data according to U.S. Energy Information Administration). The growth potential in this sector is therefore quite large, especially in view of the numerous political action plans issued by the EU and other countries to drastically lower current carbon emissions (e.g., Directive 2003/30/EC, Renewable Energy Directive 2009/28/EC, Amendment to the Fuel Quality Directive 2009/30/EC). The prospect of a steadily growing, politically enforced market has incentivized several "traditional" oil companies (e.g., Honeywell UOP, Eni, Sinopec) to increase their efforts to commercialize drop-in biofuel production with proprietary solutions.[26]

The vast majority of commercial HEFA fuel is currently produced in stand-alone units (e.g., by Neste[25]), which are typically embedded in a conventional refinery environment.[27] Even though the lipids are thus not processed in the same units as the conventional petroleum intermediates, the refinery is still an obvious location for HEFA production. This is mainly because of the existing fuel delivery network, i.e., pipelines, railway, and marine transport, and the availability of large quantities of relatively inexpensive hydrogen gas. The latter is vital for lipid conversion, as typical lipid feedstock contains about 10 to 11 % heteroatoms[2] in the form of oxygen, compared to about 1 % heteroatoms (mainly sulfur) in petroleum. This translates to a dramatically increased hydrogen consumption of roughly 300 to 400 m³ per m³ of fully deoxygenated triglyceride feedstock, whereas H_2 consumption is about a factor 10 lower for the desulfurization of 1 %-sulfur petroleum.[28]

Apart from supplying hydrogen, the refinery offers additional benefits for lipid hydroprocessing plants. Lipid hydrotreating is significantly more exothermic than conventional hydrotreating and releases correspondingly more heat, roughly in proportion to the heteroatom content.[29] Hence, it is vital to provide options for the re-utilization of excessive heat to increase the overall efficiency – a goal which is most easily achieved in a highly integrated industrial environment like the refinery. (Of course, increased heat release has to be also addressed in terms of more efficient reactor cooling systems to prevent unwanted side effects like coking, pressure build-up, and poor liquid distribution.[30]) The necessity for dewaxing is another reason why most stand-alone HEFA

plants are integrated into refineries:[2-3] After deoxygenation, the liquid hydrocarbon product consists largely of saturated, unbranched alkanes with poor cold-flow properties and a high freezing point. Dewaxing reduces both the freezing point and the viscosity by selective cracking and skeletal isomerization of paraffinic molecules over conventional Brønsted-acidic cracking catalysts.

Being a separate process, stand-alone HEFA technology cannot fully exploit the potential benefits of the refinery infrastructure. The maximum degree of refinery integration may be achieved only by "co-processing", i.e., adding lipids to crude oil fractions and processing the mixture in existing, conventional units. Of the numerous studies exploring the co-processing of lipids (recently reviewed in ref. [27]) many conclude that hydrotreaters are the most promising insertion points in the refinery process scheme (Figure 3.3). In addition to lower capital and operational expenses, a major advantage of this approach is the vast processing capacity of the existing refining units. These could generate partly fossil, partly renewable "hybrid" fuels, which may serve as an important intermediate solution on the way to a decarbonized future.
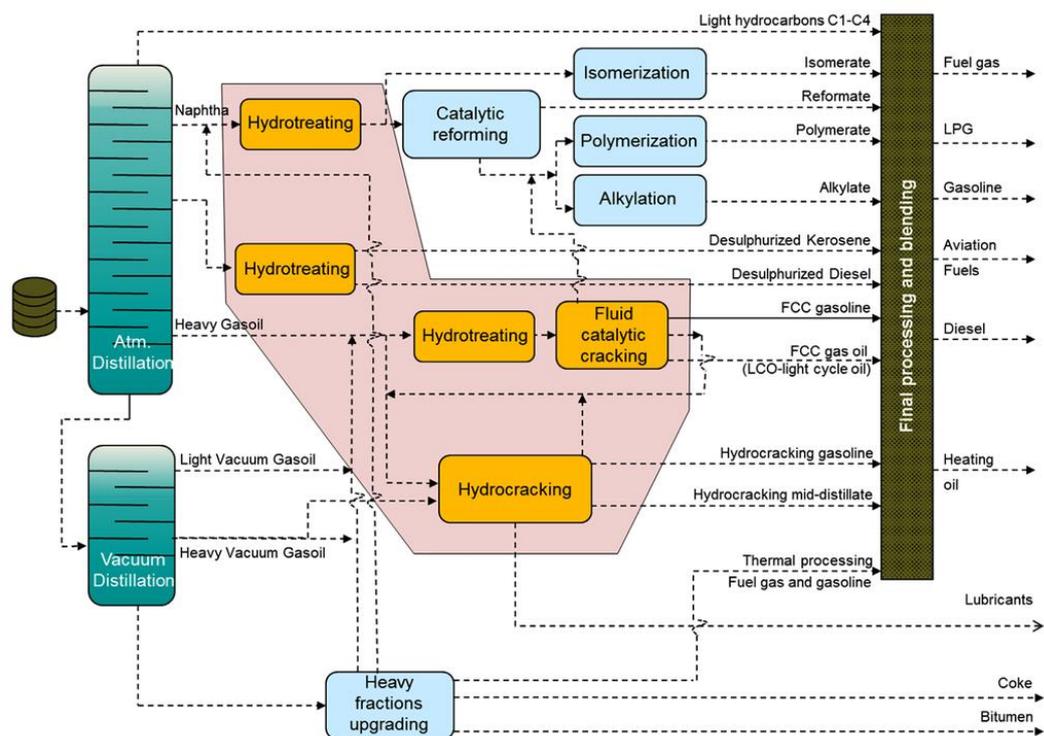

Figure 3.3. Simplified diagram of an oil refinery with possible insertion points for renewable lipid feedstock highlighted in the red area (reproduced from ref. [27]).

As of today, co-hydroprocessing has not yet reached the degree of commercialization of the more flexible stand-alone HEFA facilities. The latter produce a pure, high-value renewable product which may be sold separately or used for blending, whereas this is not the case for co-hydroprocessing. Because of this flexibility, stand-alone HEFA plants are often the preferred solution despite their higher cost.[23] However, once commercial co-hydroprocessing has been established, its biofuel output may quickly exceed that of freestanding HEFA facilities. Because of the vastly larger processing capacity, even a low percentage of lipids co-processed along with petroleum-based feedstock would have a notable impact.

The experience with co-hydroprocessing so far has shown that reactor setups and catalysts not specifically designed for renewable oils often lead to poor desulfurization of the primary feed, hydrogen starvation, and pressure drop build-up.[3] Stand-alone units have it easier in this regard because they use dedicated catalysts and process equipment. Issues of material compatibility between processing equipment and lipid feedstock are also much more easily addressed in a stand-alone unit. For example, more expensive metallurgy may be required because of the corrosiveness of lipid feedstock.[2,8,24,31] Apart from economical and technological considerations, the reaction chemistry also sets some strict boundaries on co-hydroprocessing. The concurrent treatment of chemically different feedstocks is always a challenge, and the reaction conditions will likely be sub-optimal for either of the two. Detrimental interactions between co-processed feedstocks need to be identified and properly addressed, for example, the effect of oxygenated byproducts on the HDS/HDN of the primary feed. It is therefore crucial to understand the influence of the process parameters and the working principles of the catalyst (i.e., the reaction mechanisms and structure-activity relations) to guide the process into the desired direction.

3.2 The chemistry of lipid deoxygenation

The greatest challenge in converting lipids to hydrocarbon fuels is their high oxygen content. Other heteroatoms (S, N, P) may be present, but oxygen is certainly the most abundant and problematic. In addition to reducing the fuel's energy content, it leads to a variety of other problems (like those discussed in connection with oxygenated biofuels in section 3.1.1). It is also worth noting that oxygen removal is typically the rate determining step in the conversion of lipids.[32]

3.2.1 Side chains

In contrast to oxygen removal, hydrogenation of the unsaturated side chains (Table 3.1) is less demanding and occurs at a much higher rate under typical hydrotreating conditions.[33] Deoxygenation (DO) of lipids and related compounds is therefore usually preceded by double bond saturation.[32] Side chain length and degree of saturation seem to not significantly affect DO rates and selectivity,[34-35] except for accelerated catalyst deactivation in the case of highly unsaturated feedstock.[36] Because of their marginal influence, side chain structure is thus rarely relevant for laboratory-scale DO studies. In an industrial setting, however, both length and saturation are important, as they influence H_2 consumption and product boiling range.

3.2.2 Model compounds

Deoxygenation is often investigated using model compounds instead of naturally occurring triglycerides, which is mainly done for facilitated analysis. As triglycerides easily reach molecular weights in excess of 800 g/mol (e.g., triolein with 885 g/mol), they cannot be vaporized without decomposition and are thus unsuitable for the more common analysis methods like gas chromatography. Also note that natural triglycerides contain a multitude of different side chains (Table 3.1), which further complicates sample analysis. Accordingly, when triglyceride model compounds are used, a reactant with uniform side chain length is chosen in most cases, e.g., tristearin[37], tripalmitin[38] or tricaprylin[39]. Due to the challenging analysis, a large share of studies has also been done using reactants other than triglycerides (extensively reviewed in ref.[32]). Common model compounds

include fatty acid methyl- and ethyl esters (FAME and FAEE), as well as free fatty acids. Remarkably, all these compounds exhibit deoxygenation rates and selectivities similar to those of triglycerides when subjected to the same reaction conditions (see examples in Table 3.2). This has been attributed to the existence of a common fatty acid intermediate which is formed independently of the model compound.[32]

Table 3.2. Comparison of deoxygenation activity and selectivity for triglycerides and model compounds.

Catalyst	Reactant	Reaction conditions	Initial rate ($mmol_{DO}/mmol_{metal}$)/s	Selectivity [c] (C_n/C_{n-1})
Ni/H-β[40]	microalgae oil	260 °C, 40 bar H_2	0.38	–
	stearic acid		0.33	–
Pd/C[35]	stearic acid	300 °C, 15 bar H_2	20	–
	oleic acid		21	–
Ni-MoS$_2$[20] [a]	microalgae oil	300 °C, 50 bar H_2 at 30 % conversion	–	78/22
	palmitic acid		–	79/21
Ni-MoS$_2$[20] [b]	tripalmitin	300 °C, 50 bar H_2 at 60 % conversion	–	49/51
	palmitic acid		–	49/51

Stearic acid: C18:0 fatty acid; Oleic acid: C18:3 fatty acid; Palmitic acid: C16:0 fatty acid; Tripalmitin: triglyceride with C16:0 fatty acid side chains; Microalgae oil main components: 56 % C18:2, 32 % C18:1, 4.4 % C18:0, 4.4 % C16:0, 3.2 % C20+. [a] Prepared via co-precipitation method (see section 2.3.1). [b] Prepared via thiosalt route (see section 2.3.1). [c] Selectivity (C%) to hydrocarbons of same length as reactant (C_n via HDO route) and with one C atom less than reactant (C_{n-1} via CLR). See section 3.2.4 for further information on deoxygenation pathways.

3.2.3 Initial decomposition of lipids

The decomposition of fatty acid esters in absence of water may in principle occur through one of three pathways: β-elimination, γ-H migration, or direct DO (Figure 3.4). Most deoxygenation studies[37-46] report fatty acid evolution during fatty acid ester DO, which is in nice agreement with a β-elimination mechanism. While the first side chain may be cleaved off even in absence of H_2, further eliminations are not possible without prior hydrogenation of the unsaturated diglyceride fragment. In presence of H_2 and a hydrogenation catalyst, the unsaturated fragment is further hydrogenated, thereby allowing for two further elimination steps. Finally, the glycerol backbone is released as propane (or propene in H_2-deficient atmospheres[42]), whereas the fatty acid intermediates undergo deoxygenation to C_n or C_{n-1} hydrocarbons (not depicted in Figure 3.4). Note that not all esters may undergo β-elimination. Methyl esters (FAME) lack a second C atom adjacent

to the methoxy group and must therefore decompose via a different mechanism. While the methoxy group is released as methane and/or methanol, the fate of the acyl group is not fully understood. Fatty acids can be absent in some cases and other oxygenates (aldehydes, alcohols) are suggested to be the primary intermediates instead.[47-48]
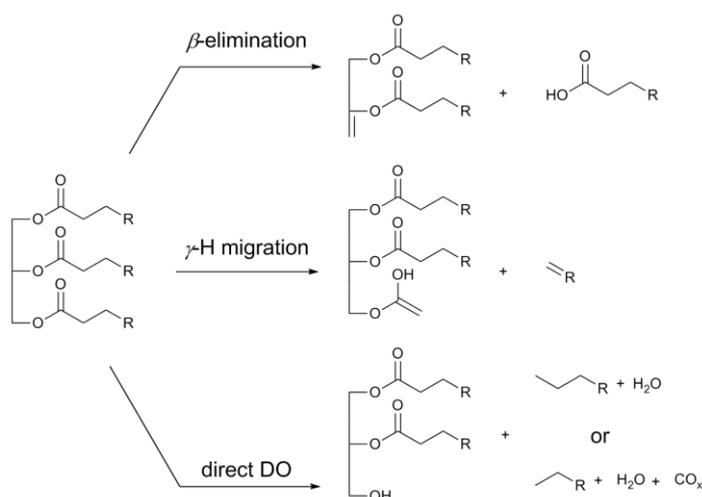
Figure 3.4. Simplified reaction scheme for triglyceride decomposition pathways[32] (DO: deoxygenation). Hydrogen consumption has been omitted in direct DO.

In contrast to β-elimination, γ-H migration involves bond cleavage outside of the ester group (between the α and β carbon atom), and the hydrocarbon chain is released in form of a C_{n-2} olefin. This pathway is usually not observed under typical hydrotreating conditions but only at higher temperature (e.g., at 450 °C[49]).

There is also limited evidence for a third pathway, direct DO, in which oxygen-free products are formed without the appearance of oxygenated intermediates (i.e., direct formation of alkanes/olefins from triglycerides, FAEE, or FAME).[50] It is questionable whether this is truly a distinct pathway, as its existence is postulated merely from the apparent absence of oxygenates. It is much more likely that these are simply not detected, for example, because of strong adsorption at the catalyst surface or fast reaction on certain catalysts.[51] Based on the available evidence, it seems that consecutive β-elimination (yielding fatty acid intermediates) is the most significant mechanism for the initial cleavage of fatty acid esters.[32,39,44,52-53]
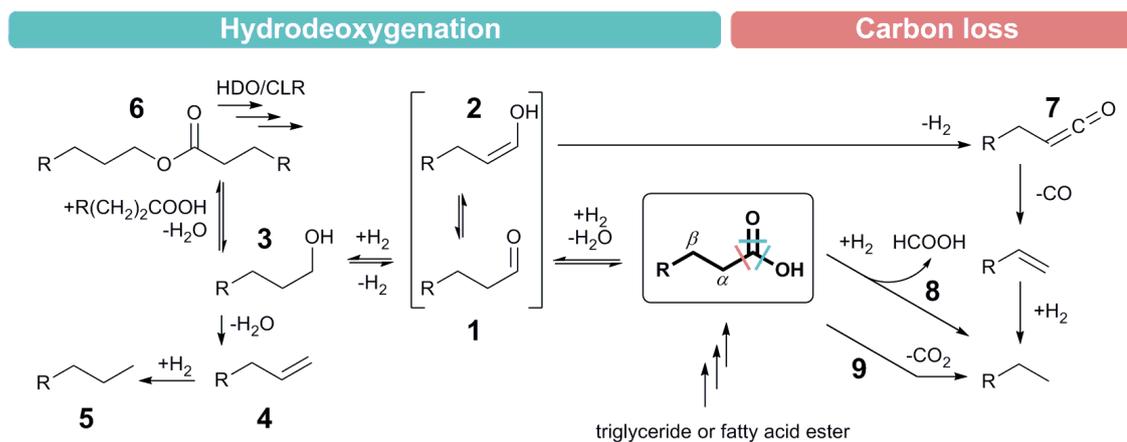
Figure 3.5. Simplified reaction scheme for oxygen removal from fatty acids (as primary reactant or intermediate from triglyceride/fatty ester DO). The numbers indicate features described in the text.

3.2.4 Deoxygenation reactions

The free fatty acid released by β-elimination can lose oxygen in a variety of ways (Figure 3.5). These are primarily distinguished by the length of the hydrocarbon products and the form in which oxygen is removed. Hydrodeoxygenation (HDO) produces hydrocarbons (alkanes, olefins) of length C_n, that is, equal to the carbon number of the fatty acid while oxygen is removed as water. In all other routes, summarized as carbon loss routes (CLR), the products are of length C_{n-1} while oxygen is released in the form of CO (decarbonylation), CO_2 (decarboxylation), or formic acid (which then decomposes to CO_2 and H_2 or CO and water).

The HDO reaction network (Figure 3.5) has been investigated with different catalyst systems and under a variety of reaction conditions. It essentially consists of a series of consecutive hydrogenation-dehydration steps in which only C-O bonds are cleaved.[32] HDO is initiated by C-O hydrogenolysis at the carboxyl carbon atom, releasing one molecule of water and an aldehyde (**1**) of the same length as the fatty acid reactant (Figure 3.5). The carbonyl group is then hydrogenated to an alcohol (**3**), from which water is eliminated to give the corresponding 1-olefin (**4**). A final hydrogenation step yields an *n*-alkane (**5**) as the end product of the reaction sequence. Intermittently, the presence of alcohol may give rise to a symmetric ester (**6**) resulting from condensation with the fatty acid reactant.[40-43,54] The ester is usually found to be a minor side product as it is hydrolyzed by water formed in other HDO steps or subjected to HDO/CLR itself.

It has also been argued that the reactive form of the aldehyde (**1**) may actually be its enol form (**2**).[47] According to this hypothesis, alcohol (**3**) and olefin (**4**) are both formed from the enol in a parallel reaction (by C-O hydrogenolysis and C=C hydrogenation, respectively), contrary to the sequential reaction given in Figure 3.5. These results were, however, obtained using ketone model compounds, and accordingly, may not be fully applicable to typical HDO chemistry.

Alcohol intermediates are observed regularly in the HDO of lipids, whereas aldehydes are detected less frequently because of their higher reactivity and correspondingly lower concentration (see refs. [39-47,51,54-60] and refs. [46-47,51,57,59-60] for reports of alcohol and aldehyde intermediates, respectively). Also note that alcohols and aldehydes, while exclusively formed via HDO, can act as intermediates in the carbon loss routes.

The reaction network of HDO is relatively indifferent to the reaction conditions and manifests itself always in more or less the same fashion. Carbon loss routes, by contrast, follow much more diverse patterns (Figure 3.5). Carbon may be eliminated in a variety of forms, e.g., as CO, CO_2, or HCOOH, and from a variety of substrates, which include intermediates formed by HDO, i.e., fatty acids, aldehydes, alcohols, or ketenes. Owing to the short-lived nature of some of these substrates and the fact that the gaseous intermediates are convertible into each other (e.g., via reverse water gas shift reaction), CLR reaction networks are more challenging to analyze than those of HDO. Accordingly, there are only few studies in which firm conclusions about the exact reaction sequence and mechanisms of lipid CLR have been obtained. Because of these difficulties, individual CLR pathways are typically not analyzed separately and in many cases little more than the overall CLR selectivity is reported, even though multiple mechanisms may be at work. In fact, some of the more detailed accounts of CLR were obtained via computational methods, used to supplement incomplete information from catalytic experiments.[57,61-62]

Several mechanisms have been proposed to explain the phenomena accompanying fatty acid (ester) CLR. The evolution of CO, for example, has been attributed to the decarbonylation of an aldehyde (**7**) which serves as a common intermediate for HDO and CLR (Figure 3.5).[40,46,58,63-65] In this scenario, aldehyde decarbonylation yields a terminal C_{n-1} olefin (which is then hydrogenated to the corresponding C_{n-1} alkane), whereas aldehyde HDO produces a C_n alkane. Theoretical calculations[57] suggest that a highly reactive

ketene is formed from the aldehyde before breaking the C-C bond and releasing CO. Even though direct experimental proof for this mechanism may not be obtained (due to the ketene's reactivity), there are several instances in which ketenes are suggested as reactive CLR intermediates over different catalyst systems (bulk Ni-MoS$_2$,[57] Ni/ZrO$_2$,[46] bulk MoP[66] and Ni$_2$P[66]).

Direct decarboxylation has also been widely reported as a possible deoxygenation mechanism.[34-35,51,56,67-72] In this case, it is suggested that fatty acids or fatty acid esters lose CO$_2$ directly to form a C$_{n-1}$ alkane (see (**9**) in Figure 3.5). It is worth noting that decarboxylation of lipids is far from being a new discovery, as petroleum is believed to have formed via natural anaerobic decarboxylation processes.[73] In organic chemistry, catalytic decarboxylation has long been known as a synthetic tool, especially in connection with short-chain carboxylic acids (e.g., acetic acid) in the gas phase.[74] However, it is debatable whether the same mechanistic principles apply to liquid-phase fatty acid deoxygenation. Most often, fatty acid decarboxylation is proposed simply because of the appearance of CO$_2$ in the gas phase, even though it could have a different origin.

Apart from direct decarboxylation and aldehyde decarbonylation, it was suggested that fatty acids could also undergo hydrogenolysis, i.e., hydrogenative C-C cleavage between the α- and the carbonyl carbon atom.[39] This would directly yield a saturated alkane of length C$_{n-1}$ and formic acid (**8**) (Figure 3.5). As formic acid rapidly decomposes to CO/H$_2$O or CO$_2$/H$_2$, there is only scarce and indirect evidence for this pathway (limited to a few cases, in which traces of formates were found during workup of the reaction mixture).[75-76] Further ambiguity is added by the fact that the gaseous carbon oxides may occur simultaneously or be interconverted, e.g., by (reverse) water-gas shift reaction. While hydrogenolysis is not yet fully understood, it can be speculated that the "direct" carbon loss routes mentioned earlier may just be hydrogenolysis in disguise. For example, CO$_2$ formation may be falsely attributed to "direct" decarboxylation of the fatty acid, when in reality a formic acid intermediate is formed first. The same applies to "direct" decarbonylation. Accordingly, the preference for "direct" decarbonylation or decarboxylation may not reflect the reactivity of the fatty acid (ester) or the catalyst, but rather that of formic acid under the present reaction.

In contrast to HDO, certain variants of CLR do theoretically not require any hydrogen to be present and could therefore be used to perform DO with massively reduced hydrogen consumption. In practice, however, there are several problems with this approach: First, CLR reduces the yield of usable liquid hydrocarbon product by eliminating one carbon atom per fatty acid molecule. Additionally, the presence of CO_x in the gas phase is a severe problem in its own right, as carbon oxides reduce H_2 partial pressure and may undergo secondary reactions that consume considerable amounts of hydrogen without contributing to the energy content of the product:

$$\text{Reverse water-gas shift reaction:} \quad CO_2 + H_2 \rightleftharpoons CO + H_2O$$

$$\text{CO methanization:} \quad CO + 3\,H_2 \rightleftharpoons CH_4 + H_2O$$
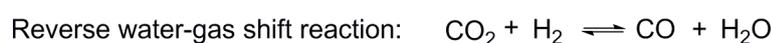
It was found, for example, that roughly 50 % of CO_2 and 30 % of CO are converted to methane during rapeseed oil deoxygenation under typical hydrotreating conditions,[47] thus negating or even inverting the potential advantages of deoxygenation via CLR. While it is possible to minimize secondary H_2 consumption by decreasing its partial pressure,[61] this is hardly feasible for a co-hydroprocessing scenario, in which the primary feed dictates a high H_2 partial pressure. In stand-alone facilities, CLR could be theoretically carried out in H_2-deficient atmosphere or even in total absence of H_2, but this comes at the price of lower conversion, lower selectivity for fuel range hydrocarbons, and rapid catalyst deactivation. Triglyceride CLR in absence of H_2 occurs only to a limited extent and generally needs higher reaction temperatures to proceed with acceptable rate.[32] This has been attributed to the cumbersome β-elimination step that becomes rate limiting when H_2 is not present in sufficient concentration (see section 3.2.3).[54] The shift in reaction kinetics and the higher temperature also promote undesired side reactions like cracking, oligomerization, cyclization, aromatization, and ketonization, thus substantially decreasing DO selectivity.[36,50,67] Needless to say that the heavy, unsaturated side products also lead to severe coking of the catalyst surface. In practice, low conversion and increased catalyst deactivation have made it difficult to obtain firm conclusions about CLR in absence of H_2.[35,71]

3.2.5   Influence of reaction conditions

Even though the catalyst is the decisive factor for DO activity and selectivity (see section 3.3), the reaction conditions can also have an important influence. The effect of temperature, H_2 partial pressure, and the nature of the solvent has been investigated in great detail in a number of studies (reviewed in refs. [27,32,52,77]). The most important findings of these works are summarized in the following.

Table 3.3. Thermodynamic balance of (overall) DO reactions.[a]

Reaction	Equation		$\Delta G°$ (273 K) kJ mol^{-1}	$\Delta G°$ (573 K) kJ mol^{-1}
Hydrodeoxygenation	R~~CO_2H $+ 3 H_2$ $\rightleftharpoons$ R~~ $+ 2 H_2O$		−122	−98
Decarbonylation	R~~CO_2H $\rightleftharpoons$ R~~ $+ CO + H_2O$		+59	−29
Decarbonylation [b]	R~~CO_2H $+ H_2$ $\rightleftharpoons$ R~~ $+ CO + H_2O$		−27	−80
Decarboxylation	R~~CO_2H $\rightleftharpoons$ R~~ $+ CO_2$		−60	−96
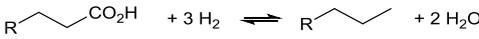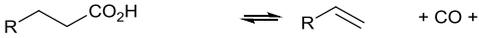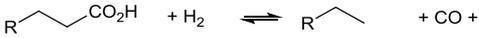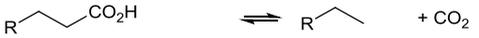
[a] Gibbs free energies calculated at 1 bar using C_3/C_4 compounds. See chapter 5 for more details. Note that the presented overall reactions omit elementary reaction steps. [b] Decarbonylation with subsequent hydrogenation of terminal olefin.

In the typical temperature range of DO studies ($\approx 300\,°C$), all reactions exhibit significantly negative free energy changes, thus indicating a favorable equilibrium situation (Table 3.3). In contrast to full HDO, where the total number of molecules is reduced, CLR reactions are entropically favorable because only little or no H_2 at all is consumed, resulting in a net gain in the number of molecules. Accordingly, when both pathways are present, the contribution of CLR generally becomes more important as the temperature increases.[75,78] Thermodynamic aspects are particularly relevant under conditions where full or near full conversion is achieved, like in industrial reactor operation. In contrast to that, thermodynamic aspects are much less relevant in laboratory scale DO studies, as these are typically conducted at conditions far from equilibrium, where kinetic effects dominate. The net effect of temperature is, however, also dependent on other temperature-related responses like inhibition by CO/CO_2 adsorption and accelerated catalyst deactivation, thus making it difficult to draw universal conclusions.

Hydrogen partial pressure has a strong influence on DO reactions. For HDO, which is a hydrogen consuming reaction, there is a positive correlation between H_2 pressure and the reaction rate, indicating that the rate limiting elementary step is dependent on H_2

coverage of the catalyst surface. This is not necessarily the case for CLR[41], as some variants may not even require the presence of hydrogen. It is also true, however, that CLR is often promoted significantly in presence of H_2, most likely due to the role of hydrogen in removing unsaturated coke precursors from the catalyst surface and regenerating active sites.[51,67,71] Note that the dependence of CLR on H_2 pressure is not monotonic, and above a certain optimum pressure[39] the opposite may be observed, i.e., inhibition of CLR by H_2. It has been suggested that a high hydrogen coverage of the catalyst surface, induced by high H_2 pressure, may inhibit reactant adsorption and hence the CLR rate. On the other hand, this would also be relevant for HDO and it is therefore not completely clear why the inhibition is selective for CLR.

In addition to pressure and temperature, also the solvent can have an impact on DO, although this is only relevant for laboratory-scale experiments using diluted reactants (industrial reactions are typically performed in bulk phase). Most studies focus on organic, practically inert solvents like decane or dodecane, and some workers have performed DO also in aqueous media.[79] While there are no reports of solvents chemically interfering with the reaction, it was observed that the solvent's physical properties (boiling point, viscosity, etc.) can indeed have an influence. For example, it was found that a lower boiling point simultaneously enhanced both HDO and CLR activity.[35,70-71] In CLR studies performed in absence of H_2, the solvent has been discussed as a potential source of in-situ produced hydrogen.[35,61]

3.3   Deoxygenation catalysts

A great number of catalyst systems has been evaluated for lipid deoxygenation. The most well-investigated among those are group 10 metals (Ni, Pd, Pt) and conventional MoS_2 based hydrotreating catalysts. Group 10 metals for lipid DO studies are usually supported on Al_2O_3[38,46,51,63,76,80-81] or carbon,[35,37,39,50,60-61,71-72,82] while some work has also been done using SiO_2,[46,63,80,83] ZrO_2,[46,63,84-87] TiO_2,[46] CeO_2,[46] or zeolites[40,63,80,88] as support. Hydrotreating catalysts containing Mo, W, Ni, and Co have been most widely employed in their alumina-supported form,[29,42-45,47,54,56,64,89-90] whereas unsupported sulfides[57,91] are used less frequently. More recently, also novel carbide and phosphide hydrotreating catalysts have entered the field of lipid DO, e.g., supported or bulk Mo_2C,[48,92-95] W_2C,[59,93,95] MoP,[58,66] and Ni_2P.[58,66]

3.3.1   Group 10 metals for lipid deoxygenation

Within this large variety of materials there is a general trend for group 10 metals to favor CLR over HDO. Because of their high CLR selectivity, there is a large body of work concerned with H_2-free deoxygenation over supported group 10 metals (extensively reviewed in ref. [32]). Note that these studies are not addressed in detail in the present work, as most aspects of DO under inert conditions are irrelevant for hydroprocessing. In hydrogen-rich atmosphere, these catalysts are highly active for the DO of lipids and show a universally high preference for C_{n-1} products, which is largely independent of the support. Cases in which the support exhibits a major influence on selectivity seem to be limited to zeolite-supported Ni (H-β and H-ZSM-5) which strongly favors HDO over CLR.[40,63] This exception has been attributed to highly Brønsted-acidic sites that facilitate alcohol dehydrogenation (**3 → 4**, Figure 3.5**)** and thereby reduce the concentration of aldehydes (**1**) which serve as the central CLR substrates. Note that also extensive cracking was observed in both cases.

In general, group 10 metals are known for being excellent hydrogenation and hydro-cracking catalysts. It is therefore not surprising that much of the reactivity seen in lipid DO is based on their well-known (de-)hydrogenation and C-C hydrogenolysis activity. This may be the reason why reaction mechanisms at the molecular level are only rarely addressed in these studies. There are a few exceptions, for example, a study by Boda et

al.[39] which explains selectivity differences between MoO_x (mainly HDO) and Pd (mainly CLR) by different adsorption modes of the fatty acid reactant (Figure 3.6 A). It is, however, debatable whether this truly represents a universal principle. Other metal oxides like WO_3/C for example are highly selective for CLR, while others like WO_2/C are completely inactive for DO.[93] Similarly, also studies performed in absence of H_2 have linked selectivity differences in fatty ester DO to different adsorption modes. For example, concerted (or "direct") CLR has been attributed to perpendicular adsorption via the C=O group, whereas "indirect" CLR via a fatty acid intermediate was concluded to require adsorption via both oxygen atoms (Figure 3.6 B).[71] A detailed molecular-level mechanism of CLR via aldehyde (and ketene) intermediates on Ni/ZrO_2 was proposed by Peng et al.[46] In this case, the metallic Ni nanoparticles and ZrO_2 support seem to act in parallel (and also synergistically) to produce an aldehyde intermediate from the fatty acid reactant. The actual C-C scission was concluded to occur only on the Ni nanoparticles and not on the functional groups of the support.
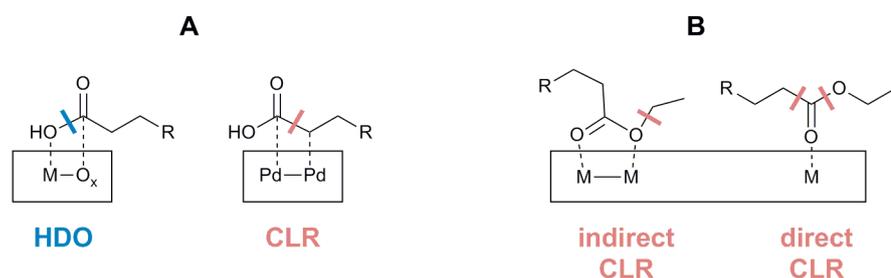
Figure 3.6 Carbon loss reaction mechanisms on metal catalysts. (**A**) C-O adsorption on ionic metal oxide leading to HDO, and C-C adsorption on non-polar metal surface leading to CLR of fatty acid reactant (adapted from ref. [39]). (**B**) Different modes of ethyl ester adsorption leading to direct and indirect CLR via fatty acid intermediate (adapted from ref. [71]).

3.3.2   Hydrotreating catalysts for lipid deoxygenation

Mo and W based hydrotreating catalysts are generally highly selective for the HDO pathway, especially non-promoted Mo or W sulfides[20,43,57,64] and carbides[48,93-94]. Phosphides are an exception to this rule because MoP may show substantial CLR activity, whereas WP is only active for HDO.[58,66] This discrepancy has been attributed to the presence of additional functional groups which are not related to the metal and alter the reaction network (e.g., Lewis-acidic P-OH groups).[66] On non-promoted MoS_2, either

supported or unsupported, CLR is usually a minor side reaction, while HDO selectivity is typically in the range of 90 % or more. For example, nearly 97 % of hydrodeoxygenated products were observed with ethyl heptanoate on bulk MoS_2[57] and about 90 % with rapeseed oil on MoS_2/Al_2O_3[43].

In analogy to HDS catalysis, coordinatively unsaturated sites (CUS) at the MoS_2 edges are believed to play a crucial role also in HDO. These vacancies expose one or more oxophilic Mo cations,[96] thereby providing an adsorption site for oxygenated reactants and intermediates. DFT studies suggest an energetically favorable bidentate adsorption of C=O groups on pairs of neighboring Mo cations (occurring in more or less the same fashion with fatty acids, fatty acid esters, and aldehydes).[57,62] Alternative adsorption modes may involve monodentate coordination of the carboxylic OH group. Subsequent hydrogen addition to the adsorbed reactant (Figure 3.5) relies on adjacent SH groups, in analogy to what is known for HDS catalysis. In addition to their vital role in hydro-genation, SH groups were proposed to act also as Brønsted acids by protonating the carboxylic OH group and thus leading to the elimination of H_2O as the initial step of fatty acid HDO.[64] While the dual nature of SH groups (and S anions) is well established in HDS,[97-100] it is questionable whether their acid strength is sufficient to protonate car-boxylic acids. (Conversely, it can be speculated that carboxylic acids are sufficiently strong to protonate basic S anions, thereby allowing a carboxylate anion to be formed. However, this option seems to have been ignored in existing theoretical studies.) Sulf-hydryl groups are also believed to play an important role in the elimination of oxygen from the alcohol intermediate: As thiols are sometimes observed in small amounts during HDO, it was suggested that the primary mechanism of alcohol DO may be a nucleophilic attack of the hydroxyl carbon by an SH group (followed by HDS of the thiol).[62] This is difficult to prove experimentally as thiols may be formed also by H_2S addition to olefins.[101]

Compared to unpromoted sulfides, Co-MoS_2 and especially Ni-MoS_2 may exhibit substantial selectivity for CLR products. On Ni-MoS_2 there is generally a significant correlation between the concentration of Ni and the selectivity for CLR products (Figure 3.7).[20,43,57] Accordingly, as the promoter content varies from study to study, it is not surprising to see a corresponding variation in the selectivity to C_{n-1} hydrocarbon products, which may reach any value in the range of about 25 to 50 % for Ni-MoS_2 and about 20 to

40 % for Co-MoS$_2$ (see refs. [43-44,47,56-57,90] and refs. [41,45,54,56], respectively). Selectivities substantially higher than 50 % have been reported as well in some cases, but those are most likely associated with additional influences like high reaction temperature[89], restricted reactivity of fatty acid methyl esters[47], or atypically high Ni content[20] as found in some bulk Ni-Mo sulfides.
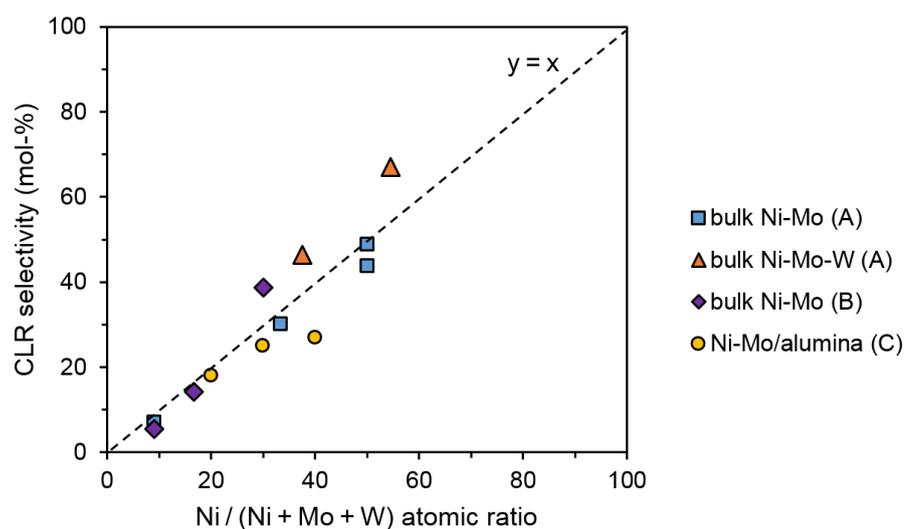
Figure 3.7. Correlation of Ni content and CLR selectivity on supported and bulk Ni-Mo(W)S$_2$ catalysts (adapted from ref. [20] (A), ref. [57] (B), and ref. [43](C)). The dashed line serves as guide for the eye only.

CLR on promoted MoS$_2$ has been attributed to the presence of segregated promoter metal sulfides, such as Ni$_3$S$_2$, Ni$_9$S$_8$, and Co$_9$S$_8$ (see section 2.3.5). This is consistent with the high preference for CLR of these phases when used in their pure form (i.e., in absence of MoS$_2$). Most notably, Ni sulfides (NiS$_x$) are essentially inactive for HDO and in most cases exclusively form CLR products.[43,55] However, the exact mechanism by which NiS$_x$ catalyze CLR is not fully understood, and atomic-level descriptions of the active species are scarce. Considering that Ni metal is highly selective for CLR (as are all group 10 metals), it can be speculated that metallic Ni formed by in-situ reduction of NiS$_x$ might be the true active species. While there is no experimental evidence to support this claim, it has been shown by theoretical methods that the native NiS$_x$ surface already exhibits a metal-like character without in-situ reduction to zero-valent Ni.[102] A combined theoretical-experimental DO study[57] similarly found that the Ni$_3$ triangular facets of Ni$_3$S$_2$

closely resemble the situation on metallic Ni, thereby enhancing the formation of surface intermediates (ketenes) that enable CLR via decarbonylation.

The combined evidence strongly supports the idea that the CLR activity of promoted MoS_2 can be at least partly explained by the presence of segregated sulfides. It is, however, difficult to determine how large this contribution is in relation to that of the binary Ni-Mo-S phase (see chapter 5 for a detailed analysis of this problem). For example, one study rules out segregated NiS_x as a relevant contribution to CLR based on the low concentration of this phase in a Ni-MoS_2/Al_2O_3 catalyst.[64] Other authors come to the opposite conclusion and attribute CLR primarily to segregated Ni sulfides, as their DFT calculations suggest that the key steps of CLR are thermodynamically less favorable on Ni-Mo-S than on segregated NiS_x.[57] It is worth noting, however, that this line of argument implicitly assumes thermodynamic control, while in reality kinetic effects might be dominant.
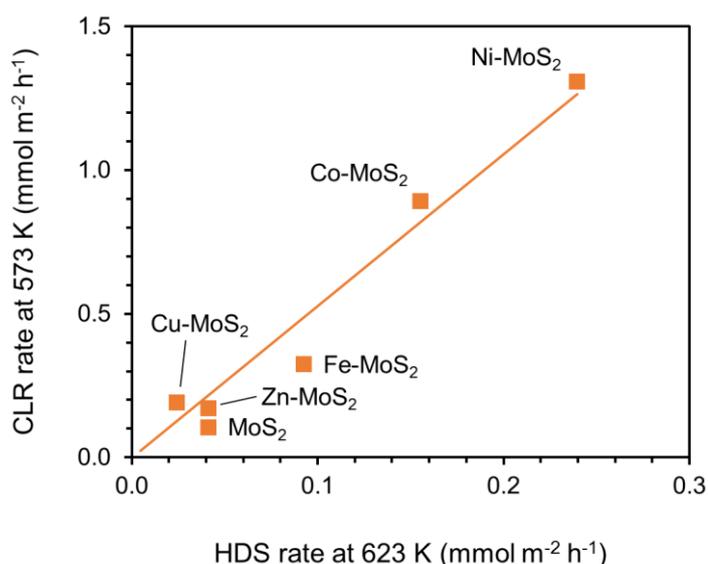
Figure 3.8. Correlation of surface-area normalized CLR and HDS rates of MoS_2 promoted by different transition metals, indicating similar reactivity for C-C bond scission of fatty acids and C-S bond scission of dibenzothiophene (CLR data: ref. [20], HDS data: ref. [103]).

The promoting effect of Ni on CLR shows parallels to the well-known promoting effect of Ni on HDS (section 2.3.4.1). This is quite remarkable in view of the completely different promoted reactions: i.e., cleavage of an essentially aliphatic C-C bond in the case of CLR, and C-S bond scission in a sterically crowded, π-electron stabilized system

in the case of HDS. It is not completely clear why this is the case, but the similarity appears to exist also for other promoter metals (Figure 3.8). In the case of Ni, it has been argued that the increased basicity of sulfur anions at the edges of the Ni-Mo-S phase might play a key role.[64] These anions are believed to facilitate H-abstraction from the reactants, thus promoting electron rearrangements that lead to the scission of the carbon-heteroatom bond in HDS and a carbon-carbon bond in CLR (Figure 3.9).[104] Note that the rationalizations outlined above for NiS$_x$ and Ni-Mo-S may also apply to the corresponding Co phases (and those of other promoter metals), but there seem to be only few dedicated studies addressing this issue in detail.[64]
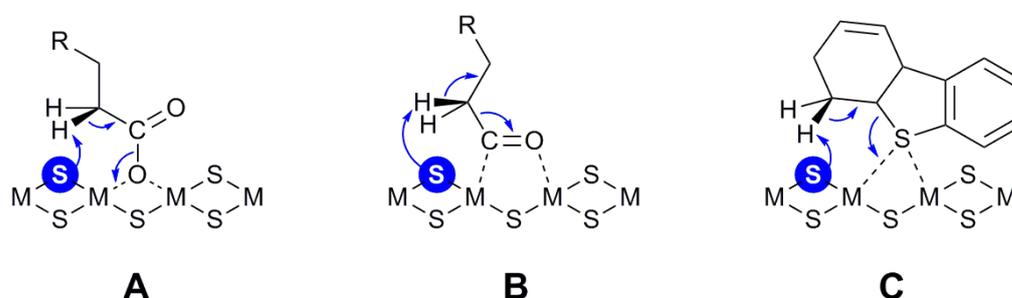
Figure 3.9. Basic sulfur anions (blue) in promoted MoS$_2$ facilitate key steps in C-C and C-S bond scission. (**A**) α-H-abstraction from adsorbed carboxylate leading to a ketene that is subsequently decarbonylated (see chapter 5). (**B**) α-H-abstraction from adsorbed acylium ion yielding CO and C$_{n-1}$ olefin.[64] (**C**) H-abstraction from partially hydrogenated, adsorbed dibenzothiophene initiating C-S bond scission.[104] Blue arrows indicate movement of electron pairs. Symbols: M = Mo or promoter metal; R = alkyl.

The pronounced promoting of effect Ni on CLR is sometimes also claimed for the HDO pathway,[57,62] while other studies[64] (including chapter 5 of the present work) have not found such effects. Part of the discrepancy likely arises because of different definitions of "promoting effect". Quite often, it may refer to the conversion of intermediates (e.g., alcohol $\rightarrow$ alkane) and not to the overall reaction (e.g., fatty acid $\rightarrow$ alkane). It is true that the concentration of alcohols and aldehydes tends to be lower on Ni-MoS$_2$ than on MoS$_2$, and a promoting effect on the conversion of these intermediates may therefore be given. The conversion of the fatty acid reactant, on the other hand, is not accelerated significantly by the presence of Ni (or Co).

3.4   References

(1)   Bryant, J. A.; Love, J. *Biofuels: The Back Story*. In *Biofuels and Bioenergy*, Love, J., Bryant, J. A. Eds. John Wiley & Sons: Chichester, West Sussex **2017**, pp 1-19.

(2)   van Dyk, S.; Jianping, S.; D. Mcmillan, J.; Saddler, J. J. *Biofuels, Bioprod. Biorefin.* **2019,** 13, 760-775.

(3)   Karatzos, S.; McMillan, J.; Saddler, J. *The Potential and Challenges of Drop-in Biofuels*. Technical report, IEA Bioenergy Task 39 **2014**, task39.ieabioenergy.com (02.05.2019).

(4)   Dabelstein, W.; Reglitzky, A.; Schütze, A.; Reders, K.; Brunner, A. *Automotive Fuels*. In *Ullmann's Encyclopedia of Industrial Chemistry*, Wiley VCH: Weinheim **2016**, pp 2-41.

(5)   Rosillo-Calle, F.; Teelucksingh, S.; Thrän, D.; Seiffert, M. *The Potential and Role of Biofuels in Commercial Air Transport - Biojetfuel*. Technical report, IEA Bionergy Task 40 **2012**, task40.ieabioenergy.com (21.06.2019).

(6)   Hileman, J.; Ortiz, D.; Bartis, J.; Wong, H.; Donohoo, P.; Weiss, M.; Waitz, I. *Near-Term Feasibility of Alternative Jet Fuels*. Technical Report TR-554-FAA, RAND Corp. with MIT **2009**, rand.org (21.06.2019).

(7)   Vennestrøm, P. N. R.; Osmundsen, C. M.; Christensen, C. H.; Taarning, E. *Angew. Chem. Int. Ed.* **2011,** 50, 10502-10509.

(8)   Karatzos, S.; van Dyk, J. S.; McMillan, J. D.; Saddler, J. *Biofuels, Bioprod. Biorefin.* **2017,** 11, 344-362.

(9)   Bryant, J. A. *Fatty Acids, Triacylglycerols and Biodiesel*. In *Biofuels and Bioenergy*, Love, J., Bryant, J. A. Eds. John Wiley & Sons: Chichester, West Sussex **2017**, pp 105-118.

(10)   Jay, M. I.; Kawaroe, M.; Effendi, H. *IOP Conference Series: Earth and Environmental Science* **2018,** 141, 012015.

(11)   Lynch, J. M. *The Sustainability of Biofuels*. In *Biofuels and Bioenergy*, Love, J., Bryant, J. A. Eds. John Wiley & Sons: Chichester, West Sussex **2017**, pp 261-272.

(12)   Ahmad, A.; Yasin, N.; Derek, C.; Lim, J. *Renewable Sustainable Energy Rev.* **2011,** 15, 584-593.

(13)   Zhao, C.; Brück, T.; Lercher, J. A. *Green Chem.* **2013,** 15, 1720.

(14)   Greenwell, H.; Laurens, L.; Shields, R.; Lovitt, R.; Flynn, K. *J. R. Soc. Interface* **2010,** 7, 703-726.

(15)   Chisti, Y. *Biotechnol. Adv.* **2007,** 25, 294-306.

(16)   Singh, J.; Gu, S. *Renewable Sustainable Energy Rev.* **2010,** 14, 2596-2610.

(17)   Brennan, L.; Owende, P. *Renewable Sustainable Energy Rev.* **2010,** 14, 557-577.

(18) Mata, T. M.; Martins, A. A.; Caetano, N. S. *Renewable Sustainable Energy Rev.* **2010,** 14, 217-232.

(19) *Projekt AUFWIND: Nachhaltiges Kerosin aus Algenöl.* Press release, Forschungszentrum Jülich **2013**, fz-juelich.de/ibg/ibg-2/ (21.06.2019).

(20) Wagenhofer, M. F.; Baráth, E.; Gutierrez, O. Y.; Lercher, J. A. *Schlussbericht zum Verbundvorhaben: AUFWIND - Algenproduktion und Umwandlung in Flugzeugtreibstoffe: Wirtschaftlichkeit, Nachhaltigkeit, Demonstration; Teilvorhaben 9: Algenöl Jet-A1 Produktion auf Basis konventioneller Raffinerietechnologien.* Technical Report FKZ22409512, Fachagentur Nachwachsende Rohstoffe e.V. **2016**, fnr.de (09.08.2019).

(21) *Algentechnikum auf dem Ludwig Bölkow Campus eröffnet.* Press release, Airbus **2015**, airbus.com/newsroom/press-releases/ (21.06.2019).

(22) Sander, K.; Murthy, G. S. *Int. J. Life Cycle Assess.* **2010,** 15, 704-714.

(23) Lestari , S.; Mäki-Arvela, P.; Beltramini, J.; Lu, G. Q. M.; Murzin, D. Y. *ChemSusChem* **2009,** 2, 1109-1119.

(24) Huber, G. W.; Corma, A. *Angew. Chem. Int. Ed.* **2007,** 46, 7184-7201.

(25) *Renewable fuels.* Product information, Neste **2018**, neste.com/companies/products/renewable-fuels/ (28.06.2019).

(26) Mawhood, R.; Gazis, E.; de Jong, S.; Hoefnagels, R.; Slade, R. *Biofuels, Bioprod. Biorefin.* **2016,** 10, 462-484.

(27) Bezergianni, S.; Dimitriadis, A.; Kikhtyanin, O.; Kubička, D. *Prog. Energy Combust. Sci.* **2018,** 68, 29-64.

(28) Egeberg, R.; Michaelsen, N.; Sykum, L.; Zeuthen, P. *Digital Refining* **2010,** 1-11.

(29) Jęczmionek, Ł.; Porzycka-Semczuk, K. *Fuel* **2014,** 131, 1-5.

(30) Egeberg, R.; Knudsen, K. G.; Nyström, S.; Grennfelt, E. L.; Efraimsson, K. *Pet. Technol. Q.* **2011,** 16, 59-65.

(31) Knothe, G. *Prog. Energy Combust. Sci.* **2010,** 36, 364-373.

(32) Gosselink, R. W.; Hollak, S. A.; Chang, S. W.; van Haveren, J.; de Jong, K. P.; Bitter, J. H.; van Es, D. S. *ChemSusChem* **2013,** 6, 1576-1594.

(33) Kubička, D. *Collect. Czech. Chem. Commun.* **2008,** 73, 1015.

(34) Simakova, I.; Simakova, O.; Mäki-Arvela, P.; Murzin, D. Y. *Catal. Today* **2010,** 150, 28-31.

(35) Immer, J. G.; Kelly, M. J.; Lamb, H. H. *Appl. Catal., A* **2010,** 375, 134-139.

(36) Mäki-Arvela, P.; Rozmysłowicz, B.; Lestari, S.; Simakova, O.; Eränen, K.; Salmi, T.; Murzin, D. Y. *Energy Fuels* **2011,** 25, 2815-2825.

(37)   Santillan-Jimenez, E.; Morgan, T.; Lacny, J.; Mohapatra, S.; Crocker, M. *Fuel* **2013,** 103, 1010-1017.

(38)   Madsen, A. T.; Ahmed, E. H.; Christensen, C. H.; Fehrmann, R.; Riisager, A. *Fuel* **2011,** 90, 3433-3438.

(39)   Boda, L.; Onyestyák, G.; Solt, H.; Lónyi, F.; Valyon, J.; Thernesz, A. *Appl. Catal., A* **2010,** 374, 158-169.

(40)   Peng, B.; Yao, Y.; Zhao, C.; Lercher, J. A. *Angew. Chem.* **2012,** 124, 2114-2117.

(41)   Kubička, D.; Bejblová, M.; Vlk, J. *Top. Catal.* **2010,** 53, 168-178.

(42)   Kubička, D.; Šimáček, P.; Žilková, N. *Top. Catal.* **2009,** 52, 161-168.

(43)   Kubička, D.; Kaluža, L. *Appl. Catal., A* **2010,** 372, 199-208.

(44)   Šimáček, P.; Kubička, D.; Šebor, G.; Pospíšil, M. *Fuel* **2009,** 88, 456-460.

(45)   Kubička, D.; Horáček, J. *Appl. Catal., A* **2011,** 394, 9-17.

(46)   Peng, B.; Yuan, X.; Zhao, C.; Lercher, J. A. *J. Am. Chem. Soc.* **2012,** 134, 9400-9405.

(47)   Donnis, B.; Egeberg, R.; Blom, P.; Knudsen, K. *Top. Catal.* **2009,** 52, 229-240.

(48)   Han, J.; Duan, J.; Chen, P.; Lou, H.; Zheng, X. *Adv. Synth. Catal.* **2011,** 353, 2577-2583.

(49)   Vonghia, E.; Boocock, D. G. B.; Konar, S. K.; Leung, A. *Energy Fuels* **1995,** 9, 1090-1096.

(50)   Snåre, M.; Kubičková, I.; Mäki-Arvela, P.; Chichova, D.; Eränen, K.; Murzin, D. Y. *Fuel* **2008,** 87, 933-945.

(51)   Do, P.; Chiappero, M.; Lobban, L.; Resasco, D. *Catal. Lett.* **2009,** 130, 9-18.

(52)   Santillan-Jimenez, E.; Crocker, M. *J. Chem. Technol. Biotechnol.* **2012,** 87, 1041-1050.

(53)   Choudhary, T. V.; Phillips, C. B. *Appl. Catal., A* **2011,** 397, 1-12.

(54)   Šimáček, P.; Kubička, D. *Fuel* **2010,** 89, 1508-1513.

(55)   Wagenhofer, M. F.; Baráth, E.; Gutiérrez, O. Y.; Lercher, J. A. *ACS Catal.* **2017,** 7, 1068-1076.

(56)   Şenol, O. İ.; Viljava, T. R.; Krause, A. O. I. *Catal. Today* **2005,** 100, 331-335.

(57)   Ruinart de Brimont, M.; Dupont, C.; Daudin, A.; Geantet, C.; Raybaud, P. *J. Catal.* **2012,** 286, 153-164.

(58)   Peroni, M.; Mancino, G.; Baráth, E.; Gutiérrez, O. Y.; Lercher, J. A. *Appl. Catal., B* **2016,** 180, 301-311.

(59)   Gosselink, R. W.; Stellwagen, D. R.; Bitter, J. H. *Angew. Chem.* **2013,** 125, 5193-5196.

(60)   Rozmysłowicz, B.; Mäki-Arvela, P.; Tokarev, A.; Leino, A.-R.; Eränen, K.; Murzin, D. Y. *Ind. Eng. Chem. Res.* **2012,** 51, 8922-8927.

(61)   Berenblyum, A. S.; Podoplelova, T. A.; Shamsiev, R. S.; Katsman, E. A.; Danyushevsky, V. Y. *Pet. Chem.* **2011,** 51, 336-341.

(62)   Dupont, C.; Lemeur, R.; Daudin, A.; Raybaud, P. *J. Catal.* **2011,** 279, 276-286.

(63)   Peng, B.; Zhao, C.; Kasakov, S.; Foraita, S.; Lercher, J. A. *Chem. Eur. J.* **2013,** 19, 4732-4741.

(64)   Brillouet, S.; Baltag, E.; Brunet, S.; Richard, F. *Appl. Catal., B* **2014,** 148-149, 201-211.

(65)   Şenol, O. İ.; Ryymin, E. M.; Viljava, T. R.; Krause, A. O. I. *J. Mol. Catal. A: Chem.* **2007,** 268, 1-8.

(66)   Peroni, M.; Lee, I.; Huang, X.; Baráth, E.; Gutiérrez, O. Y.; Lercher, J. A. *ACS Catal.* **2017,** 7, 6331-6341.

(67)   Kubičková, I.; Snåre, M.; Eränen, K.; Mäki-Arvela, P.; Murzin, D. Y. *Catal. Today* **2005,** 106, 197-200.

(68)   Snåre, M.; Kubičková, I.; Mäki-Arvela, P.; Eränen, K.; Murzin, D. Y. *Ind. Eng. Chem. Res.* **2006,** 45, 5708-5715.

(69)   Şenol, O. İ.; Viljava, T. R.; Krause, A. O. I. *Catal. Today* **2005,** 106, 186-189.

(70)   Mäki-Arvela, P.; Snåre, M.; Eränen, K.; Myllyoja, J.; Murzin, D. Y. *Fuel* **2008,** 87, 3543-3549.

(71)   Mäki-Arvela, P.; Kubickova, I.; Snåre, M.; Eränen, K.; Murzin, D. Y. *Energy Fuels* **2007,** 21, 30-41.

(72)   Snåre, M.; Kubičková, I.; Mäki-Arvela, P.; Eränen, K.; Wärnå, J.; Murzin, D. Y. *Chem. Eng. J.* **2007,** 134, 29-34.

(73)   Smith, B.; Greenwell, H. C.; Whiting, A. *Energy Environ. Sci.* **2009,** 2, 262-271.

(74)   Maier, W. F.; Roth, W.; Thies, I.; Schleyer, P. V. R. *Chem. Ber.* **1982,** 115, 808-812.

(75)   Berenblyum, A. S.; Danyushevsky, V. Y.; Katsman, E. A.; Podoplelova, T. A.; Flid, V. R. *Pet. Chem.* **2010,** 50, 305-311.

(76)   Berenblyum, A. S.; Shamsiev, R. S.; Podoplelova, T. A.; Danyushevsky, V. Y. *Russ. J. Phys. Chem. A* **2012,** 86, 1199-1203.

(77)   Dabros, T. M. H.; Stummann, M. Z.; Høj, M.; Jensen, P. A.; Grunwaldt, J.-D.; Gabrielsen, J.; Mortensen, P. M.; Jensen, A. D. *Prog. Energy Combust. Sci.* **2018,** 68, 268-309.

(78)   Huber, G. W.; O'Connor, P.; Corma, A. *Appl. Catal., A* **2007,** 329, 120-129.

(79)   Fu, J.; Lu, X.; Savage, P. E. *ChemSusChem* **2011,** 4, 481-486.

(80)   Kumar, P.; Yenumala, S. R.; Maity, S. K.; Shee, D. *Appl. Catal., A* **2014,** 471, 28-38.

(81)   Jeništová, K.; Hachemi, I.; Mäki-Arvela, P.; Kumar, N.; Peurla, M.; Čapek, L.; Wärnå, J.; Murzin, D. Y. *Chem. Eng. J.* **2017,** 316, 401-409.

(82)   Lestari, S.; Mäki-Arvela, P.; Simakova, I.; Beltramini, J.; Lu, G. Q. M.; Murzin, D. *Catal. Lett.* **2009,** 130, 48-51.

(83)   Grosso-Giordano, N. A.; Eaton, T. R.; Bo, Z.; Yacob, S.; Yang, C.-C.; Notestein, J. M. *Appl. Catal., B* **2016,** 192, 93-100.

(84)   Foraita, S.; Fulton, J. L.; Chase, Z. A.; Vjunov, A.; Xu, P.; Baráth, E.; Camaioni, D. M.; Zhao, C.; Lercher, J. A. *Chem. Eur. J.* **2014,** 21, 2423-2434.

(85)   Foraita, S.; Liu, Y.; Haller, G. L.; Baráth, E.; Zhao, C.; Lercher, J. A. *ChemCatChem* **2017,** 9, 195-203.

(86)   Denk, C.; Foraita, S.; Kovarik, L.; Stoerzinger, K.; Liu, Y.; Baráth, E.; Lercher, J. A. *Catal. Sci. Technol.* **2019,** 9, 2620-2629.

(87)   Miao, C.; Marin-Flores, O.; Davidson, S. D.; Li, T.; Dong, T.; Gao, D.; Wang, Y.; Garcia-Pérez, M.; Chen, S. *Fuel* **2016,** 166, 302-308.

(88)   Zhang, J.; Zhao, C. *ACS Catal.* **2016,** 6, 4512-4525.

(89)   Sotelo-Boyás, R.; Liu, Y.; Minowa, T. *Ind. Eng. Chem. Res.* **2010,** 50, 2791-2799.

(90)   Tiwari, R.; Rana, B. S.; Kumar, R.; Verma, D.; Kumar, R.; Joshi, R. K.; Garg, M. O.; Sinha, A. K. *Catal. Commun.* **2011,** 12, 559-562.

(91)   Zhang, H.; Lin, H.; Zheng, Y. *Appl. Catal., B* **2014,** 160-161, 415-422.

(92)   Qin, Y.; He, L.; Duan, J.; Chen, P.; Lou, H.; Zheng, X.; Hong, H. *ChemCatChem* **2014,** 6, 2698-2705.

(93)   Stellwagen, D. R.; Bitter, J. H. *Green Chem.* **2015,** 17, 582-593.

(94)   Han, J.; Duan, J.; Chen, P.; Lou, H.; Zheng, X.; Hong, H. *ChemSusChem* **2012,** 5, 727-733.

(95)   Hollak, S. A. W.; Gosselink, R. W.; van Es, D. S.; Bitter, J. H. *ACS Catal.* **2013,** 3, 2837-2844.

(96)   Kepp, K. P. *Inorg. Chem.* **2016,** 55, 9461-9470.

(97)   Gutiérrez, O. Y.; Hrabar, A.; Hein, J.; Yu, Y.; Han, J.; Lercher, J. A. *J. Catal.* **2012,** 295, 155-168.

(98)   Hein, J.; Hrabar, A.; Jentys, A.; Gutiérrez, O. Y.; Lercher, J. A. *ChemCatChem* **2014,** 6, 485-499.

(99)   Luo, W.; Shi, H.; Schachtl, E.; Gutierrez, O. Y.; Lercher, J. A. *Angew. Chem. Int. Ed.* **2018,** 57, 14555-14559.

(100)   Breysse, M.; Furimsky, E.; Kasztelan, S.; Lacroix, M.; Perot, G. *Catal. Rev.* **2002,** 44, 651-735.

(101)   Jones, S. O.; Reid, E. E. *J. Am. Chem. Soc.* **1938,** 60, 2452-2455.

(102)   Raybaud, P.; Hafner, J.; Kresse, G.; Toulhoat, H. *J. Phys.: Condens. Matter* **1997,** 9, 11107-11140.

(103)   Harris, S.; Chianelli, R. R. *J. Catal.* **1986,** 98, 17-31.

(104)   Bataille, F.; Lemberton, J.-L.; Michaud, P.; Pérot, G.; Vrinat, M.; Lemaire, M.; Schulz, E.; Breysse, M.; Kasztelan, S. *J. Catal.* **2000,** 191, 409-422.

4 Enhancing hydrogenation activity of Ni-Mo sulfide hydrodesulfurization catalysts
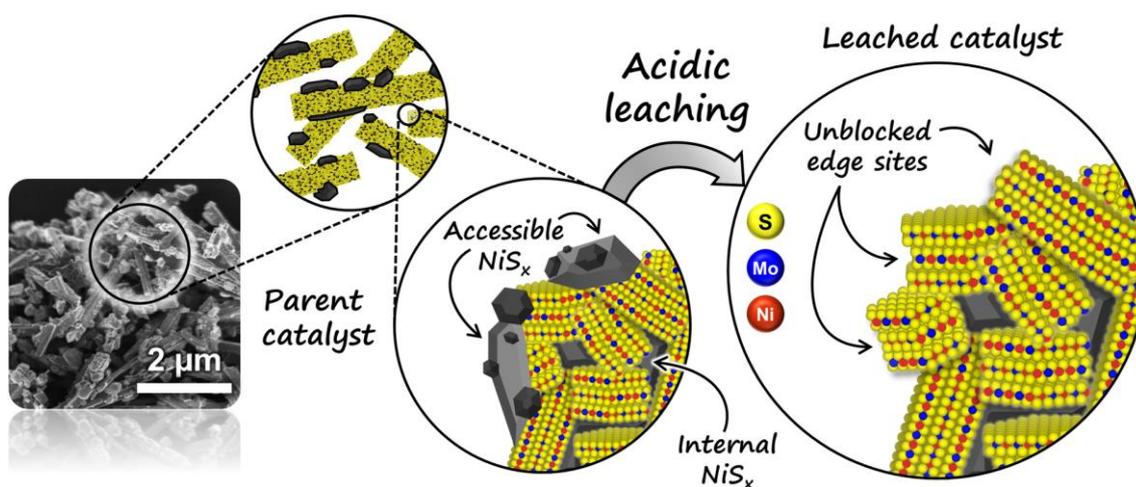
This work has been published

Reprinted with permission from: Wagenhofer, M. F.; Shi, H.; Jentys, A.; Gutierréz, O. Y.; Lercher, J. A. *Science Advances* **2020**, 6, eaax5331. DOI: 10.1126/sciadv.aax5331

Abstract

Unsupported Ni-Mo sulfides have been hydrothermally synthesized and purified by HCl leaching to remove Ni sulfides. Unblocking of active sites by leaching significantly increases the catalytic activity for dibenzothiophene hydrodesulfurization. The site-specific rates of both direct (hydrogenolytic) and hydrogenative desulfurization routes on these active sites that consist of coordinatively unsaturated Ni and sulfhydryl groups were identical for all unsupported sulfides. The hydrogenative desulfurization rates were more than an order of magnitude higher on unsupported Ni-Mo sulfides than on Al_2O_3-supported catalysts, while they were similar for the direct (hydrogenolytic) desulfurization. The higher activity is concluded to be caused by the lower average electronegativity, i.e., higher base strength and polarity, of Ni-Mo sulfides in the absence of the alumina support, and the modified adsorption of reactants enabled by multilayer stacking. Beyond the specific catalytic reaction, the synthesis strategy points to new scalable routes to sulfide materials broadly applied in hydrogenation and hydrotreating.

4.1   Introduction

Unsupported hydrotreating catalysts are complex mixtures of transition metal sulfides that may have synergistic and antagonistic interactions among different phases. For Mo-based catalysts, the major constituents are pure MoS_2, a Ni/Co-containing MoS_2 phase having Ni and Co incorporated at the perimeter of the MoS_2 crystals, and a variety of sulfides of Ni and Co. The promoting effects of Co and Ni are typically attributed to their selective incorporation at the MoS_2 slab edge and to the associated generation of sulfhydryl groups.[1-3]

While these sites are active for hydrogenation and hydrodefunctionalization reactions (hydrodesulfurization (HDS) and hydrodenitrogenation (HDN)), nickel or cobalt metal sulfides (e.g., NiS_x) have only sites with much lower activity.[1,4,5] Though these latter phases do not significantly contribute to hydrogenation and hydrodefunctionalization, they may adversely affect the catalytic performance by adding inert mass and blocking active sites at the MoS_2 perimeter. This complicates the evaluation of structure-function relations,[6] as it obscures relations between chemical compositions, concentrations of active sites, and catalytic activity.

Segregation into inactive phases is especially severe for unsupported sulfides because sulfides with high catalytic activities require concentrations of promoter metal loadings that inevitably lead to segregation into inactive phases. To unblock active sites, post-synthetic removal of the confounding phases is a promising alternative. Phase diagrams (Figure S4.1) indicate for Ni-Mo systems that this can be achieved via concentrated acid treatment, selectively dissolving catalytically inactive forms of Ni, whereas Ni-associated active sites and the overall catalyst structure composed of stacked MoS_2 slabs appear to be unaffected.[7-10]

In the present study, we report on acid extraction as a preparative tool to obtain well-defined Ni-Mo sulfide catalysts that have an exceptionally high site-specific activity for hydrogenative desulfurization. Such cleaned mixed sulfides allow also relating nature and concentration of active sites to catalytic properties and to corroborate recent insight into active sites.[11]

4.2 Results and discussion

4.2.1 Selective removal of Ni sulfides

Ni-promoted parent MoS_2 catalysts were prepared via hydrothermal synthesis and were subsequently treated with concentrated HCl (pH = −1) to remove Ni sulfides (NiS_x). This treatment is named "leaching" or "acid treatment" in this paper.

Ni sulfides are not stable in highly acidic solutions (pH < 0).[12] We observed dissolution of NiS_x when exposing the mixed sulfide catalysts to concentrated HCl, visible by a greenish color of the solution due to the formation of aqueous Ni^{2+}, as well as by H_2S evolution. A substantial reduction (on the order of 20–30 %) of the mass of the acid-treated catalysts was observed, while the MoS_2 component remained unmodified. This was verified by exposing MoS_2 to the identical treatment without observing significant mass loss, H_2S evolution, coloration of the solution,[13] or a change in catalytic properties. This shows that MoS_2 is effectively inert even in strongly acidic solutions, as long as oxidants are absent (Figure S4.1).

X-ray diffraction patterns before leaching (Figure S4.2 A) show characteristic broad reflections of polycrystalline MoS_2 ($2\theta \approx 14$, 33, 40, and 59 °), accompanied by sharp reflections in the range of $2\theta = 27$–60 ° assigned to Ni subsulfides Ni_3S_2 and Ni_9S_8.[6,14-17] An approximate calculation of the S/Ni ratio (S/Ni = 0.83–1.21) shows that NiS_x phases with x > 1 (e.g., NiS_2, Ni_3S_4) might be also present. Note, however, that the estimated S/Ni ratio may also include (X-ray) amorphous forms of NiS_x or NiS_x present at low concentrations that are not visible by XRD.

The elemental composition (Table S4.1) of the parent catalysts was uniform, with S/(Ni+Mo) atomic ratios of about 1.5 and Ni/(Ni+Mo) atomic ratios of 0.48–0.60. The composition changed significantly after exposure to concentrated HCl. The atomic metal fraction of Ni, Ni/(Ni+Mo), decreased from 0.48–0.60 prior to leaching to 0.20–0.26 after leaching, i.e., somewhat smaller than the typical optimum of 0.3–0.4 in supported sulfides.[1,2,18] Note, however, that the Ni/(Ni+Mo) ratio in most supported catalysts also includes Ni atoms that are not associated with MoS_2, such as cations in spinels formed

with the Al_2O_3 support.[1] The "effective" Ni/(Ni+Mo) ratio may thus be lower than 0.3–0.4 and is speculated to be close to the values of the leached catalysts.

The extensive loss of Ni (69–77 %) was accompanied by a moderate, yet significant, loss of sulfur (13–28 %), whereas the concentration of Mo was not affected. These changes were also reflected in the X-ray diffractograms (Figure S4.2 B). The NiS_x reflections disappeared almost completely, while contributions of MoS_2 remained essentially unchanged (broad reflections at $2\theta \approx 14$, 33, 40, and 59 °), suggesting that the structure of MoS_2 was retained after acid treatment. This is confirmed by particle size analysis via transmission electron microscopy (TEM) and XRD line broadening, which both suggest similar crystalline dimensions of the primary MoS_2 domains before and after treatment (Table S4.1).

While the dimensions of the primary MoS_2 domains were barely affected by leaching, fundamental changes in the overall morphology were observed. Scanning electron micrographs (SEM) of the catalysts before acid treatment showed two major structural features (Figure 4.1 A; see Figure S4.3 for supplementary micrographs). The bulk of the material consisted of rod-shaped structures of about 100 nm in diameter and 0.5–2 μm in length, intermixed with randomly distributed, compact particles of irregular shape and sizes no larger than 200 nm. These compact particles were absent after acid treatment (Figure 4.1 B) and their sizes in the parent materials agreed with those of the NiS_x domains as determined by XRD (about 75–150 nm). Thus, we assign the compact, irregular particles to segregated NiS_x.

Accordingly, we assign the refractory rod-like structures to a MoS_2-rich phase, likely containing the remaining Ni (Ni-Mo-S phase). The NiS_x particles visible in SEM were primary crystallites, while the rod-like MoS_2 phase is a secondary structure, composed of nanometer-sized MoS_2 domains (Figure 4.1 E). We would like to point out that the rod-like morphology was already present in the oxide precursors (Figure 4.1 D) and was retained throughout sulfidation and acid treatment. Such structural features seem to be common for hydrothermally prepared MoS_2.[14,19]

In the case of NiMo-4, we observed leaching-resistant agglomerates of 10–50 nm particles (Figure 4.1 F), a structural feature that was not present in the other catalysts, in addition to the previously discussed MoS_2-rods and compact NiS_x crystals. Because of

their refractory behavior in acidic solution, we conclude that the agglomerates are not entirely composed of NiS_x. We speculate that these entities are either MoS_2-particles with an atypical morphology or Ni sulfides encapsulated by MoS_2.[20]
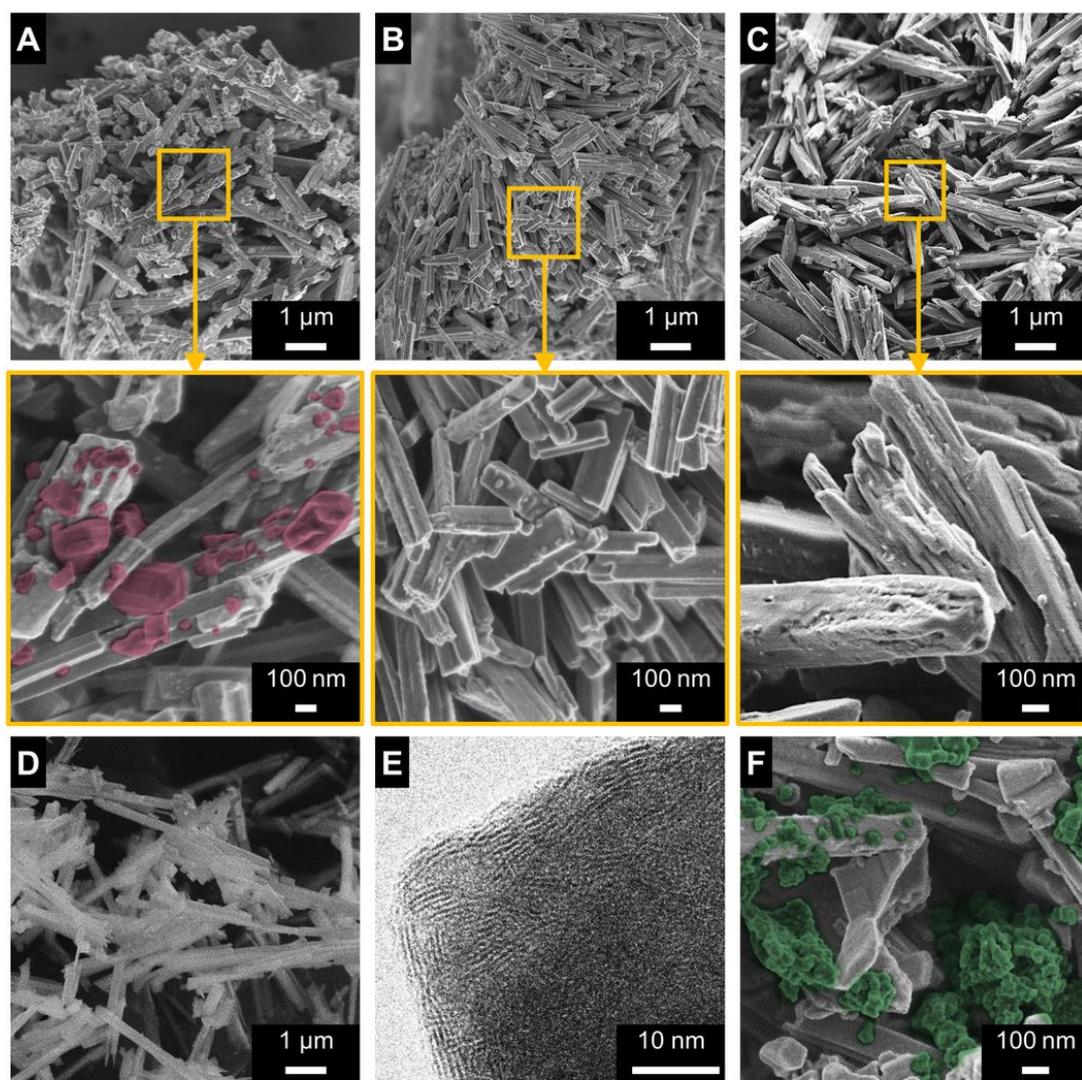
Figure 4.1. Electron micrographs. (**A**) Scanning electron micrograph (SEM) of NiMo-3 before leaching with enlarged view below showing MoS_2 rods and compact NiS_x particles in false color. (**B**) SEM of NiMo-3 after leaching showing only MoS_2 rods. (**C**) SEM of NiMo-1 after leaching with enlarged view below showing corrugated surface of MoS_2 rods. (**D**) MoO_3 catalyst precursor used in hydrothermal synthesis. (**E**) Transmission electron micrograph of sulfided NiMo-3 after acid treatment. (**F**) SEM showing agglomerates of unidentified fine particles on NiMo-4 before leaching.

Acid treatment led to substantially increased specific surface areas and pore volumes in the first three catalysts (Table S4.1). This textural improvement is attributed to the

uncovering of pore openings and corrugated surface regions previously blocked by NiS_x (Figure 4.1 C). Specific surface areas were roughly doubled by acid treatment for all but NiMo-4-p, for which specific surface area and pore volume were not significantly affected (see the discussion accompanying Figure S4.1).

Based on elemental composition, XRD, TEM, and SEM we conclude that segregated NiS_x is removed selectively without affecting the structural integrity of the MoS_2-rich constituent. We speculate that the acid-resistant Ni is incorporated in MoS_2.

4.2.2 Interatomic coordination

Extended X-ray absorption fine structure (EXAFS) at the Ni K-edge indicates a similar NiS_x phase mix in all of the parent catalysts (Table S4.2), which is consistent with XRD results (Table S4.1). Because the spectra (Figure 4.2) could be modeled satisfactorily using only Ni-S and Ni-Ni scattering paths (Table S4.3), we hypothesize that the fraction of Ni atoms in the promoted Ni-Mo-S phase is small compared to the number of Ni atoms in segregated Ni sulfides (see Figure S4.4 for the complete set of spectra in *k*- and *R*-space). This is supported by the analysis of chemical composition before and after leaching (Table S4.1), which suggests that more than 70 % of Ni in the parent samples is present as acid-leachable Ni sulfides. After leaching, by contrast, we found that a Mo scatterer at 2.86 Å was required to fit the data. This is in good agreement with literature reports[16-18,21-25] and also with the overall picture drawn by the other characterization techniques, i.e., as the majority of segregated NiS_x is removed during acidic treatment, Ni-Mo contributions from the promoted Ni-Mo-S phase become more predominant in relation to contributions from NiS_x.

In addition to the appearance of a Ni-Mo contribution, we also found that average Ni-S distance was significantly and consistently smaller after leaching (2.22 Å compared to 2.26 Å). This distance is too short for crystalline Ni sulfides (Table S4.3) and clearly shows that a significant part of the Ni atoms in acid-treated catalysts is not located in segregated NiS_x phases. In agreement with reports on supported sulfides,[21,23,24] we conclude that the short Ni-S bonds are associated with the Ni-Mo-S phase. Figure 4.2 C shows a possible configuration of Ni at the metal edge of MoS_2 that is consistent with the observed EXAFS parameters (see also Table S4.2 and accompanying discussion).
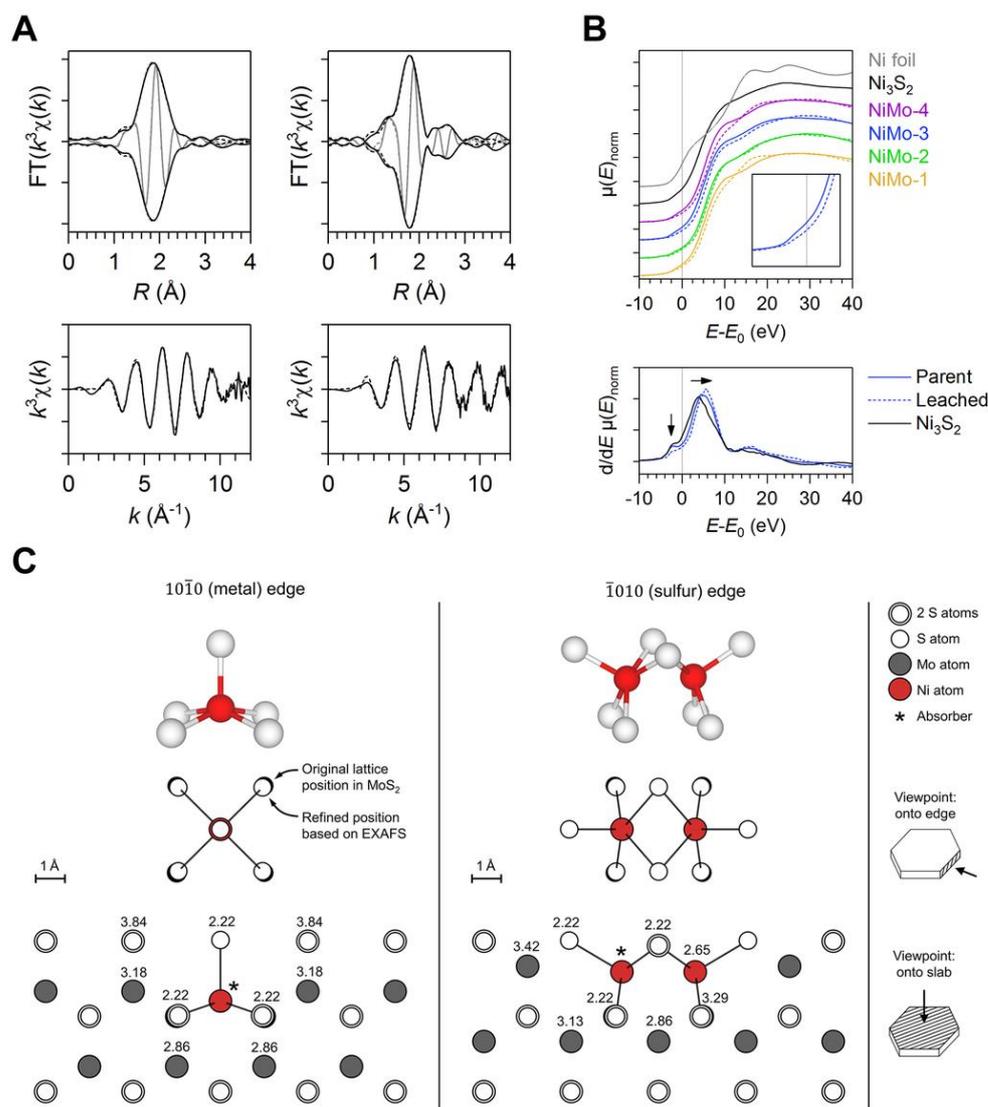
Figure 4.2. Results of XAS at the Ni K-edge and structural model. (**A**) Top row: magnitude (black) and imaginary part (grey) of the k^3-weighted Fourier-transform before leaching (left) and after leaching (right) with best fit (dashed line). Bottom row: k^3-weighted EXAFS and best fit (dashed line) before (left) and after leaching (right). The distance between two vertical tick marks is 5 $Å^{-3}$ (*k*-space) and 5 $Å^{-4}$ (*R*-space). See Figure S4.4 for EXAFS of NiMo-1, NiMo-2, and NiMo-4. (**B**) Top: normalized near-edge absorption ($E_0 = 8333$ eV) of Ni-Mo sulfide catalysts, Ni_3S_2, and Ni metal. The inset shows an enlarged view of the pre-edge. Arrows highlight features discussed in the text. Bottom: derivative of normalized absorption of Ni_3S_2, NiMo-3-p, and NiMo-3-L. Continuous and dotted lines correspond to parent and leached samples, respectively. (**C**) Proposed local environments of Ni derived from EXAFS results. Single Ni atom incorporated at the metal edge and neighboring Ni atoms incorporated at the sulfur edge of MoS_2 shown from different perspectives (2D projections to scale, 3D representation schematic). The numbers indicate the distance to the Ni absorber in Å (absorber denoted with asterisk).

Leaching-associated changes were also noticed in the Ni-Ni coordination, which appeared at a significantly larger average distance of 2.63 Å instead of 2.56 Å in the parent sulfides (Table S4.2). The fact that Ni-Ni scattering was still observed after leaching could indicate that some NiS_x phases persisted after HCl treatment. On the other hand, Ni-Ni scattering is not necessarily associated only with segregated Ni sulfides and could also originate from neighboring Ni atoms in Ni-Mo-S. One example of a dinuclear Ni-Ni entity that is consistent with the present EXAFS analysis is shown in Figure 4.2 C for the sulfur edge (see also Table S4.2 and accompanying discussion). Based on DFT calculations, such Ni-Ni pairs were proposed and predicted to be stable.[26,27] The suggested structure at the sulfur edge closely resembles the main structural motif of naturally occurring NiS ("Millerite").

Analysis of the near-edge structure (XANES) highlighted further important differences between parent and leached sulfides. Both the intensity of the pre-edge feature (1s-3d transition) and the edge energy were found to qualitatively correlate with the NiS_x content (Figure 4.2 B). The pre-edge signal at approximately 8332 eV was most intense in the Ni_3S_2 reference, followed by the parent catalysts and finally by the leached catalysts, in which it was barely noticeable. This sequence reflects the fact that tetrahedrally coordinated Ni, such as in Ni_3S_2, typically exhibits a more intense pre-edge than Ni in Ni-Mo-S.[24] The gradual weakening of the pre-edge in the sequence Ni_3S_2 > NiMo-p > NiMo-L was accompanied by a blue-shift in the edge-energy following the same sequence and pointed to changes in the overall electron density of Ni. The gradual shift suggests that the average oxidation state of Ni increases as edge-incorporated Ni atoms become more and more significant in concentration compared to NiS_x (a mixture of phases with formal oxidation states +1.3 to +2).

4.2.3   Distribution of Ni among active and inactive phases

To analyze the distribution of Ni among active (Ni-Mo-S) and inactive (NiS_x) phases, we compare the total Ni content to the maximum concentration of Ni that could be theoretically incorporated at the edges (Figure 4.3 E). The latter is given by the number of edge metal atoms and may be estimated from TEM data using a geometric model (see supplementary methods). The analysis of the parent catalysts clearly shows that much

more Ni is present than potential sites that exist at MoS_2 edges (Figure 4.3 E). Even after acid treatment, the residual amount of Ni exceeds that of available edge positions. If we further consider that usually not all edge sites can be occupied by Ni, the discrepancy becomes even more pronounced. Thus, we reason that also leached catalysts contain some segregated Ni sulfides or small NiS_x clusters.
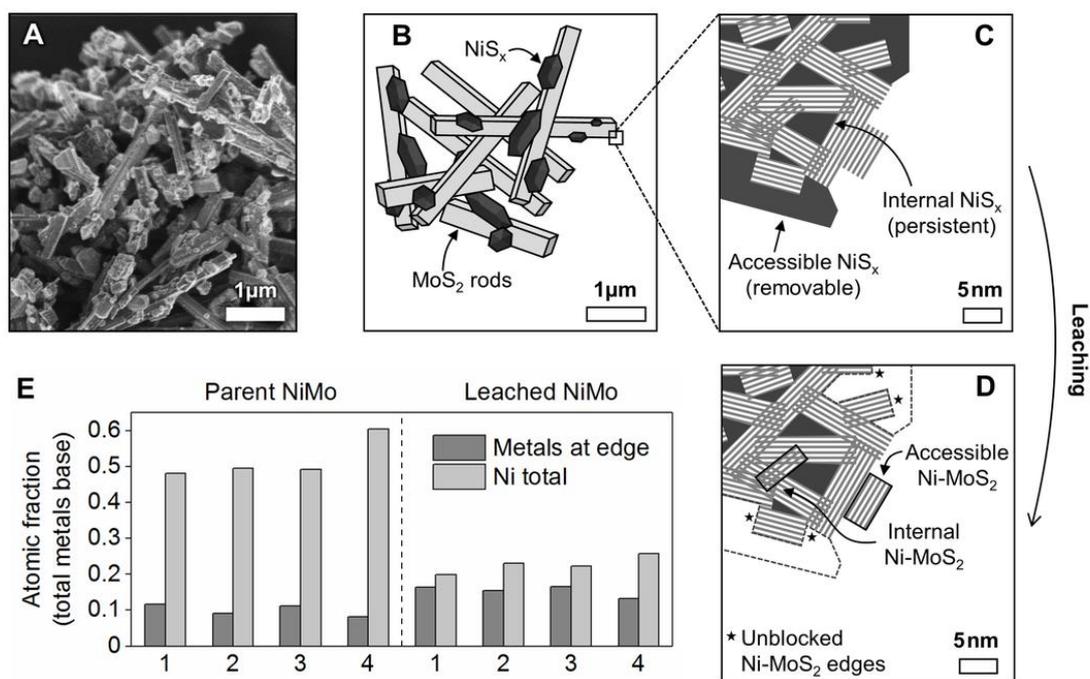
Figure 4.3. Ni distribution among active and inactive phases. (**A**) Representative SEM micrograph and (**B**) schematic representation of NiMo-3 before leaching, showing secondary rod-like MoS_2 phase intermixed with crystalline NiS_x. (**C**) Enlarged cross-section of the corner of one rod-like particle before leaching. (**D**) Cross-section after leaching. (**E**) Comparison of total amount of Ni present in the catalysts ("Ni total" determined via elemental analysis) with amount of available edge positions ("Metals at edge" determined via TEM) before and after leaching.

Thus, we conclude that the removal of NiS_x was not quantitative. This raises the question about the nature of such acid-resistant NiS_x phases. While XRD showed that Ni sulfides were absent after leaching (Figure S4.2), the remaining NiS_x might exist as X-ray amorphous domains. However, as Ni sulfides are readily soluble in concentrated HCl, such acid-resistant NiS_x phases are concluded to be at inaccessible locations, for example, within the rod-like structures (Figure 4.3 A to D) or in the form of MoS_2-coated particles.[5] Being confined by the densely packed MoS_2 matrix, the size of such NiS_x domains may be rather small. EXAFS of leached samples (Table S4.2) supports the hypothesis of

internal NiS_x reservoirs by showing a Ni-Ni contribution similar to that of bulk Ni sulfides.

Having hypothesized that internal NiS_x phases may be present after leaching, we are now in a position to estimate their proportion among the pool of Ni species (see supplementary methods and discussion of Table S4.4). For this, we compare the amount of edge-incorporated Ni to the total amount of Ni in the catalysts. We employed nitric oxide (NO) chemisorption to determine the concentration of Ni atoms at the accessible surface, which we then extrapolated to the inaccessible bulk of the material. The implicit assumption is that NO adsorbs predominantly on Ni-associated edge sites and that MoS_2 domains in the bulk ("internal MoS_2", Figure 4.3 D) have the same degree of edge substitution by Ni as those at the accessible surface ("accessible MoS_2", Figure 4.3 D). The results suggest that 24–40 % of Ni atoms in the leached catalysts are incorporated in Ni-Mo-S (Table S4.4), while the remainder of 60–76 % exists as inaccessible NiS_x. The corresponding figures for the parent catalysts indicate a much lower incorporation of Ni, with only 8–10 % of all Ni atoms located at MoS_2 edges. This is fully consistent with the conclusions from EXAFS, suggesting that the contribution of edge-incorporated Ni atoms prior to leaching was masked by the much more predominant NiS_x phase mix.

As for the degree of edge substitution by Ni, we determined values of 31–43 % for three of the leached catalysts, which is in good agreement with typical maxima reported in the literature.[28,29] In the case of NiMo-4-L, the calculated edge substitution degree was significantly higher than in the other catalysts (78 %). Alternatively, this large value could indicate that the fraction of edge metal atoms (derived from TEM) was underestimated because particularly small MoS_2 particles may be present in this material. Figure 4.1 F shows a very heterogeneous distribution of secondary structures, i.e., rods and agglomerates, for this particular sample.

4.2.4 Dibenzothiophene hydrodesulfurization

Having shown that accessible Ni sulfides are removed selectively by acid treatment, we now discuss its catalytic consequences for the hydrodesulfurization (HDS) of dibenzothiophene (DBT). The conversion of DBT follows two distinct pathways, hydrogenation (HYD) and hydrogenolysis (also referred to as direct desulfurization or DDS.[1,30-32] In

DDS, C-S hydrogenolysis to biphenyl (BP) takes place first and aromatic ring saturation occurs later. In the HYD route, the initial step consists of a gradual saturation of one aromatic ring to yield 1,2,3,4-tetrahydro-DBT and 1,2,3,4,4a,9b-hexahydro-DBT (4HDBT and 6HDBT, respectively). This is followed by hydrogenolysis of the C-S bond to cyclohexyl benzene (CHB), which is then hydrogenated to the final product bicyclo-hexyl (BCH). Note that this sequence may contain other (short-lived) intermediates such as the reactive thiol (CHB-SH) shown in Figure 4.4 A, which we directly observed via mass spectrometry. Dihydrodibenzothiophenes (a possible class of intermediates involved in both HYD and DDS[33] or 2-biphenylthiol (an intermediate formed after the cleavage of the first C-S bond along the DDS path[33]) was not detected.
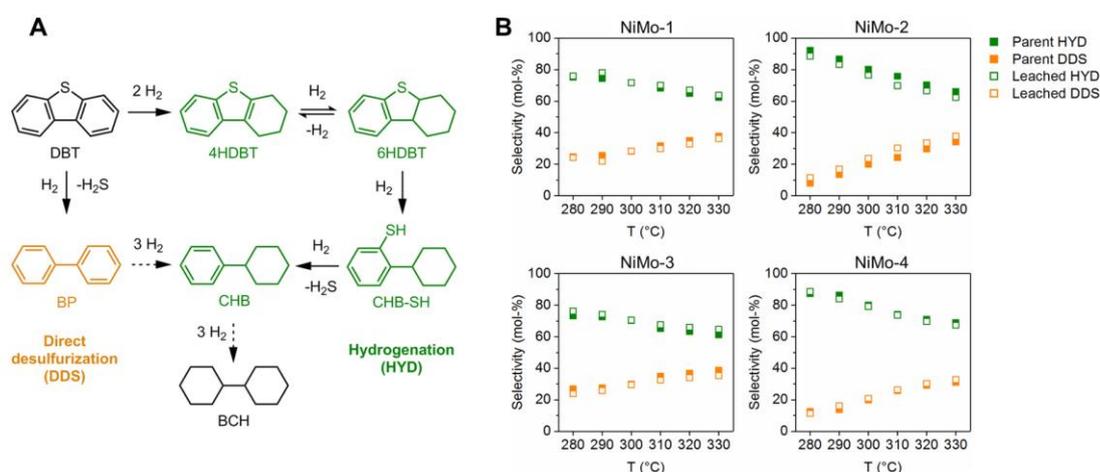
Figure 4.4. Dibenzothiophene (DBT) hydrodesulfurization network and measured selectivities. (**A**) Reaction network. (**B**) Selectivity for direct desulfurization (DDS) and hydrogenation (HYD) of dibenzothiophene on Ni-Mo sulfide catalysts before and after acid treatment as a function of temperature (trickle-bed reactor, 280–330 °C, 50 bar total pressure (H_2), 1 wt% DBT in decalin, gas/liquid = 500 Nm³/Nm³, WHSV = 1).

The main products under most conditions were biphenyl (BP) and cyclohexyl benzene (CHB). Relevant concentrations of partially hydrogenated intermediates (4HDBT and 6HDBT) were only observed at low conversions and temperatures < 290 °C, while the fully saturated product, bicyclohexyl (BCH), was never observed in significant concentrations. On parent and leached MoS_2, we also observed a CHB-SH intermediate (with the SH group at the aromatic ring) at low conversions and temperatures. The parent catalysts converted DBT predominantly via the HYD pathway (Figure 4.4 B). With increasing temperature, the selectivity to DDS increased substantially but never exceeded

that of HYD. This preference contrasts that observed for supported catalysts (e.g., ~90 % DDS and ~10 % HYD on a sulfided Ni-Mo/Al$_2$O$_3$ sample, see Table S4.5; also see refs. [33-35]). Varying the residence-time at 330 °C resulted in constant DDS and HYD selectivity over the whole range of DBT conversions (< 45 %) on MoS$_2$ and Ni-Mo sulfides (Figure S4.5). Thus, the product distribution in the present analysis only depends on the temperature and is not affected by the simultaneous changes in DBT conversion, i.e., the selectivities of different catalysts at a specific temperature can be compared directly.

Table 4.1. Initial DDS and HYD reaction rates and apparent energies of activation.

Catalyst	Initial rates (mmol g^{-1} h^{-1} or mol mol$_{Mo}^{-1}$ h^{-1}) ^{a}			E$_A$ (kJ mol^{-1}) ^{b}		
	Total	DDS	HYD	Total	DDS	HYD
NiMo-1-p	1.5 (0.36)	0.58 (0.14)	0.96 (0.22)	152 ± 4	177 ± 4	140 ± 5
NiMo-2-p	1.4 (0.34)	0.46 (0.12)	0.89 (0.22)	164 ± 5	239 ± 12	145 ± 6
NiMo-3-p	2.6 (0.49)	1.0 (0.19)	1.6 (0.30)	153 ± 10	176 ± 12	142 ± 9
NiMo-4-p	6.9 (2.02)	2.1 (0.63)	4.7 (1.39)	151 ± 4	205 ± 9	136 ± 4
MoS$_2$-p	2.5 (0.39)	0.46 (0.07)	2.0 (0.32)	–	–	–
NiMo-1-L	2.3 (0.41)	0.83 (0.15)	1.5 (0.26)	147 ± 5	174 ± 8	135 ± 5
NiMo-2-L	2.9 (0.53)	1.1 (0.20)	1.8 (0.33)	157 ± 5	220 ± 12	138 ± 5
NiMo-3-L	4.5 (0.86)	1.6 (0.30)	2.9 (0.56)	144 ± 3	170 ± 5	134 ± 3
NiMo-4-L	11.0 (2.23)	3.7 (0.73)	7.7 (1.50)	156 ± 4	214 ± 8	139 ± 4
MoS$_2$-L	2.4 (0.39)	0.41 (0.07)	2.0 (0.32)	–	–	–

^{a} Initial rates (±5 %) at 330 °C; values outside and in the parentheses are normalized to the catalyst mass and to the total amount of Mo, respectively. ^{b} Temperature range: 280–330 °C.

The product distribution in the whole temperature range was very similar on all parent Ni-Mo sulfide catalysts (for example, S_{HYD} = 62–69 % and S_{DDS} = 31–38 % at 330 °C). This implies a similar composition of active sites, i.e., a similar distribution of Ni among DDS- and HYD-selective sites. At the same time, however, substantial differences in the distribution of Ni among active (edge-incorporated Ni) and inactive (NiS$_x$) phases must exist. We conclude this from the considerable variations in HDS activity (r_{HDS} = 1.5–6.9 mmol g^{-1} h^{-1}, Table 4.1), which does not track the almost constant Ni content (7.0–8.8 at%, Table S4.1). This discrepancy arises because mass specific activity is not only determined by the concentration of incorporated Ni but also by the proportion of inert mass (NiS$_x$) and to the extent NiS$_x$ blocks active sites.

The mass-specific rate increased by a factor of 1.6–2.3 after leaching, which clearly exceeds the sole effect of mass loss (Figure S4.6 A). Assuming all sites are equally active, we estimate the fraction of sites blocked by NiS_x in the parent catalysts to be between 0.05 and 0.46. A correlation between the fraction of removed mass and the extent of site unblocking was not observed (Figure S4.6 B).

Despite the marked effect on reaction rates, the product distribution was essentially unchanged after acid treatment (Figure 4.4 B), which implies that DDS and HYD pathways were enhanced by the same factor. This leads to the conclusion that newly exposed and pre-existing active sites are identical. Acid leaching also did not significantly alter activation energies (E_A) as shown in the parity plot in Figure S4.7.

Activation energies (Table 4.1) for the HYD pathway were consistently lower than those of the DDS pathway, which agrees with the fact that the rate determining step differs between the two pathways. It is noteworthy that $E_{A,HYD}$ was nearly identical, whereas $E_{A,DDS}$ showed considerable variations among different catalysts (Table 4.1). While the $E_{A,HYD}$ values (134–139 kJ mol^{-1}) indicate a corresponding uniformity of HYD-selective sites, the $E_{A,DDS}$ values vary in a relatively broad range, as multiple types of DDS sites differing in the steric environment and the basicity of the remaining S^{2-} anions in the vicinity of the vacancy exist at S- and Mo-edges.[36] More studies are, however, needed to differentiate between these two options.

4.2.5   Structure-Activity Relations

Despite the complexity of active sites, agreement exists on the key roles of coordinatively unsaturated sites (CUS or "sulfur vacancies") and sulfhydryl (SH) groups. The most important function of CUS is to coordinate with the organic sulfur (σ or η^1(S) adsorption for DDS of less sterically hindered S-containing molecules), while also providing a pathway for activating hydrogen and transiently forming SH. Hydrogen is provided by nearby SH groups for both DDS and HYD.[37] We have recently highlighted the direct role of SH groups in aromatics hydrogenation over supported sulfides and found that SH groups associated with Ni edge atoms exhibited a constant intrinsic activity independent of the overall composition of the catalyst.[11] Applying this analysis, CUS and SH groups were quantified using NO chemisorption and steady-state H_2/D_2 isotopic

exchange. We would like to point out that SH groups present under the conditions of NO chemisorption are likely to undergo NO/SH exchange and may thus be titrated along with CUS. In the following, we choose to include these SH groups, converted to CUS, in the total CUS count unless otherwise specified. Total CUS concentration was calculated directly from NO uptake assuming dinitrosyl-type adsorption,[38,39] whereas SH concentration is represented indirectly by a proportional quantity, that is, H_2/D_2 isotopic exchange rates (IER). Note that H/D exchange is directly involving SH, but CUS are part of the catalytically active site.[40] Both methods are discussed in more detail in connection with Table S4.6 and Figure S4.8 in the supplementary materials.

The linear correlation between CUS concentrations and the IER values observed for the leached series of catalysts (Figure 4.5 A) indicates that CUS are needed for H/D exchange. The absence of such a functional dependency for the parent samples demonstrates that a major fraction of CUS exist in an environment that does not have a large concentration of SH groups. We surmise that these are a fraction of CUS in NiS_x. The direct proportionality suggests a fixed ratio between CUS and SH sites in the treated samples as we have also observed with supported sulfide catalysts.[11] Therefore, we used the CUS concentration (half of NO uptake) as a quantity for the concentration of active sites in the studied materials, while noting that some of the CUS from non-promoted sites contribute only to a minor extent to DDS and HYD activities.
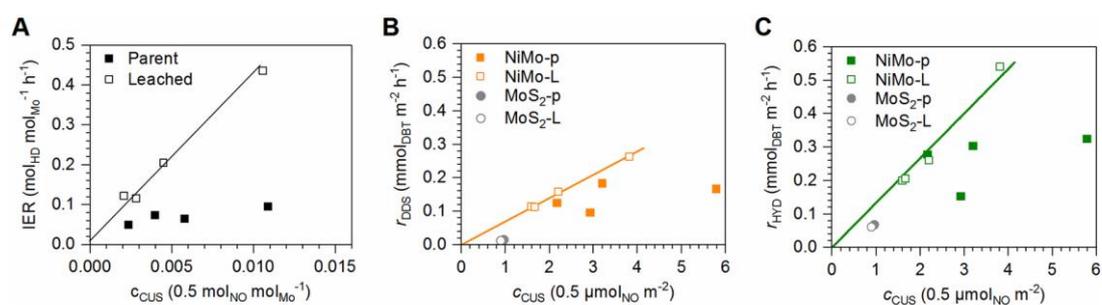
Figure 4.5. Correlations between the reaction rates, isotopic exchange rate (IER) and the total CUS concentration. (**A**) IER as a function of total CUS concentration (normalized to total Mo content) as determined by NO chemisorption on parent (closed symbols) and leached catalysts (open symbols). Note that the factor 0.5 on the x-axis results from assuming dinitrosyl adsorption at Ni-associated edge sites. (**B**) Initial DDS rate and (**C**) initial HYD rate normalized to surface area as a function of total CUS surface density in parent (closed symbols) and leached catalysts (open symbols).

Figure 4.5 B shows DDS and HYD rates of parent and leached catalysts as functions of areal CUS concentrations. For the leached samples a direct linear dependence of the rates was observed for both reaction pathways, DDS and HYD, substantiating the absence of accessible, inactive NiS_x phase (i.e., they are located at inaccessible spaces as discussed earlier) that would distort the linearity. This suggests that the turnover frequency, based on total CUS, was identical for these samples, the one for DDS ($70\,h^{-1}$) being about a factor of 2 lower than for HYD ($140\,h^{-1}$). Similarly, CUS-normalized turnover frequencies were also estimated for the DDS and HYD routes over a sulfided $Ni-Mo/Al_2O_3$ catalyst (with a similar average slab length but a lower stacking degree than the bulk sulfides; see Table S4.5). The TOF of DDS was $97\,h^{-1}$, comparable to that obtained on bulk sulfides, whereas the TOF of HYD was only $9\,h^{-1}$, which was about 15 times smaller than that on bulk sulfides. The results suggest that the intrinsic catalytic activity of sites for DDS is rather insensitive to the variations in the geometric and electronic properties of the sulfide phase when changing the support (Al_2O_3 or the sulfide itself). In contrast, sites active for HYD appear to have a much greater structure sensitivity arising from support-induced variations in the ability to stabilize SH groups (originating from CUS) and the intrinsic activity of SH in mediating H-addition. We tentatively attribute this to the absence of Mo-O-Al linkages, leading to a higher polarity of metal-sulfur bonds and thus to an increased stability and concentration of SH groups. Apart from these considerations, it is worth noting that also differences in stacking likely contribute to the enhanced HYD activity of bulk sulfides.[20] In particular, it is expected that flat adsorption of DBT (via dispersive interactions with the π-aromatic system) is possible on the multilayered sulfides, while being at least unfavorable on monolayer-dominated $Ni-Mo/Al_2O_3$ (Table S4.5).

Unpromoted MoS_2 exhibited a significantly smaller areal concentration of CUS, consistent with its greater metal-sulfur bond strength ($>160\,kJ\,mol^{-1}$) than those in NiS_x ($<100\,kJ\,mol^{-1}$) and the Ni-Mo-S phase ($120–130\,kJ\,mol^{-1}$).[3] While the much higher activity of NiMo catalysts compared to that of MoS_2 is well documented in the literature on HDS, we notice here that the difference in the TOFs between non-promoted Mo sites and promoted sites was significantly smaller for the HYD pathway than for the DDS pathway (Figure 4.5 B and C). In this connection, we note that TOFs of hydrogenation of aromatics, e.g., biphenyl[41], decrease in a much less pronounced manner than TOFs of desulfurization reactions, with M-S bond energies increasing beyond the optimal values

(120–140 kJ mol^{-1}), i.e., going from Ni-MoS$_2$ to MoS$_2$. These observations seem compatible with the consideration that H-addition rates are jointly affected by M-S and S-H bond properties, in contrast to the rates of direct C-S cleavage that are mainly determined by the nature of M-S bonds.[3]

4.3 Conclusions

Acid treatment removes a large fraction of NiS_x from Ni-Mo sulfide catalysts, leading to highly active materials, whose activity depends solely on the concentration of active sites consisting of CUS and SH groups. While the majority of Ni after such treatment is incorporated in the Ni-Mo-S phase, a remaining fraction of NiS_x exists in the interior of secondary MoS_2 structures.

Unblocking of previously covered (sterically inaccessible) active sites and elimination of catalytically inert mass jointly increase HDS rates. After leaching, all Ni-Mo sulfides show the same TOF (CUS-normalized) for DDS and HYD (70 and 140 h^{-1}, respectively, at 330 $^{\circ}$C). The rate of the HYD pathway is significantly higher on bulk Ni-Mo sulfides than that observed on the Al_2O_3-supported catalyst, which showed much higher selectivity to DDS ($\sim 90\%$). The relative rates for the two pathways are not affected by acid treatment, implying that uncovered sites have the same properties as those accessible in the parent bulk sulfides. Strikingly, the DDS turnover frequencies were nearly identical for bulk and supported Ni-Mo sulfides. Therefore, we conclude that reaction pathways for DDS are insensitive to support effects.

However, the HYD turnover frequency on the CUS related active sites of bulk sulfides were more than an order of magnitude higher than that obtained for Al_2O_3-supported Ni-Mo sulfide catalysts. At present, we note two possible explanations for this unusually high rate. On one hand, the absence of sulfide-Al_2O_3 interactions leads to a lower averaged Sanderson electronegativity and a higher polarity of the metal-sulfur bonds, altering the bonding of the reactants and the stabilization of reactive intermediates as well as the concentration of SH groups. On the other hand, we would like to point to the substantial morphological differences, in particular, stacking degree, and their implications for reactant adsorption.

While these hypotheses require more investigations, the present study shows a promising guideline to maximize the catalytic activity in Ni-Mo-S based catalysts especially for the hydrogenation pathway, which is of central importance for the hydro-desulfurization of very heavy feedstocks.

4.4   Materials and methods

4.4.1   Catalyst preparation

Mixed metal oxide precursors were synthesized by hydrothermal reaction[15] of molybdenum(VI) oxide (MoO_3, *Sigma*, 99.5 %) and nickel(II) carbonate hydroxide tetrahydrate ($2 Ni(CO_3)_2 \cdot 3 Ni(OH)_2 \cdot 4 H_2O$, *Aldrich*, 45.0–52.5 % Ni) in a PTFE-lined, stainless steel autoclave of 80 mL volume. Mo oxide was suspended in 50 mL of deionized water followed by the addition of Ni carbonate. The following amounts of Mo oxide and Ni-carbonate were used for NiMo-1, NiMo-2, NiMo-3, and NiMo-4, respectively: 1.92 g and 0.82 g; 1.73 g and 0.98 g; 1.44 g and 1.22 g; 1.15 g and 1.47 g). After sealing the vessel, the reaction mixture was heated in a rotatory furnace (30 rpm) at a rate of about 10 °C min^{-1} to 175 °C and kept at this temperature for 17 h. The autoclave was cooled to room temperature in a water bath and the solid material separated by filtration. After drying at 120 °C (in air) for 12 h, the yellow-greenish precipitate was ground to a fine powder and pressed into pellets of 255–350 μm diameter.

For sulfidation, about 500 mg of oxidic precursor was mixed with 1.5 g of SiC (*ESK*, 63–90 μm) and placed in a glass-coated, stainless steel tubular reactor of 4 mm internal diameter. The material was then dried for 1 h at 120 °C (ramp: 1 °C min^{-1}) under nitrogen flow at ambient pressure (100 mL min^{-1} g$_{cat}$$^{-1}$). Subsequently, nitrogen was replaced by hydrogen (200 mL min^{-1} g$_{cat}$$^{-1}$) and the pressure increased to 2.0 MPa. At the same time, a solution of DMDS (dimethyl disulfide, *Aldrich*, 99 %) in decalin (*Merck*, 99 %), adjusted to contain 8 wt.% sulfur, was introduced into the reactor at a rate of 0.4 mL min^{-1} g$_{cat}$$^{-1}$ and maintained till the end of the sulfidation procedure. During sulfidation, temperature was increased from 120 to 250 °C at a rate of 1 °C min^{-1} and kept at this temperature for 4 h. This was followed by a final heating phase at 350 °C (1 °C min^{-1}) for 2 h. The gas/liquid flow and the pressure were maintained until the reactor was cooled to room temperature. The reactor was then successively purged with toluene, hexane, and nitrogen to fully remove any residues of the sulfidation feed. Finally, the sulfided catalyst pellets were separated by sieving and stored under nitrogen until use. Catalyst samples denoted as "parent" (suffix "-p") were not treated any further.

In addition to the mixed Ni-Mo sulfides, a MoS_2 and a Ni_3S_2 reference sample were included in the study. MoS_2 was prepared by dissolving 8.29 g of ammonium heptamolybdate tetrahydrate (($NH_4)_6Mo_7O_{24} \cdot 4\,H_2O$, *Merck,* "extra pure") in 40 mL water and adding 65 mL of aqueous ammonium sulfide solution (20–24 wt% ($NH_4)_2S$, *Aldrich,* 99 %). The mixture was stirred at 60 °C for 1 h and then cooled in ice for 3 h. The red crystals of ammonium tetrathiomolybdate (($NH_4)_2MoS_4$) were washed successively with cold water and cold acetone and then dried in ambient air over night at room temperature. The material was ground and pelletized to particles of 255–350 μm diameter. MoS_2 was obtained by subsequent heating in hydrogen (100 mL min^{-1} g^{-1}) to 400 °C at a rate of 3 K min^{-1} and holding this temperature for 4 h.

Ni_3S_2 was prepared by dissolving 10.9 g of Ni(II) nitrate hexahydrate ($Ni(NO_3)_2 \cdot 6\,H_2O$, *Alfa Aesar,* 99.9985 % (metals basis)) in 150 mL water and slowly (1.5 h) adding a solution of 6.00 g sodium sulfide nonahydrate ($Na_2S \cdot 9\,H_2O$, Aldrich, 99.99 % (metals basis)) in 150 mL water. The black precipitate was successively washed with water and acetone, dried overnight in vacuum and pelletized to particles of 255–350 μm diameter. To obtain Ni_3S_2, the material was first heated to 300 °C at a ramp rate of 3.3 °C min^{-1} in H_2S (10 % in H_2, 40 mL min^{-1} g^{-1}) and held at this temperature for 3 h. Then, the flow was changed to hydrogen (40 mL min^{-1} g^{-1}) and the temperature held for further 4 h before naturally cooling to room temperature.

For acid treatment, a portion of the parent sulfide, approximately 200 mg, was placed in a wide beaker and the pellets fully covered with about 10 mL of concentrated hydrochloric acid (*Fluka,* 37 %, fuming, trace analysis grade). After 1 h at room temperature, the greenish solution (colorless in the case of MoS_2) was decanted and discarded, before a new portion of HCl was added to the pellets. This procedure was repeated 3 times per sample. Subsequently, the pellets were washed several times with water, and finally, with acetone before being left to dry at room temperature in ambient air over night. Samples subjected to acid treatment are denoted as "leached" (suffix "-L").

4.4.2 Characterization

Elemental analysis of sulfided catalyst samples was performed by acidic digestion and subsequent photometric determination using a *Shimadzu UV-160* photometer (for Ni,

Mo). An *Elementar Vario EL* combustion analyzer was employed for CHNS analysis. Textural parameters were determined by nitrogen physisorption using an automated *PMI Sorptomatic 1990* instrument at liquid nitrogen temperature. The samples were outgassed in vacuum at 120 °C for 2 h prior to adsorption. Specific surface areas were obtained by applying BET theory on the adsorption branch of the isotherms.

X-ray diffraction (XRD) was performed on a *Philips X'Pert Pro* diffractometer in Bragg-Brentano geometry using Cu-Kα radiation (Kα_2/Kα_1 = 0.5) operating at 45 kV and 40 mA. XRD measurements were carried out using a rotating zero-diffraction plate (single crystal of Si cut in special orientation). The step size was fixed to 0.017 °θ with a dwell time of 115 ms per step. Crystallite sizes were determined using the Scherrer equation (see supplementary methods).

Scanning electron micrographs were obtained on a *JEOL JSM 7500F* instrument using secondary electron detection and operating at an acceleration voltage of 1.0 kV. Transmission electron microscopy was performed on a *JEOL JEM-2011* instrument at an acceleration voltage of 120 kV. Prior to analysis, the samples were suspended in absolute ethanol and dispersed ultrasonically before being deposited on a carbon coated copper mesh.

Hydrogen-deuterium isotopic exchange was carried out at 100 °C and ambient pressure in a fixed-bed reactor attached to a mass spectrometer. The catalyst pellets, typically 100 mg, were placed in a quartz tube of 4 mm inner diameter and then re-sulfided in a flow of H_2S (10 % in H_2, 100 mL min^{-1} g^{-1}) by heating to 320 °C (5 °C min^{-1}) and holding this temperature for 2 h. During this procedure, desorption of water (m/z = 18) was noticed but no measurable uptake of H_2S. After naturally cooling to room temperature, a 1:1 mixture of H_2 and D_2 in N_2 was introduced into the reactor at varying total flow rates, while the ratio of the reactants was kept constant (17 vol% H_2, 17 vol% D_2, balance: N_2). HD concentration was monitored using the signal at m/z = 3. Initial HD formation rate was calculated at conversions < 5 % (H_2 or D_2) according to the following equation:

$$r_{HD} = \chi_{HD} \cdot \frac{\dot{n}_{total}}{m_{cat}} \tag{4.1}$$

where χ is the molar fraction of HD, $\dot{n}_{total}$ is total molar flow to the reactor, and m_{cat} is the mass of the catalyst.

Nitric oxide chemisorption was carried out at ambient temperature and pressure following H_2-D_2 isotopic exchange experiments. While under constant He flow (100 mL min^{-1} g^{-1}), a pulse of NO (10 % in He) was dosed into the reactor every 30 min by an automated valve (24 pulses in total, 6.82 μmol of NO per pulse). Specific NO uptakes were calculated by subtracting each residual peak area (i.e., NO not adsorbed) from the averaged peak area after saturation with NO and adding up the differences. NO concentration was monitored using the signal at m/z = 30.

X-ray absorption spectra were collected at the *P65 XAFS* beamline at the *PETRA III* synchrotron light source at *DESY* (Hamburg, Germany). All data were recorded in fluorescence yield mode at the Ni K-edge at 8333 eV using an Si (111) monochromator. Energy alignment was performed by using a metallic Ni foil placed behind the sample and measured at the same time (in transmission mode). The sulfided catalyst was diluted with boron nitride and placed in a quartz capillary of 1 mm inner diameter. To ensure complete sulfidation of the catalysts' surface, the capillary was then heated from ambient temperature to 350 °C at a rate of 5 °C min^{-1} and held at this temperature for 1 h. A heated gas blower (*Oxford laboratories*) was used for this purpose. Prior to re-sulfidation the capillary with the catalyst was purged with He, after which the flow was changed to H_2S (10 % in H_2) and maintained during the whole procedure. The spectra (8133–8883 eV) were recorded after cooling down to 30 °C and purging with He. Four spectra were collected per sample, normalized to the absorption edge height, and averaged before further data treatment. Energy-dependent edge height normalization, merging of spectra, background subtraction, and self-absorption correction were done using built-in capabilities of the *ATHENA* software package.[42] Absorption edge height was determined as the difference of extrapolated pre-edge and post-edge intensities. The k^3-weighed spectra were then Fourier-transformed in the k-range 3–10.5 Å^{-1} (parent) or 3–12.4 Å^{-1} (leached) and multiplied with a window function to avoid cut-off effects (Hann function[43] of width 1 Å^{-1}). The EXAFS was fitted using the *ARTEMIS* software package[42] with included *IFFEFIT*[44] functionality. Further details of the fitting model are explained in detail in the supplementary methods.

4.4.3   Kinetic measurements

In a typical run, about 25 mg of sulfided catalyst pellets (parent or leached) were mixed with 1 g of SiC (63–90 μm) and placed in the tubular reactor described above. The reaction mixture was then fed to the reactor together with hydrogen at a total pressure of 5.0 MPa and a gas to liquid ratio of 500 (volumetric base). The liquid feed consisted of 1 wt% dibenzothiophene (DBT, *Aldrich*, 99 %) in decalin and 0.15 wt% of DMDS (= 1000 ppm S). In temperature variation experiments, the weight hourly space velocity (WHSV) was kept constant at 1.9 h^{-1}. Where necessary (contact time variation), the WHSV was changed by adjusting the flow rate of liquid and gaseous reactants, while keeping their ratio constant. After heating to reaction temperature (330 °C at 1 °C min^{-1}) the catalyst was stabilized for a period of 12 h, after which liquid samples were collected in periodic intervals (typically 3 samples per operating condition). The stability of the catalyst was verified by comparing the conversion at the beginning and at the end of one catalytic run at identical conditions.

Liquid reaction products were analyzed off-line in an *HP 6890* gas chromatograph equipped with a flame ionization detector and an *HP-1701* fused silica capillary column (14 % cyanopropyl-phenyl-methylpolysiloxane; 60 m × 250 μm × 0.25 μm). Quantification was performed by external calibration with solutions of reference compounds of known concentration. The carbon balance across the reactor was 97 % or better in the studied range of conversions (typically < 40 %). Conversion was calculated on the basis of reacted DBT according to the following equation:

$$X = \frac{c_{DBT}(inlet) - c_{DBT}(outlet)}{c_{DBT}(inlet)} \cdot 100 \text{ \%} \qquad (4.2)$$

where $\dot{n}_{DBT}$ is the molar flow of DBT at the reactor inlet and outlet, respectively. The selectivity for the DDS pathway was based on the BP product, while the selectivity for the HYD pathway was based on the sum of 4HDBT, CHB, and BCH. Selectivities were calculated as follows:

$$S_{DDS} = \frac{c_{BP}}{c_{BP} + c_{4HDBT} + c_{CHB} + c_{BCH}} \cdot 100 \text{ \%} \qquad (4.3)$$

$$S_{HYD} = \frac{c_{4HDBT} + c_{CHB} + c_{BCH}}{c_{BP} + c_{4HDBT} + c_{CHB} + c_{BCH}} \cdot 100 \text{ \%} \qquad (4.4)$$

where c_i is the concentration of the respective product at the outlet of the reactor. Rates were directly calculated from selectivity and conversion according to the following equations:

$$r_{DBT} = \frac{X}{100\,\%} \cdot \frac{\dot{n}_{DBT}(inlet)}{m_{cat}} \tag{4.5}$$

$$r_{DDS} = \frac{S_{DDS}}{100\,\%} \cdot \frac{X}{100\,\%} \cdot \frac{\dot{n}_{DBT}(inlet)}{m_{cat}} \tag{4.6}$$

$$r_{HYD} = \frac{S_{HYD}}{100\,\%} \cdot \frac{X}{100\,\%} \cdot \frac{\dot{n}_{DBT}(inlet)}{m_{cat}} \tag{4.7}$$

where X and S_i are the conversion and selectivity, respectively, $\dot{n}_{DBT}(inlet)$ is the molar flow of DBT at the reactor inlet, and m_{cat} is the catalyst mass. Note that the resulting rates are considered as initial rates, irrespective of conversion, because DBT consumption followed an apparent zero order dependence in DBT. Further, DDS and HYD selectivities were not dependent on conversion (see Figure S4.7).

4.5 Acknowledgements

4.6 References

(1)   Prins, R. *Hydrotreating*. In *Handbook of Heterogeneous Catalysis*, Ertl, G., Knözinger, H., Schüth, F., Weitkamp, J. Eds. Wiley-VCH: Weinheim, Germany **2008**, pp 2695-2718.

(2)   Topsøe, H.; Clausen, B. S.; Massoth, F. E. *Hydrotreating Catalysis*. In *Catalysis: Science and Technology*, Anderson, J. R., Boudart, M. Eds. Springer Berlin Heidelberg: Berlin, Heidelberg **1996**, pp 1-269.

(3)   Toulhoat, H.; Raybaud, P. *Catalysis by Transition Metal Sulphides: From Molecular Theory to Industrial Application*. Editions Technip: Paris **2013**, 832 pages.

(4)   Eijsbouts, S.; Heinerman, J. J. L.; Elzerman, H. J. W. *Appl. Catal. A Gen.* **1993,** 105, 69-82.

(5)   Eijsbouts, S.; Li, X.; Bergwerff, J.; Louwen, J.; Woning, L.; Loos, J. *Catal. Today* **2017,** 292, 38-50.

(6)   Albersberger, S.; Hein, J.; Schreiber, M. W.; Guerra, S.; Han, J.; Gutiérrez, O. Y.; Lercher, J. A. *Catal. Today* **2017,** 297, 344-355.

(7)   Bachelier, J.; Duchet, J.; Cornet, D. *Bull. Soc. Chim. Fr.* **1978,** I, 112-118.

(8)   Bachelier, J.; Duchet, J.; Cornet, D. *Bull. Soc. Chim. Fr.* **1979,** I, 221-228.

(9)   Bachelier, J.; Tilliette, M. J.; Duchet, J. C.; Cornet, D. *J. Catal.* **1984,** 87, 292-304.

(10)   Landau, M. V.; Nikulina, L. I.; Nefedov, B. K.; Slinkin, A. A. *React. Kinet. Catal. Lett.* **1984,** 25, 115-119.

(11)   Luo, W.; Shi, H.; Schachtl, E.; Gutierrez, O. Y.; Lercher, J. A. *Angew. Chem. Int. Ed. Engl.* **2018,** 57, 14555-14559.

(12)   Glemser, O.; Schwarzmann, E. *Kobalt, Nickel*. In *Handbuch der Präparativen Anorganischen Chemie*, Brauer, G. Ed. Enke Verlag: Stuttgart **1981**, pp 1659-1703.

(13)   Berzelius, J. J. *Ann. Phys.* **1826,** 82, 369-392.

(14)   Sanders, J. V.; Pratt, K. C. *J. Catal.* **1981,** 67, 331-347.

(15)   Eijsbouts, S.; Miseo, S.; Plantenga, F. L.; Soled, S. L. *Hydroprocessing using hydrothermally-prepared bulk multimetallic catalysts*. US 7,686,943 B2, **2010**.

(16)   Hein, J.; Hrabar, A.; Jentys, A.; Gutiérrez, O. Y.; Lercher, J. A. *ChemCatChem* **2014,** 6, 485-499.

(17)   Hein, J.; Gutiérrez, O. Y.; Albersberger, S.; Han, J.; Jentys, A.; Lercher, J. A. *ChemCatChem* **2017,** 9, 629-641.

(18)   Schachtl, E.; Zhong, L.; Kondratieva, E.; Hein, J.; Gutiérrez, O. Y.; Jentys, A.; Lercher, J. A. *ChemCatChem* **2015,** 7, 4118-4130.

(19)   Atuchin, V. V.; Gavrilova, T. A.; Kostrovsky, V. G.; Pokrovsky, L. D.; Troitskaia, I. B. *Inorg. Mater.* **2008,** 44, 622.

(20)   Garreau, F. B.; Toulhoat, H.; Kasztelan, S.; Paulus, R. *Polyhedron* **1986,** 5, 211-217.

(21)   Bouwens, S. M. A. M.; Koningsberger, D. C.; de Beer, V. H. J.; Louwers, S. P. A.; Prins, R. *Catal. Lett.* **1990,** 5, 273-283.

(22)   Hein, J.; Gutierrez, O. Y.; Schachtl, E.; Xu, P. H.; Browning, N. D.; Jentys, A.; Lercher, J. A. *ChemCatChem* **2015,** 7, 3692-3704.

(23)   Louwers, S. P. A.; Prins, R. *J. Catal.* **1992,** 133, 94-111.

(24)   Niemann, W.; Clausen, B. S.; Topsøe, H. *Catal. Lett.* **1990,** 4, 355-363.

(25) Topsøe, H.; Clausen, B. S.; Topsøe, N.-Y.; Pedersen, E.; Niemann, W.; Müller, A.; Bögge, H.; Lengeler, B. *J. Chem. Soc. Farad. Trans. 1* **1987,** 83, 2157-2167.

(26) Krebs, E.; Silvi, B.; Raybaud, P. *Catal. Today* **2008,** 130, 160-169.

(27) Krebs, E.; Daudin, A.; Raybaud, P. *Oil Gas Sci. Technol.* **2009,** 64, 707-718.

(28) Marchand, K.; Legens, C.; Guillaume, D.; Raybaud, P. *Oil Gas Sci. Technol.* **2009,** 64, 719-730.

(29) Houssenbay, S.; Kasztelan, S.; Toulhoat, H.; Bonnelle, J. P.; Grimblot, J. *J. Phys. Chem.* **1989,** 93, 7176-7180.

(30) Houalla, M.; Nag, N. K.; Sapre, A. V.; Broderick, D. H.; Gates, B. C. *AlChE J.* **1978,** 24, 1015-1021.

(31) Singhal, G. H.; Espino, R. L.; Sobel, J. E. *J. Catal.* **1981,** 67, 446-456.

(32) Girgis, M. J.; Gates, B. C. *Ind. Eng. Chem. Res.* **1991,** 30, 2021-2058.

(33) Wang, H.; Prins, R. *J. Catal.* **2009,** 264, 31-43.

(34) Egorova, M.; Prins, R. *J. Catal.* **2004,** 225, 417-427.

(35) Sun, Y.; Prins, R. *J. Catal.* **2009,** 267, 193-201.

(36) Daage, M.; Chianelli, R. R. *J. Catal.* **1994,** 149, 414-427.

(37) Topsøe, N. Y.; Topsøe, H. *J. Catal.* **1993,** 139, 641-651.

(38) Candia, R.; Clausen, B. S.; Topsøe, H. *Bull. Soc. Chim. Belg.* **1981,** 90, 1225-1232.

(39) Lauritsen, J. V.; Helveg, S.; Lægsgaard, E.; Stensgaard, I.; Clausen, B. S.; Topsøe, H.; Besenbacher, F. *J. Catal.* **2001,** 197, 1-5.

(40) Schachtl, E.; Kondratieva, E.; Gutiérrez, O. Y.; Lercher, J. A. *J. Phys. Chem. Lett.* **2015,** 6, 2929-2932.

(41) Luo, W.; Shi, H.; Schachtl, E.; Gutierrez, O. Y.; Lercher, J. A. *Angew. Chem. Int. Ed. Engl.* **2018**.

(42) Ravel, B.; Newville, M. *J. Synchrotron Radiat.* **2005,** 12, 537-541.

(43) Blackman, R. B.; Tukey, J. W. *Bell Syst. Tech. J.* **1958,** 37, 185-282.

(44) Newville, M. *J. Synchrotron Radiat.* **2001,** 8, 322-324.

(45) Zabinsky, S. I.; Rehr, J. J.; Ankudinov, A.; Albers, R. C.; Eller, M. J. *Phys. Rev. B* **1995,** 52, 2995-3009.

(46) Fleet, M. *Acta Crystallogr. C* **1987,** 43, 2255-2257.

(47) Søtofte, I. *Acta Chem. Scand.* **1976,** 30A, 157-162.

(48) Brillouin, L. *Science and Information Theory*. Academic Press: New York **1956**, 320 pages.

(49) Bevington, P. R.; Robinson, D. K. *Data Reduction and Error Analysis for the Physical Sciences*. McGraw-Hill: New York **1992**, 336 pages.

(50)   Ravel, B. *Quantitative EXAFS analysis*. In *X-Ray Absorption and X-Ray Emission Spectroscopy: Theory and Applications*, van Bokhoven, J., Lamberti, C. Eds. Wiley: **2016**, pp 281-302.

(51)   Peters, E. *Metall. Trans. B* **1976,** 7, 505-517.

(52)   Landau, M.; Agievskii, D.; Slinkin, A.; Kipnis, M.; Alekseenko, L.; Fedorovskaya, E.; Pavlova, L.; Kucherovat, T. *Kinet. Catal. (Engl. Transl.)* **1983,** 23, 815-823.

(53)   Gurvitsch, L. *J. Phys. Chem. (Moscow, Russ. Fed.)* **1915,** 47, 805-827.

(54)   Topsøe, N.-Y.; Topsøe, H. *J. Catal.* **1983,** 84, 386-401.

(55)   Silvy, R. P.; Delannay, F.; Grange, P.; Delmon, B. *Polyhedron* **1986,** 5, 195-198.

(56)   Agudo, A. L.; Gil Llambías, F. J.; Tascón, J. M. D.; Fierro, J. L. G. *Bull. Soc. Chim. Belg.* **1984,** 93, 719-726.

(57)   Topsøe, N.-Y.; Topsøe, H.; Sørensen, O.; Clausen, B. S.; Candia, R. *Bull. Soc. Chim. Belg.* **1984,** 93, 727-734.

(58)   Topsøe, N.-Y.; Tuxen, A.; Hinnemann, B.; Lauritsen, J. V.; Knudsen, K. G.; Besenbacher, F.; Topsøe, H. *J. Catal.* **2011,** 279, 337-351.

(59)   Caron, F.; Rivallan, M.; Humbert, S.; Daudin, A.; Bordiga, S.; Raybaud, P. *J. Catal.* **2018,** 361, 62-72.

(60)   Portela, L.; Grange, P.; Delmon, B. *Catal. Rev.* **1995,** 37, 699-731.

Note: References 44–60 refer to the supplementary materials (sections 4.7 to 4.9).

4.7   Supplementary methods

4.7.1   Calculation of mass loss

The simple comparison of elemental composition before and after acid treatment does not allow any conclusions about the loss of one specific component because calculating the "loss" requires a fixed point of reference: i.e., a component that is not affected by the treatment and may thus act as an internal standard. In this case, we normalized the atomic fractions of interest to the fraction of Mo because the amount of Mo does not change throughout the procedure. The refractory character of MoS_2 in acidic solution was verified by exposing MoS_2 to the same procedure as the Ni-Mo sulfide samples. During acid treatment of MoS_2 we did not observe anything indicating sulfide dissolution (i.e., coloration of the solution, gas evolution, mass loss). The loss of Ni and S with respect to the initial amount of Ni or S is calculated according to equations S4.1 and S4.2.

$$\Delta Ni = \left(1 - \left(\frac{\chi_{Ni}}{\chi_{Mo}}\right)_L \cdot \left(\frac{\chi_{Mo}}{\chi_{Ni}}\right)_p \right) \cdot 100 \; [\% \; Ni] \tag{S4.1}$$

$$\Delta S = \left(1 - \left(\frac{\chi_S}{\chi_{Mo}}\right)_L \cdot \left(\frac{\chi_{Mo}}{\chi_S}\right)_p \right) \cdot 100 \; [\% \; S] \tag{S4.2}$$

4.7.2   Approximate composition of Ni sulfides

Assuming an ideal stoichiometry of the MoS_2 phase, and assuming that Ni is exclusively present in segregated Ni sulfide phases, we estimate the atomic S/Ni ratio as follows:

$$S/Ni = (\chi_S - 2 \cdot \chi_{Mo})/\chi_{Ni} \tag{S4.3}$$

with:

ΔNi	loss of Ni relative to the initial amount of Ni	% Ni
ΔS	loss of S relative to the initial amount of S	% S
χ_i	atomic fraction of element i	mol mol^{-1}
p, L	indicates parent and leached samples	–

4.7.3   Particle (crystallite) size analysis via XRD and TEM

XRD line broadening analysis is performed by applying the Scherrer formula (eq. S4.4) to the (002) reflection of MoS_2, located at about $2\theta = 14°$. The resulting quantity $\bar{H}$ is the mean stacking height of the coherently scattering MoS_2 domains ("stacks"). In TEM, by comparison, a large number (j) of MoS_2 stacks are counted and the individual stacking heights H_i measured graphically and averaged (eq. S4.5). In both cases, the mean stacking degree $\bar{N}$ is calculated from the stacking height according to eq. S4.6, where 0.62 nm is the interlayer separation.

$$\bar{H}\,[nm] = \frac{K\,\lambda}{\beta\,\cos\theta} \tag{S4.4}$$

$$\bar{H}\,[nm] = \frac{\sum_i^j H_i}{j} \tag{S4.5}$$

$$\bar{N} = \frac{\bar{H}}{0.62\text{ nm}} + 1 \tag{S4.6}$$

with:

K Shape factor (= 0.9)

λ Wavelength of incident x-rays (0.15418 nm for Cu Kα)

β Line width at half maximum, corrected by instrumental line broadening (0.1 rad)

θ Diffraction angle (°)

4.7.4   EXAFS fitting model

Ni-S, Ni-Ni, and Ni-Mo single scattering paths used in the fitting procedure were calculated from crystallographic data using the *ARTEMIS* software package.[42] The built-in *FEFF6* program[45] was used to model Ni-S and Ni-Ni scattering paths from the Ni_9S_8 crystal structure.[46] Ni_9S_8 was preferred over other sulfide phases (Ni_3S_2, NiS) because it contains a variety of Ni-S subunits in different configurations and thus closely reflects the situation in the catalysts. To account for the eight different crystallographic positions of Ni in Ni_9S_8, we performed a so-called "aggregation" by running *FEFF* multiple times on the same input file (but each time for a different crystallographic position of the absorber). The Ni-Mo scattering path was modeled using the crystal structure of

$((C_6H_5)_4P)_2Ni(MoS_4)_2$, in which Ni is coordinated by four S atoms (square planar) at a distance of 2.23 Å and by two Mo atoms at a distance of 2.80 Å.[47]

Each scattering path in the fit used an independent variable for the coordination number, whereas some of the other parameters were set to be dependent upon each other. Energy shifts, for example, were allowed to vary from path to path but were set to be equal for all four catalysts in one group (i.e., parent group or leached group). A more severe restriction was applied to the Ni-Mo scattering path, which not only used a common ΔE_0 for all four leached catalysts, but also a common distance, and a common value for σ^2. This is a strong but reasonable limitation: while Ni atoms may be incorporated in more than one way (e.g., differently at sulfur and metal edges), the resulting local configurations are probably identical for a set of closely related catalysts. In other words, the local environment of a single Ni atom at a specific edge will look the same on two different catalysts and produce identical fitting parameters. This approach works well under condition that all included catalysts have a similar MoS_2 morphology and a similar distribution of Ni among crystallographically different sites. However, if one catalyst exhibits a distinct MoS_2 morphology, it could allow for additional local configurations of Ni that are not well represented in the other catalysts. In this case, the evaluated common parameters will not accurately represent the situation of this specific catalyst. We suspect this to be the case for NiMo-4-L because its Ni-Mo coordination number (0.9) falls out of the general trend (close to 2). This is supported by electron microscopy results, which show some unique structural features that were not observed in the other catalysts.

The discussed restrictions are a result of the limited information content of the data, which restricts the number of free variables. Spectral information was limited by the upper boundary of the useful k-range (10.5 Å^{-1} for parent, and 12.4 Å^{-1} for leached catalysts). Oscillations beyond this range were dominated by noise. The useful range for the reverse FT was limited to 1–3.2 Å as there were no contributions beyond this distance. With these limitations, about 2/3 of the available information were utilized for the fit (estimated using the Nyquist criterion[48]). The exact values are: 42 available independent points for the simultaneous fit of the parent catalysts, of which 26 ($= 62\,\%$) were used, and 53 available independent points for the simultaneous fit of the leached catalysts, of which 33 ($= 63\,\%$) were used. Fitting of reverse Fourier-transformed spectra ("q-space" fit) was done in terms of a conventional Levenberg-Marquardt non-linear minimization[49]

included in *ARTEMIS*. The fitting statistics are reported as a fractional misfit ("R-factor") between data and fit, calculated according to reference [50].

4.7.5 Calculation of the edge fraction

For a given MoS$_2$ stack, the edge fraction f_{Mo_e} is given by the ratio of Mo atoms exposed at edges (Mo_e) to the totality of Mo atoms (Mo) in that stack. Assuming a regular hexagonal geometry, it is sufficient to calculate f_{Mo_e} if the diameter (L) of the regular hexagon is known. The diameter L of the stacks is obtained by statistically evaluating such features in representative TEM micrographs. For convenience, the quantity n is introduced (eq. S4.7), which is derived from L and gives the number of Mo atoms residing along one side of the hexagon (Mo-Mo distance = 0.32 nm). If the calculation is performed for an ensemble of i stacks, the global edge fraction can be calculated according to eq. S4.8. (Note: for the sake of simplicity, we use plain element symbols, e.g., Ni or Mo, to refer to the number of atoms or moles of that element. An element symbol without an index indicates the total number of atoms/moles of that element.)

$$n_{Mo_e,i} = \frac{\left(\frac{L_i}{0.32\,nm}+1\right)}{2} \text{[Mo atoms]} \qquad (S4.7)$$

$$f_{Mo_e} = \frac{Mo_e}{Mo} = \frac{\sum_i(6n_i-6)}{\sum_i(3n_i^2-3n_i+1)} \text{ [at\%]} \qquad (S4.8)$$

4.7.6 Calculation of the maximum amount of Ni incorporated at edges

For a specific catalyst, the maximum number of Ni atoms that can be incorporated at the edges is given by the number of edge Mo atoms, i.e., $Ni_{e,max} = Mo_e = f_{Mo_e} \cdot Mo$, where Mo is the total number of Mo atoms in that catalyst. We compare this to the actual amount of Ni as determined by elemental analysis (c_{Ni}) according to equations S4.9 and S4.10.

$$c_{Ni} = \frac{Ni}{m_{cat}} \left[\frac{mol}{g}\right] \qquad (S4.9)$$

$$\frac{Ni}{Ni_{e,max}} = \frac{Ni}{Mo_e} = \frac{c_{Ni}}{f_{Mo_e} \cdot c_{Mo}} \text{ [at\%]} \qquad (S4.10)$$

4.7.7 Calculation of edge decoration

The term edge decoration (ED) refers to the degree of substitution of edge Mo atoms by Ni (eq. S4.11). Note that Mo_e stands for the total number of Mo at the edge in the absence of Ni.

$$ED = \frac{Ni_e}{Mo_e} \text{ [at\%]} \qquad\qquad (S4.11)$$

In practice, adsorption of probe molecules is used to quantify the areal concentration (number density) of edge atoms, meaning that only accessible surfaces are measurable whereas Ni and Mo atoms incorporated at the edges of inaccessible ("internal" or "buried") MoS$_2$ domains cannot be directly determined. Our approach to estimating the global edge decoration (i.e., on the surface and in the bulk) is based on the assumption that MoS$_2$ stacks at the accessible surface have the same degree of edge decoration as those in the bulk (that is, a globally homogeneous distribution of Ni). Further, we assume that the accessible stacks are randomly oriented. Under these assumptions, we may extrapolate the properties of the average MoS$_2$ stack (with known dimensions from TEM) to the whole catalyst.

From a geometric perspective, the fraction of edge area to total area (basal plane area + edge area) for the whole catalyst ($f_{edge\ area}$) can be calculated from the known dimensions of an ensemble of MoS$_2$ stacks, the shape of which is assumed as a regular hexagonal prism (eq. S4.12). The index e or $edge$ refers to edge planes and b to basal planes, whereas H_i is the height of one specific stack i and l_i its side length.

$$f_{edge\ area} = \frac{A_e}{A_e + A_b} = \frac{\sum_i (6 \cdot H_i \cdot l_i)}{\sum_i \left(6 \cdot H_i \cdot l_i + 2 \cdot \left(\frac{3}{2}\sqrt{3} \cdot l_i^2\right)\right)} \text{ [area-\%]} \qquad\qquad (S4.12)$$

As alluded to above, the fraction of edge area is assumed to be equal for accessible and inaccessible particles. Accessible surfaces are measured by N$_2$ sorption, i.e., SA_{BET} (in the unit of m^2 per g catalyst). Knowing this specific surface area and the fraction of edge area, we obtain the accessible edge area ($SA_{edge,acc.}$):

$$SA_{edge,acc.} = f_{edge\ area} \cdot SA_{BET} \left[\frac{\text{m}^2 \text{ edge}}{\text{g}_{cat}}\right] \qquad\qquad (S4.13)$$

We approximate the concentration of accessible edge-incorporated Ni atoms (c_{Ni_e}) via nitric oxide (NO) chemisorption, assuming selective adsorption of NO dimers on accessible edge-incorporated Ni atoms for the leached series (eq. S4.14). We discuss in a separate section to what extent this assumption can be considered as being valid (see discussions accompanying Table S4.4 and Table S4.6).

$$c_{Ni_e} = \frac{[NO]_{ads}}{2 \cdot m_{cat}} \left[\frac{mol}{g}\right] \tag{S4.14}$$

The areal number density of Mo at edge-related surfaces (ND_{Ni_e}, the number of Ni per surface area of edge, in the unit of mol per m^2 edge) can be calculated from the accessible edge area ($SA_{edge,acc.}$, eq. S4.13) and the above c_{Ni_e}:

$$ND_{Ni_e} = \frac{c_{Ni_e}}{SA_{edge,acc.}} \left[\frac{mol}{m^2 \, edge}\right] \tag{S4.15}$$

The resulting areal number density ND_{Ni_e} is valid across the whole catalyst, i.e., for the edge planes of MoS$_2$ stacks at the accessible surface and also for the edge planes of inaccessible MoS$_2$ stacks.

We now use geometric considerations to calculate the areal number density of Mo at edge-related surfaces (ND_{Mo_e}, the number of Mo per surface area of edge, in the unit of mol per m^2 edge). Specifically, this quantity is calculated from $A_{e,i}$ (edge area of stack i), l_i (side length of stack i), $n_{Mo_e,i}$ (number of Mo atoms residing along one side of the hexagon with side length l_i, see eq. S4.7), and N_i (stacking degree of stack i), all of which are obtained from TEM measurements:

$$ND_{Mo_e} = \frac{\sum_i \left(6 \cdot (n_{Mo_e,i} - 1) \cdot N_i\right)}{\sum_i A_{e,i}} = \frac{\sum_i \left(6 \cdot (n_{Mo_e,i} - 1) \cdot N_i\right)}{\sum_i (6 \cdot H_i \cdot l_i)} \left[\frac{mol}{m^2 edge}\right] \tag{S4.16}$$

Finally, we use the areal number density of Ni and Mo to calculate global ED:

$$ED = \frac{ND_{Ni_e}}{ND_{Mo_e}} \, [at\%] \tag{S4.17}$$

4.7.8 Calculation of the fraction of Ni incorporated at edges

With the global edge decoration known, one can now calculate how Ni is distributed among edges and segregated phases. The fraction of Ni incorporated at edges (accessible and inaccessible) is given by eq. S4.18, whereas the fraction of Ni present as NiS_x (internal) is calculated according to eq. S4.19.

$$\frac{Ni_e}{Ni} = \frac{f_{Mo_e} \cdot Mo \cdot ED}{Ni} \ [at\%] \tag{S4.18}$$

$$\frac{Ni_{NiSx}}{Ni} = 1 - \frac{Ni_e}{Ni} \ [at\%] \tag{S4.19}$$

4.7.9 Calculation of rate enhancement factors

Rate enhancement factors were calculated from experimental data by dividing the total HDS rate (i.e., sum of DDS and HYD) of one leached catalyst by the total HDS rate of its parent form (eq. S4.20). This was done separately for each reaction temperature (Figure S4.6) and the individual rate enhancement factors then averaged (eq. S4.21).

$$RE(T) = \frac{r_{HDS,p}(T)}{r_{HDS,L}(T)} \tag{S4.20}$$

$$RE = \frac{\sum_i RE(T)}{i} \tag{S4.21}$$

4.8 Supplementary figures

Figure S4.1. Pourbaix diagrams. (**A**) Ni-S-H$_2$O system and (**B**) Mo-S-H$_2$O system at standard ambient temperature and pressure (reproduced with permission from ref. [51]). Vertical axis: voltage potential with respect to the standard hydrogen electrode (SHE). (**C**) Leaching solutions of sequential acid treatments (photo credit: Manuel F. Wagenhofer, Technische Universität München).

Pourbaix diagrams, or potential/pH-diagrams, are used to map out predominant ions in solution depending on pH and electrochemical potential of the environment. Each area enclosed by a set of straight lines is labeled with the predominant species in this specific region, whereas the straight lines themselves indicate equal activities of the species to their left and right. Note that these diagrams are only valid in thermodynamic equilibrium and do not account for kinetic effects. While one species may be predominant under certain combinations of pH and potential, the transformation into this species might be very slow and thus practically not observable. Figure S4.1 A and B show the Pourbaix-diagrams of the systems Ni-S-H$_2$O and Mo-S-H$_2$O, respectively. The relevant conditions for acidic leaching with concentrated HCl as carried out in this work are found at 0 V (standard hydrogen electrode) and pH of -1.

As predicted by the Pourbaix-diagram (Figure S4.1), MoS_2 is stable in concentrated HCl and cannot be dissolved in the absence of a sufficient potential difference. Accordingly, the mass of a MoS_2 reference compound remained constant when subjected to HCl treatment at ambient temperature. Nickel sulfides, on the other hand, are easily and quantitatively dissolved under these conditions. The Pourbaix-diagram (Figure S4.1) shows that aqueous Ni^{2+} is the predominant species under the relevant conditions. The reaction is driven to completion by the formation of gaseous H_2S by-product, which is constantly removed from the solution. Landau et. al.[10,52] used a similar procedure to extract Ni from unsupported MoS_2. They added an amount of concentrated HCl (37 %) corresponding to 3 equivalents of Ni in the catalyst and left the mixture for 3 h at ambient temperature before washing with water. Another method was employed by Bachelier et. al.[7,8] for the extraction of Ni from Al_2O_3-supported Ni-Mo sulfides: while this group also used concentrated HCl (37 %) at ambient temperature, the duration of the treatment was 24 h. The proportion of HCl and Ni, however, was not specified. In our case, we used a large excess of concentrated HCl (37 %), about 10 mL for 200 mg of catalyst, which corresponds to approx. 200 equivalents of HCl per Ni atom. Further, we repeated the procedure three times (1 h each repetition) instead of only once to ensure full dissolution of extractable Ni species. The progress of Ni removal was roughly examined by monitoring the color of the acidic solution after each treatment (Figure S4.1 C). The gradual discoloration indicates that relevant concentrations of soluble Ni phases were absent after the third cycle.

Figure S4.2. X-ray diffraction patterns. **(A)** Diffractograms of Ni-promoted and non-promoted MoS_2 catalysts before acid treatment with reference patterns of identified NiS_x phases. **(B)** XRDs after acid treatment of the catalysts, with the stick pattern of MoS_2.

Parent | Leached

Figure S4.3. Supplementary SEM micrographs of the four Ni-MoS$_2$ catalysts.

Figure S4.4. EXAFS at the Ni K-edge. Each top row: magnitude (black) and imaginary part (grey) of the k^3-weighted Fourier-transform before leaching and after leaching including the best fit (dashed lines). Each bottom row: k^3-weighted EXAFS and best fit (dashed line) before and after leaching. The distance between two vertical tick marks is 5 Å^{-3} (k-space) and 5 Å^{-4} (R-space).

Figure S4.5. Residence-time dependent experiments. (**A**) DBT conversion on NiMo-2-L as a function of residence time at 330°C. (**B**) HYD and DDS selectivity as a function of DBT conversion under the same conditions (trickle-bed, 1 wt% DBT in decalin, total pressure: 50 bar (H_2)).

Figure S4.6. Rate enhancement factors. (**A**) RE factor as a function of reaction temperature (280–330 °C). The horizontal lines represent the average value for each catalyst. See supplementary methods for details on the calculation. (**B**) RE factor as a function of experimental mass loss. The dashed line represents a hypothetical rate enhancement function resulting solely from the loss of inert mass (calculated).

Figure S4.7. Temperature-dependence of reaction rates. (**A**) Initial dibenzothiophene hydrogenation (HYD) and direct desulfurization (DDS) rates on parent and leached Ni-MoS$_2$ catalysts as a function of inverse temperature (log. y-axis). Reaction conditions: trickle-bed reactor, 280–330 °C, 50 bar total pressure (H$_2$), 1 wt% DBT in decalin, gas/liquid ratio = 500 Nm³/Nm³, WHSV = 1. (**B**) Parity plot of activation energies before and after leaching. Data points are shown as intersecting error bars.

Figure S4.8. Correlation of HDS rates with isotopic exchange rates. Specific initial DDS rates (**A**) and HYD rates (**B**) as a function of H_2-D_2 isotopic exchange rate (IER) in parent and leached catalysts.

SH groups were characterized by measuring the rate of HD formation in an equimolar flow of H_2 and D_2 (referred to as isotopic exchange rate or IER). HDS rates and IERs correlated linearly in case of the leached catalysts (Figure S4.8) but not in case of the parent catalysts, in which IERs were essentially uniform, whereas HDS rates varied considerably. We have shown in a previous work that IER and SH group concentration are proportional in supported catalysts – at least in those with low to moderate Ni content[40] (atomic Ni/(Ni+Mo) ratios ≤ 0.33). Catalysts with higher concentrations of Ni and an accordingly higher concentration of segregated NiS_x were shown to deviate from this correlation[40] (observed for atomic Ni/(Ni+Mo) ratios ≥ 0.49). Since the parent catalysts in the present study fall within this second Ni-rich regime, their IERs do probably not well reflect their SH group concentration; it is thus not surprising that HDS rates, which directly depend on SH group concentration, do not seem to be connected to IER in this case. After leaching, however, when the available surface is free of segregated Ni sulfides, IERs can be expected to be proportional to SH group concentration. And since SH groups directly determine the surface concentration of dissociated hydrogen, IERs should also be proportional to catalytic HDS rates, which is in agreement with our observations.

We attribute the lack of proportionality between HDS rates and IERs prior to leaching to differences in the nature of the information provided by the two characterization techniques. Isotopic scrambling was performed at ambient pressure and a temperature of 100 °C, which is quite different from the reaction conditions used in HDS (50 bar, 280–330 °C). While Ni_3S_2 alone was only poorly active for H_2 activation in the H_2-D_2 regime

(< 0.1 mmol g^{-1} h^{-1}), it might contribute significantly to H$_2$ activation in the HDS regime. We speculate that the IERs of the parent catalysts reflect only "conventional" SH groups, i.e., those at the (un-)promoted MoS$_2$ edges, while ignoring hydrogen activation by segregated NiS$_x$ at more severe conditions (HDS regime). After leaching, this discrepancy disappears because the surface concentration of active hydrogen is only dependent on conventional SH groups and not additionally on NiS$_x$. The offset in the abscissa (Figure S4.8) may simply indicate that not all SH groups probed by H$_2$/D$_2$ are available also for HDS. This could be related to the fact that dibenzothiophene is much larger than hydrogen (or deuterium) and thus not able to interact with SH groups in confined environments.

4.9   Supplementary tables

Table S4.1. Physico-chemical characterization results.

Sample [a]	$\frac{Ni}{Ni+Mo}$	$\frac{S}{Ni+Mo}$	ΔNi [b]	Mo [c]	Ni [c]	S [c]	Surface area [d]	Pore volume [e]	Stacking (XRD) [f]	Stacking (TEM) [f]
	atomic	atomic	%	at%	at%	at%	$m^2\,g^{-1}$	$cm^3\,g^{-1}$	–	–
NiMo-1-p	0.48	1.44	–	21.3	19.7	59.0	3.1	0.003	5.0	4.4 (±1.4)
NiMo-2-p	0.50	1.61	–	19.3	19.0	61.7	2.7	0.003	5.0	5.0 (±1.8)
NiMo-3-p	0.49	1.52	–	20.2	19.6	60.3	8.1	0.014	4.9	5.0 (±1.8)
NiMo-4-p	0.60	1.43	–	16.3	24.9	58.8	17	0.036	5.2	4.7 (±1.9)
MoS$_2$-p	–	2.03	–	33.0	–	67.0	32	0.053	5.2	–
NiMo-1-L	0.20	1.83	73.2	28.3	7.0	64.6	7.3	0.010	5.0	4.9 (±1.9)
NiMo-2-L	0.23	1.82	69.4	27.2	8.2	64.6	6.9	0.014	4.8	5.1 (±1.7)
NiMo-3-L	0.22	2.03	70.5	25.7	7.3	67.0	14	0.027	5.2	4.6 (±1.6)
NiMo-4-L	0.26	1.93	77.2	25.3	8.8	65.9	14	0.035	5.5	5.3 (±2.1)
MoS$_2$-L	–	2.06	–	32.7	–	67.3	30	0.046	5.1	–

[a] Suffixes "-p" and "-L" denote parent and leached samples, respectively; [b] Percent of Ni atoms removed by acidic extraction. See supplementary methods for further details; [c] Atomic-% normalized to the sum of Mo, Ni, and S; [d] Determined via N_2 physisorption using BET method; [e] Total pore volume by Gurvitsch method[53] at $p/p_0 = 0.95$; [f] Stacking degree, i.e., average number of S-Mo-S layers per primary crystallite, determined via line broadening analysis of (002) reflection (see supplementary methods). Interplanar distance (Mo–Mo) was taken as 0.62 nm. Stacking from TEM data was determined by graphically analyzing approximately 300 primary particles per catalyst.

Table S4.2. Best-fit results of k³-weighted Ni K-edge EXAFS.

Coordination shell	Catalyst	N atoms	R Å	σ^2 10^3 Å²	ΔE_0 eV
Ni-S	NiMo-1-p	4.6 (± 0.4)	2.26 (± 0.01)	5.2 (± 1.2)	1.3 (± 0.7)
	NiMo-2-p	5.0 (± 1.2)	2.25 (± 0.01)	5.9 (± 3.0)	
	NiMo-3-p	4.6 (± 0.4)	2.26 (± 0.01)	5.6 (± 0.9)	
	NiMo-4-p	4.8 (± 0.5)	2.26 (± 0.01)	6.2 (± 1.3)	
	NiMo-1-L	4.6 (± 0.3)	2.22 (± 0.01)	5.5 (± 0.6)	-2.0 (± 0.6)
	NiMo-2-L	4.9 (± 0.3)	2.22 (± 0.01)	6.2 (± 0.6)	
	NiMo-3-L	4.8 (± 0.7)	2.22 (± 0.01)	6.7 (± 1.2)	
	NiMo-4-L	5.2 (± 0.4)	2.22 (± 0.01)	7.0 (± 0.7)	
Ni-Ni	NiMo-1-p	1.0 (± 0.5)	2.56 (± 0.02)	4.9 (± 4.4)	-0.2 (± 4.5)
	NiMo-2-p	1.0 (± 1.1)	2.56 (± 0.03)	3.6 (± 9.5)	
	NiMo-3-p	0.6 (± 0.2)	2.56 (± 0.02)	4.5 (± 2.7)	
	NiMo-4-p	0.8 (± 0.5)	2.57 (± 0.02)	4.4 (± 5.3)	
	NiMo-1-L	0.4 (± 0.2)	2.62 (± 0.03)	2.3 (± 3.8)	6.4 (± 6.1)
	NiMo-2-L	0.5 (± 0.3)	2.65 (± 0.03)	4.1 (± 4.1)	
	NiMo-3-L	0.8 (± 0.9)	2.63 (± 0.04)	7.8 (± 8.4)	
	NiMo-4-L	0.4 (± 0.3)	2.62 (± 0.03)	4.7 (± 4.5)	
Ni-Mo	NiMo-1-p	—	—	—	—
	NiMo-2-p	—	—	—	—
	NiMo-3-p	—	—	—	—
	NiMo-4-p	—	—	—	—
	NiMo-1-L	1.7 (± 0.6)	2.86 (± 0.03)	14.0 (± 4.0)	16.0 (± 2.2)
	NiMo-2-L	1.9 (± 1.0)			
	NiMo-3-L	2.0 (± 0.7)			
	NiMo-4-L	0.9 (± 0.5)			

Abbreviations: N (coordination number), R (distance), σ^2 (mean square displacement), ΔE_0 (energy shift, inner potential). Parent catalysts were fitted simultaneously with one common ΔE_0 for each coordination shell (R-factor = 0.0024). Leached catalysts were fitted simultaneously with one common ΔE_0 for each coordination shell, one common R_{Ni-Mo}, and one common σ^2_{Ni-Mo} (R-factor = 0.0031).

Ni-Mo coordination numbers of approximately 2 were observed in the first three of the leached catalysts (1.7–2.0, Table S4.2), which is fully consistent with the edge structure shown in Figure 4.2 C for the metal edge. In this structure, the Ni atom is "retracted" into the edge by about 0.35 Å with respect to the lattice position of the Mo atom it replaces. The distance to the two Mo neighbors at the bottom is thus decreased to 2.86 Å, while the distance to the left and right Mo neighbors increased to 3.18 Å. The Ni-Mo contributions of the more distant Mo atoms were not observed due to the strong structural disorder for the Mo atoms at longer distances and, therefore, only the two nearest Mo neighbors at 2.86 A contribute to the EXAFS. In addition, the contributions of backscattering atoms

decrease with $1/r^2$, which will further decrease their relative contributions compared to the two Mo atoms in closer distance. Note that the structural adjustments (shown in Figure 4.2 C for the metal edge), required to match the experimental Ni-S distances and coordination numbers, are small. The four S atoms at the base of the tetragonal NiS_5 pyramid need to move about 0.08 Å towards their common center and upwards by 0.03 Å (toward the tip of the pyramid). The original position of the S atoms within the MoS_2 lattice is indicated by the black shadows in Figure 4.2 C. Ni-Mo coordination numbers significantly smaller than 2, such as in NiMo-4-L (Table S4.2), suggest a different configuration at the edge. A potential structure with only one Mo atom at 2.86 Å is shown in Figure 4.2 C for the sulfur edge. The distortion of the four S atoms at the base of the Ni-S cluster is even smaller than at the metal edge. Based on DFT calculations, such Ni-Ni pairs were proposed and predicted to be stable by Krebs and coworkers.[26,27] Also, note that the dinuclear Ni entity at the sulfur edge closely resembles the main structural motif of NiS ("Millerite"). As pointed out above, such structure is hypothesized to partly account for the observed Ni-Ni scattering at 2.63 Å.

Table S4.3. Average interatomic distances and coordination numbers in relevant Ni sulfides.

Compound	S/Ni atomic	N_{Ni-S} [a] atoms	R_{Ni-S} [b] Å	N_{Ni-Ni} atoms	R_{Ni-Ni} Å	Ref. [c]
Ni_3S_2 [d]	0.67	3.9	2.27	3.9	2.52	This work
Ni_3S_2	0.67	4.0	2.26	4.0	2.48	27521
Ni_9S_8	0.89	4.4	2.27	2.2	2.60	63080
NiS	1.00	5.0	2.31	2.0	2.53	40054
NiS_2	2.00	6.0	2.39	12	4.01	79671

[a] Average Ni-S coordination number of all Ni-S pairs with similar separation (aggregation margin = 0.3 Å). [b] Average Ni-S distance (aggregation margin = 0.3 Å). [c] Inorganic Crystal Structure Database (ICSD) reference number. [d] Commercial Ni_3S_2 reference sample.

Table S4.4. Calculated quantities for the analysis of Ni distribution.

Catalyst	M_{edge}/M_{total} "Fraction of edge metal atoms"	Ni_{total}/M_{total}	Ni_{edge}/M_{edge} "Edge decoration"	Ni_{edge}/Ni_{total} "Ni incorporation"
NiMo-1-p	0.12	0.48	–	0.08
NiMo-2-p	0.09	0.50	–	0.08
NiMo-3-p	0.11	0.49	–	0.07
NiMo-4-p	0.08	0.60	–	0.10
NiMo-1-L	0.16	0.20	0.31	0.25
NiMo-2-L	0.15	0.23	0.43	0.29
NiMo-3-L	0.17	0.22	0.32	0.24
NiMo-4-L	0.13	0.26	0.78	0.40

Symbols: M_{total} = total number of metal atoms (Ni+Mo), Ni_{total} = total number of Ni atoms, M_{edge} = total number of metal atoms at edges (Ni+Mo), Ni_{edge} = number of Ni atoms at edges. The numbers reported in this table were obtained by the combined results of elemental analysis, NO chemisorption, and TEM (see section 4.7 "Supplementary methods" for further details).

For the purpose of determining edge decoration by Ni (Table S4.4), we simplistically assumed that all edge incorporated Ni atoms are titrated by NO, that is, all Ni atoms in the leached catalysts give rise to edge sites that interact with NO. This is inferred from the weakening of M-S bonds upon incorporation of Ni, leading to a higher propensity to form sulfur vacancies. In the leached Ni-MoS$_2$ catalysts, not containing accessible NiS$_x$, the amount of adsorbed NO can thus be directly used to quantify edge-incorporated Ni atoms (using a 2:1 stoichiometry of NO and CUS). We refer to Table S4.6 for an extended discussion of our complete set of assumptions and a description of some complicating aspects of using NO chemisorption for the quantification of edge sites.

Concerning the values tabulated above, please note the possibility of some corrections related to the co-titration of Ni- and Mo-associated sites by NO. Specifically, the edge decorations are likely to be overestimated to some extent because NO also adsorbs on edge vacancies not associated with Ni, whereas we related NO uptake solely to edge-incorporated Ni atoms (eq. S4.14). In the following, we estimate a lower limit of edge decoration (ED_{min}) by attempting to correct for NO adsorption on unpromoted sites. On unpromoted MoS$_2$, the areal number density of adsorbed NO (ND_{NO}) is measured to be 1.8 molecules per nm^2 edge area (Table S4.6). We now subtract this value from ND_{NO} of the Ni-MoS$_2$ catalysts as calculated from mass-specific NO uptake, BET and TEM

structural parameters (Table S4.6). This corrected ND_{NO}, now containing only contributions of Ni-associated sites, is then used for calculating the lower bound of edge decoration (ED_{min}) according to eq. S4.22:

$$ED_{min} = \frac{ND_{NO}(\text{NiMo-X-L}) - ND_{NO}(\text{MoS}_2)}{2 \cdot ND_{metal\ atoms}} \qquad \text{(S4.22)}$$

where $ND_{metal\ atoms}$ is the areal number density of metal atoms in an unperturbed edge plane (~6 metal atoms per nm² edge area; see also eq. S4.16) and the factor two is the stoichiometric coefficient relating the number of adsorbed NO to the number of edge metal (Ni) atoms. In the following we perform an exemplary calculation using eq. S4.22 for NiMo-1-L:

$$ED_{min} = \frac{3.7\left[\frac{\text{molec. NO}}{\text{nm}^2\ \text{edge area}}\right] - 2.0\left[\frac{\text{molec. NO}}{\text{nm}^2\ \text{edge area}}\right]}{2\left[\frac{\text{molec. NO}}{\text{edge metal atom}}\right] \cdot 6.0\left[\frac{\text{edge metal atoms}}{\text{nm}^2\ \text{edge area}}\right]} = 0.14$$

The lower bounds of ED for NiMo-1-L, -2-L, -3-L and 4-L are thus calculated to be 0.14, 0.25, 0.16 and 0.61 (in lieu of 0.31, 0.43, 0.32 and 0.78 as tabulated in Table S4.4).

In writing eq. S4.22, it is simplistically assumed that the unsubstituted edge domains and Ni-substituted edge domains each have their own independent areal number density of probed metal atoms, i.e., between 1.0 and max. ~6 per nm² edge area, respectively, while in reality, there will be an overlap for which we cannot correct. It is thus important to note that the real values of ED will be somewhere between the corrected (lower limit) and the uncorrected values (upper limit). At the lower bound of ED for each sample, the degree of Ni incorporation into edges (Ni_{edge}/Ni_{total} in the last column of Table S4.4) will become 0.03, 0.05, 0.04 and 0.08 for the four parent samples and 0.11, 0.17, 0.12 and 0.31 for the four leached samples in that order. As a result, at the lower bound of ED, our statement will have to be slightly corrected in quantitative terms: "The results suggest that 11–31 % of Ni atoms in the leached catalysts are incorporated in Ni-Mo-S (Table S4.4), while the remainder of 69–89 % exists as inaccessible NiS_x. The corresponding figures for the parent catalysts indicate a much lower incorporation of Ni, with only 3–8 % of all Ni atoms located at MoS_2 edges." It is important to stress that even at the lower bounds of ED, none of our conclusions is affected.

Table S4.5. Summary of key properties of Al_2O_3-supported MoS_2 and $Ni-MoS_2$ samples.

Sample	Ni/(Ni+Mo)	Slab length [a]	Stacking degree [a]	f_{Mo} [b]	NO_{ads} [c]	r_{HYD} [d]	r_{DDS} [d]
	(mol mol^{-1})	(nm)	(–)	(at./at.)	(µmol g^{-1})	(mmol g^{-1} h^{-1})	
Ni-MoS$_2$/Al$_2$O$_3$	0.33	4.5 ± 1.9	1.9 ± 0.9	0.26	298	0.86	9.28
MoS$_2$/Al$_2$O$_3$	–	5.2 ± 2.2	1.5 ± 0.7	0.22	151	n.d.	n.d.

[a] All slab properties are determined by statistical analysis of TEM micrographs. [b] f_{Mo} represents the fraction of Mo atoms at the edges of the sulfide slab, calculated by assuming a perfect hexagonal geometry for the MoS$_2$ crystals. [c] NO adsorption measured by pulse experiments at RT. [d] Reaction conditions: 330 °C, 50 bar H$_2$, 1 wt% DBT in decalin, gas/liquid = 500 Nm³/Nm³. Further details on this sample are given in our previous work[18]. "n.d.": not determined.

To compare the intrinsic activity (TOF) of bulk Ni-Mo sulfides in this work with that of Al$_2$O$_3$-supported Ni-MoS$_2$, we selected a well-characterized sample whose properties (Table S4.5) had been reported in our previous work.[18] With regard to active site quantification via NO adsorption, the same considerations apply for this supported sample as those described for the bulk sulfides (see discussion accompanying Table S4.6). While known to be significantly less active than Ni-promoted edge sites, it is expected that Mo-associated edge sites contributed significantly to the site count determined from adsorbed NO for the Ni-MoS$_2$/Al$_2$O$_3$ catalyst. We infer this from the substantial concentration of adsorbed NO on an unpromoted but otherwise similar, supported MoS$_2$ catalyst (151 µmol/g; Table S4.5). In order not to underestimate the TOFs of the promoted sample by falsely including the Mo-associated CUS in the site count, we attempted to correct for NO adsorption on these essentially inactive sites. For the correction, it is hypothesized that the relative fraction of Ni- and Mo-associated CUS scales with the relative concentrations of Ni and Mo at the slab edge, that is, no difference in the actual capability for CUS generation is taken into account (in reality, there is likely a difference due to the weakening effect of Ni on edge Mo-S bonds, causing a higher propensity for vacancy formation; see discussion accompanying Table S4.4). The mass-specific NO uptake of the promoted Ni-Mo sample (298 µmol/g) was thus corrected by subtracting the contribution of Mo-associated NO adsorption (151 µmol/g). The latter was scaled by the relative fraction of Mo atoms found at the edges of the promoted sample. Because the edge decoration degree (by Ni) was determined to be 0.30 in this sample,[18] leaving a fraction of 0.70 as Mo-associated sites, the concentration of NO adsorbed on Ni-associated CUS in this sample is estimated to be:

$$(298 - 0.7 \cdot 150)\ \mu mol/g = 192\ \mu mol/g.$$

When calculating the CUS concentration, it was assumed that NO adsorbs on Ni-associated and Mo-associated CUS with the same 2:1 NO-to-Mo_{CUS} (Ni_{CUS}) stoichiometry. Thus, the Ni-associated CUS was determined to be:

$$(192 \cdot 0.5)\ \mu mol/g = 96\ \mu mol/g.$$

The TOF based on this CUS count was calculated to be 9 h^{-1} and 97 h^{-1} for the HYD and DDS route, respectively, using the rates presented in Table S4.5.

Table S4.6. NO chemisorption capacity.

Catalyst	NO uptake [a] (µmol g^{-1})	CUS conc. (µmol g^{-1})	NO areal density [b] (µmol m^{-2} total)	CUS areal density (µmol m^{-2} total)	NO areal num. density [c] (molec. nm^{-2} edge)	CUS areal num. density (sites nm^{-2} edge)
NiMo-1-p	20	10	6.3	3.2	n.a.	n.a.
NiMo-2-p	32	16	11.6	5.8	n.a.	n.a.
NiMo-3-p	48	24	5.9	3.0	n.a.	n.a.
NiMo-4-p	74	37	4.3	2.2	n.a.	n.a.
NiMo-1-L	23	12	3.2	1.6	3.7	1.8
NiMo-2-L	30	15	4.3	2.2	5.0	2.5
NiMo-3-L	47	24	3.3	1.7	4.0	2.0
NiMo-4-L	108	54	7.6	3.8	9.2	4.6
MoS$_2$-L	53	27	1.8	0.9	2.0	1.0

[a] Determined by pulsed NO chemisorption at 25 °C and atmospheric pressure. [b] NO uptake divided by the specific (BET) surface area of the catalyst as determined by nitrogen physisorption. [c] Areal number density of NO at edge planes (molecules NO per nm² edge area) as determined by a combination of TEM, BET, and NO pulsing (see supplementary methods). Notes: (1) All CUS-related quantities were calculated from the respective NO-related quantity by multiplying with 0.5 (i.e., assuming dinitrosly adsorption). (2) "n.a.": not applicable to parent catalysts, as NO adsorption occurred also on segregated NiS$_x$, where edges are not defined. (3) In the context of determining edge decoration (Table S4.4), the concentration (or areal density) of CUS is taken to be equivalent with the concentration (or areal density) of edge-incorporated Ni. We refer to Table S4.4 for further information on this aspect of NO chemisorption.

NO adsorbs at the unpromoted and promoted MoS$_2$ edges but not on fully sulfided edges not containing SH, nor on basal planes.[54-59] This reasonably site-specific behavior, despite somewhat controversial, has its undeniable usefulness and has been studied in depth, mostly for unpromoted and Co-promoted MoS$_2$.[58,59] Some studies argued that the adsorption occurs via a push-pull type mechanism involving simultaneous vacancy creation (initially present as SH), adsorption of NO and release of H$_2$S.[58] This, in turn, means that NO is capable of probing both stable CUS (existing prior to adsorption) and SH groups, the latter by reactive NO/SH exchange involving the transient formation of CUS. In this context, "CUS" are meant to include SH groups unless otherwise specified.

As for the assumption of selective NO adsorption (i.e., adsorption exclusively on Ni-associated CUS), we would like to mention that metal-sulfur bonds are significantly weakened (compared to Mo-S) upon the substitution of Ni atoms into the slab edge. Accordingly, a dominant fraction of NO adsorption should take place at CUS (and SH groups) associated with Ni edge atoms. Moreover, our data show that while NO adsorbs also on unpromoted edge sites (2.0 molec. per nm² edge), Ni substitution dramatically

increases the tendency to generate edge vacancies in the form of stable and transient CUS, thus increasing the areal number density to 3.7–9.2 molec. per nm² edge (Table S4.6). Also bear in mind that the contribution of unpromoted Mo edge sites to total NO uptakes is diminished due to the fact that fewer Mo atoms will be present at the edge after Ni incorporation. Because of the expected low concentration of Mo-associated edge sites and the stronger tendency of Ni-associated edge sites to form vacancies, we used the simplified assumption that adsorbed NO mainly corresponds to Ni-associated edge sites. Of course, this is only valid for Ni-promoted samples after leaching, that is, when segregated Ni sulfides are absent at the accessible surface.

Concerning the use of dinitrosyl adsorption stoichiometry in our calculations (i.e., the adsorption of two NO molecules per CUS), we would like to point to previous works,[58,59] where such stoichiometry was observed experimentally. It was proposed that the mutual interaction between the unpaired electrons of two NO molecules helps the stabilization of the dimer or dinitrosyl form at high NO coverages.[60] In view of some complications associated with its adsorption sites and stoichiometry,[21,23,25] NO chemisorption studies are often performed in combination with infrared or Raman spectroscopy, which allow isolating the relevant interactions. Given the high opacity of bulk sulfides, however, this is highly challenging (if not practically impossible). In such cases, one may only determine the total NO uptake, which includes the contributions of the confounding NiS_x species (a substantial NO uptake of 57 μmol g^{-1} was measured on a homemade Ni_3S_2 sample). Removing segregated NiS_x at the accessible surface is thus expected to substantially improve the validity of using NO chemisorption measurements to quantify CUS concentration.

With regard to the CUS counts used to calculate TOFs of the bulk sulfide samples, we see a possibility for some corrections related to the simultaneous titration of Ni- and Mo-associated vacancies by NO. Even though the latter are significantly less active than the former, it is unquestionable that some contribution of Mo-associated CUS to both the site count and the catalytic rates exists. This should be particularly important for the HYD pathway, for which MoS_2 alone apparently has a non-negligible activity (Table 4.1 and Figure 4.5 in the main text). Although it is not possible to quantitatively single out the individual contributions of NO adsorbed on Ni- and Mo-associated CUS from any direct measurements (due to the lack of spectroscopic differentiations as outlined above), we

attempted to do so by assuming that the relative fractions of Ni- and Mo-associated CUS scale with the relative atomic fractions of Ni and Mo at the slab edge, i.e., without taking into account any difference in the CUS generation capability. From the edge decoration (ED) degree by Ni in the sulfide samples (Table S4.4), the remaining non-promoted (i.e., Mo-associated) edge fraction can be calculated as $1 - ED$. This relative fraction, representing the unpromoted edge sites, is then multiplied with the intrinsic activity (mmol/(m^2 h)) and CUS areal density (mmol/m²) of unpromoted MoS_2, and subsequently subtracted from the corresponding quantities of each Ni-Mo sulfide. It must be noted that this correction method does not degrade the linear correlations or significantly change the average TOFs derived from the slope of the correlation plot. Accordingly, none of our conclusions are affected. We attribute this insensitivity to the small areal concentration of CUS and area-normalized reaction rates found in MoS_2 (used for the correction) compared to those of the Ni-MoS_2 catalysts. Due to some of the unjustified assumptions involved in this calculation, however, we chose to report still the average TOF slightly convoluted by the Mo-CUS contributions, that is, 70 h⁻¹ for DDS and 140 h⁻¹ for HYD, instead of the "corrected" values of 75 h⁻¹ and 146 h⁻¹.

5 Carbon-carbon bond scission pathways in the deoxygenation of fatty acids on transition-metal sulfides
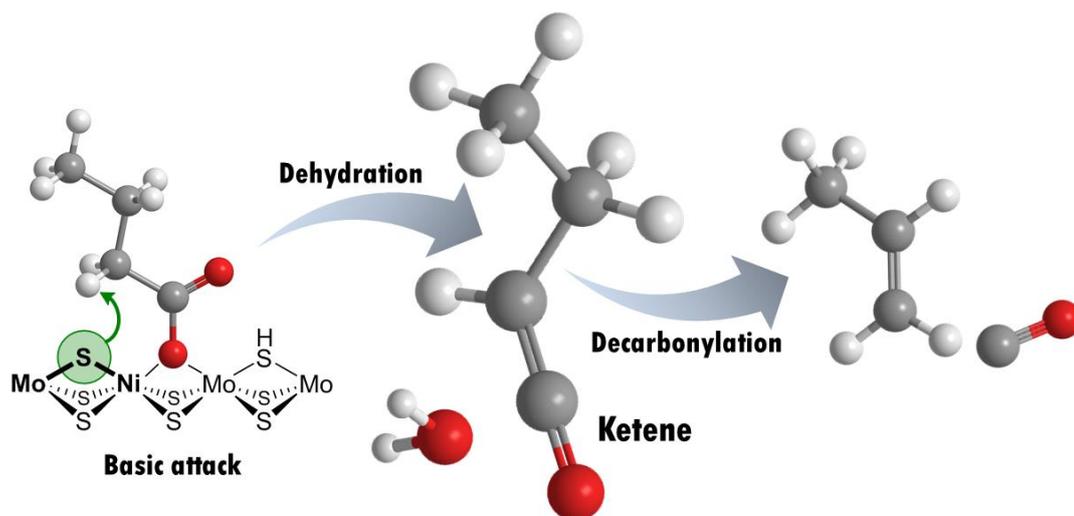
This work has been published

Reprinted with permission from: Wagenhofer, M. F.; Baráth, E.; Gutiérrez, O. Y.; Lercher, J. A. *ACS Catalysis* **2017**, 7, 1068-1076. DOI: 10.1021/acscatal.6b02753

Copyright 2017 *American Chemical Society*.

Abstract

The mechanism of the deoxygenation of fatty acids on transition-metal sulfides was determined on the basis of kinetic data obtained with fatty acids, their reaction intermediates (aldehyde and alcohol), and reactants of restricted reactivity (adamantanyl-substituted carboxylic acids). Deoxygenation on MoS_2 proceeds exclusively via hydrogenolysis to aldehyde, followed by hydrogenation to the corresponding alcohol, consecutive dehydration to the olefin, and hydrogenation to the alkane. In contrast, the selectivity on Ni-MoS_2 and on Ni_3S_2 substantially shifts toward carbon oxide elimination routes: i.e., direct production of C_{n-1} olefins and alkanes. The carbon losses occur by decarbonylation of a ketene intermediate, which forms only on sites associated with Ni. The rate determining steps are the cleavage of the C−C bond and the removal of oxygen from the surface below and above, respectively, 2.5 MPa of H_2. The different reaction pathways catalyzed by MoS_2 and Ni-MoS_2 are attributed to a preferred deprotonation of a surface acyl intermediate formed upon the adsorption of the fatty acid on Ni-MoS_2. The shift in mechanism is concluded to originate from the higher basicity of sulfur induced by nickel.

5.1   Introduction

Research on alternative sources for hydrocarbon fuels has gained importance over the past decades.[1] As legislations impose the use of bio-oil to obtain transportation fuels, the coprocessing of vegetable oils in conventional hydrotreating units is a promising option since it relies on existing infrastructure and technologies.[2–4] Sulfides are the catalyst of choice for defunctionalization reactions in industrial hydrotreating units due to their optimum compromise among cost, metal functionality, and poison and coke resistance.[3,5–7] To fully exploit the potential of hydrotreating biogenic feedstocks on sulfides, however, one has to consider possible limitations arising due to their oxygen content. Although the presence of S during cofeeding would help to stabilize sulfide catalysts,[8,9] the detrimental effects of water on catalyst stability and excessive consumption of hydrogen due to subsequent reactions with carbon oxides are among the most imminent problems.[6,10–12] Several studies have therefore tried to elucidate the mechanisms of triglyceride deoxygenation (DO) on transition-metal sulfides.[4,13–21] The motivation behind these investigations is to obtain structure—activity correlations, which may aid in the development of future generations of hydrotreating catalysts.

Deoxygenation of triglycerides and related compounds can be divided into two distinct pathways.[22] One pathway is hydrodeoxygenation (HDO), which is characterized by the sequential reduction of the oxygenate to a saturated hydrocarbon, with oxygen being removed as water and the number of carbon atoms being retained throughout the whole reaction sequence. In the other pathway oxygen is removed in the form of carbon oxides, thus decreasing the number of carbon atoms of the reactant. The term "carbon loss reactions" (CLR) will be used here to refer to these pathways. HDO and CLR pathways occur not only with triglyceride reactants but also with structurally related molecules, such as free fatty acids and fatty acid alkyl esters, that have been employed as model compounds in a large fraction of existing DO studies.[13,14,16,23–25] Fatty acids have been chosen as reactants, as they were repeatedly shown to be the major primary products during triglyceride DO over most supported metal and metal sulfide catalysts.[26] An overview of deoxygenation-related reactions occurring with fatty acids is given in Table 5.1. All possibilities have negative free energies at relevant reaction temperatures. Thus, although the thermodynamic driving force has to be taken into account, it is likely that

kinetics and the intrinsic functionality of the catalyst determine the routes dominating the transformation of fatty acids.

Table 5.1. Overview of possible reactions occurring during fatty acid deoxygenation. [a]

Entry	Reaction	Structural representation	$\Delta_r G°$ (273 K) kJ mol^{-1}	$\Delta_r G°$ (573 K) [b] kJ mol^{-1}
1	Direct decarboxylation	$R\text{—}C(=O)OH \rightarrow R\text{—} + CO_2$	-60.4	-96.4
2	Dehydration-decarbonylation	$R\text{—}C(=O)OH \rightarrow R\text{=} + CO + H_2O$	58.7	-29.0
3	Aldehyde decarbonylation	$R\text{—}C(=O)H \rightarrow R\text{—} + CO$	-39.0	-76.0
4	Hydro-decarboxylation	$R\text{—}C(=O)OH \xrightarrow{H_2} R\text{—} + [HCO_2H]$	-28.7 [c]	-9.9 [c]
		$R\text{—}C(=O)OH \xrightarrow{H_2} R\text{—} + CO + H_2O$	-30.8 [d]	-78.7 [d]
5	Full hydrodeoxygenation	$R\text{—}C(=O)OH \xrightarrow{3 H_2} R\text{—} + 2 H_2O$	-121.5	-98.2
6	Partial hydrodeoxygenation	$R\text{—}C(=O)OH \xrightarrow{H_2} R\text{—}C(=O)H + H_2O$	8.3	-2.8
7	Reverse hydroformylation	$R\text{—}C(=O)H \rightarrow R\text{=} + CO + H_2$	50.4	-26.3

[a] Thermodynamic data calculated at 10^5 Pa using gaseous C_4/C_3 compounds (HSC Chemistry 6 software). [b] Values of $\Delta_r G°$ are expected to be similar in liquid and gas phase because of the absence of phase transitions and the similar structure of reactants and products. [c] Value is given for the formation of 0.5 equivalents of H-bonded formic acid dimer. [d] Change in Gibbs energy, when decomposition of formic acid dimer into carbon monoxide and water is taken into account.

The catalysts studied are unsupported MoS_2, some modified with Ni to maximize the hydrogenation activity. The significant influence of Ni on the activity of MoS_2 for hydro-desulfurization (HDS) and hydrodenitrogenation (HDN) is often attributed to changes in the adsorption constants of the reacting substrates or to higher rate constants, rather than to changes in the reaction mechanism.[27] In HDS, for example, Ni influences the electron density of sites at the perimeter of MoS_2,[28] possibly shifting the rate-determining step. In deoxygenation, however, the result of Ni incorporation is quite different; while the rate enhancements are not as pronounced as those observed in HDS and HDN, the changes in selectivity are radical. More specifically, Ni enables additional reaction routes that involve the breaking of C−C bonds (CLR) and that are not observed with MoS_2.[4]

Since a consistent molecular-level mechanism for CLR of triglyceride-related molecules on transition-metal sulfides has not been identified, we have chosen to evaluate existing proposals and consider reaction routes that have previously not been taken into

account. Proposed mechanisms for the CLR of triglyceride-related feedstock (Table 5.1) include decarboxylation,[3,21,29−34] decarbonylation of aldehyde intermediates,[13,19,33,35−38] sequential dehydration−decarbonylation,[14] formic acid elimination,[16,39,40] and decarbonylation of anhydride intermediates.[33,41] Among these proposals only a few have been studied in connection with sulfide catalysts.[3,13,14,19,21] The present study thus aims to improve the current mechanistic understanding of both HDO and particularly carbon loss reactions of fatty acids on transition-metal sulfides. It is limited to unsupported catalysts to eliminate potential interferences of a support, which are known to influence both the properties of metal sulfides[42−44] and the pathways of fatty acid deoxygenation.[45] The focus is on Ni-promoted MoS_2, while Ni_3S_2 and MoS_2 are included as reference materials. For the sake of brevity, experimental details and physicochemical properties of the catalysts are presented in sections 5.6.1 and 5.6.2 in the Supporting Information.

5.2　　Results and discussion

5.2.1　　Reaction network of hexadecanoic acid deoxygenation

The reaction network of hexadecanoic acid deoxygenation on bulk MoS_2 catalysts is outlined in Scheme 5.1 Depending on the catalyst, the prevalent reaction route is either hydrodeoxygenation or decarbonylation (DCO), leading to hexadecane (route **1**) and pentadecane (routes **2** and **3**), respectively. The main products on MoS_2 are hydrocarbons of the C_{16} fraction, containing n-hexadecane as well as a mixture of hexadecene isomers. The concentration profiles obtained on this highly selective HDO catalyst (Figure 5.1) suggest a cascade reaction for HDO. It starts with the formation of aldehyde via C−O hydrogenolysis, releasing one molecule of water from the fatty acid and forming hexadecanal as the main primary product. Subsequent hydrogenation of the aldehyde yields hexadecanol, which is in turn converted to hexadecenes and hexadecane.
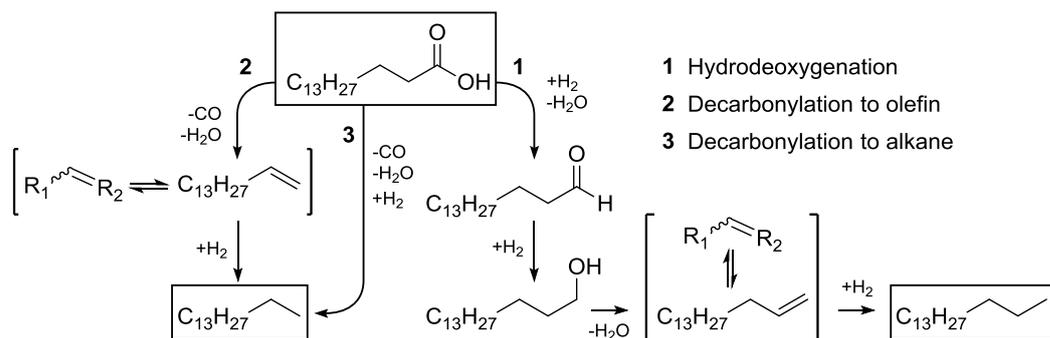
Scheme 5.1. Proposed reaction network of hexadecanoic acid deoxygenation on bulk MoS_2-based catalysts. Ester formation between fatty acid and alcohol is not included in the scheme because it occurred only as a minor side reaction under the tested conditions. Due to the high dilution of the reactant (0.02 M), bimolecular reactions are strongly disfavored.

The prevalence of hexadecenes over hexadecane during the first 2 h of the experiment (Figure 5.1) indicates that dehydration to 1-hexadecene and subsequent hydrogenation to hexadecane is the major pathway for alcohol conversion. Substantiating this conclusion, we noted that the molar fractions of 1-hexadecene in the hexadecene pool were substantially higher (slowly decreasing from an initial 50 % to equilibrium) than those corresponding to an equilibrated mixture of hexadecenes at reaction temperature (Figure S5.3 in the Supporting Information). This is consistent with a dehydration mechanism in

which 1-hexadecene is continuously supplied to the hexadecene pool by dehydration of hexadecanol. In turn, the observed accumulation of hexadecenes agrees well with the low initial rate of olefin hydrogenation measured in a separate experiment in comparison to the global initial rate of hexadecanoic acid consumption (17.9 and 48.3 mmol $g^{-1} h^{-1}$, respectively). While direct hydrogenolysis of the C−O bond cannot be ruled out, hexadecanol conversion should not proceed via the nucleophilic substitution of the OH group by a surface SH group (followed by hydrodesulfurization of the resulting thiol),[15] because thiols or other sulfur-containing products were not observed. This indicates also that sulfur leaching from the catalyst did not occur to a significant extent. We wish to point out that the catalysts were stable on the time scale of the experiments: i.e., catalyst deactivation (by sulfur leaching, coking, or other mechanisms) was not observed (see also section 5.6.10 in the supporting information for a more detailed discussion of this issue).

The Ni-promoted catalyst showed a selectivity of 43.5 % toward C_{15} hydrocarbons (Figure 5.2), while MoS_2 was highly selective for the HDO route (94.3 %). The initial rate of hexadecanoic acid consumption on Ni-MoS_2 (51.8 mmol $g^{-1} h^{-1}$) was slightly higher than that on MoS_2 (48.3 mmol $g^{-1} h^{-1}$). At the same time, the olefin concentration was much lower on Ni-MoS_2 than on MoS_2, with maximum values of 6 % and 46 %, respectively. In a separate experiment, the initial rate of olefin hydrogenation on Ni-MoS_2 was about 15 times higher (260 mmol $g^{-1} h^{-1}$) than that on MoS_2 (Figure S5.4 in the Supporting Information). This indicates that the low olefin concentration observed with Ni-MoS_2 is caused by the significant enhancement of hydrogenation rates in the presence of Ni. Hexadecanoic acid conversion on Ni_3S_2 resulted in C_{15} hydrocarbons accounting for approximately 95 % of the products, whereas C_{16} hydrocarbons were observed as minor side products (Figure 5.3). Ni_3S_2 also converted hexadecanoic acid with a much lower initial specific rate (7.0 mmol $g^{-1} h^{-1}$) than MoS_2 and Ni-MoS_2, mainly due to its considerably lower specific surface area (Table S5.1 in the Supporting Information). We reached this conclusion after normalizing the initial rates to the surface area, which showed that the conversion proceeds at similar rates on Ni_3S_2 and MoS_2 per unit of exposed surface area (Table 5.2). Although we cannot quantify the surface density of active sites on MoS_2 and Ni_2S_3, the distinct product distributions clearly show the different catalytic behaviors.
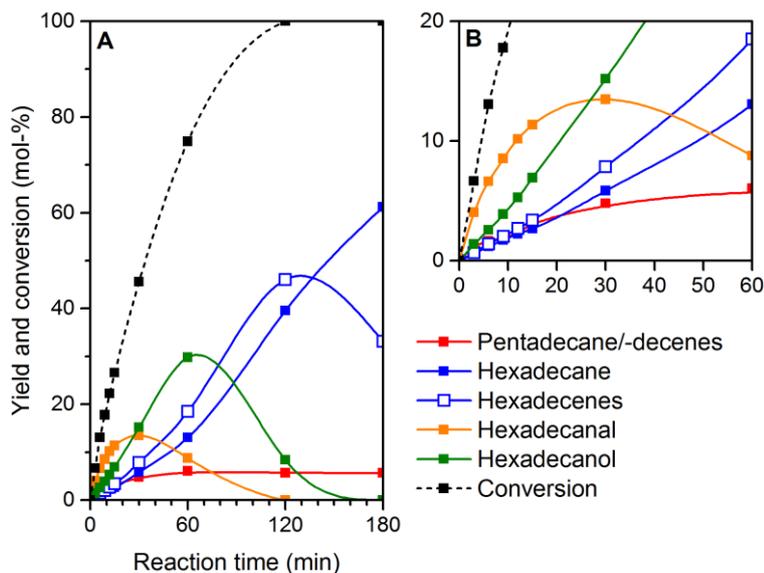
Figure 5.1. Conversion of hexadecanoic acid and yields of products as a function of reaction time on MoS$_2$ (**A**) and an enlarged representation of the initial region (**B**). Reaction conditions: batch reactor, 573 K, 5.0 MPa of H$_2$, catalyst (powder, 0.50 g L^{-1}), hexadecanoic acid (5.0 g L^{-1}), solvent (*n*-dodecane, 100 mL).
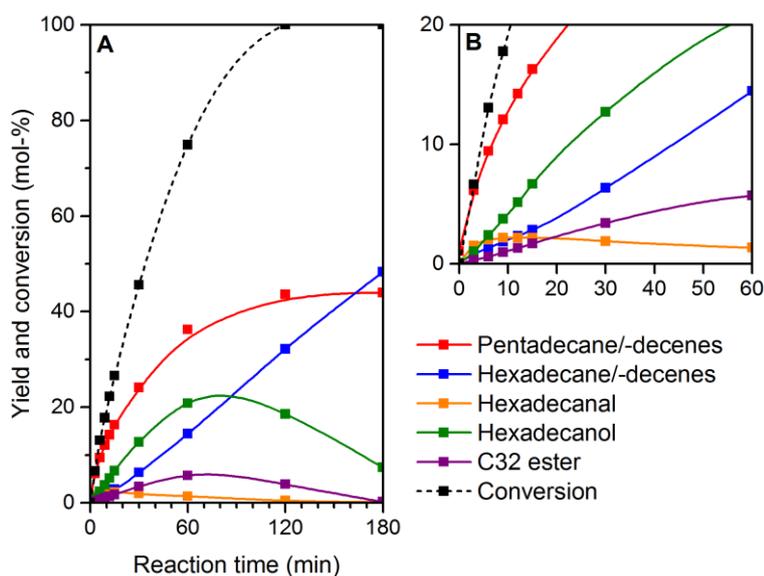
Figure 5.2. Conversion of hexadecanoic acid and yields of products as a function of reaction time on Ni-MoS$_2$ (**A**) and an enlarged view of the initial region (**B**). Reaction conditions: see Figure 5.1.
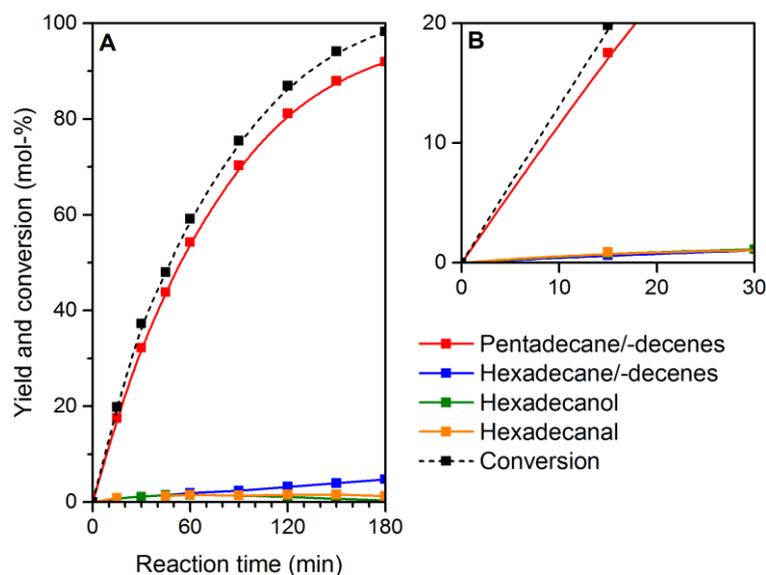
Figure 5.3. Conversion of hexadecanoic acid and yields of products as a function of reaction time on Ni_3S_2 (**A**) and an enlarged view of the initial region (**B**). Reaction conditions: see Figure 5.1 (with catalyst concentration 2.5 g L^{-1}).

Having shown that two distinct deoxygenation routes exist on MoS_2 and Ni-MoS_2, we discuss next whether these routes are interconnected by a common reaction intermediate. For MoS_2 we conclude that the hydrodeoxygenation pathway consists of the reaction steps: fatty acid → aldehyde → alcohol → olefin → alkane. Separate experiments, conducted using the intermediates as reactants, showed that hexadecanal and hexadecanol were rapidly converted to C_{16} hydrocarbons on MoS_2 and Ni-MoS_2 (Table 5.3). Thus, we conclude that the reaction sequence for HDO determined on MoS_2 is also valid for Ni-MoS_2. As hardly any smaller alkanes were observed, we conclude that aldehyde or alcohol are not likely intermediates for CLR.

HDO of the carboxylic acid apparently occurs in a similar fashion on MoS_2 and Ni-MoS_2. Hexadecanal, however, was consumed much more rapidly on Ni-MoS_2 as indicated by its comparably low concentration (Figure 5.2). Indeed, the presence of Ni enhanced the initial rate of acid conversion by factors of 1.2 and 1.4 (hexadecanoic acid consumption normalized to catalyst mass and specific surface area, respectively). This is in good agreement with previous contributions, reporting stronger promoter effects on the rate of aldehyde conversion than of fatty acids.[13,14] The presence of Ni influenced the product distribution remarkably. C_{15} hydrocarbons are a substantial product fraction on

Ni-MoS$_2$ and are virtually the only product on Ni$_3$S$_2$. The tendency to form these products from hexadecanoic acid is negligible on MoS$_2$.

Table 5.2. Initial rates of carbon loss reactions (CLR) and hydrodeoxygenation (HDO). [a]

Pathway	Mass normalized rates (mmol g^{-1} h^{-1})			Surface normalized rates (mmol m^{-2} h^{-1})		
	MoS$_2$	Ni-MoS$_2$	Ni$_3$S$_2$	MoS$_2$	Ni-MoS$_2$	Ni$_3$S$_2$
HDO	45.5	23.4	0.5	1.52	0.89	0.11
CLR	2.8	28.4	6.5	0.09	1.08	1.38
Total	48.3	51.8	7.0	1.62	1.96	1.49

[a] Reaction conditions: 573 K and 5.0 MPa H$_2$ at conversions below approx. 20 %.

5.2.2 Reaction pathways for C−C bond scission in DO reactions

Hexadecanal was selectively converted to HDO products on both MoS$_2$ and Ni-MoS$_2$. Thus, we conclude that aldehyde decarbonylation is not a relevant route for carbon loss on Ni-promoted sulfides. This is in line with the fact that the change in Gibbs energy associated with this route ($-76\,\text{kJ mol}^{-1}$) is considerably less negative than that of alternative pathways (Table 5.1). For instance, fatty acid decarboxylation and hydro-deoxygenation are both accompanied by a $\Delta_r G°$ value of nearly $-100\,\text{kJ mol}^{-1}$.

Table 5.3. Molar product selectivities near full conversion of single reactants and reactant mixtures.

| Reactant [a]	C$_{15}$: C$_{16}$ molar selectivity (%) [b]		
	MoS$_2$	Ni-MoS$_2$	Ni$_3$S$_2$
Hexadecanoic acid	6 : 94	45 : 55	94 : 6
Hexadecanal	5 : 95	7 : 93	–
Hexadecanol	1 : 99	2 : 98	–
Hexadecanal [c]	–	8 : 92	–

[a] Reaction conditions: 573 K and 5.0 MPa H$_2$ at conversions exceeding 90 %. [b] Pentadecane/pentadecenes (C$_{15}$), hexadecane/hexadecenes (C$_{16}$). [c] Hexadecanal in presence of equimolar concentration of octadecanoic acid.

In separate experiments, an equimolar mixture of hexadecanal and octadecanoic acid was reacted on MoS$_2$ and Ni-MoS$_2$ (Table 5.3). The addition of octadecanoic acid did not influence the transformation of hexadecanal to a significant extent, and the high selectivity to hexadecane (∼93 %) was maintained in the absence and in the presence of

octadecanoic acid. Thus, the presence of the acid, accompanied by competitive adsorption and consumption of surface hydrogen, does not influence the nature of the surface intermediate relevant for CLR.

Having eliminated aldehyde decarbonylation as a feasible pathway in the DO of fatty acids, we discuss next the direct decarboxylation of the fatty acid as the relevant route for carbon loss. Decarboxylation is a thermodynamically attractive route with a change in Gibbs energy of $-96 \, \text{kJ} \, \text{mol}^{-1}$ (Table 5.1). Decarboxylation has been repeatedly invoked to account for carbon loss on bulk Ni(Co)-MoS$_2$,[21] Ni-MoS$_2$/Al$_2$O$_3$,[3] and other metal and oxide catalysts.[26,30,32–34] However, the concentrations of CO_2 in the gas phase are usually not equal to the concentration of C_{n-1} products in the liquid phase. This is explained by the reverse water-gas shift reaction ($CO_2 + H_2 \rightleftharpoons CO + H_2O$), which can be catalyzed by sulfides under a variety of reaction conditions.[46,47]

The product distribution during hexadecanoic acid deoxygenation on Ni-MoS$_2$ shows that the formation of C_{15} hydrocarbons was accompanied by an equimolar amount of CO, while CO_2 was not detected (Figure S5.5 in the Supporting Information). Carbon dioxide could be masked by a reverse water-gas shift reaction but not beyond the equilibrium composition, corresponding to a CO/CO_2 ratio of approximately 3/1 (Figure S5.6 in the Supporting Information). Thus, the lack of CO_2 allows us to rule out decarboxylation as a relevant pathway for carbon losses under the presently used reaction conditions.
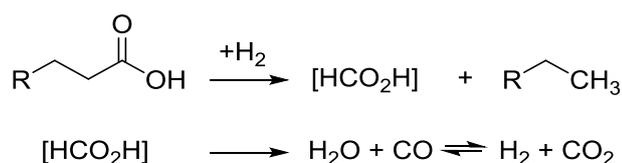
Scheme 5.2. C-C hydrogenolysis of a carboxylic acid to C_{n-1} alkane and formic acid with subsequent decomposition to H_2/CO_2 or H_2O/CO.

CO_x evolution could also originate from an indirect carbon oxide elimination, where the immediate gas-phase product is formic acid instead of CO or CO_2 (Scheme 5.2). In this case, a C_{n-1} alkane would be formed as the primary product by hydrogenolysis of the α C−C bond, while the formic acid byproduct would quickly decompose to either CO_2/H_2 or CO/ H_2O.[16,39,40] This mechanism could explain the fact that pentadecane was formed with a finite initial rate and, therefore, appeared as a primary product (Figure 5.4).

However, characteristic byproducts of C−C hydrogenolysis, such as formate esters and gaseous formic acid, were not detected. The substantial concentrations of pentadecenes, observed along with pentadecane despite the high rate of olefin hydrogenation on Ni-MoS$_2$ (9 times faster than the formation of C$_{15}$ hydrocarbons), points to a sequential mechanism, in which 1-pentadecene is the main primary product and pentadecane is formed successively by pentadecene hydrogenation.
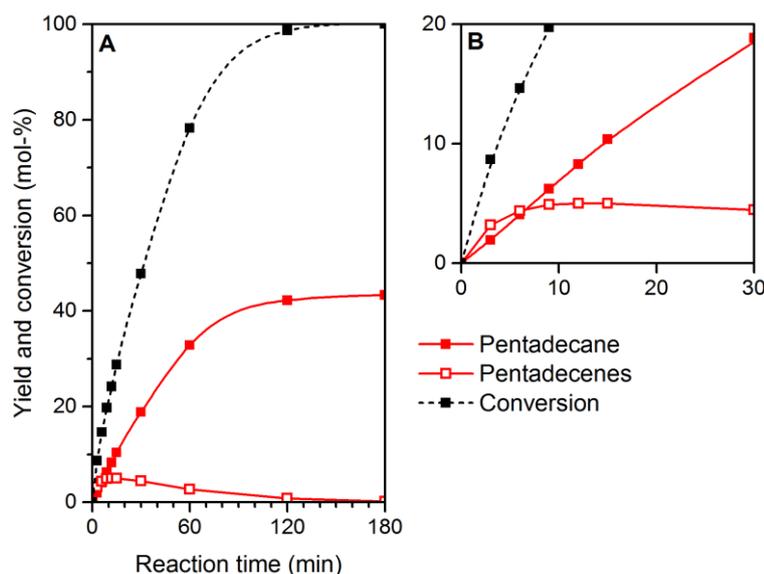

Figure 5.4. Evolution of pentadecane and pentadecenes as a function of time during the deoxygenation of hexadecanoic acid on Ni-MoS$_2$ (**A**) and an enlarged representation of the initial region (**B**). Reaction conditions: see Figure 5.1.

Hence, we conclude that C−C bond scission of hexadecanoic acid on Ni-MoS$_2$ results in the elimination of CO directly from the fatty acid reactant via a surface intermediate. Accordingly, the carbon loss could be explained in terms of a sequential dehydration-decarbonylation (DCO) pathway as suggested in another report.[14] In this scenario, an acylium ion is formed by dehydration of the carboxylic acid and subsequently decarbonylated to a terminal C$_{n-1}$ olefin. We tested this hypothesis with a quaternary carbon compound, 2-adamantanylacetic acid (AAc), which precludes the formation of an olefin and has a molecular weight comparable to that of hexadecanoic acid (Scheme 5.3).
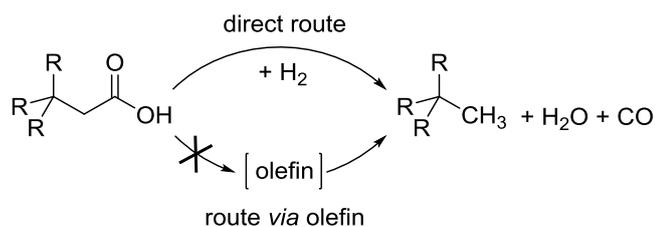
Scheme 5.3. Dehydration−decarbonylation of carboxylic acids with quaternary β carbon atom. An indirect mechanism via an olefin intermediate is not possible due to the lack of hydrogen substituents at the quaternary β carbon atom.

The deoxygenation of AAc on Ni-MoS$_2$ resulted in high concentrations of the carbon loss product (Figure 5.5) and CO as the only gas-phase product. Products of additional reaction pathways, potentially enabled by the highly branched structure of AAc (e.g., ring expansion of the adamantanyl cage), were not detected. Thus, we conclude that decarbonylation occurs in a similar fashion for carboxylic acids containing secondary and quaternary β carbon atoms. A further implication is that both the direct formation of an alkane and the indirect formation via a terminal olefin are possible. The former situation was observed with AAc (where β H atoms are absent) and the latter situation with hexadecanoic acid (where β H atoms are available).
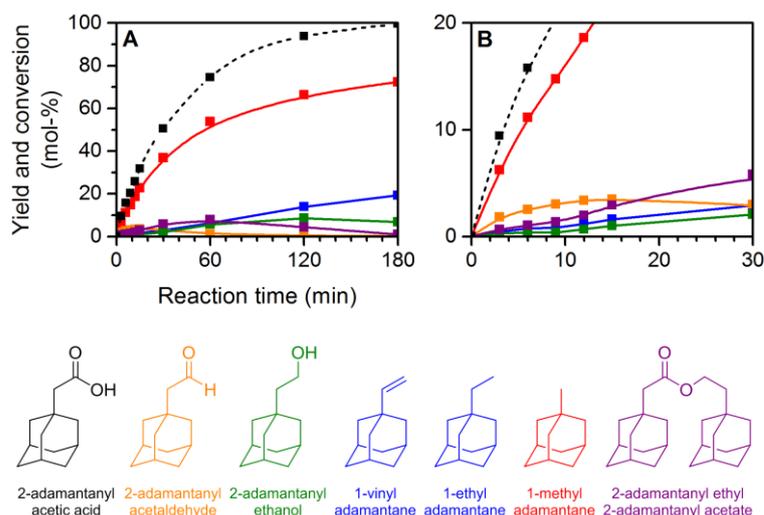

Figure 5.5. Conversion of 2-adamantanylacetic acid and product yields as a function of reaction duration on Ni-MoS$_2$ (**A**) and an enlarged representation of the initial region (**B**). Reaction conditions: see Figure 5.1 (except for solvent: decane).

5.2.3 Pressure dependence of hexadecanoic acid deoxygenation

The dependence of decarbonylation initial rates on the partial pressure of H_2 was determined within the 1.0−7.5 MPa range (Figure 5.6). The reaction order of decarbonylation rates with respect to H_2 was 0 in the higher range of pressures (2.5 to 7.5 MPa). Thus, the rate-determining elementary step in this region does not involve hydrogen, which is in line with the fact that H_2 is not needed by the stoichiometry of the decarbonylation reaction to proceed. In contrast, a positive reaction order of 0.5 was observed for lower H_2 pressures (1.0−2.5 MPa), indicating a transition to a rate deter-mining step that requires H_2. The HDO pathway, on the other hand, exhibits a reaction order of 1.2 in H_2 partial pressure along the whole range explored.
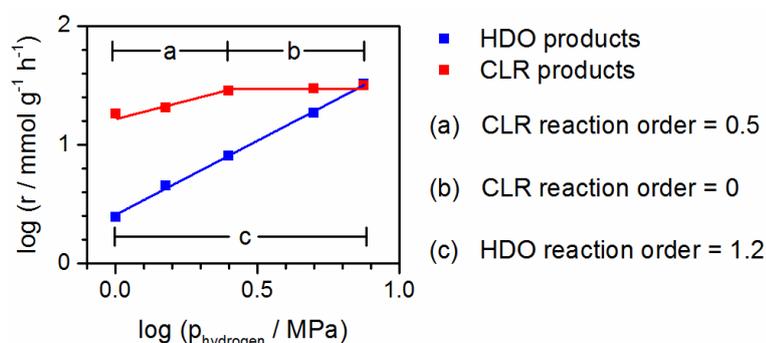

Figure 5.6. Initial rate of formation of hydrodeoxygenation (HDO) and carbon loss reaction (CLR) products on Ni-MoS$_2$ catalyst as a function of hydrogen partial pressure from 1.0 to 7.5 MPa (9.0 MPa total pressure). HDO products include hexadecane and hexadecenes, hexadecanal, hexadecanol, and hexadecyl hexadecanoate. Reaction conditions: see Figure 5.1.

5.2.4 Active sites and molecular level mechanism of C−C bond scission

The reference reactions with Ni_3S_2 showed that this phase is highly selective for CLR (Table 5.2). In line with this, some studies have attributed the carbon loss pathways to segregated Ni_3S_2, which was repeatedly observed in Ni-promoted MoS_2.[13] Along this line of thought, the binary metal sulfide catalyst may act as a physical mixture of MoS_2 and Ni_3S_2, in which each component selectively catalyzes one reaction pathway: i.e., either HDO or CLR. This assumption, however, is not in line with the amount of exposed Ni_3S_2 surface, which is very low and hence only weakly contributes to catalytic reactions. We calculated the surface-normalized CLR rate of Ni_3S_2 in the single-phase catalyst and in

the binary Ni−Mo sulfide (section 5.6.7 in the Supporting Information). The calculation shows that the segregated Ni sulfide in Ni-MoS$_2$ would have to be more than 4 times as active per unit of surface area as in pure Ni sulfide. We dismiss, therefore, segregated Ni$_3$S$_2$ as the major source of CLR products on Ni-MoS$_2$. This is also supported by postreaction X-ray characterization of Ni-MoS$_2$, in which we noticed changes in the structure of the segregated Ni sulfide; however, these changes were not accompanied by any significant difference in the reaction rate (see sections 5.6.2 and 5.6.10 in the Supporting Information).

Further evidence against a significant participation of Ni$_3$S$_2$ in the mixed-metal sulfide catalyst arises from the different energy of activation for CLR, which was significantly higher on pure Ni$_3$S$_2$ with 130 kJ mol^{-1} in comparison to 87 kJ mol^{-1} on Ni-MoS$_2$ (Figure 5.7). This large difference suggests that CLR (more specifically DCO) on Ni-MoS$_2$ is not associated with sites in Ni$_3$S$_2$ but with a different type of site. Nickel must, of course, still be involved, as CLRs are only observed on the Ni-containing catalyst.
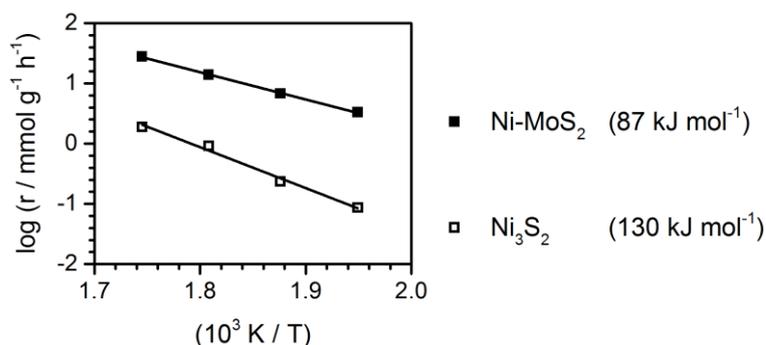

Figure 5.7. Arrhenius plot for the formation of carbon loss reaction products on Ni-MoS$_2$ and Ni$_3$S$_2$. Reaction conditions: 513−573 K (other parameters: see Figure 5.1).

With the negligible contribution of segregated Ni$_2$S$_3$ to the activity of Ni-MoS$_2$ and the different catalytic performances (product distribution and activation energies) of MoS$_2$ and Ni$_3$S$_2$, we conclude that the dominant active phase in Ni-MoS$_2$ is MoS$_2$ with Ni incorporated at the edges. The existence of such a promoted phase is evidenced in previous studies, where kinetic characterization was complemented with spectroscopic characterization of materials prepared by the same procedure as used in this work.[48,49]

The active sites of MoS$_2$-based hydrotreating catalysts are widely accepted to be located at the (10$\bar{1}$0) and ($\bar{1}$010) surface of the MoS$_2$ crystals: i.e., at their metal and sulfur

edges.[50−52] Sulfur vacancies or coordinatively unsaturated sites (CUS) in these edges play a key role in the removal of heteroatoms. The hydrogen needed for hydrotreating is provided by SH groups formed upon H_2 dissociation. These surface species also exhibit Brønsted acidity.[53−58] The partial substitution of Mo by Ni or Co at the edges leads to a decreased binding energy of sulfur atoms, resulting in an increasing concentration of sulfur vacancies.[59−61] It is known that the CUS in Ni-modified MoS_2 provides the basis for highly enhanced desulfurization and denitrogenation activity.[48,49,62] Our results suggest that, in the HDO of carboxylic acids, Ni-associated CUS are involved in deoxygenation. However, decarbonylation is favored over hydrogenation.

The decreased metal−sulfur bond strength induced by Ni or Co also results in a higher electron density (basicity) on neighboring sulfur atoms.[27,63] Thus, these sulfur atoms may act as basic sites, capable of deprotonating carboxylic acid groups and structures with strongly polarized C−H bonds. Thus, we propose that coordinatively unsaturated Ni and the associated more basic sulfur act as the active sites for decarbonylation within the mechanism proposed in the following (Scheme 5.4).
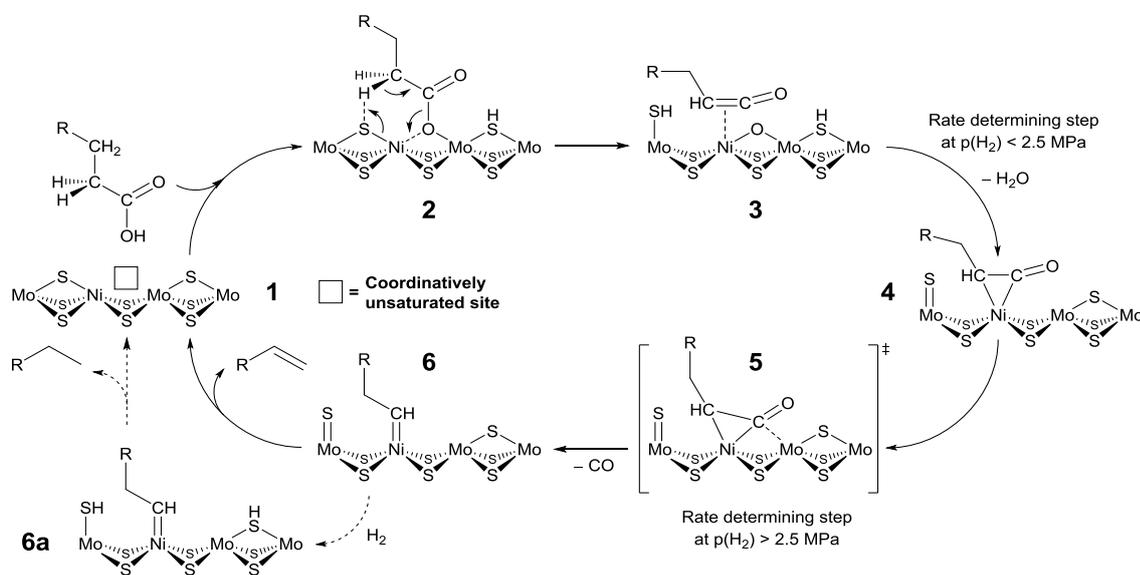
Scheme 5.4. Suggested mechanism for the decarbonylation of fatty acids on Ni-MoS_2 catalyst under an H_2 atmosphere.

In a mechanism where the primary adsorption sites are CUS, the fatty acid binds dissociatively, forming a Ni−O bond. The proton of the OH group attaches to the adjacent bridging sulfur atom (Scheme 5.4, step **1 → 2**). In the next step the C−O bond cleavage

is induced by strong interaction with the oxophilic Mo cation, comparable to the situation encountered on reducible oxides, such as ceria and zirconia.[24,64] It is important to note that structure **2** corresponds to an activated acyl compound ("acyl pseudo-halide") with a strongly polarized C−H bond in the α position (because the strong electron withdrawal from the activated carbonyl group stabilizes the conjugate base). An adjacent basic sulfur atom abstracts one of the α protons to form the ketene intermediate **3** coordinated to Ni. From an organic chemistry point of view, the formation of ketenes from activated acyl compounds has been long known as a route to ketenes.[65] In turn, ketene intermediates have been reported in connection with fatty acid deoxygenation on Pd/Al$_2$O$_3$ and Ni/ZrO$_2$.[33,38] Once a ketene is formed from the adsorbed carboxylic acid, the preferred coordination geometry is a η^2(C−C) complex (**4**).[66,67] This requires the prior removal of oxygen from the CUS; otherwise, complex formation may be hindered due to steric and electronic restraints (heptacoordinate Ni(II) complexes are extremely rare[68]). The dependence of decarbonylation initial rates on an H$_2$ pressure below 2.5 MPa indicates that the H$_2$-assisted oxygen removal from the surface is indeed the rate-determining step at low hydrogen coverages. At high H$_2$ pressure, when the regeneration of the CUS by activated hydrogen does not limit the reaction, the rate-determining step consists of the cleavage of the ketene C−C bond (**5**), resulting in the elimination of CO. It should be noted in passing that ketenes are highly prone to decarbonylation.[69]

In the present case, decarbonylation of the ketene is aided by an adjacent Mo atom, further weakening the C−C bond by interacting with the carbonyl carbon. A carbene-like surface species (**6**) is suggested to form as a result of this reaction, in analogy to the well-known thermal decomposition of ketenes.[70] The final step of the catalytic cycle has two potential pathways for the elimination of the surface carbene **6**: i.e., the isomerization to a terminal olefin with simultaneous Ni−C bond cleavage or the sequential hydrogen addition to the corresponding alkane **6a**. We conclude that the olefin formation is kinetically favored because pentadecenes were the primary decarbonylation products of hexadecanoic acid. On the other hand, decarbonylation can also directly produce alkanes without intermediate olefin formation as was the case with the 2-adamantanylacetic acid reactant.

According to this mechanistic description the key surface species for decarbonylation on Ni-MoS$_2$ is a ketene intermediate, formed by deprotonation of the adsorbed acyl

compound (Scheme 5.4, steps **2** and **3**). The proton acceptor site required is the basic sulfur species close to Ni. The same acyl intermediate helps to explain the catalytic pathway on MoS_2. In this case, the lower electron density of S^{2-} on MoS_2 drastically decreases the ability to abstract H^+ from the β carbon atom, hindering the ketene formation (Scheme 5.5). Thus, the carboxylic acid is selectively reduced to an aldehyde by the hydrogenolytic cleavage of the C−O bond. As H_2 adsorbs dissociatively on sulfides, forming surface SH groups, the reaction order in H_2 for HDO (close to 1) points to a stepwise hydrogen addition, where the addition of the second hydrogen atom is the rate-determining step for the formation of the aldehyde.[46−51] Note that the complete absence of sulfur containing products led us to conclude that nucleophilic OH to SH exchange reactions do not occur.
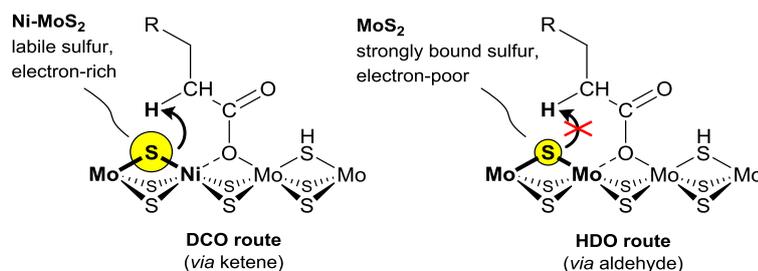
Scheme 5.5. Different chemical nature of S atoms adjacent to the vacancy determines the reactivity toward the activated acyl compound (adsorbed carboxylic acid).

5.3   Conclusions

Hydrodeoxygenation (HDO) of fatty acids on MoS_2 occurs through a stepwise reaction initiated by C−O hydrogenolysis of the fatty acid to the aldehyde, followed by hydrogenation to the corresponding alcohol. The final transformation of the alcohol to the fully deoxygenated product occurs by sequential dehydration−hydrogenation, indicated by the high concentration of 1-olefin in the olefin isomer fraction as well as the global prevalence of olefins over alkanes at intermediate fatty acid conversions.

Carbon loss reactions (CLR), leading to C_{n-1} hydrocarbons, occur in parallel to HDO. In comparison to MoS_2, the Ni-promoted catalyst and especially Ni_3S_2 drastically enhance the formation of carbon loss products, highlighting the key role of Ni^{2+} in C−C bond scission reactions. However, different experimental activation barriers for the formation of carbon loss products on Ni-MoS_2 and Ni_3S_2 and differences in activity normalized per surface area indicate that promoted Ni−Mo sites, rather than segregated Ni sulfides in Ni-MoS_2, catalyze CLR.

Scission of C−C bonds, related to Ni-associated vacancies, results in the concurrent formation of equimolar amounts of CO and C_{n-1} hydrocarbons, exposing the decarbonylation−type nature of the carbon loss route. The high selectivities toward the HDO products observed with aldehyde and alcohol reactants – also in the presence of competing fatty acid compounds – allow us to conclude that the HDO and decarbonylation pathways are not interconnected by an aldehyde or alcohol intermediate.

Thus, the decarbonylation of fatty acids occurs through a sequential dehydration-decarbonylation mechanism, in which a ketene is the key intermediate for the subsequent C−C cleavage. An increasing reaction order in H_2 at decreasing partial pressures marks the transition of the rate-determining step from C−C cleavage toward the regeneration of active sites. Experiments with branched fatty acids reveal that the immediate product of the C−C cleavage is not necessarily an olefin, although olefin formation is kinetically preferred with a linear reactant. Where α hydrogen atoms are not available, the decarbonylation directly produces an alkane. The fundamentally different reactivity of Ni-MoS_2 in comparison to MoS_2 is interpreted in terms of labilized, electron-rich sulfur sites resulting from the presence of Ni.

5.4 Acknowledgements

5.5 References

(1)   Communication from the Commission to the European Parliament, COM(2014) 748 final 2012/0288 (COD); The European Commission: Brussels, **2014**.

(2)   Choudhary, T. V.; Phillips, C. B. *Appl. Catal., A* **2011**, 397, 1-12.

(3)   Huber, G. W.; O'Connor, P.; Corma, A. *Appl. Catal., A* **2007**, 329, 120-129.

(4)   Kubička, D.; Kaluža, L. *Appl. Catal., A* **2010**, 372, 199-208.

(5)   da Rocha Filho, G. N.; Brodzki, D.; Djéga-Mariadassou, G. *Fuel* **1993**, 72, 543-549.

(6)   Donnis, B.; Egeberg, R.; Blom, P.; Knudsen, K. *Top. Catal.* **2009**, 52, 229-240.

(7)   Bellussi, G.; Rispoli, G.; Landoni, A.; Millini, R.; Molinari, D.; Montanari, E.; Moscotti, D.; Pollesel, P. *J. Catal.* **2013**, 308, 189-200.

(8)   Şenol, O. İ.; Viljava, T. R.; Krause, A. O. I. *Appl. Catal., A* **2007**, 326, 236-244.

(9)   Şenol, O. İ.; Viljava, T. R.; Krause, A. O. I. *Catal. Today* **2005**, 106, 186-189.

(10)   Huber, G. W.; Corma, A. *Angew. Chem. Int. Ed.* **2007**, 46, 7184-7201.

(11)   Santillan-Jimenez, E.; Crocker, M. *J. Chem. Technol. Biotechnol.* **2012**, 87, 1041-1050.

(12)   Laurent, E.; Delmon, B. *J. Catal.* **1994,** 146, 281-291.

(13)   Ruinart de Brimont, M.; Dupont, C.; Daudin, A.; Geantet, C.; Raybaud, P. *J. Catal.* **2012,** 286, 153-164.

(14)   Brillouet, S.; Baltag, E.; Brunet, S.; Richard, F. *Appl. Catal., B* **2014,** 148-149, 201-211.

(15)   Dupont, C.; Lemeur, R.; Daudin, A.; Raybaud, P. *J. Catal.* **2011,** 279, 276-286.

(16)   Boda, L.; Onyestyák, G.; Solt, H.; Lónyi, F.; Valyon, J.; Thernesz, A. *Appl. Catal., A* **2010,** 374, 158-169.

(17)   Kubička, D.; Horáček, J. *Appl. Catal., A* **2011,** 394, 9-17.

(18)   Şenol, O. İ.; Ryymin, E. M.; Viljava, T. R.; Krause, A. O. I. *J. Mol. Catal. A: Chem.* **2007,** 277, 107-112.

(19)   Şenol, O. İ.; Ryymin, E. M.; Viljava, T. R.; Krause, A. O. I. *J. Mol. Catal. A: Chem.* **2007,** 268, 1-8.

(20)   Şenol, O. İ.; Viljava, T. R.; Krause, A. O. I. *Catal. Today* **2005,** 100, 331-335.

(21)   Zhang, H.; Lin, H.; Zheng, Y. *Appl. Catal., B* **2014,** 160-161, 415-422.

(22)   Mohammad, M.; Kandaramath Hari, T.; Yaakob, Z.; Chandra Sharma, Y.; Sopian, K. *Renewable Sustainable Energy Rev.* **2013,** 22, 121-132.

(23)   Peng, B.; Yao, Y.; Zhao, C.; Lercher, J. A. *Angew. Chem.* **2012,** 124, 2114-2117.

(24)   Peng, B.; Yuan, X.; Zhao, C.; Lercher, J. A. *J. Am. Chem. Soc.* **2012,** 134, 9400-9405.

(25)   Lestari, S.; Mäki-Arvela, P.; Simakova, I.; Beltramini, J.; Lu, G. Q. M.; Murzin, D. *Catal. Lett.* **2009,** 130, 48-51.

(26)   Gosselink, R. W.; Hollak, S. A.; Chang, S. W.; van Haveren, J.; de Jong, K. P.; Bitter, J. H.; van Es, D. S. *ChemSusChem* **2013,** 6, 1576-1594.

(27)   Bataille, F.; Lemberton, J.-L.; Michaud, P.; Pérot, G.; Vrinat, M.; Lemaire, M.; Schulz, E.; Breysse, M.; Kasztelan, S. *J. Catal.* **2000,** 191, 409-422.

(28)   Harris, S.; Chianelli, R. R. *J. Catal.* **1986,** 98, 17-31.

(29)   Gosselink, R. W.; Stellwagen, D. R.; Bitter, J. H. *Angew. Chem.* **2013,** 125, 5193-5196.

(30)   Mäki-Arvela, P.; Kubickova, I.; Snåre, M.; Eränen, K.; Murzin, D. Y. *Energy Fuels* **2006,** 21, 30-41.

(31)   Kubičková, I.; Snåre, M.; Eränen, K.; Mäki-Arvela, P.; Murzin, D. Y. *Catal. Today* **2005,** 106, 197-200.

(32)   Snåre, M.; Kubičková, I.; Mäki-Arvela, P.; Eränen, K.; Murzin, D. Y. *Ind. Eng. Chem. Res.* **2006,** 45, 5708-5715.

(33)   Hollak, S. A. W.; Bitter, J. H.; van Haveren, J.; de Jong, K. P.; van Es, D. S. *RSC Adv.* **2012,** 2, 9387-9391.

(34)   Maier, W. F.; Roth, W.; Thies, I.; Schleyer, P. V. R. *Chem. Ber.* **1982,** 115, 808-812.

(35)   Chen, L.; Fu, J.; Yang, L.; Chen, Z.; Yuan, Z.; Lv, P. *ChemCatChem* **2014,** 6, 3482-3492.

(36)   Do, P.; Chiappero, M.; Lobban, L.; Resasco, D. *Catal. Lett.* **2009,** 130, 9-18.

(37)   Foraita, S.; Fulton, J. L.; Chase, Z. A.; Vjunov, A.; Xu, P.; Baráth, E.; Camaioni, D. M.; Zhao, C.; Lercher, J. A. *Chem. - Eur. J.* **2014,** 21, 2423-2434.

(38)   Peng, B.; Zhao, C.; Kasakov, S.; Foraita, S.; Lercher, J. A. *Chem. Eur. J.* **2013,** 19, 4732-4741.

(39)   Berenblyum, A. S.; Danyushevsky, V. Y.; Katsman, E. A.; Podoplelova, T. A.; Flid, V. R. *Pet. Chem.* **2010,** 50, 305-311.

(40)   Berenblyum, A. S.; Podoplelova, T. A.; Shamsiev, R. S.; Katsman, E. A.; Danyushevsky, V. Y. *Pet. Chem.* **2011,** 51, 336-341.

(41)   Li, W.; Gao, Y.; Yao, S.; Ma, D.; Yan, N. *Green Chem.* **2015,** 17, 4198-4205.

(42)   Eijsbouts, S.; Mayo, S. W.; Fujita, K. *Appl. Catal., A* **2007,** 322, 58-66.

(43)   Ninh, T. K. T.; Laurenti, D.; Leclerc, E.; Vrinat, M. *Appl. Catal., A* **2014,** 487, 210-218.

(44)   Gutiérrez, O. Y.; Singh, S.; Schachtl, E.; Kim, J.; Kondratieva, E.; Hein, J.; Lercher, J. A. *ACS Catal.* **2014,** 4, 1487-1499.

(45)   Peroni, M.; Mancino, G.; Baráth, E.; Gutiérrez, O. Y.; Lercher, J. A. *Appl. Catal., B* **2016,** 180, 301-311.

(46)   Osaki, T.; Narita, N.; Horiuchi, T.; Sugiyama, T.; Masuda, H.; Suzuki, K. *J. Mol. Catal. A: Chem.* **1997,** 125, 63-71.

(47)   Sasaki, T.; Suzuki, T. *Appl. Catal., A* **2014,** 484, 79-83.

(48)   Hein, J.; Gutierrez, O. Y.; Schachtl, E.; Xu, P. H.; Browning, N. D.; Jentys, A.; Lercher, J. A. *ChemCatChem* **2015,** 7, 3692-3704.

(49)   Hein, J.; Hrabar, A.; Jentys, A.; Gutiérrez, O. Y.; Lercher, J. A. *ChemCatChem* **2014,** 6, 485-499.

(50)   Sun, M.; Nelson, A. E.; Adjaye, J. *J. Catal.* **2004,** 226, 32-40.

(51)   Raybaud, P. *Appl. Catal., A* **2007,** 322, 76-91.

(52)   Lauritsen, J. V.; Kibsgaard, J.; Olesen, G. H.; Moses, P. G.; Hinnemann, B.; Helveg, S.; Nørskov, J. K.; Clausen, B. S.; Topsøe, H.; Lægsgaard, E.; Besenbacher, F. *J. Catal.* **2007,** 249, 220-233.

(53)   Schachtl, E.; Kondratieva, E.; Gutiérrez, O. Y.; Lercher, J. A. *J. Phys. Chem. Lett.* **2015,** 6, 2929-2932.

(54)   Schachtl, E.; Zhong, L.; Kondratieva, E.; Hein, J.; Gutiérrez, O. Y.; Jentys, A.; Lercher, J. A. *ChemCatChem* **2015,** 7, 4118-4130.

(55)   Wright, C. J.; Sampson, C.; Fraser, D.; Moyes, R. B.; Wells, P. B.; Riekel, C. *J. Chem. Soc., Faraday Trans. 1* **1980,** 76, 1585-1598.

(56)   Sundberg, P.; Moyes, R. B.; Tomkinson, J. *Bull. Soc. Chim. Belg.* **1991,** 100, 967-976.

(57)   Topsøe, N.-Y.; Topsøe, H.; Massoth, F. E. *J. Catal.* **1989,** 119, 252-255.

(58)   Travert, A.; Maugé, F. *Stud. Surf. Sci. Catal.* **1999,** 127, 269-277.

(59)   Byskov, L. S.; Bollinger, M.; Nørskov, J. K.; Clausen, B. S.; Topsøe, H. *J. Mol. Catal. A: Chem.* **2000,** 163, 117-122.

(60)   Byskov, L. S.; Nørskov, J. K.; Clausen, B. S.; Topsøe, H. *J. Catal.* **1999,** 187, 109-122.

(61)   Raybaud, P.; Hafner, J.; Kresse, G.; Kasztelan, S.; Toulhoat, H. *J. Catal.* **2000,** 190, 128-143.

(62)   Chianelli, R. R.; Berhault, G.; Torres, B. *Catal. Today* **2009,** 147, 275-286.

(63)   Hrabar, A.; Hein, J.; Gutiérrez, O. Y.; Lercher, J. A. *J. Catal.* **2011,** 281, 325-338.

(64)   Pestman, R.; Koster, R. M.; Pieterse, J. A. Z.; Ponec, V. *J. Catal.* **1997,** 168, 255-264.

(65)   Staudinger, H. *Chem. Ber.* **1911,** 44, 1619-1623.

(66)   Geoffroy, G. L.; Bassner, S. L. In *Advances in Organometallic Chemistry*, Stone, F. G. A.; West, R., Eds. Academic Press: New York **1988**; Vol. 28, pp 1-83.

(67)   Miyashita, A.; Grubbs, R. H. *Tetrahedron Lett.* **1981,** 22, 1255-1256.

(68)   Regueiro-Figueroa, M.; Lima, L. M. P.; Blanco, V.; Esteban-Gómez, D.; de Blas, A.; Rodríguez-Blas, T.; Delgado, R.; Platas-Iglesias, C. *Inorg. Chem.* **2014,** 53, 12859-12869.

(69)   Kumar, P.; Troast, D. M.; Cella, R.; Louie, J. *J. Am. Chem. Soc.* **2011,** 133, 7719-7721.

(70)   Staudinger, H.; Endle, R. *Chem. Ber.* **1913,** 46, 1437-1442.

5.6 Supporting information

5.6.1 Experimental procedures

Preparation of catalysts

All chemicals and reagents were used without further purification. Ammonium molybdate tetrahydrate (99.98 % trace metal basis), sodium sulfide nonahydrate (99.99 % trace metal basis), maleic acid (> 99 %), ammonium hydroxide solution (28–30 wt%), and ammonium sulfide solution (40–48 wt%) were supplied by *Sigma-Aldrich*. Nickel nitrate hexahydrate (99.9985 % trace metals basis) was purchased from *Alfa-Aesar*. Dodecane (> 99 %, *Sigma-Aldrich*), hexadecanoic acid (analytical standard, *Fluka*), hexadecanal (> 97 %, *TCI*), hexadecanol (analytical standard, *Fluka*), and heptadecane (analytical standard, *Fluka*) were used without further purification. Gases were of 99.995 % purity and supplied by *Westfalen*.

Ni-Mo mixed oxide, serving as a precursor for unsupported Ni-MoS$_2$, was synthesized by pH controlled co-precipitation in alkaline aqueous solution.[1] First, a solution of 5.30 g (3.00 mmol Mo) of $(NH_4)_6Mo_7O_{24}\cdot 4\,H_2O$ in 120 mL deionized water was prepared by stirring at ambient temperature. The pH was then adjusted to 9–10 by adding 4.5 mL of aqueous NH$_4$OH (28–30 %) after which the solution was heated to 363 K. Subsequently, a solution of 8.73 g (3.00 mmol Ni) of $Ni(NO_3)_2\cdot 6\,H_2O$ in 7.5 mL water was heated to 333 K and slowly added to the alkaline molybdate solution during 30 min while stirring vigorously. The pH was maintained constant at 9-10 during the first 10 min by adding appropriate amounts of NH$_4$OH solution. During the addition of Ni-nitrate, a yellow-greenish slurry was formed, which was stirred at 363 K for an additional 30 min period. While still hot, the mixture was filtered and the precipitate dispersed in a solution of 0.264 g of maleic acid in 45 mL of water. After stirring the resulting slurry at 343 K for 30 min, the precipitate was filtered once more, washed with 10 mL of water and dried over night at room temperature. Finally, the pre-dried solid was heated to 393 K for 6 h in a flow of synthetic air (40 mL min^{-1} g^{-1}) using a heating rate of 1 K min^{-1}. After grinding in a mortar, 5.5 g of yellow-greenish Ni-Mo mixed oxide powder were obtained.

Unpromoted MoS$_2$ catalyst was prepared by decomposition of ammonium tetrathio-molybdate (ATM).[2] ATM was prepared by adding a large excess of aqueous ammonium

sulfide solution (64.0 g, 40–48 %, *Sigma-Aldrich*) to a solution of 8.00 g $(NH_4)_6Mo_7O_{24} \cdot 4 H_2O$ in 40 mL water while stirring at ambient temperature. The resulting solution was heated to 333 K and maintained at this temperature for 1 h, after which it was cooled in an ice bath for 3 h. Washing with dry 2-propanol and subsequent drying in vacuum at ambient temperature over night yielded 10.5 g of red ATM crystals. Decomposition of ATM to MoS_2 was performed by subjecting it to the sulfiding procedure described below.

Ni_3S_2 was prepared using a low temperature procedure.[3] A solution of 6.00 g (25.0 mmol) of $Na_2S \cdot 9 H_2O$ in 150 mL of water was slowly added to a solution of 10.9 g (37.5 mmol) of $Ni(NO_3)_2 \cdot 6 H_2O$. The addition was performed at room temperature during 1 h under vigorous stirring. The black precipitate was filtered, washed several times with water and once with acetone. After drying in air at room temperature over night, the black powder was heated to 573 K at a rate of 3.3 K min^{-1} in a flow of 40 mL min^{-1} g^{-1} of H_2S (10 vol% in H_2) for 3 h and subsequently in H_2 for 4 h at the same flow rate and temperature.

The typical sulfiding procedure consisted of mixing approximately 0.5 g of precursor in powder form with 1.50 g of SiC (0.5–1 mm fraction) and placing the solid mixture inside a glass coated tubular fixed bed reactor of 4 mm inner diameter. Sulfidation (decomposition) was then carried out during 8 h in a flow of 20 mL min^{-1} g^{-1} of H_2S (10 vol% in H_2) at 673 K and atmospheric pressure using a heating rate of 5 K min^{-1}.

Characterization methods

Elemental analysis of sulfided catalyst samples was performed after acidic digestion and subsequent photometric determination using a *Shimadzu UV-160* photometer (for Co, Ni, Mo). For determination of the sulfur content an *Elementar Vario EL* combustion analyzer was employed. Textural parameters were determined by nitrogen physisorption performed on an automated *PMI Sorptomatic 1990* instrument at liquid nitrogen temperature. The samples (ca. 250 mg) were outgassed in vacuum at 523 K for 2 h prior to adsorption. Specific surface areas (m² g^{-1}) were obtained by applying BET theory on the adsorption isotherms. Sulfided catalyst samples were also characterized by X-ray diffraction (XRD) with a *Philips X'Pert Pro* diffractometer in Bragg-Brentano geometry using Cu-Kα radiation (K$_{\alpha2}$/K$_{\alpha1}$ = 0.5) operating at 45 kV/40 mA. XRD measurements were carried out using a rotating zero-diffraction plate (single crystal of Si cut in special

orientation). The step size was fixed to 0.017 °θ with a dwell time of 115 ms per step. Crystallite size and stacking degree of MoS_2 phase was calculated from the (002) reflection using the Scherrer equation with a shape factor of 0.9. An average distance of 0.62 nm between two slabs was assumed for calculation of the stacking degree. Ni_3S_2 crystallite size was determined in a similar way from the (110) reflection.

Catalytic tests

Kinetic measurements were performed in batch mode using a 300 mL stirred tank reactor supplied by *Parr Instrument Company*. In a typical experiment, the reactor was loaded with 50 mg of catalyst powder and 100 mL of reactant solution at a concentration of 5 g L^{-1} in dodecane. Note the different catalyst loading in olefin hydrogenation experiments (25 mg) and hexadecanoic acid deoxygenation with Ni_3S_2 (250 mg). The reactor was then closed and purged with ca. 1 MPa of nitrogen for six times, after which it was left with atmospheric pressure of nitrogen and heated to reaction temperature under mild stirring (200 rpm) to obtain a homogeneous heat distribution. At the desired reaction temperature, a reference sample of the liquid phase (t = 0 min) was taken from a built-in sampling valve equipped with a 2 μm filter while still in nitrogen atmosphere. At this stage the conversion was always below 3 %. Then, the stirring rate was increased to 600 rpm and the reaction was started by applying the desired pressure of hydrogen (typically 5 MPa). Under operating conditions the partial pressures of hydrogen, solvent and nitrogen were 5.0, 0.4 and 0.2 MPa, respectively. Liquid samples of approximately 0.5 mL were taken at predetermined time intervals, amounting to a loss of 5 % of the liquid phase by the end of the experiment, which typically lasted 3 h. Gas phase samples were taken at the same time as liquid phase samples. For this purpose, a small portion of the gaseous mixture in the head-space of the reactor was released through a separate transfer line, which was directly connected to the inlet of a gas chromatograph. When gas phase analysis was not performed, the total pressure in the reactor remained virtually constant over the whole duration of the experiment. In the cases where gas phase analysis was employed, the pressure loss was about 0.05 MPa per sample, amounting to approximately 0.5 MPa in total.

$$\text{Conversion } = \left(1 - \frac{c_r(t_0) - c_r(t)}{c_r(t_0)}\right) \times 100 \text{ mol\%} \qquad \text{(S5.1)}$$

$$\text{Yield} = \left(\frac{c_i(t)}{c_r(t_0)}\right) \times \left(\frac{\mu_r}{\mu_i}\right) \times 100 \text{ mol\%} \tag{S5.2}$$

$$\text{Selectivity} = \left(\frac{c_i(t)}{c_r(t_0) - c_r(t)}\right) \times \left(\frac{\mu_r}{\mu_i}\right) \times 100 \text{ mol\%} \tag{S5.3}$$

Conversion, selectivities, and yields were calculated according to equations (S5.1–3), where c_r indicates the concentration of a reactant species r, and c_i indicates the concentration of a product or intermediate species i. Yield was defined as the amount of reactant r to form a specific product i per amount of reactant present initially. Selectivity was defined as the amount of reactant r to form a specific product i per amount of reactant consumed. Stoichiometric coefficients for product and reactant species are given by factors μ_i and μ_r, respectively. All concentrations are given in mol L^{-1}. Reaction rates are given as initial rates in the unit of millimol of reactant consumed or millimol of product formed per gram catalyst and hour. Rates were determined as the slope of concentration versus time data obtained at low conversions (typically below 15 %). For all experiments reported herein the molar balance in the liquid phase was equal to or better than 97 %. All measurements were conducted under kinetically limited conditions (see section 5.6.11).

Sample analysis

Liquid samples were analyzed offline in an *Agilent 7890B* gas chromatograph equipped with a flame ionization detector (FID) and an *Agilent 5977A* mass spectrometer. The liquid sample (1 µl) was injected onto a *HP 5ms* column (30 m × 0.25 mm × 0.25 µm) at an inlet temperature of 573 K using a split ratio of 50 (He). The column temperature was initially held at 353 K for 1 min, then increased to 573 K at a rate of 20 K min^{-1} and held at this final temperature for further 11 min, while the column flow was maintained constant at 1 mL min^{-1} (He) for the whole duration of the measurement. The FID was operated at 573 K. Identification of analytes was performed using the retention times of commercially available pure substances or via the attached mass spectrometer, where necessary. Quantification of reactants via the FID-signal, especially hexadecanoic acid, required chemical derivatization with a silylation reagent to convert reactive hydroxyl and carboxyl groups to the respective trimethylsilyl esters. For this purpose, an excess of *Supelco Sylon BFT* (i.e., N,O-Bis(trimethylsilyl)trifluoroacetamide with trimethylchloro-silane, 99:1) was added to each sample, which was then heated to 353 K for 1 h before analysis. For quantification of fatty acid anhydrides, a different procedure was employed:

0.5 mL of liquid sample was first diluted with an equal volume of $CHCl_3$ and agitated until a clear solution was obtained. Each sample was then separated into two equal portions, the first one being derivatized with *Sylon BFT* for fatty acid determination, the other one being mixed with an excess of diethylamine followed by heating to convert fatty acid anhydrides to the corresponding diethyl amides.

For the majority of our analyses it was not necessary to distinguish between alkanes and olefins of the same carbon number. These compounds were therefore referred to as C_{15} hydrocarbons and C_{16} hydrocarbons, i.e., pentadecane with pentadecenes and hexadecane with hexadecenes, respectively. Where a distinction between olefins and alkanes was necessary, it was achieved by manual separation of the overlapping GC-FID signals using an appropriate number of Gaussian functions. A physical separation could not be obtained on the installed GC column.

Gas phase samples were analyzed online in an *Agilent HP 6890* GC equipped with a thermal conductivity detector, a bonded polystyrene-divinylbenzene column (*HP PLOT-Q*, 30 m, 0.53 mm, 40 μm, column "A") and a packed molsieve column (*HP PLOT-MS5A*, 30 m, 0.32 mm, column "B"). The gaseous reactor effluent was directly transferred via a tube from the reactor into a sample loop (250 μL volume), constantly heated to 353 K, and then injected onto column A at 373 K using a split ratio of 10 (He). After elution and detection of CO_2 from column A, an internal valve was activated to pass the remaining analytes onto column B for further separation. The temperature of the column compartment was held constant at 323 K for 5 min and then heated to the final temperature of 473 K at a rate of 10 K min^{-1}. The column flow was maintained constant at 2 mL min^{-1}. The detector used He as a reference gas and was constantly heated to 523 K.

5.6.2   Catalyst characterization

Elemental analysis of the material obtained by thermal decomposition of $(NH_4)_2MoS_4$ in reductive environment at 673 K conformed to a mostly pure molybdenite $(Mo_{1.0}S_{2.1})$ having minor impurities of sulfur-rich phase as indicated by the slight excess of sulfur (Table S5.1).

Table S5.1. Physicochemical properties of metal sulfide catalysts and specific rates for hexadecanoic acid deoxygenation (573 K, 5.0 MPa hydrogen).

Catalyst	Elemental composition (atomic-%)			XRD phases	Specific surface area ($m^2\ g^{-1}$)
	Mo	Ni	S		
MoS_2	32.6	–	67.4	MoS_2	29.8
$Ni-MoS_2$	19.7	21.1	59.2	MoS_2, Ni_3S_2, Ni_9S_8	26.4
Ni_3S_2	–	59.7	40.3	Ni_3S_2	4.7

The mixed Ni-Mo sulfide had a composition according to the formula $Ni_{1.0}Mo_{1.0}S_{3.0}$ and thus exactly reflected the 1:1 molar ratio of Ni to Mo used in the preparation of the oxide. The lower metal to sulfur ratio in this material indicates the presence of sulfide species with sub-stoichiometric concentrations of sulfur. Indeed, X-ray diffraction patterns evidence the existence of crystalline NiS_{1-x} phases in addition to MoS_2 (Figure S5.1). The main constituent of nickel subsulfide phase was Ni_3S_2 with a minor contribution by Ni_9S_8, which can be expected to transform into Ni_3S_2 under reaction conditions (Figure S5.2).

The presence of segregated Ni-sulfides is a consequence of the high concentration of Ni in multimetallic precursors prepared by precipitation (effectively limiting the molar metal fraction of Ni to 0.5) and of the absence of a support.[4] To assess the reactivity of segregated Ni sulfide, a Ni_3S_2 sample was included in the study and characterized by the same means as MoS_2 and $Ni-MoS_2$. The surface area of Ni_3S_2 ($4.7\ m^2\ g^{-1}$) was considerably lower than that of MoS_2 and $Ni-MoS_2$ with 29.8 and $26.4\ m^2\ g^{-1}$, respectively. This conforms to the sharp and intense reflections found by XRD for pure Ni_3S_2, which are characteristic for a highly crystalline material with large particle size (Figure S5.1). Applying the Scherrer equation on the (110) reflection of Ni_3S_2, an average crystal

size of 214 nm was obtained for the pure material, whereas 75–217 nm were obtained for segregated Ni_3S_2 in Ni-MoS_2 (see section 5.6.7) From the average crystallite size, a surface area of 4.8 m² g^{-1} could be calculated for the pure Ni_3S_2, which is in excellent agreement with the value determined by N_2 physisorption (4.7 m² g^{-1}). An identical calculation performed for Ni_3S_2 in Ni-MoS_2 yielded a specific surface area of 5.5–16 m² g^{-1}, indicating that Ni_3S_2 in Ni-MoS_2 was moderately better dispersed than in pure Ni_3S_2. While Ni-sulfide dispersion was different, a corresponding analysis of the MoS_2 reflections revealed similar properties for MoS_2 and Ni-MoS_2: the respective crystallite size was 4.6 nm and 3.9 nm, corresponding to a stacking degree of 7.4 and 6.3.
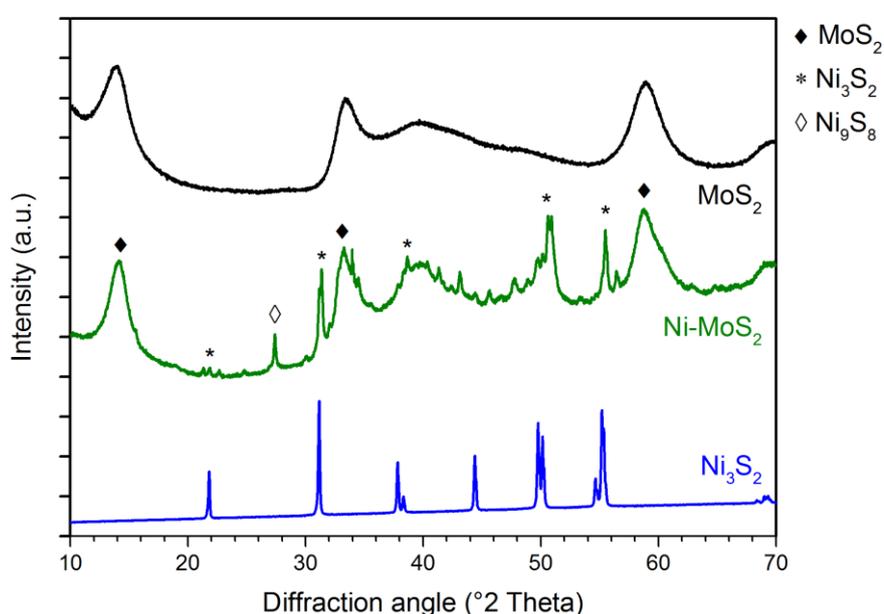

Figure S5.1. Powder X-ray diffractograms of transition metal sulfide catalysts before reaction. Intensity of Ni_3S_2 not to scale.

Post-reaction characterization in the case of Ni-MoS_2 showed dramatic changes to the segregated Ni sulfide components, while the MoS_2 phase was not affected by the catalytic test reactions (Figure S5.2). X-ray diffractograms of the used Ni-MoS_2 catalyst showed phase transformation of the Ni sulfide phases. While the fresh catalyst (before reaction) showed reflections attributed to Ni_3S_2 and Ni_9S_8, the spent catalyst (after 2 reactions at full conversion) shows only Ni_3S_2 reflections, which in addition are sharper and more intensive than in the fresh sample. Both diffractograms also exhibit characteristic MoS_2 reflections, but these are not affected by the catalytic test runs (unchanged position and stacking degree).

The disappearance of Ni_9S_8 in parallel with the intensification of Ni_3S_2 reflections indicate the transformation of one phase to the other in agreement to the known reduction of Ni_9S_8 (and other Ni sulfides) to Ni_3S_2 in the presence of hydrogen at elevated temperatures. The transition among the NiS_x phases does not affect our conclusions because they are not catalytically relevant.

The fact that Ni_3S_2 reflections were more intensive and sharper after reaction indicates the sintering of originally small particles to larger ones. This means that their specific surface area decreases, and therefore, their potential contribution to the total reaction rate decreases as well. This supports our conclusion that Ni sulfides are mere spectator species because the reaction rate is the same when a recycled catalyst is used instead of a fresh one, despite drastic transformations in the NiS_x phases (see section 5.6.10 for a more detailed discussion of catalyst stability).
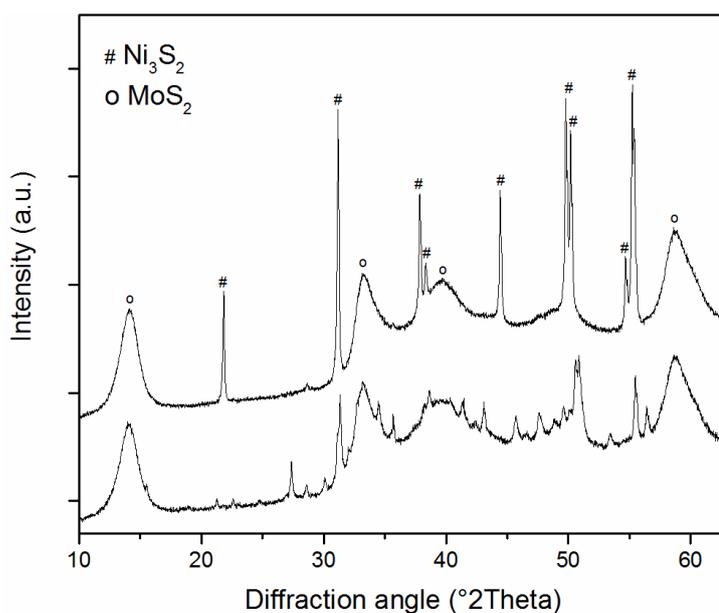

Figure S5.2. Powder X-ray diffractograms of Ni-MoS2 before (bottom) and after reaction (top).

5.6.3 Alkane/alkene equilibrium during HDO of fatty acids

We compared the observed molar fraction of 1-hexadecene in the hexadecene pool with the calculated molar fraction in an isomeric equilibrium mixture at reaction temperature (Figure S5.3). Note that the calculation was performed with octenes instead of hexadecenes because detailed thermodynamic data for the latter were not available. For the parameters of interest, however, it is expected that the calculations on octene give a good indication for the thermodynamics of hexadecene.
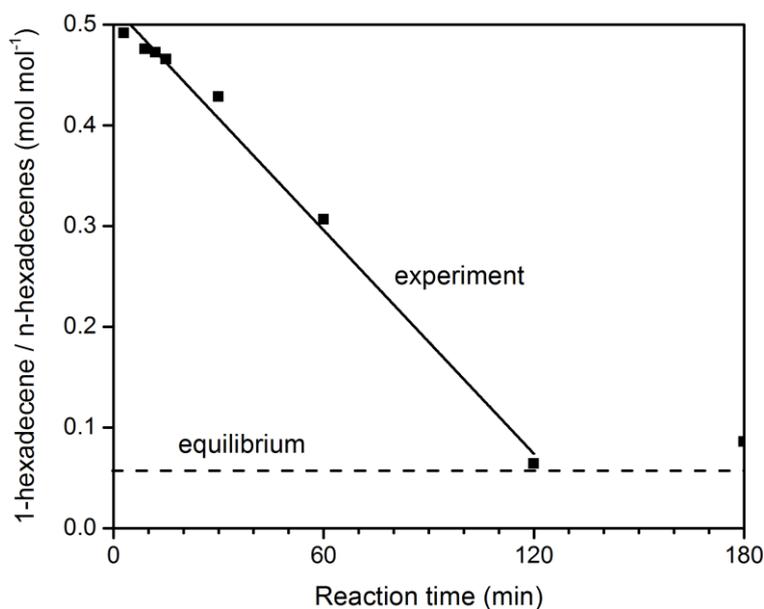

Figure S5.3. Experimental molar fraction of 1-hexadecene in the hexadecene pool and calculated molar fraction in an equilibrated isomeric mixture of hexadecenes. Reaction conditions: batch reactor, 573 K, 5.0 MPa H_2, catalyst (0.50 g L^{-1}), hexadecanoic acid (5.0 g L^{-1}), solvent (n-dodecane, to 100 mL).

5.6.4 Olefin hydrogenation on Ni-MoS$_2$ and MoS$_2$
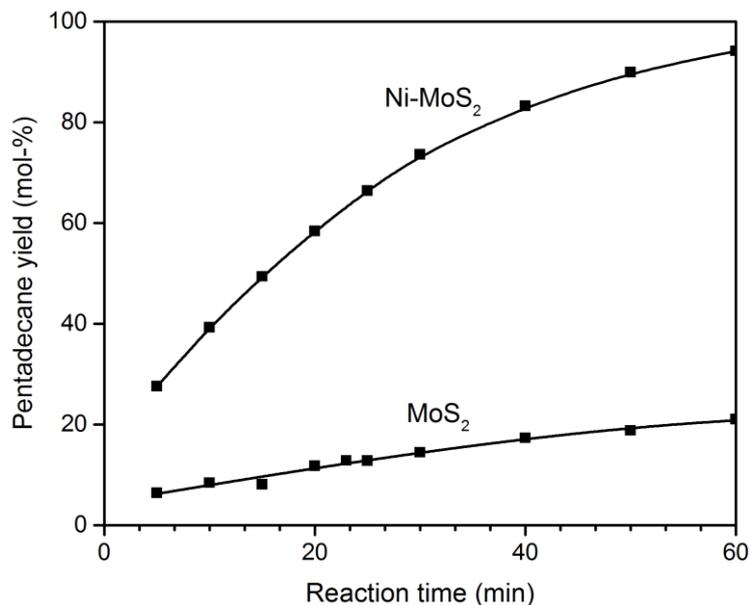
Figure S5.4. Concentration profiles obtained during hydrogenation of 1-pentadecene on Ni-MoS$_2$ and MoS$_2$ catalysts. Reaction conditions: batch reactor, 573 K, hydrogen (5.0 MPa), catalyst (0.25 g L^{-1}), 1-pentadecene (5.0 g L^{-1}), dodecane (to 100 mL).

5.6.5 Parallel evolution of CO and pentadecane/-decenes
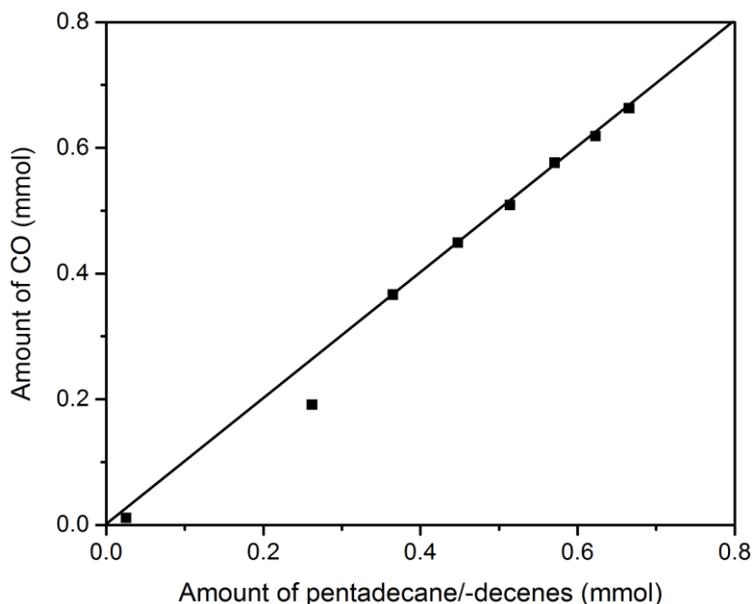
Figure S5.5. Parallel equimolar evolution of CO and pentadecane/-decenes during the deoxygenation of hexadecanoic acid on Ni-MoS$_2$. Reaction conditions: 573 K, hydrogen (5 MPa), hexadecanoic acid (5 g L^{-1}), catalyst (0.5 g L^{-1}), solvent (dodecane, to 100 mL).

5.6.6   Water-gas-shift equilibrium
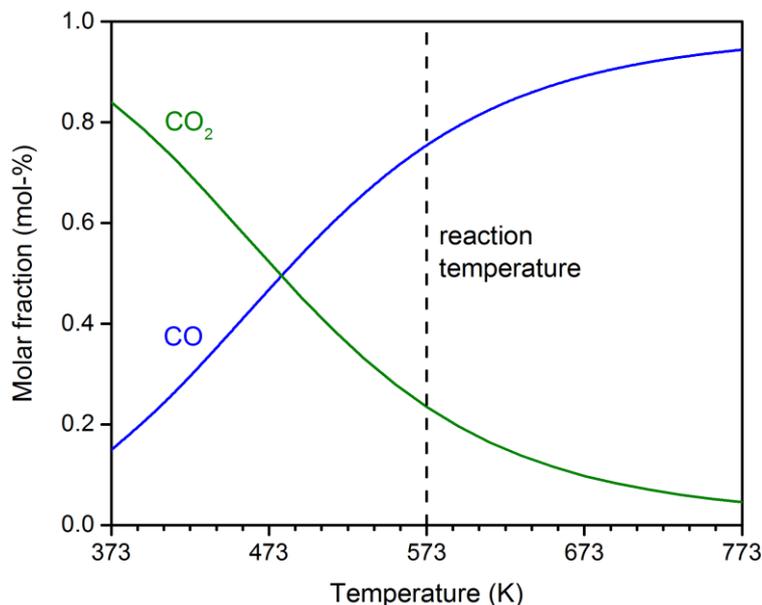
Figure S5.6. Calculated water-gas-shift equilibrium as a function of temperature for a 100-fold excess of hydrogen (1 mol CO_2, 100 mol H_2) at 5.0 MPa total pressure. The parameters were chosen as to represent the situation in the reactor during the deoxygenation of hexadecanoic acid (H_2 / reactant = 107 mol mol^{-1}).

5.6.7   Discrepancy between calculated/observed CLR rate on Ni-MoS$_2$

The specific decarbonylation rate of pure Ni_3S_2 was determined to be 6.5 mmol g^{-1} h^{-1}. This catalyst had a specific surface area of 4.7 m² g^{-1} (BET), which agrees well with the surface area estimated from XRD peak width using the Scherrer equation (4.8 m² g^{-1}). Accordingly, the surface-normalized decarbonylation rate amounts to 1.4 mmol m^{-2} h^{-1}. Ni-MoS$_2$ on the other hand, showed a specific decarbonylation rate of 28.4 mmol g^{-1} h^{-1}, which converts to a value of 99.0 mmol g^{-1} h^{-1}, if the rate is normalized to the mass of segregated Ni_3S_2 only (with 0.287 g of Ni_3S_2 per g of Ni-MoS$_2$, assuming all Ni is present in the form of Ni_3S_2). The surface area of segregated Ni_3S_2 was estimated to be between 5.5 and 16 m² g^{-1} from XRD peak width using the Scherrer equation (details below). Assuming that only the segregated Ni_3S_2 in Ni-MoS$_2$ is responsible for decarbonylation, its surface-normalized rate would need to be a factor 4.5 to 13 larger than in pure Ni_3S_2. Without introducing additional hypotheses to account for this discrepancy, we may, therefore, dismiss extra-crystalline Ni_3S_2 as the relevant active sites for decarbonylation in Ni-MoS$_2$.

Details of the calculation: baseline correction was done according to the Sonneveld-Visser algorithm in the *HighScore Plus* software package (*PANalytical*). For the 'strong' background correction a bending factor of 5 and a granularity of 30 were used, while for the 'weak' correction the corresponding parameters were 0 and 100, respectively. A series of Pseudo-Voigt functions were fitted under selected reflections assigned to segregated Ni-sulfides at the positions 27.4, 31.2 and 31.4 °2θ. Applying the Scherrer-formula with shape factor 0.9 to the respective peak widths (FWHM), we obtained a range of crystallite diameters between 75 and 217 nm (Table S5.2). These were then used to calculate the specific surface area of segregated Ni_3S_2 in $Ni\text{-}MoS_2$ (between 16 and 5.5 $m^2\,g^{-1}$).

Table S5.2. Observed powder diffraction parameters of segregated Ni_3S_2 in $Ni\text{-}MoS_2$ and calculated physical properties (crystallite size and specific surface area).

Position °2Theta	Strong background correction			Weak background correction		
	FWHM °2Theta	Diameter nm	Surface area $m^2\,g^{-1}$	FWHM °2Theta	Diameter nm	Surface area $m^2\,g^{-1}$
27.4	0.160	136.3	8.8	0.209	75.0	16.0
31.2	0.183	99.4	12.1	0.206	77.8	15.4
31.4	0.138	217.1	5.5	0.158	143.5	8.4

5.6.8   Possible role of reactive anhydride intermediates

Reactive anhydride intermediates have recently been proposed as a key species in the decarbonylation of carboxylic acids. Such species could form by condensation of two carboxylic acid molecules and subsequently decarbonylate to one terminal C_{n-1} olefin and one C_n carboxylic acid. While there are no reports in connection with sulfide catalysts yet, fatty acid decarbonylation was reported to proceed over anhydride intermediates on Pd/Al_2O_3 and $Ni(OAc)_2$ in nitrogen atmosphere.[5,6] Judging from our experimental results, however, the formation of reactive anhydride intermediates is an unlikely explanation for the decarbonylation of hexadecanoic acid. When hexadecanoic acid anhydride (HAA) was heated in hydrogen atmosphere in presence of $Ni\text{-}MoS_2$ catalyst (Figure S5.7), it was fully converted before the desired reaction temperature was reached (573 K). Up to a temperature of 473 K (46 % conversion) extensive hydrolysis of the anhydride was

observed and hexadecanoic acid was the only product present. Even though care was taken to perform the experiment in an anhydrous environment, residual trace amounts of water were obviously sufficient to hydrolyze a substantial fraction of the anhydride before other reactions started to set in. Only after significant concentrations of hexadecanoic acid were present, other products started to form, i.e., pentadecane and pentadecenes, as well as the HDO products hexadecanal, hexadecanol, hexadecane and hexadecenes. This supports the view that those products are formed from hexadecanoic acid. In addition, there was no direct evidence for anhydrides when the reactant was hexadecanoic acid, i.e., neither HAA itself could be detected, nor characteristic products, such as dipentadecyl ketone or hentriacontane. The fact that HAA was readily hydrolyzed in an almost anhydrous environment, even at moderate temperatures, clearly disfavors its suggested key role in hexadecanoic acid decarbonylation on Ni-MoS$_2$.
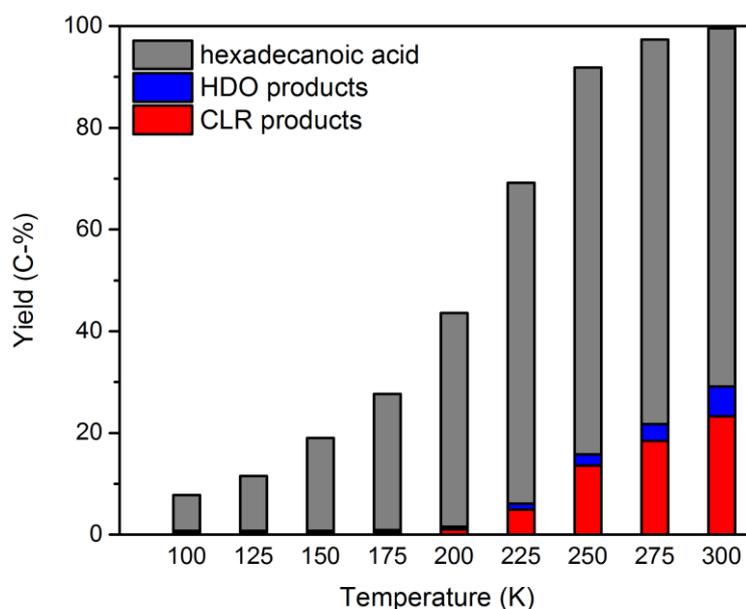
Figure S5.7. Temperature dependent product yields during the conversion of hexadecanoic acid anhydride on Ni-MoS$_2$. Reaction conditions: batch reactor, hydrogen (5.0 MPa), catalyst (0.5 g L^{-1}), hexadecanoic acid anhydride (5 g L^{-1}), dodecane (to 100 mL).

5.6.9   Temperature-dependent concentration profiles
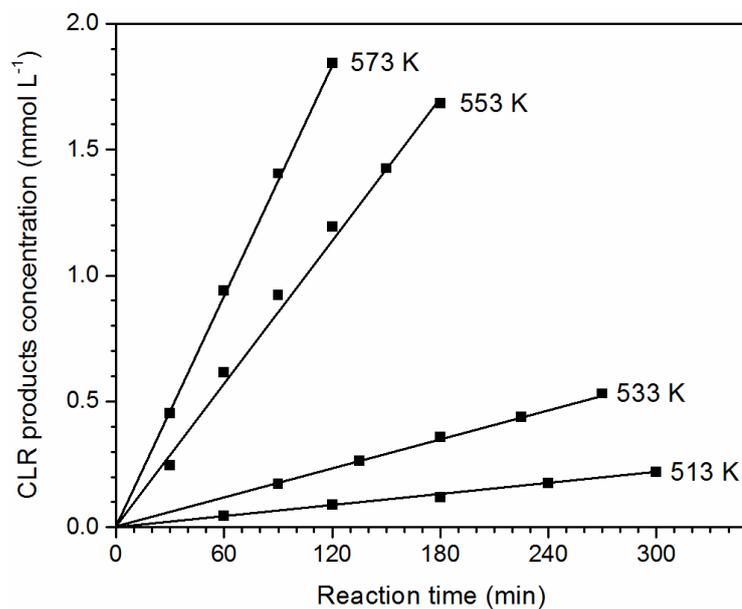
Figure S5.8. Initial evolution of pentadecane and pentadecenes products during hexadecanoic acid deoxygenation at different temperatures on Ni_3S_2. Reaction conditions: batch reactor, hydrogen (5.0 MPa), catalyst (0.5 g L^{-1}), hexadecanoic acid (5 g L^{-1}), dodecane (to 100 mL).
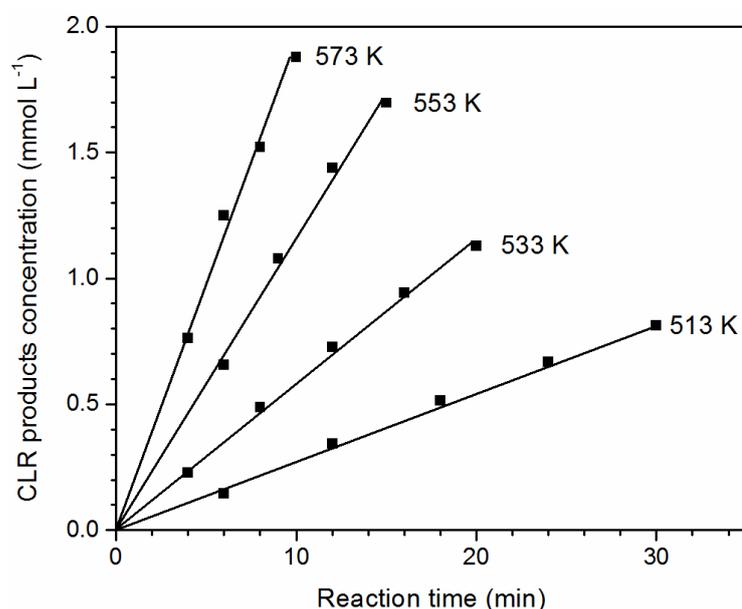
Figure S5.9. Initial evolution of pentadecane and pentadecenes products during hexadecanoic acid deoxygenation at different temperatures on Ni-MoS_2. Reaction conditions: batch reactor, hydrogen (5.0 MPa), catalyst (0.5 g L^{-1}), hexadecanoic acid (5 g L^{-1}), dodecane (to 100 mL).

5.6.10   Catalyst stability

Potential catalyst deactivation has to be considered when interpreting kinetic data. To rule out deactivation on the time scale of our experiments, we looked at the correlation of the logarithmic reactant molar fraction (ln $[c/c_0]$) and reaction time, which were linear in all cases. A deactivating catalyst would notably deviate from the linear correlation (see Figure S5.10).

In addition, we performed recycling experiments with used catalysts instead of freshly sulfide ones. For this purpose, we cooled down the reactor while still in hydrogen atmosphere after fully converting the first batch of reactant. Then a second batch of reactant was added and the reaction repeated under identical conditions. We obtained comparable rates in both catalytic test runs, indicating that deactivation did not occur under the tested conditions. On Ni-MoS$_2$, for example, the specific rates were 51.8 mmol g^{-1} h^{-1} and 53.0 mmol g^{-1} h^{-1} in the first and second run, respectively (the rates can be considered as equal within the experimental margin of error of approximately $\pm$ 5 %).
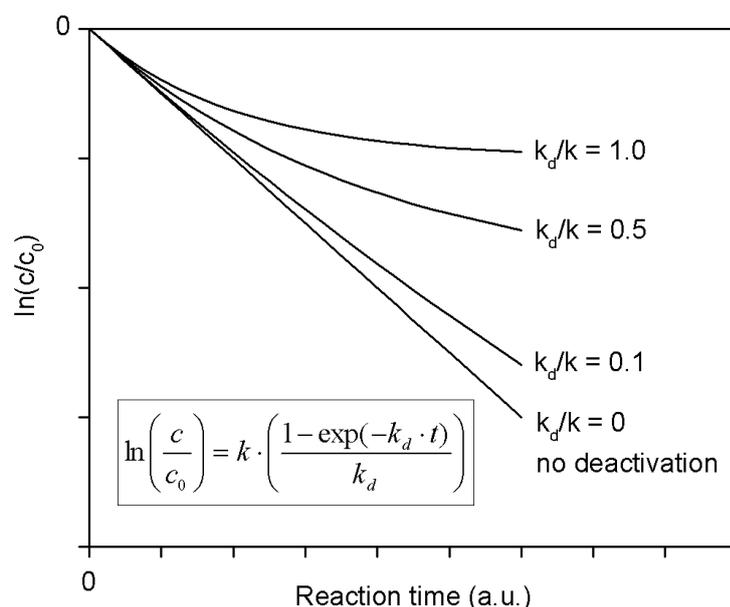

Figure S5.10. Linearized concentration-vs.-time plot for a first order reaction with different deactivation severity. The deactivation is modeled in terms of decreasing active site concentrations (i.e., site concentration decreases as a function of time and deactivation rate constant, see equations below).

Derivation of linearized first-order rate equation with first-order deactivation:

$$\frac{dc}{dt} = -k \cdot c \cdot N_S \tag{S5.4}$$

$$N_S = N_{S,0} \cdot e^{-k_d t} \tag{S5.5}$$

$$\frac{dc}{dt} = -k \cdot c \cdot N_{S,0} \cdot e^{-k_d t} \tag{S5.6}$$

$$\frac{1}{c(t)} dc = -k \cdot N_{S,0} \cdot e^{-k_d t} dt \tag{S5.7}$$

$$\int_c^{c_0} \frac{1}{c(t)} dc = -k \cdot N_{S,0} \cdot \int_0^t e^{-k_d t} \, dt \tag{S5.8}$$

$$\ln\left(\frac{c}{c_0}\right) = -k \cdot N_{S,0} \cdot \frac{1 - e^{-k_d t} dt}{k_d} \tag{S5.9}$$

with

$\frac{dc}{dt}$	Rate of reactant consumption
k	Rate constant
k_d	Deactivation rate constant
N_S	Number of sites
$0, t$	At $t = 0$, $t = t$

5.6.11   Influence of mass transfer limitations

To ensure that the measurements were conducted in absence of external mass transfer limitations, a series of experiments with varying stirring rate was performed, showing no further increase of the hexadecanoic acid consumption rate above 500 rpm. To exclude internal mass transfer limitations, we used a theoretical approach and calculated the effectiveness factor as a function of particle diameter (Figure S5.11). Using a simple digital microscope (Figure S5.12) we recorded micrographs of the powders, which show loose agglomerates of very fine particles (estimated diameter 5–10 µm). This results in effective-ness factors very close to 1 and indicates that internal diffusion limitations are not relevant under the studied reaction conditions.

The binary diffusion coefficient of hexadecanoic acid in dodecane was calculated following the empirical Wilke-Chang formula[7]:

$$D_{AB} = 7.4 \times 10^{-8} \cdot \frac{T}{\mu_B} \cdot \frac{(x \cdot M_A)^{\frac{1}{2}}}{V_A^{0.6}} \qquad \text{(S5.10)}$$

with:

D_{AB} Binary diffusion coefficient of solute A in solvent B

                (1.58×10^{-4} cm²/s)

T Temperature (573 K)

μ_B Dynamic viscosity of solvent at T (0.100 cP = mPa s, obtained by extrapolation from 473 K to 573 K using a power law)

x Association parameter (1 for hydrocarbons)

M_A Molecular weight of solvent (170 g/mol)

V_A Molecular volume of solute at normal boiling point (379 cm³/mol, using additive method according to Le Bas[8])

The binary diffusion coefficient D_{AB} was then used to calculate an effective diffusion coefficient for the diffusion in the catalyst pores:

$$D_{AB,pore} = D_{AB} \cdot (1 - \lambda)^4 = D_{AB} \cdot \left(1 - \frac{d_S}{d_{pore}}\right)^4 \qquad \text{(S5.11)}$$

with:

$D_{AB,pore}$ Effective diffusion coefficient in porous solid (1.04×10^{-4} cm²/s)

D_{AB} Binary diffusion coefficient in bulk (1.58×10^{-4} cm²/s)

λ Hindrance factor (0.1)

d_S Effective (smallest) diameter of solute

            (5 Å for linear hydrocarbons)

d_P Diameter of pores (50 Å, median pore diameter from BJH analysis)

Calculation of the Thiele modulus and effectiveness factor (for spherical particle):

$$\phi = \frac{R_p}{3} \cdot \sqrt{\frac{k}{D_{AB,pore}}} \qquad \eta = \frac{\tanh(\phi)}{\phi} = \frac{k_{obs}}{k} \qquad (S5.12)$$

with:

ϕ	Thiele modulus (calculated for different particle radii)
R_p	Particle radius (from 0.5 to 5000 µm)
k_{obs}	Observed rate constant (0.737 cm³/(g s))
k	True rate constant in absence of mass transfer limitations
$D_{AB,pore}$	Effective diffusion coefficient in porous solid (1.04×10^{-4} cm²/s)

The two expressions (for ϕ and η) were then combined and iteratively solved for k at different particle radii. The results are given in the diagram below. While effectiveness factors are already a good indicator for the influence of mass transfer, it is also useful to apply the Weisz-Prater criterion ($\Psi = \eta \cdot \phi^2 < 1$ in absence of internal diffusion limitations), which is easily fulfilled in our case. Ψ becomes much smaller than 1 for particle diameters below 200 µm, while we determined the particle size in our catalysts to be approximately 5–10 µm.
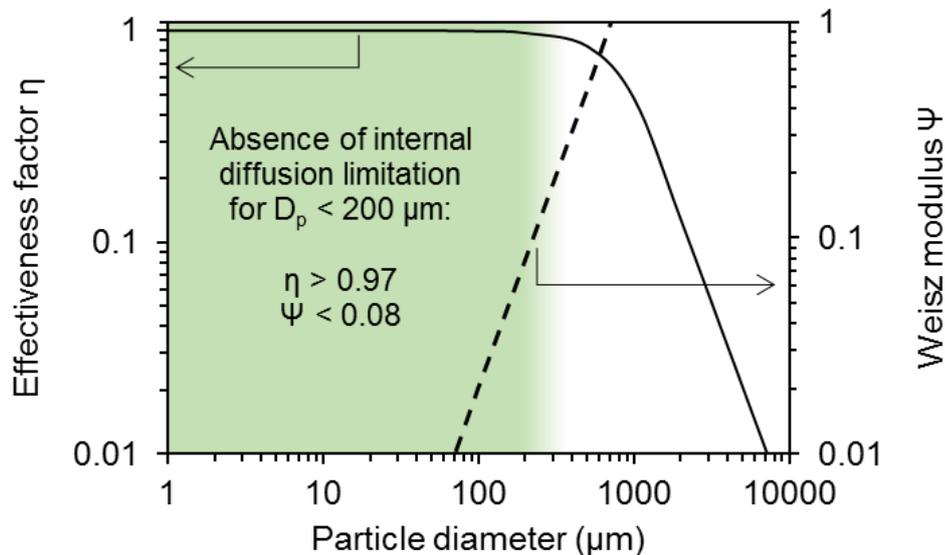
Figure S5.11. Effectiveness factor and Weisz modulus calculated for Ni-MoS₂ as a function of particle diameter. The highlighted area corresponds to particle diameters < 200 µm, where the influence of internal diffusion can be neglected.
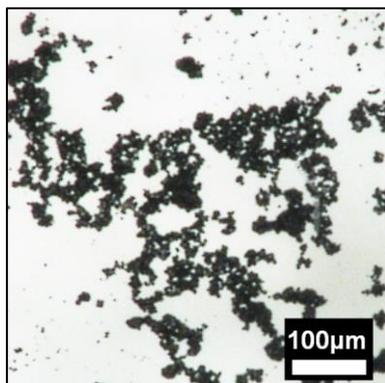
Figure S5.12. Optical micrograph of the catalyst powder (Ni-MoS$_2$). Loose aggregates of fine primary particles (5–10 μm) are visible.

5.6.12   References for supporting information

(1)   Maesen, T. L. M.; Kuperman, A. E. *Patent* US 8,702,970 B2, **2014**.

(2)   Ruinart de Brimont, M.; Dupont, C.; Daudin, A.; Geantet, C.; Raybaud, P. *J. Catal.* **2012**, 286, 153-164.

(3)   Bezverkhyy, I.; Danot, M.; Afanasiev, P. *Inorg. Chem.* **2003**, 42, 1764-1768.

(4)   Hein, J.; Hrabar, A.; Jentys, A.; Gutiérrez, O. Y.; Lercher, J. A. *ChemCatChem* **2014**, 6, 485-499.

(5)   Hollak, S. A. W.; Bitter, J. H.; van Haveren, J.; de Jong, K. P.; van Es, D. S. *RSC Adv.* **2012**, 2, 9387-9391.

(6)   Li, W.; Gao, Y.; Yao, S.; Ma, D.; Yan, N. *Green Chem.* **2015**, 17, 4198-4205.

(7)   Wilke, C. R.; Chang, P. *AlChE J.* **1955**, 1, 264-270.

(8)   Arnold, J. H. *Ind. Eng. Chem.* **1930**, 22, 1091-1095.

6   Concluding summary

Hydrotreating is one of the most important industrial applications of heterogeneous catalysis. In this process, petroleum fractions are exposed to hydrogen at high temperature and pressure to remove heteroatoms bound in organic compounds and to saturate olefins and aromatics. The removal of heteroatoms, in particular sulfur and nitrogen, is not only necessary because of increasingly demanding environmental regulations but also because catalysts used in other refinery processes are irreversibly poisoned by these elements. The catalysts employed in hydrotreating contain transition metal sulfides (TMS) as the active phase, most typically alumina-supported MoS_2 promoted by Ni or Co. In recent years, also highly active unsupported catalysts have started to become more common in industry mainly as a result of tighter fuel specifications and the need to upgrade "heavier" feedstock (i.e., petroleum of poor quality). The historical development and the current state-of-the-art of hydrotreating catalysis are reviewed in chapter 2 of this thesis.

In addition to being the workhorse of today's refineries, transition metal sulfides may also play a key role in the production of sustainable hydrocarbon fuels. Hydrotreating of lipid biomass could be a practical alternative to the petroleum based process, as the resulting biofuels are chemically and functionally identical to their conventional pendants. Hydrotreated lipids could be merged with relative ease into the existing network of fuel distribution and refining, which is not possible with contemporary biofuels like biodiesel and bioethanol. The potential challenges and benefits of lipid hydrotreating, as well as our current understanding of the science behind these transformations are reviewed in chapter 3.

The present work is focused on unsupported ("bulk") catalysts, which is not only because of the recent industrial interest in these materials but also because only the absence of a support allows one to isolate the properties of the active sulfide phase (no confounding support interactions). Unfortunately, some valuable characterization techniques like infrared spectroscopy are not applicable to bulk sulfides. In addition, bulk sulfides are particularly affected by promoter segregation, which further adds to their complicated characterization. Essential questions regarding the catalytic features of bulk TMS have thus been left unanswered. Most importantly, it has proven difficult to establish

firm structure-activity relationships, even though these are vital for the development of more active and selective catalysts. Note that this lack of knowledge applies similarly to catalysts used in conventional applications, e.g., desulfurization of petroleum fractions, and those envisaged for novel process, such as lipid hydrotreating. Regarding hydrodesulfurization (HDS) catalysts, enhancing the hydrogenation performance will be a key step towards the conversion of increasingly refractory feedstock at moderate temperature (chapter 4). By contrast, one of the greatest challenges concerning catalysts for lipid hydrotreating will be to understand and control the formation of carbon oxides, as these by-products severely decrease the overall efficiency of the process (chapter 5). Accomplishing these tasks requires that the active structures and their interaction with reactants are sufficiently well understood.

The first piece of original research in this thesis (chapter 4) is focused on bulk Ni-Mo sulfides as catalytic materials for HDS. The major objective is the identification, quantification, and the structural and electronic characterization of the active sites in the Ni-Mo-S phase (as compared to the inactive segregated Ni sulfides, NiS_x). For this purpose, four unsupported MoS_2-based catalysts with varying Ni content were prepared by hydrothermal reaction and subsequent sulfidation in liquid phase. Unpromoted MoS_2 and Ni_3S_2 were used as reference compounds. One portion of each material was further subjected to an acidic treatment ("leaching"), which consisted in repeatedly soaking the pressed sulfide powders in concentrated HCl. This procedure was accompanied by gas evolution (H_2S) and a greenish coloration of the solution, indicating dissolution of NiS_x. As a result, all catalyst samples, except unpromoted MoS_2, exhibited a substantial mass loss on the order of 25 wt%.

All mixed Ni-Mo sulfides showed poorly defined reflections of nanocrystalline MoS_2 in their X-ray powder diffractograms, while reflections of Ni sulfides were only present in the untreated ("parent") sulfides. In agreement with these results, elemental analysis showed a substantial decrease in the atomic Ni/(Ni+Mo) ratio after leaching (from 0.48–0.60 to 0.20–0.26). Similarly, scanning electron microscopy evidenced the disappearance of particles identified as segregated Ni sulfides, while MoS_2 was not affected. Based on the combined evidence, it is concluded that HCl selectively removes NiS_x particles without reacting with MoS_2. The stability of MoS_2 in presence of HCl was confirmed experimentally and is also supported by thermodynamic considerations (Pourbaix

diagram). Furthermore, a substantial increase in the specific surface area of the Ni-MoS$_2$ catalysts was noted upon acid exposure (factor 2), with the exception of one sample. The changes in surface area are attributed to the uncovering of pore openings and corrugated surface regions previously blocked by NiS$_x$.

Extended X-ray absorption fine structure (EXAFS) at the Ni K-edge evidenced the presence of a Ni-Mo contribution in the leached sulfides. The Ni-Mo distance was determined to be 2.86 Å and thus somewhat shorter than between Mo atoms in MoS$_2$ (3.2 Å). This close proximity indicates that Ni atoms are chemically bound to MoS$_2$, forming a bimetallic Ni-Mo-S phase ("incorporated" Ni). In the parent sulfides, by contrast, no Ni-Mo contribution was observed, which was attributed to the predominance of segregated NiS$_x$ combined with the averaging nature of the measurement. Similar conclusions can be drawn from leaching-associated changes in the near-edge structure (XANES). Leaching also led to a significantly smaller average Ni-S distance (2.22 Å vs. 2.26 Å), which is incompatible with any known Ni sulfide and was therefore assigned to Ni-S bonds in the Ni-Mo-S phase. Fitting of EXAFS results with simulated spectra of model clusters showed that approximately square-pyramidal NiS$_5$ units are the most likely structure of Ni at the MoS$_2$ edge (similar to the structural motif of millerite (NiS), a naturally occurring Ni sulfide).

The distribution of Ni among the active Ni-Mo-S phase and inactive NiS$_x$ was analyzed using a combination of site titration and geometric considerations (obtained by transmission electron microscopy). For the purpose of site quantification, NO was used as a probe molecule, as it selectively adsorbs on coordinatively unsaturated metal cations (CUS) at the edges of Ni-MoS$_2$, which are generally accepted as the active sites in HDS. Untreated samples were estimated to have a 4- to 5-fold excess of Ni with respect to the calculated maximum amount of Ni incorporable at the MoS$_2$ edges. It is therefore concluded that the vast majority of Ni in the parent sulfides is present as segregated NiS$_x$ (90–92 % of Ni), which is in good agreement with EXAFS results. Accordingly, the proportion of Ni in the active Ni-Mo-S phase was estimated to be a mere 8–10 %. Even though the excess of Ni was much smaller after leaching (< 2-fold), it is likely that the treated sulfides still contained considerable amounts of NiS$_x$ (60–76 % of Ni in NiS$_x$ vs. 24–40 % in Ni-Mo-S). It is speculated that NiS$_x$ in the latter might be present in the form of inaccessible ("internal") domains.

As expected from the higher surface area and higher fraction of "active" Ni (Ni-Mo-S), the leached sulfides converted dibenzothiophene (DBT) with much higher mass-specific activity (factor 1.6–2.3) under the studied reaction conditions (330 °C, 50 bar H_2, bench-scale trickle-bed reactor). It is important to note that the rate enhancement exceeded the effect of inert mass loss, that is, the concentration of active sites was increased by acid treatment ("unblocking" of sites). The product distribution was similar across all catalysts and not affected by leaching, which indicates a similar composition of newly uncovered and previously blocked active surfaces.

The combination of HDS activity data and site titration revealed a linear correlation between CUS concentration and direct desulfurization rates (DDS), indicating the presence of active sites with identical intrinsic activity (turn-over frequency: $70 \, h^{-1}$ for DDS and $140 \, h^{-1}$ for HYD). By contrast, no correlation was found for the parent samples, which was attributed to added inert mass and site blocking by NiS_x at the accessible surface. For the leached sulfides, a correlation was also found between CUS and SH group concentration. While CUS serve as "primary" active sites for reactant adsorption and coordination, SH groups are critical for supplying dissociated hydrogen for hydrogenolysis and hydrogenation reactions. Accordingly, this second correlation stresses the importance of SH groups for HDS catalysis and confirms earlier proposals of fixed CUS-SH stoichiometry.

Equivalent kinetic and titration measurements on alumina supported $Ni-MoS_2$ showed a comparable site-normalized DDS activity. The hydrogenation activity, on the other hand, was much higher on the bulk sulfides (factor 15). It is speculated that the lower averaged Sanderson electronegativity (due to the lack of Mo-O-Al linkages) and the possibility of planar π-adsorption of DBT on the stacked edges of bulk $Ni-MoS_2$ jointly increase the intrinsic hydrogenation activity of CUS.

From an academic perspective, acidic treatment is a valuable pre-analytic technique for reducing the contribution of segregated sulfides to analytic results (e.g., EXAFS spectra), even though it is obviously incapable of completely eliminating the problem. The most important reason for this is the fact that a considerable portion of NiS_x, located at the interior of the MoS_2 structure, is not dissolved by the acid. Future studies should therefore focus on the preparation of bulk catalysts that lack such internal NiS_x domains. This may

be achieved, for example, by impregnating well-defined MoS_2 crystals with a Ni(II) salt solution, followed by sulfidation and finally acidic treatment. In contrast to the present synthesis protocol, this modified sequence would ensure that Ni atoms are exclusively present at the accessible edges of MoS_2. The combination of the total absence of NiS_x with a well-defined MoS_2 structure may further enhance the validity of analytical measurements. Of course, the approach may be extended to other metal combinations of interest, for example, Ni-WS_2, which is expected to give similar results due to the similar chemistry of Mo and W. That said, even supported sulfides might be in the scope of such treatments, although care should be taken to consider additional effects of the acid on the support. From an applied point of view, acidic treatment could be a scalable route for optimizing the performance of bulk catalysts employed in the more demanding hydrotreating operations like residue HDS. Hydrogenation activity is often the bottleneck in such applications, as heavy feedstocks contain large amounts of polynuclear aromatics that can only be defunctionalized after prior hydrogenation (i.e., H_2 addition before C-S bond scission).

The second piece of original research (chapter 5) is dedicated to the deoxygenation (DO) of renewable lipid feedstock on hydrotreating catalysts. Also in this case and for the reasons mentioned earlier, bulk sulfides were chosen as a basis for the study. In view of the complex composition of naturally occurring lipids, test reactions were performed with fatty acid model compounds and their derivatives to facilitate product analysis. The reactions were carried out in liquid phase (reactant diluted in dodecane) using a bench-scale autoclave reactor operated in batch mode at 300 °C and 5.0 MPa H_2.

The main objective of the study is the elucidation of the reaction network and the molecular-scale reaction mechanism of fatty acid deoxygenation on bulk Ni-MoS_2. To achieve this goal, a set of catalysts was prepared with the aim to obtain maximal differences in selectivity towards the DO of the primary model compound, hexadecanoic acid (C_{16}). Of these three materials, unpromoted MoS_2 had the highest preference for the hydrodeoxygenation pathway (94 mol% HDO). During this sequential reduction, oxygen is eliminated as water and the corresponding alkane (hexadecane) is formed, while the number of carbon atoms of the fatty acid remains unchanged. In contrast to that, Ni_3S_2 converted the fatty acid primarily via carbon-loss routes (CLR), that is, by C-C scission

at the carboxyl carbon atom (94 mol% CLR). The mixed Ni-Mo sulfide catalyst, on the other hand, showed a balanced product distribution of 45 % HDO and 55 % CLR.

These vastly different selectivities proved to be essential for separating the reaction pathways and understanding the reaction network. It was found that HDO consists of a series of subsequent reactions initiated by C-O hydrogenolysis. The formation of the primary product, hexadecanal, is followed by hydrogenation to the corresponding alcohol, dehydration to 1-hexadecene, and finally hydrogenation to hexadecane. An alternative conversion route for the alcohol, C-O hydrogenolysis, was excluded by analyzing the olefin isomer fraction and the olefin/alkane ratio during the course of the reaction. Similarly, nucleophilic substitution by surface SH groups was ruled out by excluding the presence of thiols and other S containing derivatives, and by analyzing the spent catalyst for losses of sulfur. As expected from the simultaneous presence of fatty acids and alcohols, C_{32} ester formation was observed as a minor side reaction in HDO.

Concerning CLR, an analysis of the gas phase showed that the formation of liquid C_{n-1} products (pentadecane and pentadecenes) was accompanied by the evolution of an equimolar amount of CO. However, as the detection of CO is compatible with several mechanistic proposals, additional experiments had to be performed to narrow down the pool of hypotheses. Specifically, CO formation could also result from the following reactions:

(i) Primary CO_2 release and subsequent reverse water-gas shift reaction ("masked" decarboxylation): This possibility was excluded based on the total absence of CO_2, even though the equilibrium concentration of CO_2 as predicted by thermodynamics would have been well within the detection limit.

(ii) Decarbonylation of hexadecanal formed in the HDO route: This reaction was excluded by running an experiment with hexadecanal as the primary reactant, which was converted almost exclusively according to the HDO pathway over Ni-MoS$_2$ (93 % selectivity). The experiment was repeated in presence of excess fatty acid to rule out competitive effects.

(iii) Direct C-C hydrogenolysis of hexadecanoic acid to pentadecane and formic acid (i.e., CO formation by decomposition of formic acid to CO and H_2O): This alternative is

deemed unlikely because neither formate esters nor gaseous formic acid could be detected. The high selectivity for pentadecenes in the initial reaction stage also disagrees with C-C hydrogenolysis, as the latter would directly lead to pentadecane formation.

(iv) Decarbonylation of surface acylium ions ($R–C^+=O$) to terminal C_{n-1} olefins: While this mechanism could not be generally excluded, it was shown that an alternative mechanism whose primary product is a C_{n-1} alkane must exist. For this purpose, an experiment was performed using a carboxylic acid with a tertiary β C atom (2-adaman-tanylacetic acid). Even though this compound does not allow for C_{n-1} olefin formation, it was still converted via CLR just like the linear fatty acids.

It is inferred from the combined evidence that a ketene is the most likely primary intermediate in CLR. The ketene is formed by dehydration (C-O cleavage) of the fatty acid on the coordinatively unsaturated sites of Ni-MoS$_2$, a process assisted by adjacent basic S anions. The following regeneration of the active site (i.e., removal of O) can be the rate determining step, if H$_2$ partial pressure is lower than about 2.5 MPa. By contrast, the rate determining step at higher H$_2$ partial pressure (>2.5 MPa) was determined to be the decarbonylation (i.e., the C-C cleavage) of the ketene, which is present in form a η^2(C-C) adsorption complex. The shift of the rate determining step is inferred from the observed variations in reaction order resulting from different H$_2$ pressure. Subsequent elimination of CO from the adsorption complex results in the formation of a Ni-bound carbene-like species, which then reacts to a C_{n-1} alkane (by hydrogenation) or to a terminal C_{n-1} olefin (by rearrangement and simultaneous Ni-C cleavage), depending on the availability of β H atoms. This mechanistic proposal for the catalytic cycle of CLR is in agreement with the well-known reactivity of ketenes and, in particular, with their pronounced tendency to undergo decarbonylation. The fundamentally different reactivity of Ni-MoS$_2$ as compared to MoS$_2$ is attributed to the labilized, electron-rich S sites resulting from the presence of Ni. It should be acknowledged that also Ni sulfides, represented by Ni$_3$S$_2$ in this study, showed a pronounced selectivity for CLR, even though their contribution was determined to be much smaller than that of the Ni-promoted sites in the Ni-Mo-S phase. Furthermore, apparent activation energies on NiS$_x$ and Ni-MoS$_2$ were substantially different, thus indicating that CLR on Ni-MoS$_2$ was not associated with the simultaneous presence of NiS$_x$.

The present results on fatty acid DO show that C-C bond scission is inherently linked to the primary active sites of sulfide-based hydrotreating catalysts. That is, the catalytic features that enable high HDS and HDN activity in the processing of petroleum-based feedstock are the very same that lead to undesirable CO formation in the processing of renewable lipids. This is an unfortunate situation, because catalyst-related strategies for limiting CO formation in co-processing could have adverse effects on the conversion of the primary HDS/HDN feed. While part of this dilemma might be resolved by rational catalyst design, other parameters like temperature, pressure, and feedstock composition have to be considered as well, if the large-scale co-processing of renewable lipids is to become an industrial reality. As these trade-offs have to be assessed individually for each application, hydrotreating of lipids is expected to remain a highly challenging topic.

7 Abschließende Zusammenfassung

Hydrotreating ist eine der bedeutendsten industriellen Anwendungen von heterogener Katalyse. In diesem Prozess werden Erdölfraktionen bei hohem Druck und hoher Temperatur mit Wasserstoff umgesetzt, um Heteroatome aus organischen Verbindungen zu entfernen. Unter diesen Bedingungen findet auch eine teilweise Sättigung von Olefinen und Aromaten statt. Die Entfernung von Heteroatomen, insbesondere Schwefel und Stickstoff, ist nicht nur wegen der immer strikteren Umweltschutzvorschriften nötig, sondern auch weil Katalysatoren, die in anderen Raffinerieprozessen verwendet werden, durch diese Elemente irreversibel vergiftet werden. Die Katalysatoren, die beim Hydrotreating zum Einsatz kommen, enthalten Übergangsmetallsulfide (TMS) als aktiven Bestandteil. Üblicherweise handelt es sich dabei um Alumina-geträgertes MoS_2, das mit Ni oder Co promotiert ist. In jüngerer Zeit finden zunehmend auch hochaktive, ungeträgerte Katalysatoren Anwendung. Dies ist hauptsächlich auf strengere Kraftstoffspezifikationen zurückzuführen und auf die Notwendigkeit, immer „schwerere" Ausgangsstoffe verarbeiten zu müssen (also Rohöle von schlechterer Qualität). Die historische Entwicklung der Hydrotreating-Katalyse und der aktuelle Stand der Technik werden in Kapitel 2 dieser Arbeit ausführlich erörtert.

Neben ihrer Bedeutung als „Arbeitspferde" der modernen Raffinerie könnten Übergangsmetallsulfide auch bei der Produktion von nachhaltigen, kohlenwasserstoffbasierten Kraftstoffen eine Schlüsselrolle spielen. Hydrotreating von Lipidbiomasse könnte dabei eine praktikable Alternative zum erdölbasierten Prozess sein, da die entstehenden Produkte chemisch und funktional identisch zu ihren konventionellen Gegenstücken sind. Solche Biokraftstoffe könnten relativ einfach in bestehende Raffinerie- und Verteilungsnetzwerke eingebunden werden, was mit den heutigen Biokraftstoffen wie Biodiesel und Bioethanol nicht möglich ist. Kapitel 3 dieser Arbeit fasst den heutigen Wissensstand über das Hydrotreating von Lipidbiomasse zusammen und erörtert, welche Herausforderungen und Möglichkeiten sich dadurch ergeben.

Der Schwerpunkt dieser Dissertation liegt auf ungeträgerten Katalysatoren. Dies ist nicht nur dem gegenwärtigen industriellen Interesse an solchen Materialien geschuldet,

sondern auch der Tatsache, dass sich die Eigenschaften der aktiven Phase erst in Abwesenheit der Trägersubstanz offenbaren (weil dann keine störenden Wechselwirkungen mit dem Träger vorliegen). Leider sind einige sehr aussagekräftige Charakterisierungstechniken, wie beispielsweise die Infrarotspektroskopie, nicht für die Anwendung mit ungeträgerten Sulfiden geeignet. Deren Charakterisierung wird außerdem noch dadurch erschwert, dass diese Stoffe in hohem Maße zur Segregation der Promotormetalle neigen. Grundlegende Fragen bezüglich ihrer katalytischen Merkmale sind daher unbeantwortet geblieben. So hat es sich etwa als besonders schwierig erwiesen, robuste Struktur-Aktivitätsbeziehungen aufzustellen, obwohl dies die Grundvoraussetzung für die Entwicklung von aktiveren und selektiveren Katalysatoren darstellt. Diese Wissenslücke betrifft sowohl Katalysatoren für konventionelle Anwendungen, etwa für die Entschwefelung von Erdölfraktionen, als auch solche, die für neuartige Prozesse gedacht sind, wie etwa für das Hydrotreating von Lipidbiomasse. Bei den Katalysatoren für Hydroentschwefelung (HDS) wird vor allem die Verbesserung der Hydrieraktivität ein Schlüsselschritt sein, wenn es darum geht zunehmend schwerer umzusetzende Ausgangsstoffe bei moderaten Temperaturen zu verarbeiten. Im Gegensatz dazu besteht die größte Herausforderung bei den Katalysatoren für Lipid-Hydrotreating darin, die Bildung von Kohlenoxiden zu verstehen und zu kontrollieren, da solche Nebenprodukte die Gesamteffizienz der Prozesskette erheblich verringern. Um diese Ziele zu erreichen, ist es unbedingt nötig die aktiven Strukturen und ihre Wechselwirkung mit den Reaktanden in ausreichendem Maße zu verstehen.

Der erste Teil der eigentlichen Forschungsarbeit (Kapitel 4) befasst sich mit ungeträgerten Ni-Mo-Sulfiden als HDS-Katalysatoren. Hauptziel der Arbeit ist die Identifizierung und Quantifizierung sowie die strukturelle und elektronische Aufklärung der Eigenschaften der aktiven Zentren in der Ni-Mo-S-Phase (im Gegensatz zu den inaktiven segregierten Ni-Sulfiden, NiS_x). Zu diesem Zweck wurden zunächst vier ungeträgerte MoS_2-basierte Katalysatoren mit veränderlichem Ni-Gehalt hergestellt, wofür eine hydrothermale Syntheseroute mit anschließender Sulfidierung in Flüssigphase zum Einsatz kam. Nicht-promotiertes MoS_2 und Ni_3S_2 dienten als Referenzsubstanzen. Ein Teil eines jeden Materials wurde zusätzlich einer Säurebehandlung unterzogen, wobei die gepressten Sulfidpulver mehrere Male einer konzentrierten HCl-Lösung ausgesetzt

wurden. Während dieses Vorgangs kam es zu Gasentwicklung (H_2S) und zu einer Grün-färbung der Lösung, was auf eine Auflösung von NiS_x hindeutet. Infolgedessen wiesen alle Proben bis auf MoS_2 einen erheblichen Massenverlust in der Größenordnung von 25 % auf.

Alle Ni-Mo-Mischsulfide wiesen im Röntgen-Pulverdiffraktogramm schlecht defi-nierte Reflexe von nanokristallinem MoS_2 auf, während nur bei den unbehandelten Sulfiden auch Reflexe von Ni-Sulfiden sichtbar waren. In Übereinstimmung mit diesem Ergebnis ergab die Elementaranalyse eine erhebliche Abnahme des Ni/(Ni+Mo)-Verhältnisses infolge der Säurebehandlung (von 0.48–0.60 auf 0.20–0.26). Mittels Rasterelektronenmikroskopie konnte gezeigt werden, dass die als Ni-Sulfid identifi-zierten Partikel entfernt worden waren, während MoS_2 unverändert zurückblieb. Auf Grundlage der gesammelten Erkenntnisse ist davon auszugehen, dass HCl in der Lage ist, NiS_x selektiv zu entfernen ohne mit MoS_2 zu reagieren. Die Stabilität von MoS_2 in Gegenwart von HCl wurde experimentell bestätigt und wird außerdem von thermodyna-mischen Betrachtungen gestützt (Pourbaix-Diagramm). Zusätzlich zu den angeführten Veränderungen wurde auch eine erhebliche Vergrößerung der spezifischen Oberfläche der Ni-MoS_2-Katalysatoren beobachtet (Faktor 2, mit der Ausnahme eines Katalysators). Dies wird auf das Freilegen von rauen („zerfurchten") Oberflächen und Porenöffnungen zurückgeführt, die zuvor von NiS_x bedeckt waren.

Die Röntgen-Feinstrukturanalyse (EXAFS) an der Ni K-Kante ergab bei den säure-behandelten Sulfiden Hinweise auf die Anwesenheit einer Ni-Mo-Komponente. Der Abstand zwischen Ni und Mo wurde dabei zu 2.86 Å bestimmt, was etwas kürzer ist als der Abstand zwischen zwei Mo-Atomen in MoS_2 (3.2 Å). Diese räumliche Nähe deutet darauf hin, dass die Ni-Atome chemisch an MoS_2 gebunden (also darin „eingebaut") sind, was auf eine bimetallische Ni-Mo-S-Phase schließen lässt. Im Unterschied dazu wurde bei den unbehandelten Sulfiden keine Ni-Mo-Komponente beobachtet. Dies wird auf die Prävalenz von NiS_x zurückgeführt und auf den Umstand, dass das Messergebnis eine Mittelung über alle Ni-Spezies darstellt. Ähnliche Schlussfolgerungen konnten aufgrund der Ergebnisse der Röntgen-Nahkantenspektroskopie (XANES) gezogen werden. Die Säurebehandlung führte darüber hinaus auch zu einem im Durchschnitt signifikant kürzeren Ni-Ni-Abstand (2.22 Å gegenüber 2.26 Å), was mit den Bindungsabständen der bekannten Ni-Sulfide unvereinbar ist und daher der Ni-Mo-S-Phase zugeschrieben

wurde. Der Vergleich der EXAFS-Ergebnisse mit simulierten Spektren von Modell-Clustern ergab, dass die Ni-Atome an den MoS$_2$-Kanten höchstwahrscheinlich als annähernd quadratisch-pyramidale NiS$_5$-Einheiten vorliegen (ähnlich zu den Grund-einheiten von Millerit (NiS), einem natürlich vorkommenden Ni-Sulfid).

Die Verteilung von Ni zwischen der aktiven Ni-Mo-S-Phase und inaktivem NiS$_x$ wurde mittels einer Kombination von Titration und geometrischen Betrachtungen analysiert (letztere auf Grundlage der Transmissionselektronenmikroskopie). Zum Zweck der Quantifizierung der Ni-Zentren kam das Sondenmolekül NO zum Einsatz, da es selektiv an koordinativ ungesättigten Metallkationen (CUS) an den Kanten von Ni-MoS$_2$ adsor-biert. Diese betrachtet man gemeinhin als die primären aktiven Zentren von HDS-Katalysatoren. Bei den unbehandelten Sulfiden wurde im Verhältnis zur maximal an den MoS$_2$-Kanten aufnehmbaren Ni-Menge ein vier- bis fünffacher Überschuss ermittelt. Daraus lässt sich schließen, dass der größte Teil des Nickels in Form von segregiertem NiS$_x$ vorlag (90–92 % des gesamten Ni), was gut mit den EXAFS-Ergebnissen überein-stimmt. Dementsprechend wurde der als Ni-Mo-S vorliegende Ni-Anteil zu lediglich 8–10 % bestimmt. Obwohl der Ni-Überschuss nach Säurebehandlung viel geringer war (weniger als zweifach), ist anzunehmen, dass die behandelten Sulfide dennoch erhebliche Mengen an NiS$_x$ enthielten (60–76 % Ni als NiS$_x$ gegenüber 24–40 % als Ni-Mo-S). Es liegt nahe, dass diese säureresistenten Ni-Sulfide als nicht zugängliche („innere") Domänen vorliegen.

Wie durch die höhere spezifische Oberfläche und den höheren Anteil an „aktivem" Ni-Mo-S zu erwarten war, wurde Dibenzothiophen (DBT) an den säurebehandelten Sulfiden mit viel höherer massenspezifischer Aktivität umgesetzt (Faktor 1.6–2.3 bei 330 °C und 50 bar Wasserstoffdruck; gemessen in einem Rieselbettreaktor im Labormaß-stab). Es ist wichtig zu erwähnen, dass die Erhöhung der Rate den Effekt des bloßen Verlusts an inerter Masse übertraf. Das heißt also, dass die Konzentration an aktiven Zentren durch die Säurebehandlung erhöht wurde (durch das Freilegen von Zentren). Die Produktverteilung war über alle Katalysatoren hinweg nahezu identisch und wurde durch die Säurebehandlung nicht beeinflusst, was darauf hindeutet, dass die Zusammensetzung der zuvor bedeckten und im Anschluss freigelegten Oberflächen ähnlich gewesen sein muss.

Die Kombination der HDS-Aktivitätsdaten mit den Titrationsergebnissen ergab eine lineare Korrelation zwischen der CUS-Konzentration und der Rate der direkten Entschwefelung (DDS), was auf das Vorliegen von Zentren mit für sich identischer Aktivität hindeutet (katalytische Wechselzahl: $70\,h^{-1}$ für DDS und $140\,h^{-1}$ für HYD). Im Unterschied dazu wurde bei den unbehandelten Sulfiden keine solche Korrelation beobachtet, was auf die zusätzliche inerte Masse und das Blockieren von aktiven Oberflächenzentren durch NiS_x zurückgeführt wird. Bei den säurebehandelten Sulfiden wurde außerdem auch eine Korrelation zwischen der Konzentration der CUS und der SH-Gruppen ermittelt. Während den CUS als „primären" aktiven Zentren vorwiegend die Aufgabe der Adsorption und Koordination der Reaktanden zukommt, spielen SH-Gruppen bei der Bereitstellung von dissoziiertem Wasserstoff für Hydrierung und Hydrogenolyse eine zentrale Rolle. Dementsprechend unterstreicht diese zweite Korrelation die allgemeine Bedeutung von SH-Gruppen für die HDS-Katalyse und bestätigt frühere Arbeiten, deren Ergebnisse eine feste CUS-SH-Stöchiometrie vermuten ließen.

Die gleichen kinetischen Messungen und Titrationen wurden auch an einem typischen Alumina-geträgerten Ni-MoS$_2$ durchgeführt, wobei sich pro Ni-Atom eine vergleichbare DDS-Aktivität ergab. Im Gegensatz dazu war die Hydrieraktivität bei den ungeträgerten Sulfiden ungleich höher (Faktor 15). Es lässt sich vermuten, dass dies mit einer geringeren mittleren Sanderson-Elektronegativität zusammenhängt, die sich aus der Abwesenheit von Mo-O-Al-Bindungen ergibt. Andererseits ist auch anzunehmen, dass an den gestaffelten Kanten von ungeträgertem Ni-MoS$_2$ eine planare π-Adsorption möglich ist. Diese zusätzliche Adsorptionskonfiguration könnte ebenso zu der gesteigerten Hydrieraktivität beitragen.

Aus akademischer Sicht stellt die Säurebehandlung eine nützliche Prozedur im Vorfeld analytischer Messungen dar. Sie reduziert den Beitrag von segregierten Sulfiden zu Messergebnissen deutlich (z.B. zu EXAFS-Spektren), auch wenn sie das Problem offenbar nicht vollständig löst. Der Hauptgrund dafür liegt in ihrem Unvermögen, die beträchtlichen Mengen an NiS_x aufzulösen, die sich im Inneren der MoS$_2$-Struktur befinden. Zukünftige Arbeiten sollten daher auf die Synthese von ungeträgerten Katalysatoren abzielen, die frei von eben solchen „eingebetteten" NiS_x-Domänen sind. Dies lässt sich beispielsweise dadurch erreichen, dass man gut definierte MoS$_2$-Kristalle mit einer

Ni(II)-Salzlösung versetzt, anschließend sulfidiert und letztendlich einer Säurebehandlung unterzieht. Im Unterschied zum gegenwärtigen Syntheseprotokoll würde diese modifizierte Prozedur sicherstellen, dass Ni-Atome ausschließlich an den zugänglichen MoS_2-Kanten vorhanden wären. Die Abwesenheit von NiS_x bei gleichzeitig gut definierten Strukturparametern der MoS_2-Phase würde die Aussagekraft von Analyseergebnissen wohl deutlich verbessern. Auch ließe sich diese Herangehensweise sicherlich auf andere Metallkombinationen übertragen, z.B. auf Ni-WS_2, für das man aufgrund der ähnlichen Chemie von Mo und W entsprechend ähnliche Ergebnisse erwarten würde. Andererseits könnten sogar geträgerte Sulfide für eine derartige Anwendung geeignet sein, wobei mögliche Einflüsse der Säure auf den Träger sorgfältig ausgeschlossen werden müssten. Aus der Sicht industrieller Anwendung ergibt sich durch die Säurebehandlung eine skalierbare Möglichkeit zur Optimierung von ungeträgerten Katalysatoren. Dies gilt besonders für jene, die bei den anspruchsvolleren Hydrotreating-Prozessen zum Einsatz kommen, beispielsweise bei der HDS von Destillationsrückständen. Die Hydrieraktivität ist dabei oft der sprichwörtliche Flaschenhals, da diese schweren Ausgangsstoffe große Mengen von mehrkernigen Aromaten enthalten, die erst nach einer (Teil-)hydrierung defunktionalisiert werden können (d.h. die H_2-Addition muss vor dem C-S-Bindungsbruch erfolgen).

Der zweite Teil der eigentlichen Forschungsarbeit (Kapitel 5) ist der Deoxygenierung von nachwachsenden Lipiden an Hydrotreating-Katalysatoren gewidmet. Aus den zuvor genannten Gründen wurden auch hier ungeträgerte Sulfide als Grundlage für die Studie gewählt. Angesichts der komplexen Zusammensetzung von natürlich vorkommenden Lipiden wurden die Testreaktionen stattdessen mit Fettsäuren und deren Derivaten als Modellkomponenten durchgeführt, um die Produktanalyse zu vereinfachen. Hierfür kam ein absatzweise betriebener Rührkesselreaktor im Labormaßstab zum Einsatz, wobei die Modellreaktanden in Dodekan verdünnt und bei 300 °C und 5.0 MPa Wasserstoffdruck umgesetzt wurden.

Das Hauptziel der Arbeit bestand darin, das Reaktionsnetzwerk der Fettsäuredeoxygenierung an ungeträgertem Ni-MoS_2 aufzuklären und den dabei ablaufenden Reaktionsmechanismus auf Molekülebene zu verstehen. Um dieses Ziel zu erreichen, wurde eine Reihe von Katalysatoren synthetisiert, die den primären Reaktanden (Hexadekansäure, C_{16}) mit maximal unterschiedlicher Selektivität umsetzen sollten. Von diesen drei

Materialien wies das nicht-promotierte MoS_2 die höchste Selektivität für den Reaktionsweg der Hydrodeoxygenierung auf (94 mol% HDO). Dabei wird der Reaktand unter Wasserabspaltung schrittweise zum entsprechenden Alkan (Hexadekan) reduziert, wobei die Kohlenstoffanzahl der Fettsäure beibehalten wird. Im Gegensatz dazu lief die Reaktion an Ni_3S_2 überwiegend unter Kohlenstoffverlust ab, d. h. es erfolgte eine C-C-Bindungsspaltung am Kohlenstoffatom der Carboxylgruppe (94 mol% Selektivität für die Kohlenstoffverlust-Route, CLR). Das gemischte Ni-Mo Sulfid wies mit einer Selektivität von 45 % HDO und 55 % CLR eine ausgeglichene Produktverteilung auf.

Diese dramatischen Selektivitätsunterschiede erwiesen sich als entscheidender Faktor für die Trennung der Reaktionswege und die Aufklärung des Reaktionsnetzwerks. Es wurde ermittelt, dass die HDO aus einer Reihe von Folgereaktionen besteht, an deren Anfang die C-O-Hydrogenolyse der Fettsäure steht. Auf die Bildung des primären Produkts, Hexadekanal, folgt die Hydrierung zum entsprechenden Alkohol, dann die Dehydratisierung zu 1-Hexadecen und schlussendlich die Hydrierung zu Hexadekan. Eine alternative Reaktionsroute, bei der der Alkohol statt durch Dehydratisierung, durch C-O-Hydrogenolyse umgesetzt wird, konnte experimentell ausgeschlossen werden. Dies erfolgte durch die Analyse der Zusammensetzung der Olefinfraktion und des Olefin-zu-Alkan-Verhältnisses im Verlauf der Reaktion. In ganz ähnlicher Weise konnte anhand der Abwesenheit von Thiolen und der Analyse der gebrauchten Katalysatoren gezeigt werden, dass keine nukleophile Substitution durch SH-Gruppen stattfindet. Wie aufgrund der gleichzeitigen Anwesenheit von Fettsäure und Alkohol zu erwarten war, wurde die Bildung eines C_{32}-Esters als geringfügige Nebenreaktion beobachtet.

Bei der Untersuchung der CLR zeigte sich, dass zusammen mit den flüssigen C_{n-1}-Produkten (Pentadekan und Pentadecene) eine äquimolare Menge CO gebildet wurde. Da sich mit dem Nachweis von CO allein keine Aussage zum genauen Reaktionsmechanismus treffen lässt, wurden Experimente zur weiteren Differenzierung durchgeführt. Insbesondere die folgenden Möglichkeiten zur CO-Bildung wurden dabei betrachtet:

(i) Primäre Bildung von CO_2 und anschließende „Maskierung" durch umgekehrte Wassergas-Shift-Reaktion: Das Vorliegen einer solchen Situation wurde dadurch ausgeschlossen, dass kein CO_2 nachweisbar war, obwohl die berechnete Gleichgewichtskonzentration von CO_2 innerhalb der Nachweisgrenze gewesen wäre.

(ii) Decarbonylierung von Hexadekanal aus der HDO-Route: Der Ausschluss dieser Reaktion erfolgte auf Grundlage von Versuchen mit Hexadekanal als primärem Reaktanden. Dabei wurde Hexadekanal an Ni-MoS_2 fast ausschließlich entsprechend der HDO-Route umgesetzt (mit einer Selektivität von 93 mol%). Der Versuch wurde zudem in Anwesenheit eines Überschusses an Fettsäure wiederholt, um kompetitive Effekte auszuschließen.

(iii) Direkte C-C-Hydrogenolyse von Hexadekansäure zu Ameisensäure und Pentadekan (mit anschließender Zersetzung der Ameisensäure zu CO/H_2O): Diese Alternative wird als unwahrscheinlich erachtet, da weder Formiate, noch gasförmige Ameisensäure nachgewiesen wurden. Gegen eine C-C-Hydrogenolyse der Fettsäure spricht auch die hohe Selektivität für Pentadecene während der Anfangsphase der Reaktion, da C-C-Hydrogenolyse direkt zur Bildung von Pentadekan führen würde.

(iv) Decarbonylierung von oberflächengebundenen Acylium-Ionen zu endständigen C_{n-1}-Olefinen: Dieser zuvor in der Literatur beschriebene Mechanismus konnte nicht eindeutig ausgeschlossen werden. Es wurde aber gezeigt, dass ein alternativer Reaktionsweg existieren muss, dessen Primärprodukt ein C_{n-1}-Alkan ist. Zu diesem Zweck wurde ein Versuch mit einer Fettsäure durchgeführt, die über ein tertiäres β-Kohlenstoffatom verfügt (2-Adamantanylessigsäure). Obwohl diese Verbindung keine Olefinbildung zulässt, wurde sie genauso wie die lineare Fettsäure unter Kohlenstoffverlust umgesetzt.

Die Gesamtheit der Ergebnisse lässt darauf schließen, dass höchstwahrscheinlich ein Keten das primäre Intermediat der CLR ist. Das Keten bildet sich durch Dehydratisierung (C-O-Bindungsspaltung) der Fettsäure an den koordinativ ungesättigten Zentren von Ni-MoS_2 (CUS), die dabei von benachbarten SH-Gruppen unterstützt werden. Die nachfolgende Regenerierung des aktiven Zentrums (Entfernung von gebundenem O) kann für die Gesamtreaktion geschwindigkeitsbestimmend sein, wenn der H_2-Partialdruck geringer als etwa 2.5 MPa ist. Bei höherem Druck (> 2.5 MPa) ist der geschwindigkeitsbestimmende Schritt hingegen die Decarbonylierung des Ketens, welches dabei als η^2(C-C)-Adsorptionskomplex vorliegt. Auf diese Verschiebung des geschwindigkeitsbestimmenden Schritts deuten die in Abhängigkeit vom H_2-Druck beobachteten Veränderungen der Reaktionsordnung hin. Die nachfolgende Eliminierung von CO aus dem Adsorptionskomplex führt zur Bildung einer Ni-gebundenen Carben-ähnlichen Spezies.

Abhängig davon, ob β-H-Atome verfügbar sind, bildet sich daraus im Anschluss entweder ein C_{n-1}-Alkan oder ein endständiges C_{n-1}-Olefin (durch Hydrierung bzw. durch Umlagerung und gleichzeitiger Ni-C-Bindungsspaltung). Dieser mechanistische Ansatz für den katalytischen CLR-Zyklus stimmt gut mit der wohlbekannten Reaktivität von Ketenen überein, insbesondere mit ihrer ausgeprägten Neigung zur Decarbonylierung. Die im Vergleich zu MoS_2 grundsätzlich verschiedene Reaktivität von Ni-MoS_2 wird auf die Anwesenheit von Ni und die damit verbundenen labileren, elektronenreicheren Schwefelzentren zurückgeführt. Es ist zu beachten, dass Ni-Sulfide (hier in Form von Ni_3S_2) ebenfalls eine ausgeprägte Selektivität für CLR aufweisen, wenngleich ihr Beitrag im Vergleich zu den Ni-promotierten Zentren der Ni-Mo-S-Phase vernachlässigbar ist. Auch die signifikanten Unterschiede in der scheinbaren Aktivierungsenergie deuten darauf hin, dass NiS_x kaum an der CLR-Aktivität von Ni-MoS_2 beteiligt ist.

Die hier vorgestellten Ergebnisse über Fettsäuredeoxygenierung zeigen, dass die Fähigkeit zur Spaltung von C-C-Bindungen eine inhärente Eigenschaft der aktiven Zentren von sulfidischen Hydrotreating-Katalysatoren ist. Das heißt, die katalytischen Merkmale, die eine hohe HDS- und HDN-Aktivität bei erdölbasierten Ausgangsstoffen ermöglichen, sind gleichzeitig auch jene, die zur unerwünschten CO-Bildung beim Hydrotreating von erneuerbaren Lipiden führen. Besonders im Hinblick auf die angestrebte Lipid-beimischung zu Erdölfraktionen (Co-Processing) erweist sich dieser Umstand als sehr ungünstig, da rein katalysatorbasierte Strategien zur CO-Vermeidung zu nachteiligen Effekten bei der Umsetzung des primären Ausgangsstoffs führen könnten. Möglicherweise könnte ein planvolles, rationales Vorgehen bei der Katalysatorentwicklung diesen Widerspruch zumindest teilweise auflösen. Es ist dennoch nötig, weitere Prozess-parameter wie die Temperatur, den Druck und die Zusammensetzung des Ausgangs-gemisches zu berücksichtigen, um das Co-Processing von erneuerbaren Lipiden im großen Maßstab zu realisieren. Da diese Zielkonflikte für jeden Einzelfall gesondert betrachtet werden müssen, ist zu erwarten, dass das Hydrotreating von Lipiden auch weiterhin eine große Herausforderung bleibt.

List of publications

Research articles published in peer-reviewed journals (first author)

Wagenhofer, M. F.; Shi, H.; Jentys, A.; Gutiérrez, O. Y.; Lercher, J. A. Enhancing hydrogenation activity of Ni-Mo sulfide hydrodesulfurization catalysts. *Sc. Adv.* **2020**, 6**,** eaax5331.

Wagenhofer, M. F.; Baráth, E.; Gutiérrez, O. Y.; Lercher, J. A. Carbon-carbon bond scission pathways in the deoxygenation of fatty acids on transition-metal sulfides. *ACS Catal.* **2017**, 7, 1068-1076.

Research articles published in peer-reviewed journals (co-author)

Albersberger, S.; Wagenhofer, M. F.; Han, J.; Gutiérrez, O. Y.; Shi, H.; Lercher, J. A. On the enhanced catalytic activity of acid-treated, trimetallic Ni-Mo-W sulfides for quinoline hydrodenitrogenation. *J. Catal.* **2019**, 380, 332-342.

Luo, W.; Shi, H.; Wagenhofer, M. F., Gutiérrez, O. Y., Lercher, J. A. Maximizing Active Site Concentration at Ni-substituted WS_2 Edges for Hydrogenation of Aromatic Molecules. *J. Phys. Chem. Lett.* **2019**, 10, 5617-5622.

El-Sayed, H. A.; Burger, V. M.; Miller, M.; Wagenbauer, K.; Wagenhofer, M. F.; Gasteiger, H. A. Ionic Conductivity Measurements: A Powerful Tool for Monitoring Polyol Reduction Reactions. *Langmuir* **2017**, 33, 13615-13624.

Schallmoser, S.; Ikuno, T.; Wagenhofer, M. F.; Kolvenbach, R.; Haller, G. L.; Sanchez-Sanchez, M.; Lercher, J. A. Impact of the local environment of Brønsted acid sites in ZSM-5 on the catalytic activity in n-pentane cracking. *J. Catal.* **2013**, 316, 93-102.

Conference contributions

Albersberger, S.; Wagenhofer, M. F.; Gutiérrez, O. Y.; Lercher, J. A. Hydrogenation and C-N bond cleavage of aromatic compounds on Ni-Mo-W sulfides. Poster presentation, *25th North American Catalysis Society Meeting* **2017**, Denver (Colorado), United States.

Wagenhofer, M. F.; Gutiérrez, O. Y.; Lercher, J. A. Less is More: Post-synthetic Removal of Inactive Nickel from Ni-MoS$_2$ Hydrotreating Catalysts. Poster presentation, *50. Jahrestreffen Deutscher Katalytiker* **2017**, Weimar, Germany.

Albersberger, S.; Wagenhofer, M. F.; Gutiérrez, O. Y.; Lercher, J. A. Hydrogenation and C-N bond cleavage of aromatic compounds on Ni-Mo-W sulfides. Poster presentation, *50. Jahrestreffen Deutscher Katalytiker* **2017**, Weimar, Germany.

Wagenhofer, M. F.; Baráth, E.; Gutiérrez, O. Y.; Lercher, J. A. Fourth-row transition metals as promoters in biomass deoxygenation. Poster presentation, *7th International Symposium on the Molecular Aspects of Catalysis by Sulfides* **2016**, Doorn (Utrecht), The Netherlands.

Wagenhofer, M. F.; Baráth, E.; Gutiérrez, O. Y.; Lercher, J. A. Teaching new tricks to an old catalyst: Optimization of conventional hydrotreating catalysts for the co-processing of biomass-derived oils. Poster presentation, *48. Jahrestreffen Deutscher Katalytiker* **2015**, Weimar, Germany.

Gärtner, C. A.; Wagenhofer, M. F.; Müller, S.; van Veen, A. C.; Lercher, J. A. Kinetic and mechanistic aspects of the oxidative dehydrogenation of ethane over supported eutectic alkali-chloride catalysts. Poster presentation, *45. Jahrestreffen Deutscher Katalytiker* **2012**, Weimar, Germany.

Other contributions

Wagenhofer, M. F.; Baráth, E.; Gutiérrez, O. Y.; Lercher, J. A., Schlussbericht zum Verbundvorhaben AUFWIND – Algenproduktion und Umwandlung in Flugzeugtreibstoffe: Wirtschaftlichkeit, Nachhaltigkeit, Demonstration; Teilvorhaben 9: Algenöl Jet-A1 Produktion auf Basis konventioneller Raffinerietechnologien. *Fachagentur Nachwachsende Rohstoffe e.V.* **2016**, Gülzow-Prüzen, Germany, www.fnr.de (09.08.2019).